

Vector Chiral Phases in Frustrated Systems



Inaugural-Dissertation
zur
Erlangung des Doktorgrades
der Mathematisch-Naturwissenschaftlichen Fakultät
der Universität zu Köln
vorgelegt von

Hannes Schenck
aus Berlin-Wilmersdorf

Universität zu Köln
2015

Berichterstatter: Prof. Dr. Thomas Nattermann
Prof. Dr. Joachim Krug

Tag der letzten mündlichen Prüfung: 23.06.2015

Diese Arbeit ist meinen Eltern *Ingolf & Annette* gewidmet

Zusammenfassung

Die vorliegende Dissertation setzt sich aus zwei verschiedenen Teilen zusammen. Der erste Teil der Arbeit befasst sich mit der Untersuchung von chiraler Ordnung und ihrem Ursprung in frustrierten Wechselwirkungen. Zunächst wird das Konzept von Phasenübergängen und deren Relation zu der dem System zugrunde liegenden Symmetrie beschrieben. Hier wird diskutiert wie die diskrete \mathbb{Z}_2 -Symmetrie der Ising-Spins und die kontinuierliche $SO(2)$ -Symmetrie der XY-Spins in zwei Dimensionen zu fundamental verschiedenen Phasenübergängen führen. Als nächstes werden verschiedene Formen von chiraler Ordnung diskutiert, sowie deren experimentelle Realisierung. Chirale Ordnung bricht die diskrete Inversions-Symmetrie (\mathbb{Z}_2), die simultan mit der $SO(2)$ -Symmetrie der XY-Spins auftreten kann. Eine zentrale Fragestellung der Arbeit ist, zu klären, wie die Phasenübergänge sich durch das Auftreten der zusätzlichen Symmetrien verändern. Als archetypisches Modell für das gleichzeitige Auftreten von diskreter und kontinuierlicher Symmetrie wird das sogenannte helikale XY-Modell untersucht. Das Modell selbst wird als Erweiterung des klassischen XY-Modells eingeführt und ausführlich diskutiert. Es wird beschrieben, wie durch die Einführung einer frustrierten Wechselwirkung das System einen chiralen Grundzustand ausbilden kann und welche verschiedenen Ansätze es gibt, die simultanen Symmetrien zu untersuchen. Zusätzlich wird eine mesoskopische Version des Modells abgeleitet.

Zunächst wird der Phasenübergang der chiralen Ordnung diskutiert. Hier wird mittels des Variationsprinzips die kritische Temperatur für den Übergang gefunden sowie die Abhängigkeit der Temperatur vom Spiral-Winkel θ der Grundzustandsspirale. Anschließend wird der Effekt von chiraler Ordnung auf den Berezinskii-Kosterlitz-Thouless (BKT) Übergang der $SO(2)$ -Symmetrie in dem Modell untersucht. Die für den BKT-Übergang verantwortlichen Vortizes werden auf kleinen und großen Skalen diskutiert und die Energiekosten des Vortex-Kerns abgeschätzt. Mittels Renormierungsgruppen-Rechnung werden die Effekte der Vortizes auf den Phasenübergang untersucht und deren kritische Exponenten bestimmt. Anschließend wird die anomale Skalierungsdimension des chiralen Übergangs bestimmt. Die Daten der numerischen Simulationen von Sorokin et al. werden verwendet, um die kritischen Exponenten zu bestimmen und mit den errechneten Werten zu vergleichen. Das entstehende Phasendiagramm wird beschrieben sowie mögliche experimentelle Systeme und die Relation zu anderen theoretischen Arbeiten werden diskutiert.

Weiterführend wird näher auf den Zusammenhang zwischen chiraler Ordnung und Polarisation in multiferroischen Systemen eingegangen. Verschiedene Mechanismen für die Kopplung von magnetischer und elektrischer Ordnung werden diskutiert und ausgehend von Symmetrie-Überlegungen wird das HXY-Modell um eine Wechselwirkung mit einem elektrischen Feld erweitert. Diskutiert werden die Effekte der Polarisation auf die Domänenwände im System. Die resultierenden Sattelpunktgleichungen werden näherungsweise gelöst und mit numerischen Resultaten verglichen. Des Weiteren wird die effektive Wechselwirkung zwischen den chiralen Domänenwänden und den Domänenwänden in der Polarisation ermittelt und als gegenseitige Anziehung identifiziert.

Als konkretes Beispiel eines multiferroischen Materials wird das Material $MnWO_4$ näher diskutiert. Hier koppelt chirale Ordnung an Polarisation gekennzeichnet durch einen magnetischen Phasenübergang, der mit dem Auftreten einer messbaren Polarisation einhergeht. Hier wurde in Zusammenarbeit mit der Arbeitsgruppe von Prof. J. Hemberger das kritische Verhalten an dem Phasenübergang untersucht. Zunächst werden die beobachteten Phasenübergänge in $MnWO_4$

beschrieben und näher auf die Kristallsymmetrie eingegangen. Ausgehend von der von Tolédano bestimmten Ginzburg-Landau Freien Energie des Systems wird der Phasenübergang klassifiziert und das kritische dynamische Verhalten bestimmt. Die resultierenden Exponenten werden mit der experimentellen Arbeit der Arbeitsgruppe von Prof. J. Hemberger verglichen.

Im zweiten Teil der Arbeit wird das dynamische Verhalten von Vortizes in dünnen supraleitenden Filmen untersucht. Zunächst wird ein historischer Überblick über die Entdeckung der Supraleitung gegeben und anschließend auf deren phänomenologische Beschreibung eingegangen. Danach wird das Phänomen von supraleitenden Vortizes diskutiert und auf die Besonderheiten von Vortizes in dünnen Filmen eingegangen sowie deren Wechselwirkung mit einem extern angelegten Strom.

Zu Beginn wird der experimentelle Aufbau, der von der Arbeitsgruppe um Prof. E. Zeldov verwendet wird, beschrieben. Studiert werden hier Vortizes in dünnen supraleitenden Blei Filmen mittels SQUID-on-tip Raster-Mikroskopie. Bei angelegtem Strom können Vortizes in den Film eintreten indem sie eine Eintrittsbarriere überwinden. Diese Barrieren werden diskutiert und der Effekt auf die messbaren Strom-Spannungskurven wird bestimmt. Die Resultate werden mit den zur Verfügung stehenden experimentellen Werten verglichen.

Abschließend wird die Dynamik der Vortizes in den Filmen untersucht. Hier liegt das Augenmerk vor allem auf dem Effekt einer inhomogenen Stromdichte resultierend aus der experimentell angebrachten Verengung der dünnen Bleistreifen. Erklärt werden soll die Linienbildung der sich bewegenden Vortices, sowie das Entstehen von Verzweigungspunkten in diesen Linien. Es werden verschiedene Ansätze und effektive Modelle für die wechselwirkenden Vortizes diskutiert und deren Schwachstellen dargestellt.

Abstract

The present dissertation consists of two parts. The first part of this work deals with the study of chiral order that has its origin in frustrated interactions. First of all, the basic concept of phase transitions and their relation to the underlying symmetry will be described. Here we will discuss how the discrete \mathbb{Z}_2 symmetry of the Ising spins and the continuous $\text{SO}(2)$ symmetry of the XY spins leads to fundamentally different phase transitions. Next, different forms of chiral order will be discussed, as well as their experimental realizations. Chiral order breaks the discrete inversion symmetry (\mathbb{Z}_2), which can appear simultaneously with the $\text{SO}(2)$ symmetry of the XY spins. One of the central questions of this work is how the phase transitions are influenced by the additional symmetries. As an archetypical model for the simultaneous existence of both a discrete and continuous symmetry, the so-called helical XY model will be studied. The model itself will be introduced as an extension to the classical XY model and will be discussed in detail. It will be described how the addition of a frustrated interaction leads to a chiral ground state and different approaches to dealing with these simultaneous symmetries are mentioned. Additionally, the mesoscopic version of the model will be derived.

We will start with the discussion of the chiral order phase transition. Using a variational method, the critical temperature of the transition and its dependence on the chiral pitch angle θ will be found. Afterwards, the effect of the chiral order on the Berezinskii–Kosterlitz–Thouless (BKT) transition of the $\text{SO}(2)$ symmetry will be studied. The vortices responsible for the BKT transition will be discussed on short and large length scales and the energy cost of the vortex cores is estimated. Using the renormalization group technique, the effects of the vortices on the phase transition is studied and their critical exponents are estimated. Afterwards, the anomalous scaling dimension of the chiral transition is calculated. The data of the numerical simulations done by Sorokin et al. are used to determine the critical exponents and compare them to the analytic calculations. The resulting phase diagram for the HXY model is calculated and its relation to possible experimental systems and other theoretical works is discussed.

We will continue with a closer look at the relation between chiral order and polarization in multiferroic systems. Different mechanisms for the coupling of magnetic and electric order are discussed and, starting from a symmetry argument, the HXY model will be extended by an interaction with the electric field. The effect of the polarization on the domain walls of the system will be studied. The resulting saddle-point equations will be solved perturbatively and are compared to numerical results. Additionally, an effective interaction between the chiral domain walls and the polarization walls will be derived and identified as an attractive interaction.

As a concrete example of a multiferroic material, the material MnWO_4 will be studied. Here the chiral order couples to the polarization, as indicated by a magnetic phase transition with an accompanied onset of polarization. In collaboration with D. Niermann and the group of Prof. J. Hemberger, the critical behavior of the phase transition was studied. First the different phase transitions in MnWO_4 will be described and the crystal symmetry will be discussed. Starting from the Ginzburg–Landau free energy expansion done by Tolédano, the phase transitions will be classified and the critical dynamical behavior described. The resulting critical exponents are compared to the experimental work of the group of Prof. J. Hemberger.

In the second part of this work, the dynamical behavior of vortices in thin superconducting films is studied. First, a historical overview of the discovery of superconductivity is given,

followed by a discussion of its phenomenological description. Afterwards, the phenomenon of superconducting vortices is discussed and the special features of vortices in thin films and their interaction with an applied current are presented.

We start with a description of the experimental setup used in the group of Prof. E. Zeldov. They study vortices in thin superconducting lead films with the SQUID-on-tip raster microscopy. In the presence of an applied current, vortices can enter the thin strips by overcoming an entry barrier. These barriers are discussed and their effect on the measurable current–voltage curves is calculated. The results are compared to the available numerical data.

Finally, we study the dynamics of the vortices in thin films. The focus is on the effect of inhomogeneous current densities, a result from experimentally imposed constrictions in the thin films themselves. The task is to explain the formation of lines in the moving vortices and the existence of bifurcation points in said lines. Several approaches and effective models are used to study the interacting vortices, the results and shortcomings are discussed.

Contents

Contents	vii
I Vector-Chirality and Spin-Liquid in Frustrated Systems	1
1 Introduction	3
1.1 Magnetic systems	4
1.2 Discrete and continuous symmetry in ferromagnets	6
1.3 Vector and scalar chiral order parameters	9
1.4 Physical realizations and experimental systems	11
1.5 Outline	13
2 The Model	15
2.1 The classical model	15
2.2 Quantum chain	20
2.3 Landau–Ginzburg–Wilson Hamiltonian	22
3 Chiral Transition	27
3.1 The variational approach	27
3.2 The solutions	31
3.3 Discussion	33
4 Renormalization Group	35
4.1 Vortices	35
4.2 Long–range interaction in Ising order parameter model	36
4.3 RG - small scales	37
4.4 RG - large scales	38
4.5 Anomalous dimension of chiral transition	42
4.6 Comparison to numerics	44
4.7 Phase diagram	45
4.8 Discussion	48
5 Multiferroics	53
5.1 Connection between chiral order and polarization	54
5.2 One–dimensional domain wall	56
5.3 Two–dimensional domain wall	65
5.4 Domain wall in “four-state” model	67
6 MnWO₄	71
6.1 Material properties and observed phase transitions	71
6.2 Group theory construction of Ginzburg–Landau free energy	71
6.3 Classification of phase transitions and critical dynamics	74
6.4 Dynamical exponent at AF3 → AF2	76

6.5	Discussion	79
II	Vortices in Supraconducting Thin Films	81
7	Introduction	83
8	Experimental Data	85
8.1	Experimental setup	85
8.2	Current–Voltage curves	88
8.3	Vortex dynamics	89
9	Superconductivity	91
9.1	Vortices	93
9.2	Vortex interaction	95
10	Current–Voltage Curves	97
10.1	Bardeen–Stephen flow	99
10.2	Surface barrier	101
10.3	Discussion	106
11	Vortex Dynamics	107
11.1	The Corbino disk setup	107
11.2	The current distribution in the Corbino disk	109
11.3	Non–local theory	110
11.4	Simple model for current–vortex interaction	114
11.5	Vortex–Current interaction - thin strip	117
11.6	Vortex–Current interaction - Corbino disk	120
11.7	Discussion	123
III	Appendix	125
A	Appendix: Model	127
A.1	XY quantum chain	127
A.2	Kolezhuk mapping	129
B	Appendix: Renormalization Group	131
B.1	Vortex core energy integral	131
B.2	Fourier transform in x -direction	132
B.3	Calculating the constant pre-factor $f(0)$	133
B.4	Calculating the $f(z \rightarrow \infty)$ limit	135
B.5	Solving the full Fourier transform	135
B.6	Solving $f(z)$ via ODE	136
B.7	Numerical calculation of the constant c_x	137
B.8	Numerical data from Sorokin et al.	138
C	Appendix: Multiferroics	141
C.1	Integral Approximation	141
C.2	Python code for numerics	142

D Appendix: MnWO₄	147
D.1 Different forms of order parameters	147
D.2 Transition at T_N : temperature fluctuations in \tilde{S}_1	148
D.3 Transition at T_2 : Frozen \tilde{S}_1 order parameter	150
E Appendix: Experiment	153
E.1 Material properties of lead	153
F Appendix: Vortex Dynamics	155
F.1 Detailed overview of current distribution	155
F.2 Derivation of main equations	159
F.3 Limiting cases and solutions to integral equations	162
F.4 Numerical approach	165
Bibliography	171

Part I

Vector-Chirality and Spin-Liquid in
Frustrated Systems

1. Introduction

A material can be classified by its macroscopic properties such as density, volume, magnetization, resistivity and many more. In some cases, the macroscopic state can be changed by continuously varying an external parameter, such as the temperature, the applied magnetic field or the pressure. The system will undergo an abrupt change in one or more of its physical properties at a certain point in the parameter space of the external fields.

There are many examples of phase transitions in nature. To give a little idea of their diversity, we want to name just a few. The most commonly known example is the melting of a solid, as can be seen in water when melting an ice cube. Here the system changes from a ridged solid to a fluid. Another example is the ferromagnet to paramagnet transition in magnetic materials such as iron (Fe). Here, the magnetization vanishes at the Curie temperature when heating up the material. There are also structural phase transitions. In the material bariumtitanat (BaTiO_3), varying the temperature results in a change of the crystal structure, [1]. This is accompanied by a resulting electric dipole moment in each crystal cell and a global electric polarization. Another famous example are superconductors like lead (Pb). Here, the system switches from a finite resistance to superconductivity after the system is cooled below a critical temperature. A more detailed list and other examples can be found in standard literature such as [1, 2].

Essentially there are two ways in which a system can change from one phase to another. In the first case, the phases on either side of the transition line also coexist exactly at the transition, [3]. The phases still carry their distinct microscopical properties and are still distinguishable from each other despite the system being at phase transition. Away from the transition, the system will be in a unique phase that is continuously connected to the coexistence phase at the transition. One example for this type of transition is the melting of a solid in three dimensions, e.g. ice. In this case both the solid and liquid phase of water coexist. Additional heat is needed to drive the transition while there is no increase in the observed temperature of the mixture. In a situation like this, we expect a discontinuity in one or more thermodynamic quantities, [3]. In the case of melting, this is reflected by a discontinuous change in entropy (first derivative of the free energy with respect to the temperature) of the system and the accompanied latent heat. Systems like this, where the phases coexist and the first derivative of the thermodynamic potential is discontinuous, are classified as first order or discontinuous transitions, [3]. In general they display a finite correlation length.

In the case of continuous phase transitions, the correlation length diverges at the critical point. Fluctuations are then correlated on all length scales throughout the whole system, forcing it into a unique state at the phase transition, [3]. In the case of a ferromagnet approaching the Curie temperature, the magnetization (first derivative of the free energy in respect to the applied field) continuously varies to zero. At the critical point the system is in a unique state without magnetization. As opposed to the first order transition, in this case we cannot identify coexisting regions with and without magnetization. However the susceptibility (second derivative of the free energy with respect to the applied field) diverges at the transition. This is an example of a second order or continuous phase transition. In general a phase transition in a system is connected to a singularity in the appropriate thermodynamic potential or its derivatives, [2].

In a lot of cases it is possible to identify a phase by its symmetry properties. A crystal for example, depending on its crystal structure, is invariant under certain discrete translations, discrete rotations around selected axis and points and other operations, all systematically classified

in the so called space groups, [1]. After melting, the system turns into a liquid that now exhibits continuous translation and rotation symmetry.

1.1 Magnetic systems

The microscopic origin of the magnetization is due to the spin of electrons in incomplete atomic shells, such as the f and d shell of transition metal atoms in iron, nickel, and cobalt, [4]. Each electron carries one Bohr magneton μ_B of magnetic moment, [4]. In the ferromagnetic phase all these moments are aligned, resulting in a global magnetization of the material. This is due to an interaction between the magnetic moments that favors alignment in the ferromagnetic case and anti-alignment in the antiferromagnetic case.

Naively one might expect that the magnetic moments mainly interact via their magnetic dipoles. This is not the case. The magnetic interaction strength of two magnetic moments is of the order of $\mu_B^2/d^3 \sim 1K$, where we estimate the average distance d between the atoms with 1\AA , [5]. Comparing this to the observed Curie temperature in e.g. Fe with $T_C \sim 1043K$, we see that the interaction energy is lower by several orders of magnitudes. The dipole-dipole interaction is not strong enough to explain the high transition temperature.

Even without a direct force interaction between the spins, the quantum-mechanical symmetry constrain placed on the wave function will lead to an effective spin-spin interaction. To simplify the discussion, we will consider the case of two atoms with one free electron each. The complete wave function of the system is antisymmetric when switching the two electrons, due to their fermionic nature. Ignoring relativistic effects, the Schrödinger equation does not take the spin of the particles into account. The spin wave function and the orbital or position wave function are then independent of each other and the full wave function can be represented as the product of both, [6]. A symmetric orbital wave function then implies an anti-symmetric spin wave function and vice versa, in order to satisfy the anti-symmetry constraint of the full wave function. The system can now reduce the Coulomb repulsion between the two electrons by forming a symmetric spin state. In this case, the state of the two electrons is antisymmetric with a nodal point in between the two atoms. The probability of the electrons is now lowered in the exact region where their coulomb repulsion would be the strongest. On the other hand, the kinetic energy, i.e. gradient terms, associated with the anti-symmetric wave function is higher then for the symmetric one. Now depending on the ratio of repulsion energy versus kinetic energy, the system will favor the alignment or anti-alignment of the spins. In the case of iron the Coulomb repulsion term dominates, leading to the system favoring the alignment of the spins, i.e. ferromagnetic interaction. In the H_2 molecule, the actual overlap of the orbitals is small and the kinetic energy is the more important term, favoring anti-alignment of the spins. This is an easy example of anti-ferromagnetic interaction, [7, 8]. The interaction between the neighboring spins \hat{S}_1 and \hat{S}_2 can be simplified as $J\hat{S}_1\hat{S}_2$, where all the microscopic details are absorbed in the constant J . The sign of J determines the type of interaction and is ferromagnetic for $J < 0$ and anti-ferromagnetic for $J > 0$.

In materials like iron, the melting temperature T_M is significantly higher than the Curie temperature T_C . In the case of iron we have $T_M - T_C \sim 800K$. When focusing on the magnetic transitions around T_C , we are far away from the melting transition and can ignore structural changes in the lattice configuration. The system can then be treated as a collection of interacting spins on a fixed lattice as

$$H = \sum_{ij} J_{ij} \hat{S}_i \hat{S}_j \quad (1.1)$$

where the lattice information is contained in the coefficients J_{ij} . Depending on the lattice

anisotropies or crystal fields from neighboring atoms, the spins $\hat{\mathbf{S}}_i$ can be restricted to a plane (XY spins) or even to just one axis (Ising spins). The complete structure of the phases and the physics of the phase transition is encoded in the configuration of the spins $\{\hat{\mathbf{S}}_i\}$ on the sites i .

Let us look at the example of a simple uniaxial ferromagnet, where crystal field anisotropies restrict the spin on each site to one axis, allowing only the alignment or anti-alignment with said axis, [3]. Ignoring quantum effects, we can replace the spin at each site by a classical variable s_i that can take on the values ± 1 . In general, the phases can be classified by the n -point correlation function

$$G_n = \underbrace{\langle s_i s_j \dots s_k \rangle}_n. \quad (1.2)$$

Here, the different phases can be classified by the one-point correlation function G_1 , i.e. the average magnetization $m = G_1 = \langle s_i \rangle$. In the ground state of the system all spins will be aligned and form the ferromagnetic phase $m = \pm 1$. In the paramagnetic phase at high temperatures, the spins will fluctuate and, on average, not take on a specific value. In this case the magnetization vanishes and we have $m = 0$. The change of magnetization as a function of temperature $m(T)$ without an applied field is shown in figure 1.1. We see that the magnetization continuously goes to zero and we are dealing with a second order or continuous phase transition at the Curie temperature.

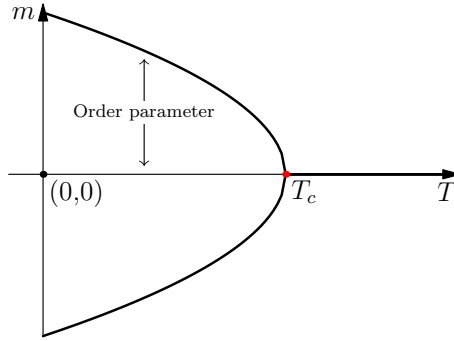


Figure 1.1: Zero-field magnetization of a classical ferromagnet without an applied field $H = 0$. We see a spontaneous magnetization $\pm m(T)$ below the critical temperature. The graphic is similar to the one used in [2].

One can also look at this phase transition in terms of a change in symmetry. Imagine the magnetic moment being caused by a circular current. Reversing time will now reverse the direction of the current and consequently flip the sign of the resulting magnetic moment. In mathematical language this means that the time reversal operator $\hat{T} : t \mapsto -t$ will flip the spin $\hat{\mathbf{S}}_i$ as $\hat{T}\hat{\mathbf{S}}_i\hat{T}^{-1} = -\hat{\mathbf{S}}_i$. We can see that the simple magnetic Hamiltonian (1.1) is invariant under time reversal. The magnetization $\langle \hat{\mathbf{S}}_i \rangle$, however, is not. In the present case of classical discrete spins s_i this means that $m(T) \mapsto -m(T)$ under time reversal, making the ground state $m(T) \neq 0$ doubly degenerate. The paramagnetic case $m(T) = 0$, the state of the system is invariant under time reversal. Once we cool the system below the critical temperature, the magnetization takes on either a positive or negative magnetization. The state $m(T) \neq 0$ is not invariant under time reversal and the transition has broken said symmetry. Which sign it chooses is determined by chance and the whole process is referred to as spontaneous symmetry breaking. This discrete symmetry, where the ground state with m and $-m$ is doubly degenerate, is mathematically described by its associated symmetry group \mathbb{Z}_2 , containing the symmetry operations leaving

the system invariant. Here it consists just of the identity and time reversal operation \hat{T} . The breaking of the symmetry is shown in figure 1.1.

In addition to the temperature T , we can also vary the applied field H . The phase diagram of this general ferromagnet to paramagnet transition is shown in figure 1.2. Here a line of first order transition connects the origin ($T = 0, H = 0$) with the critical point ($T = T_C, H = 0$). In

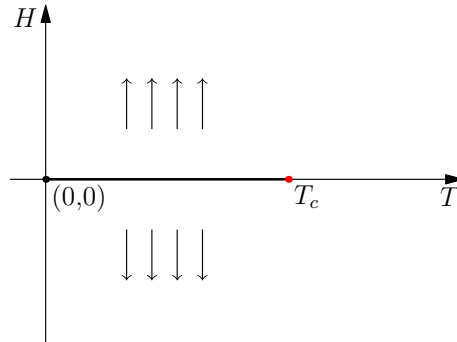


Figure 1.2: General phase diagram of a ferromagnet and the zero field magnetization, similar to the one shown in, [2]. The phase diagram shows a line of first order transition for $H = 0$ that ends in the critical point at T_C .

the case of an applied field $H \neq 0$, the spins try to align with it. For $T < T_C$, approaching the $H = 0$ line will now depend on the history of H , since the limits $H \rightarrow 0+$ and $H \rightarrow 0-$ give different values $\pm m(T)$, [3]. Going from $H > 0$ to $H < 0$ we will now encounter a sudden jump in the magnetization when crossing $H = 0$. As discussed earlier, this discontinuity marks a first order transition. For $T > T_C$ the system moves continuously from one state to the other and since the correlation length stays finite, no phase transition occurs. Only when moving through the critical point at ($T = T_C, H = 0$) will we encounter a diverging correlation length and second order phase transition. We see that the simple uniaxial ferromagnet is a good example for both first and second order phase transitions. Additionally this shows how phases can be classified by their n -point correlation function and their symmetry. There are different types of symmetry besides the simple time reversal symmetry and as we will see now, they determine the types of possible phase transition. We will now take a closer look at the difference between discrete symmetries, e.g. time reversal, and continuous symmetries, e.g. rotations, by looking at different example systems.

1.2 Discrete and continuous symmetry in ferromagnets

In statistical physics one of the most studied systems is the classical Ising model for ferromagnetism. Like in the case of the uniaxial ferromagnet, the spins $s_i = \pm 1$ are taken to be discrete. They are placed on a lattice, with the sites labeled by the index i , and interact only with their nearest neighbors. The ground state of the system is doubly degenerate with all spins being up $s_i = +1$ or all spins being down $s_i = -1$, which classifies as the discrete \mathbb{Z}_2 symmetry. The case of the one-dimensional Ising chain was solved by Ising himself in 1924 during his dissertation done under Lenz, [9], and does not show a phase transition for a finite temperature $T \neq 0$. This can be understood when looking at the energy cost of a simple domain wall. In discrete systems, such as the classical Ising model, the domain wall energy scales as $L^{(d-1)}$, [10]. For a one-dimensional chain, the domain wall (DW) energy is constant and does not scale with the

system size. The Ising model without on-site disorder is invariant under translations by multiples of the lattice constant. The energy of the domain wall is therefore not dependent on its absolute position in the chain and once it is created, moving the domain wall does not cost additional energy. This freedom in placement of the DW means that the system can increase its entropy and therefore lower its free energy by creating such a wall. The entropy gain is dependent on the possible positions of the DW and therefore on the system size. In the thermodynamic limit of the one-dimensional system, meaning an infinite chain, the entropy gain S diverges, while the DW energy E is a finite quantity. We can easily see that the free energy

$$F = E - TS \tag{1.3}$$

will favor the creation of DW for any temperature $T \neq 0$. The system stays in the paramagnetic phase for all finite temperatures and no phase transition occurs. The situation is different in two dimensions, where the DW energy scales with the system size. Now one has to look exactly at their scaling to see whether or not there is a finite temperature after which the system will favor DW and destroy any magnetization. Here the system does exhibit ferromagnetic order. This was first proven in 1936 by Peierls, [11]. Taking a fixed array of spins, he introduced boundaries passing between spins with opposite sign, separating the system in open and closed boundaries. Open boundaries start and end on the edges of the arrays, while closed ones encircle a finite area inside the array. He could show that for sufficiently low but finite temperature, the area covered by these open and closed boundaries is small compared to the system size. The majority of spins is therefore aligned and the system shows ferromagnetic order, [11]. Later the model was solved analytically by Onsager in 1944, [12], showing the existence of a phase transition.

The situation is different for two-dimensional magnetic systems with a continuous symmetry $SO(2)$, such as the classical XY model. They are known to exhibit no true long-range order for any finite temperature $T > 0$, i.e. ferro- or anti-ferromagnetism vanishes in the onset of thermal fluctuations. In other words, the continuous symmetry of the system cannot be broken spontaneously in two dimensions. A simple physical explanation for this can be given by energy considerations of the domain wall separating different regions of magnetic order. Considering the continuously varying magnetization $\mathbf{m}(\mathbf{x})$, the energy of the domain wall of a region of size L is given by the following term in the Ginzburg–Landau expansion $\int d^d x (\nabla \mathbf{m})^2 \propto L^{d-2}$ scaling, as shown, as L^{d-2} with the general dimension d of the system, [10]. For $d = 2$ one can see that the surface energy of the magnetic domain does not increase when expanding the size of the domain itself. The finite domain wall cost is then outweighed by the entropic gain to the system, leading to the destruction of long-range order. A rigorous proof of this statement has been done by Mermin and Wagner in 1966, [10, 13]. On a first glance, one would think that there are no phase transitions in the simple XY model, with a vanishing magnetization or one-point correlation for any temperature.

However the 2D system with $SO(2)$ symmetry still exhibits a phase transition where quasi-long-range order (QLRO) is established, famously discussed by Berezinskii in 1971, [14], and Kosterlitz and Thouless in 1973, [15] now known as the *Berezinskii–Kosterlitz–Thouless transition* (BKT). The transition is well-understood as the dissociation of topological defects in the spin configuration known as vortices, [10]. In this case, the different phases are classified by the two-point correlation function $G_2 = \langle \hat{\mathbf{S}}_i \hat{\mathbf{S}}_j \rangle$. Since the BKT mechanism is important later on, we will go into a little more detail concerning the XY model.

The XY model

The XY model consists of planar Heisenberg spins $\mathbf{S}_i = (\cos(\phi_i), \sin(\phi_i), 0)$ each living on a square lattice site i . Next neighbors on the lattice are ferromagnetically coupled with $K = \beta J > 0$ as

$$\beta H_{XY} = -K \sum_{\langle i,j \rangle} \mathbf{S}_i \mathbf{S}_j = -K \sum_{\langle i,j \rangle} \cos(\phi_i - \phi_j), \quad (1.4)$$

where the sum runs over the next-neighbor pairs $\langle i, j \rangle$. As discussed in the introduction and known from the Mermin–Wagner theorem, a 2D system with the presented local interaction and SO(2) symmetry does not exhibit a long range ordered state for a finite temperature $T = \beta^{-1} > 0$. With the average magnetization $G_1 = \langle \mathbf{S}_i \rangle = 0$ for all $T \neq 0$, it is not suited to classify the different phases. Instead we will use the correlator $G_2 = \langle \mathbf{S}_0 \mathbf{S}_{\mathbf{r}} \rangle$. The position vector \mathbf{r} has been used instead of the simple index i for the corresponding lattice site, to illustrate the spatial dependence in the correlator better. A good discussion of the different ordered states in the XY model and the phase transition is discussed in standard textbooks, such as [10]. The short summary here will follow [10] closely.

In the low-temperature phase when $K \gg 1$, fluctuations in the phase difference $\phi_i - \phi_j$ are strongly suppressed due to their high energy cost. The phases ϕ_i will only vary slowly over distances $r \gg a$ greater than the lattice constant a . In this case, the model can be treated by continuum theory. The phase difference is then replaced by the gradient $\nabla \phi(\mathbf{r})$ with a continuous Hamiltonian

$$\beta H_{XY} = \frac{K}{2} \int d^2 r (\nabla \phi)^2. \quad (1.5)$$

The fluctuations in the phase are Gaussian. Using Wick’s theorem, [10], the correlator can be written as

$$\langle \mathbf{S}_0 \mathbf{S}_{\mathbf{r}} \rangle = \text{Re} \langle e^{i(\phi(0) - \phi(\mathbf{r}))} \rangle = \frac{1}{2} e^{-\frac{1}{2} \langle (\phi(0) - \phi(\mathbf{r}))^2 \rangle}. \quad (1.6)$$

The fluctuations in 2D are known to be logarithmic with

$$\langle (\phi(0) - \phi(\mathbf{r}))^2 \rangle = \frac{1}{2\pi K} \ln \left(\frac{|\mathbf{r}|}{a} \right) \quad (1.7)$$

resulting in a correlator that exhibits algebraic decay of the form

$$\langle \mathbf{S}_0 \mathbf{S}_{\mathbf{r}} \rangle \approx \left(\frac{a}{|\mathbf{r}|} \right)^{\frac{1}{2\pi K}} \quad (1.8)$$

This describes the so-called *quasi-long-range ordered* (QLRO) phase of the system, [10].

In the high-temperature case, $K \rightarrow 0$, the situation is different. Since K is a small parameter we can expand the partition function in terms of K as

$$Z = \int_0^{2\pi} \prod_i \frac{d\phi_i}{2\pi} e^{-\beta H_{XY}} = \int_0^{2\pi} \prod_i \frac{d\phi_i}{2\pi} \prod_{\langle i,j \rangle} [1 + K \cos(\phi_i - \phi_j) + \mathcal{O}(K^2)] \quad (1.9)$$

To lowest order in K , each term in the product is either one or $K \cos(\phi_i - \phi_j)$ and can be viewed as a “bond“ connecting neighboring sites i and j , [10]. A single connection or open bond in a configuration will vanish since $\int_0^{2\pi} d\phi_1 \cos(\phi_1 - \phi_2) = 0$. Additionally, we have the relationship

$$\int_0^{2\pi} \frac{d\phi_2}{2\pi} \cos(\phi_1 - \phi_2) \cos(\phi_2 - \phi_3) = \frac{1}{2} \cos(\phi_1 - \phi_3) \quad (1.10)$$

for two bonds meeting. Only closed loops survive, [10]. Computing the correlation function of the system in leading order of K , only closed loops connecting the sites 0 and \mathbf{r} will contribute, leading to an exponential decay

$$\langle \mathbf{S}_0 \mathbf{S}_{\mathbf{r}} \rangle \sim \left(\frac{K}{2} \right)^{|\mathbf{r}|} \sim \exp \left[-\frac{|\mathbf{r}|}{\xi} \right] \quad (1.11)$$

with the correlation length $\xi^{-1} = \ln(2/K)$. Two different phases are present in the XY model that can be identified by algebraic and exponential decay of its two-point correlation function.

The transition can be understood by the condensation of vortices in the spin configuration. The low-temperature expansion we used to calculate the algebraic decay in the correlation function deals with continuous deformations in the spin configurations. As we can see in the definition of H_{XY} the angle is fixed up to an additional constant of $2\pi n$ with n being an integer. One can now construct a configuration where the angle changes by $2\pi n$ when choosing a closed path along a certain point. This configuration cannot be destroyed by continuous deformation and the state is known to be topologically protected. This defect is known as a vortex and the winding number n associated with it is referred to as its topological charge, [10]. The energy of the vortex E_v consists of a contribution from the core, which length scale is of the order of the lattice constant a , and the “outside” of the core, resulting in

$$E_v = E_{\text{core}}(a) + \frac{J}{2} \int_a d^2r (\nabla\phi)^2 = E_{\text{core}}(a) + \pi J n^2 \ln \left(\frac{L}{a} \right) \quad (1.12)$$

where the low temperature expansion of the Hamiltonian was used and the definition of a vortex as $\oint d\mathbf{l} (\nabla\phi) = 2\pi n$ was used, [10]. Now with a core size of a^2 and a system size of L^2 , there are L^2/a^2 possible positions to place the vortex, giving a considerable entropic gain to the free energy of the system. Looking at the free energy, $k_B = 1$,

$$F = E - TS = E_{\text{core}} + (\pi J n^2 - 2T) \ln \left(\frac{L}{a} \right), \quad (1.13)$$

we see that for $T < \pi J/2$ or $K > 2/\pi$, the generation of vortices is penalized by the logarithmically divergent energy cost to the system. In this case the algebraic decay of the spin–spin correlator is protected. However, for $T > \pi J/2$ the entropic gain outweighs the energy cost of the vortex and the spontaneous formation of vortices is favored, destroying the QLRO, [10].

1.3 Vector and scalar chiral order parameters

We have seen that the type of symmetry that is broken strongly influences the type of phase transition that it exhibits. Which begs the question what will happen to the phase transitions in a system where both discrete and continuous symmetries occur simultaneously. In 1959, Villain and Yoshimori simultaneously discussed helimagnets. Here, additionally to the continuous $\text{SO}(2)$ symmetry, a discrete \mathbb{Z}_2 symmetry in form of chiral order is present, [16, 17]. A structure is called chiral if one cannot map it to its mirror image via simple rotation and translation. For example, your hands are mirror images of each other, that cannot be superposed. As a result of this, we can assign each a “handedness” or chirality by calling them left and right. In the case of helimagnets we are dealing with spins in a spiral configuration that can either turn left or right, see figure 1.3.

One generally distinguishes between vector chirality and scalar chirality. The general definition of the vector chiral order parameter as a measure of the canting between two spins \mathbf{S}_i and

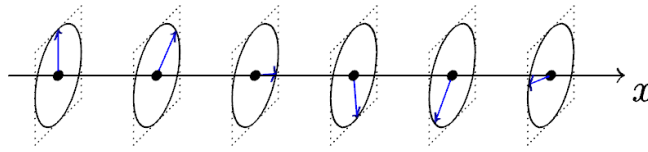


Figure 1.3: Chiral configurations on a one-dimensional chain. The graphic is similar to the one seen in [18]. In the case of \mathbf{q} being perpendicular to the rotation plane, the structure is referred to as a screw spiral.

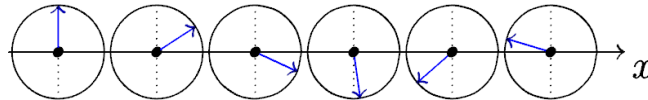


Figure 1.4: Chiral configurations on a one-dimensional chain. In this case, the propagation vector \mathbf{q} lies in the rotation plane and the structure is called cycloid.

\mathbf{S}_j on the lattice. In case of a one-dimensional chain, illustrated in figure 1.3, one focuses on the neighboring spins, choosing the chiral order parameter as

$$\boldsymbol{\kappa} = \langle \mathbf{S}_i \times \mathbf{S}_{i+1} \rangle. \quad (1.14)$$

In a situation where the spins are constricted to rotate in a plane, e.g. due to anisotropies, the vector chirality $\boldsymbol{\kappa}$ is perpendicular to that rotation plane. The example in figure 1.3 illustrates this state with $\boldsymbol{\kappa} \parallel \hat{x}$ and the sign indicating left or right handedness. In the presence of e.g. a magnetic field, the rotation plane can change causing the spins to rotate around cones as shown in figure 1.5 and 1.6. This will cause the vector chirality to rotate around a cone as well.

Magnetic order of a chain is associated with breaking time reversal symmetry, where $t \mapsto -t$ and $\mathbf{m} \mapsto -\mathbf{m}$, [19]. Since an even number of spins appears in the chiral order parameter $\boldsymbol{\kappa}$, we see that the vector chiral order does not break time reversal symmetry and $\boldsymbol{\kappa} \mapsto \boldsymbol{\kappa}$. This can be seen in the spiral configuration from figure 1.3, where inverting the spins does not change the chirality. Averaging the magnetic moments of the spins over the simple spiral, we see that there is no net magnetic moment associated with the spiral.

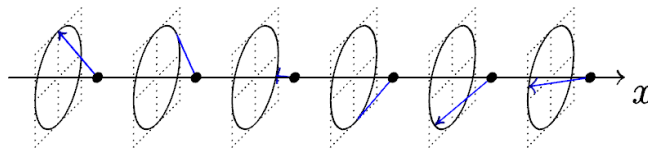


Figure 1.5: Chiral configurations on a 1D chain. The figure is similar to the one seen in [18].

The examples in figure 1.5 and 1.6 show spirals where e.g. an applied magnetic field causes the spirals to form a cone and break time reversal additional to the chiral symmetry. However, vector chiral order breaks spatial inversion symmetry $\mathbf{x} \mapsto -\mathbf{x}$. In the case of the one-dimensional chain, this means the sites i and $i + 1$ are switched. In that case, we have $\boldsymbol{\kappa} \mapsto -\boldsymbol{\kappa}$, while magnetic order is not influenced with $\mathbf{m} \mapsto \mathbf{m}$, [19].

The scalar chirality was first discussed in 1989 by Wen et al., [20], involves three spins. It is usually applied to assign chirality to a plaquette in a lattice, e.g. on a triangular cell as shown in figure 1.7. In the case of a one-dimensional chain, we can choose the three spins to be next

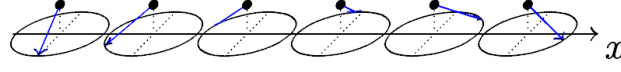


Figure 1.6: Chiral configurations on a 1D chain. The figure is similar to the one seen in [18].

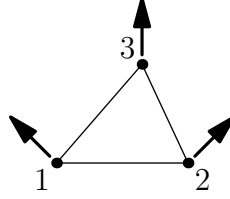


Figure 1.7: Example of a scalar chiral configuration on a triangle. The figure is similar to the one discussed in [21].

neighbors and focus on the scalar chirality as

$$\chi = \langle \mathbf{S}_{i-1}(\mathbf{S}_i \times \mathbf{S}_{i+1}) \rangle, \quad (1.15)$$

which is used in the context of isotropic spin chains, [22]. In spin chains with anisotropies that force the spins to rotate in a certain plane, e.g. spiral from figure 1.3, the scalar chirality is $\chi = 0$ for all configurations. For the canted spins shown in figure 1.5 and 1.6 we get a non-zero χ . Scalar chirality, as the vector chirality, breaks the inversion symmetry of the system with $\chi \mapsto -\chi$. In contrast to the vector chirality, it also breaks time inversion symmetry where $\mathbf{m} \mapsto -\mathbf{m}$ causes $\chi \mapsto -\chi$, due to the dependence on an odd number of spins. A scalar chiral state is therefore a magnetic state.

Symmetry	κ	χ
Time reversal	even	odd
Spatial inversion	odd	odd

Table 1.1: Transformation properties of the vector chirality κ and the scalar chirality χ .

Interestingly, there are cases where $\langle \mathbf{S} \rangle = 0$ and $\chi \neq 0$, as reported for certain parameter configurations in the kagome lattice with nearest- and next-nearest-neighbor interaction, [21, 23]. To study chiral order independent of magnetic ordering we will focus on systems where there is no scalar chiral order by restricting the spins to a fixed plane. The symmetry properties of the vector and scalar chiral order parameters are listed in table 1.1.

1.4 Physical realizations and experimental systems

Magnetic systems exhibiting this vector chiral order or helical structure are referred to as *helimagnets*. One of the first materials exhibiting helimagnetical order are the rare earth metals (REM). These elements exhibit a variety of oscillating magnetic structures, that were studied by

neutron diffraction methods. The REM forming screw or helical order at the Néel temperature are Tb, Dy and Ho, [24]. These three metals crystallize in the hexagonal closely-packed structure. In each hexagonal layer the magnetic moments are aligned. Each of these monoatomic layers has an in-plane magnetic moment perpendicular to the c -axis of the crystal. The magnetic moment of two succeeding layers along the c -axis differs by a constant angle φ_0 . Moving along the c -axis, the magnetic moments are now forming a helix as shown in 1.3, [24]. With an additional magnetic moment along the c -axis, the spins move around a cone as shown in 1.5. These cone structures are stable in holmium (Ho) and erbium (Er) at low temperatures of $T \sim 4K$, [25]. The origin of the spiral structures stems from an indirect ion-ion interaction. The total spin of the incomplete $4f$ -shells of the REMs interact with the spins of the free moving electrons, [24, 26].

Villain and Yoshimori both considered MnO_2 , [16, 17]. They explained the vector chirality as a result of frustrated interaction between the spins along their helical axis.

Other examples are the transitional metal silicates like $MnSi$, [27], and $Fe_{1-x}Co_xSi$, [28]. The later case was studied by Uchida et al. and marks the first time the helical structures have been resolved in real space, where classical neutron-diffraction studies work in Fourier space. This makes the study of domain walls in helical systems possible, showing their spatial distribution and arrangement. The study of domain walls and their control in helical magnets is i.a. important for new high performing computer memory systems, [29].

Multiferroica

Multiferroics are materials that exhibit both electric and magnetic order at the same time. They are of special interest since they allow for electric manipulation of magnetic domains and, vice versa, the control of polarization via magnetic fields. Generally, one can distinguish between two classes of multiferroics, referred to as Type I and Type II, [30]. Type I multiferroics are materials where the coupling between ferroelectricity and magnetism are rather weak and both phenomena occur largely independent. $BiFeO_3$ and $YMnO_3$ are examples of this category, [30]. For us, Type II multiferroica are of interest. Here magnetic order causes ferroelectricity. Compared to Type I multiferroics, the strength of the resulting polarization is however weaker, [30–32].

The cycloidal spin structure, shown in figure 1.4, with \mathbf{q} lying in the rotation plane of the spin, has been examined microscopically by Katsura, Nagaosa and Balatsky, [33], and phenomenologically by Mostovoy, [19]. Both show that this spin structure results in an electric dipole moment.

The alloys and compounds $RMnO_3$, $R \in \{Y, Tb, Dy\}$, [34], and $R_2Mn_2O_5$, $R \in \{Tb, Bi\}$ of the rare earth metals belong to this class. Other examples are $Tb_2Mn_2O_5$, [35], $Ni_3V_2O_8$ (NVO), [34], $LiCu_2O_2$, [36] and $MnWO_4$, [37].

These multiferroica make the electric control of magnetic structures possible. Their understanding is crucial for enhancing the coupling and resulting polarization in order to produce more effective materials.

Quantum chains

Next to the “classical” systems, such as REMs or multiferroica, vector chirality or chiral order can be found in frustrated quantum chains. These systems are complex compounds. Some examples are $LiCuVO_4$, $Rb_2Cu_2Mo_3O_{12}$, [38], Li_2ZrCuO_4 , Cs_2CuCl_4 , or the more recently discovered $Gd(hfac)_3NiTiPr$, [39]. All these chains are embedded in 3D crystals where the intrachain interactions are several orders of magnitude larger than the interactions between chains. Nevertheless, 3D fluctuations persist. Most helical structures exist at low temperatures, where there are only small thermal fluctuations. However, the interchain coupling is not entirely neglectable. As we

will see, this can influence the observed behavior. Instead of seeing the true phase transition, one observes a washed out QPT of coupled systems.

In this work, we want to focus on the competition of discrete and continuous symmetries in 2D systems. The helical XY model that will be introduced later on will be the simplest model exhibiting discrete and continuous symmetries simultaneously. For experimental validation, the helical magnets listed above are not suitable, since 3D bulk effects cannot be neglected here. To the author's knowledge, no helimagnetical thin films where the propagation vector of the chiral order lies in the plane itself has been observed. A 1D quantum chain maps to a 1+1D classical system and allows, once a suitable system is found, the experimental observation of a 2D classical system. One can either focus on a classical 2D system or a 1D quantum chain.

1.5 Outline

The presented work is outlined as follows.

Chapter 2 deals with the detailed discussion of the HXY model, its ground state diagram and its continuous approximation. It will be discussed how the frustrated interaction leads to a chiral ground state and said ground state phase diagram is presented. Several approaches to the discussion of the discrete and continuous symmetry are presented, before settling on the mesoscopic description.

Chapter 3 will present the discussion of the chiral transition. We will use a variational approach to determine the transition temperature and its dependency on the chiral pitch angle.

Chapter 4 will focus on the RG treatment of the system and its critical exponents. It will be shown that rewriting the system in terms of the chiral-order parameter will produce an Ising model with non-local interaction. This indicates that the chiral transition will not be in the Ising universality class. Calculating the exponents using ϵ expansion around $d_c = 5/2$ up to order $\mathcal{O}(\epsilon^2)$, we will see that they are anisotropic and not in the Ising–Onsager class, as expected. Afterwards, we will discuss the phase diagram of the HXY model as published in [40], combining the results from the previous chapters. Here we see that the BKT transition is triggered by the fluctuations approaching the chiral transition. For small pitch angles θ of the spirals, i.e. close to the Lifshitz point, we also find a re-entrance phase to QLRO without chiral order.

Chapter 5 deals with the connection of the chiral order to the polarization in multiferroics. The formation of polarization domain walls due to chiral domain walls is explored and possible ways of detecting such DW are briefly discussed.

Chapter 6 follows the idea of multiferroics and their connection to chiral order in the system of MnWO_4 . Here the magnetic transitions observed are related to chiral order and are accompanied by a measurable polarization. However, we will see that the dynamics of the chiral transition are driven by 3D fluctuations and therefore differs from our system. The work here is included since the work on the dynamical exponents helped to identify the critical slowing down of electro-magnons in MnWO_4 . The calculations of this chapter have been part of the publication [41].

2. The Model

The easiest model containing both the \mathbb{Z}_2 and $\text{SO}(2)$ symmetry is the classical helical XY model (HXY). The system is archetypical for frustrated systems with these two types of symmetries. Compared to more complicated models, it has the advantage of being accessible by an analytical approach. It is essentially the XY model with an additional frustration introduced in the \hat{x} direction that produces a helical ground state along that direction. The XY model itself has a prominent place in physics for exhibiting a phase transition driven by topological excitations, i.e. vortices, named after their discoverers as Berezinskii–Kosterlitz–Thouless (BKT) transition, [14, 15]. After the model and its frustrated interaction have been introduced, we will focus on its ground state properties and the symmetries of the phase diagram. Moving to scales larger than the microscopic lattice spacing a but still smaller than the pitch angle of the helical screws θ ($a \ll x \ll \theta^{-1}$) we can describe the angles ϕ_i of the spins as continuous functions $\phi(\mathbf{x})$. This mesoscopic model will be quite useful later on.

A different microscopic approach starts with a one-dimensional frustrated quantum chains. Quantum-mechanical systems in d dimensions are connected to $(d + 1)$ -dimensional classical systems via the path-integral formalism, [42]. The mapping to a quantum system is useful when trying to find experimental realizations of our model to test the theoretical predictions. A direct mapping of a frustrated quantum chain to the mesoscopic version of the HXY model has been worked out by Kolezhuk, [43], and will be discussed later in this chapter. In the case of large spins, quantum fluctuations can be ignored, [10], and the discussion of the one-dimensional quantum chain and the classical two-dimensional HXY model are identical for small pitch angles θ of the helix.

The study of the competing symmetries \mathbb{Z}_2 and $\text{SO}(2)$ can also be approached from a macroscopic point of view, using the Ginzburg–Landau theory of phase transitions. The GL-free energy for these types of systems can be derived by symmetry considerations using group theory, as done by Bak and Mukamel for several different crystal symmetry groups, [44], or by starting from the microscopic model doing an expansion around the critical modes, as done by Kawamura, [45]. We will discuss the GL-theory at the end of this chapter.

2.1 The classical model

In this section, we will expand the XY model by introducing an additional discrete symmetry through frustration, which leads to the helical XY model. We start from the discrete 2D XY model with planar Heisenberg spins $\mathbf{S}_i = (\cos(\phi_i), \sin(\phi_i), 0)$. The ferromagnetic nearest-neighbor (NN) interaction is different in the x -direction (K_0) from the one in the y -direction (K_1). Then we introduce the frustration via an anti-ferromagnetic next-nearest-neighbor (NNN) interaction in the x -direction to produce the general HXY model as

$$\begin{aligned}
 -\beta H_{HXY} &= \sum_i (K_0 \mathbf{S}_i \mathbf{S}_{i+\hat{x}} + K_1 \mathbf{S}_i \mathbf{S}_{i+\hat{y}} + K_2 \mathbf{S}_i \mathbf{S}_{i+2\hat{x}}) \\
 &= \sum_i (K_0 \cos(\phi_i - \phi_{i+\hat{x}}) + K_1 \cos(\phi_i - \phi_{i+\hat{y}}) + K_2 \cos(\phi_i - \phi_{i+2\hat{x}})) \quad (2.1)
 \end{aligned}$$

with the inverse temperature $\beta = 1/k_B T$ and the interaction parameters $K_n = \beta J_n$. The index i running over all sites of a 2D square lattice. The system in y direction is a simple NN spin

chain with a ferromagnetic ($K_1 > 0$) or anti-ferromagnetic ($K_1 < 0$) ground state.

Ground state

Let us take a closer look at the ground state properties of the system. The interaction in y -direction forces the spins to be either aligned ($K_1 > 0$) or anti-aligned ($K_1 < 0$) in that direction. The situation is not that simple in the x -direction. For the classical ground state, we can just focus on the classical linear chain in x -direction, given by

$$H_x = - \sum_i (J_0 \cos(\phi_i - \phi_{i+1}) + J_2 \cos(\phi_i - \phi_{i+2})). \quad (2.2)$$

In the case for $J_0 > 0$ and $J_2 > 0$, both interactions are ferromagnetic and force all the spins to be aligned in the ground state. The first quadrant of the ground state phase diagram in $J_2 - J_1$ is therefore in the ferromagnetic phase (FM). Changing the NN interaction to be anti-ferromagnetic, $J_0 < 0$, while keeping the NNN interaction ferromagnetic, $J_2 > 0$, the system favors anti-alignment in the ground state. The 4th quadrant of the ground state phase diagram is therefore completely located in the anti-ferromagnetic phase (AFM). The interesting effects are caused by the frustrated interaction in the x -direction, when NN is ferromagnetic $J_0 > 0$ and NNN anti-ferromagnetic $J_2 < 0$, or both are anti-ferromagnetic. In these cases the system can exhibit an additional chiral ground state depending on the parameter ratio $k = -J_0/4J_2 = -K_0/4K_2$, which was shown by Villain and Yoshimori, [16, 17].

Let us introduce the chiral angle $\theta = \phi_i - \phi_{i+1}$ as the difference between neighboring spin-angles. In the spiral case, θ is independent of the lattice site and $\theta = \text{const}$. Now, we can write the energy per site $E_N = H/N$ of the one-dimensional chain from equation 2.2 as

$$E_N = -J_0 \cos(\theta) - J_2 \cos(2\theta). \quad (2.3)$$

Computing the derivative, we obtain the following condition for the minimum

$$\partial_\theta E_N = \sin(\theta) (J_0 + 4J_2 \cos(\theta)) \stackrel{!}{=} 0, \quad (2.4)$$

which has three different solution. We have the ferromagnetic (FM) ground state with $\theta = 0$ and the anti-ferromagnetic (AFM) ground state with $\theta = \pi$ both follow from $\sin(\theta) = 0$. By setting the second factor to zero we get the chiral (Ch) ground state with

$$\cos(\theta) = -\frac{J_0}{4J_2} \equiv k \quad (2.5)$$

$$\theta = \arccos\left(-\frac{J_0}{4J_2}\right) \quad (2.6)$$

as e.g. shown in [46]. Parameter configurations for J_0 and J_2 with $|k| > 1$ have no chiral structure. The ferromagnetic phase will therefore extend up to the critical line $J_0 = -4J_2$. The anti-ferromagnetic phase will be limited by $J_0 = 4J_2$. In the parameter regime of $-1 \leq k \leq 1$, we have to compare the energies of the different phases in order to decide which one is chosen by the system. At the line $J_0 = -4J_2$, where $k = 1$ and $\theta = 0$ the energies for both phases are identical to the FM phase with

$$E_N(\theta = 0) = -|J_0| + |J_2|. \quad (2.7)$$

Now decreasing J_2 or increasing $|J_2|$ leads to $k < 1$ and $\theta > 0$. Comparing the energy for a small θ to its FM alternative we have

$$E_N(\theta) = -|J_0| \cos(\theta) + |J_2| \cos(2\theta) \approx E_N(\theta = 0) + 2\theta^2(|J_0| - 4|J_2|) + \mathcal{O}(\theta^4). \quad (2.8)$$

The last term can be written in terms of the parameter k . The difference in energy then is

$$E_N(\theta) - E_N(\theta = 0) \approx 2\theta^2 |J_0| \left(1 - \frac{1}{|k|}\right). \quad (2.9)$$

For $|k| < 1$ the difference is always negative and the chiral state is chosen. The argument for the AFM phase, where one expands around $\theta = \pi$ leads to the same expression.

We see that the chiral ground state is the lowest energy configuration for the parameter range of $-1 \leq k \leq 1$, and the complete ground state phase diagram and the chiral angle $\theta(J_0, J_2)$ are

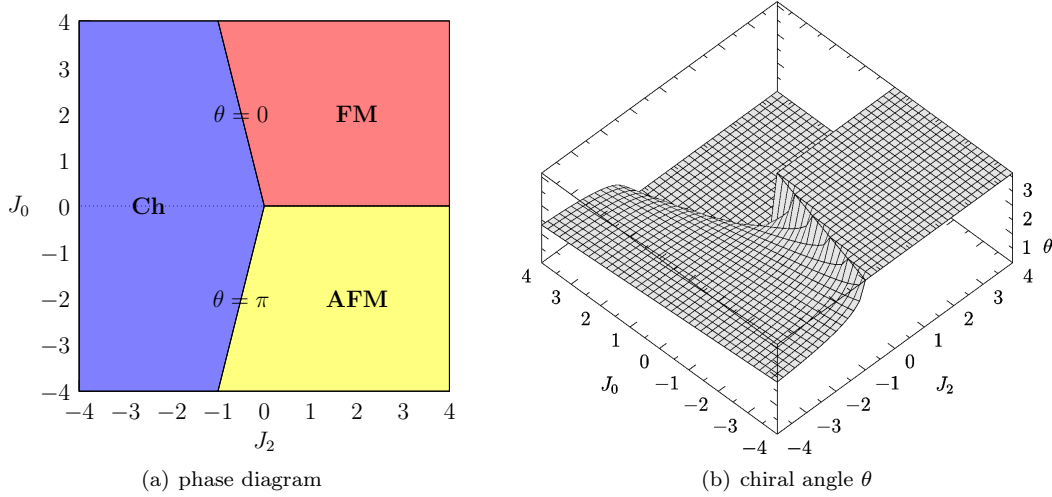


Figure 2.1: Ground state phase diagram of the classical frustrated XY chain with NN interaction K_0 and NNN interaction K_2 exhibiting ferromagnetic (FM), anti-ferromagnetic (AFM) and chiral (Ch) ordering.

shown in figure 2.1.

Symmetries and decoupling

Let us now take a closer look at some symmetries of the phase diagram. A change in the sign of the nearest-neighbor interaction J_0 can be absorbed by flipping every second spin in the x -direction as

$$\mathbf{S}_i \mapsto (-1)^i \mathbf{S}_i. \quad (2.10)$$

This mapping changes $\mathbf{S}_i \mathbf{S}_{i+1} \mapsto -\mathbf{S}_i \mathbf{S}_{i+1}$, while leaving $\mathbf{S}_i \mathbf{S}_{i+2}$ unchanged. All these transformations do not change the physics of the system. This means that the critical properties of the phase diagram are symmetric around the J_0 axis, making the expansions around $\theta = 0$ and $\theta = \pi$ equivalent.

There is no such symmetry for the next nearest-neighbor interaction J_2 . It needs to be anti-ferromagnetic, otherwise no frustration is present. For $J_2 = 0$ the system simply reduces to a ferromagnetic chain $J_0 > 0$ or an anti-ferromagnetic chain $J_0 < 0$. In the case of $J_0 = 0$, we see that the system decouples into two different chains. Looking at the one-dimensional chain in \hat{x} direction first, we can map the NN and NNN interaction to a zig-zag chain. This is illustrated in figure 2.2, similar to e.g. Nersesyan et al. [47]. We see that the frustrated chain can be viewed as two coupled chains. For $J_0 = 0$ we either get two ferromagnetic chains for $J_2 > 0$ or two anti-ferromagnetic chains for $J_2 < 0$.

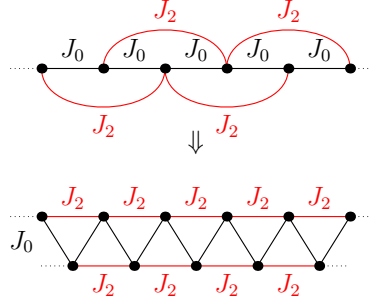


Figure 2.2: Zig-zag chain mapping of the frustrated 1D system with nearest-neighbor interaction J_0 and next-nearest-neighbor interaction J_2 .

The mesoscopic model

For low temperatures and a parameter configuration around the onset of chiral ordering ($0 < \theta \ll 1$), the variations in ϕ_i are small and take place on length scales $l \gg a$ much greater than the lattice spacing a . We will therefore switch to a continuum theory with $\phi_i \rightarrow \phi(\mathbf{x})$. We will do this for isotropic nearest neighbor interaction, meaning $K_0 = K_1$ and around the onset of chiral order $\theta \ll 1$. In order to not confuse the signs of the parameters, we set $K_2 = -|K_2|$ while $K_0 > 0$.

$$-\beta H_{HXY} = \sum_i (K_0 \cos(\phi_i - \phi_{i+\hat{x}}) + \cos(\phi_i - \phi_{i+\hat{y}}) - |K_2| \cos(\phi_i - \phi_{i+2\hat{x}})). \quad (2.11)$$

Now we can expand the $\cos(\dots)$ terms around the small deviations, since $\phi_i - \phi_{i+x}$ is of the order of $\theta \ll 1$. The expansion has been used by Hubert to study chiral domain walls in the one-dimensional chain, [46]. Here this expansion will be done for the HXY model, as defined above in equation 2.11. Let us start with just the term for the nearest-neighbor interaction in x -direction, to demonstrate the continuum expansion in full. To not confuse the simpler version with the earlier ones, we will label the angle at each site by ϑ_n . The next site along the x -direction is labeled ϑ_{n+1} and the interaction is simply $J > 0$. Additionally, we will shift the ground state energy of the interaction $-J \cos(\vartheta_n - \vartheta_{n+1})$ by NJ to be 0 for $\theta = 0$. The simple one-dimensional chain model with just nearest-neighbor interaction is given by

$$H' = J \sum_n (1 - \cos(\vartheta_{n+1} - \vartheta_n)), \quad (2.12)$$

which is identical to the model used in [46]. Following Hubert, we can substitute ϑ_n with a continuous function $\vartheta(x)$ and expanding $\vartheta_{n+1}(x) = \vartheta_n(x+a) \approx \vartheta_n(x) + a\vartheta'_n(x) + \dots$ up to fourth order

$$1 - \cos(\vartheta_{n+1} - \vartheta_n) \approx \frac{1}{2}(\vartheta'_n a)^2 + \frac{1}{8}(\vartheta''_n a^2)^2 + \frac{1}{2}a^3 \vartheta'_n \vartheta''_n + \frac{1}{6}a^4 \vartheta'_n \vartheta'''_n - \frac{1}{24}a^4 (\vartheta'_n)^4 + \mathcal{O}(a^5).$$

Now we switch the sum to an integration by

$$\sum_n a f_n \mapsto \int dx f(x). \quad (2.13)$$

Two of the terms in the expansion can be transformed using partial integration. First we note that the a^3 term

$$a^3 \int dx \vartheta'_n \vartheta''_n = -a^3 \int dx \vartheta''_n \vartheta'_n = 0 \quad (2.14)$$

vanishes. Secondly, we will simplify the $\vartheta'\vartheta''''$ term as

$$\frac{a^4}{6} \int dx \vartheta'_n \vartheta''''_n = -\frac{a^4}{6} \int dx (\vartheta''_n)^2. \quad (2.15)$$

With this, the simple model H' of equation (2.12) can be written as

$$H' = \frac{Ja}{2} \int_x \left[(\partial_x \vartheta)^2 - \frac{a^2}{12} ((\partial_x^2 \vartheta)^2 + (\partial_x \vartheta)^4) \right].$$

Since we will consider a two-dimensional system in the end, let us assume a second index j running in the y -direction, that can be transformed into a continuous variable y . Instead of ϑ_n we now have $\vartheta_{n,j}$, with the sum running over both indices $\sum_{n,j}$. The additional constant a in front can then be used for switching $a \sum_j \mapsto \int dy$, leading to

$$H' = \frac{J}{2} \int_{x,y} \left[(\vartheta')^2 - \frac{a^2}{12} ((\vartheta'')^2 + (\vartheta')^4) \right] \quad (2.16)$$

with $\vartheta \equiv \vartheta(\mathbf{x})$ and the prime denoting the derivative in x , analog to [46]. This is without any interaction in the y -direction. There is only a nearest-neighbor interaction in the y -direction, resulting in a simple coupling without the emergence of chiral order. It is not necessary to expand the $\cos(\dots)$ term beyond the quadratic terms. An isotropic NN interaction ($K_0 = K_1 = J$) then just adds a $(\partial_y \vartheta(\mathbf{x}))^2$ term to the expansion. Writing the derivatives as subindices, i.e. $\partial_{x/y} \vartheta \equiv \vartheta_{x/y}$, we have

$$H' = \frac{K_0}{2} \int_{x,y} \left[(\vartheta_x)^2 + (\vartheta_y)^2 - \frac{a^2}{12} ((\vartheta_{xx})^2 + (\vartheta_x)^4) \right]. \quad (2.17)$$

In order to obtain the continuum expansion for the NNN contribution K_2 , we have to expand $\cos(\vartheta_{n+2} - \vartheta_n)$ as

$$1 - \cos(\vartheta_{n+2} - \vartheta_n) \approx 2(\vartheta'_n a)^2 + 2(\vartheta''_n a^2)^2 + 4a^3 \vartheta'_n \vartheta''_n + \frac{8}{3} a^4 \vartheta'_n \vartheta''''_n - \frac{2}{3} a^4 (\vartheta'_n)^4 + \mathcal{O}(a^5).$$

Using partial integration we can simplify these terms again. The continuum version of just the NNN part of the expansion yields

$$H'' = -\frac{|K_2|}{2} \int_{x,y} \left[4(\vartheta_x)^2 - \frac{16a^2}{12} ((\vartheta_{xx})^2 + (\vartheta_x)^4) \right]. \quad (2.18)$$

Now we can combine all the calculations and switch back to the notation using $\phi(\mathbf{x})$ for the angle of a spin at position \mathbf{x} .

$$\beta\mathcal{H} \approx \frac{1}{2} \int d^2x \left[(K_0 - 4|K_2|)(\partial_x \phi)^2 - \frac{a^2}{12} (K_0 - 16|K_2|) ((\partial_x^2 \phi)^2 + (\partial_x \phi)^4) + K_0 (\partial_y \phi)^2 \right] + \text{const}$$

Factoring out K_0 and using $\cos(\theta) = K_0/(4|K_2|)$ we get

$$\beta\mathcal{H} \approx \frac{K_0}{2} \int d^2x \left[\left(1 - \frac{1}{\cos(\theta)}\right) (\partial_x \phi)^2 - \frac{a^2}{12} \left(1 - \frac{4}{\cos(\theta)}\right) ((\partial_x^2 \phi)^2 + (\partial_x \phi)^4) + (\partial_y \phi)^2 \right] + \text{const}$$

This can now be expanded around small θ .

$$\beta\mathcal{H} \approx \frac{K_0}{2} \int d^2x \left[-\frac{\theta^2}{2} (\partial_x \phi)^2 + \frac{1}{4} ((\partial_x^2 \phi)^2 + (\partial_x \phi)^4) + (\partial_y \phi)^2 \right], \quad (2.19)$$

where we set $a = 1$ to simplify the notation. This continuous version of the model will be used throughout the work. Shifting the ground state energy again by adding $-\frac{K_0}{2} \int d^2x \frac{1}{4} \theta^4$ we get

$$\beta\mathcal{H} = \frac{K_0}{2} \int_{\mathbf{x}} \left[\frac{1}{4} ((\partial_x \phi)^2 - \theta^2)^2 + (\partial_y \phi)^2 + \frac{1}{4} (\partial_x^2 \phi)^2 \right] \quad (2.20)$$

with the chiral or pitch angle $\theta = qa$ and $\int_{\mathbf{x}} = \int dx dy$. In this version the double minimum $\partial_x \phi = \pm\theta$ of the Hamiltonian is clearly visible. This model will mainly be used throughout the work.

2.2 Quantum chain

Now we have seen how chiral order can originate from frustrated interaction. For a fixed parameter configuration we have two different chiral ground states with $\pm\theta$. This vector chirality is another example of the \mathbb{Z}_2 symmetry. Now let us look at one-dimensional quantum chains. We already mentioned the general connection of d -dimensional quantum systems to $(d+1)$ -dimensional classical systems and here we want to discuss the corresponding quantum model to the previously discussed classical one. The quantum version is the frustrated one-dimensional XY quantum chain which is given by

$$-\beta\hat{H} = \sum_i K_0 \hat{\mathbf{S}}_i \hat{\mathbf{S}}_{i+1} + K_2 \hat{\mathbf{S}}_i \hat{\mathbf{S}}_{i+2} \quad (2.21)$$

Here we used the inverse temperature β and the interaction parameters $K_i = \beta J_i$, identical to the previous discussions. A good introduction into quantum spin chains can be found in [42].

Symmetries

Let us begin with simple symmetry considerations. Since we are dealing with operators instead of classical spins, we have to check if the classical transformations used are still applicable. The spin operators $\hat{\mathbf{S}}_i = (\hat{S}_i^x, \hat{S}_i^y, 0)$ obey the commutator relations

$$[\hat{S}_i^\alpha, \hat{S}_j^\beta] = i\delta_{ij} \varepsilon_{\alpha\beta\gamma} \hat{S}_i^\gamma. \quad (2.22)$$

For $K_2 = 0$ we are dealing purely with the nearest-neighbor interaction K_0 leading to a ferromagnetic chain in the case of $K_0 > 0$ and an anti-ferromagnetic chain for $K_0 < 0$. For classical spins \mathbf{S}_i we already discussed that one can map the ferromagnetic K_0 to the anti-ferromagnetic case $-K_0$ by flipping every second spin, i.e.

$$\mathbf{S}_i \mapsto (-1)^i \mathbf{S}_i \quad (2.23)$$

leading to the term $\mathbf{S}_i \mathbf{S}_{i+1} \mapsto -\mathbf{S}_i \mathbf{S}_{i+1}$ to pick up a minus sign, while next-nearest-neighbor interactions are unchanged with $\mathbf{S}_i \mathbf{S}_{i+2} \mapsto \mathbf{S}_i \mathbf{S}_{i+2}$. The situation is more complicated for quantum chains. Inverting all spin components \hat{S}^x , \hat{S}^y and \hat{S}^z on a sub-lattice violates the commutator relations. However it is possible to flip only two components of the spin, equivalent to a 180° -degree rotation around the axis of the third component, being

$$\begin{aligned} \hat{S}_i^x &\mapsto \tilde{S}_i^x = (-1)^i \hat{S}_i^x, \\ \hat{S}_i^y &\mapsto \tilde{S}_i^y = (-1)^i \hat{S}_i^y, \\ \hat{S}_i^z &\mapsto \tilde{S}_i^z = \hat{S}_i^z. \end{aligned}$$

When looking at the nearest-neighbor interaction for Heisenberg spins

$$\begin{aligned}\hat{\mathbf{S}}_i \hat{\mathbf{S}}_{i+1} &= \hat{S}_i^x \hat{S}_{i+1}^x + \hat{S}_i^y \hat{S}_{i+1}^y + \hat{S}_i^z \hat{S}_{i+1}^z \\ &= \frac{1}{2}(\hat{S}_i^+ \hat{S}_{i+1}^- + \hat{S}_i^- \hat{S}_{i+1}^+) + \hat{S}_i^z \hat{S}_{i+1}^z\end{aligned}\quad (2.24)$$

with $\hat{S}_i^\pm = \hat{S}_i^x \pm i\hat{S}_i^y$, we see that our transformation will flip the sign in front of the $\hat{S}_i^{x/y} \hat{S}_{i+1}^{x/y}$ terms but leave the $\hat{S}_i^z \hat{S}_{i+1}^z$ part unchanged. In the case of Heisenberg spins there is a difference for ferromagnetic and anti-ferromagnetic interactions, resulting in different dispersion relations for their spin wave excitations. The excitations in the FM Heisenberg chain behave like free particles with $\omega \sim k^2$ while the excitations in the AFM Heisenberg chain behave like phonons with $\omega \sim k$, [10, 42, 48]. In the special case of XY spins, the \hat{S}^z component does not appear in the Hamiltonian. Here the 180° rotation can absorb the changed sign in K_0 and the quantum system has the same symmetry around K_0 as the classical version discussed earlier. The quantum XY chain with only NN interaction produces a linear dispersion relation $\omega \sim k$ in both the ferromagnetic and anti-ferromagnetic case. A detailed discussion and calculation including the exactly solvable $S = 1/2$ case and the $S \gg 1$ limit can be found in appendix A.1.

Kolezhuk mapping

For low temperatures, the 1D quantum system can be mapped to a 1+1D classical system where the spatial extension of the system along the imaginary time axis τ is

$$L_\tau = \frac{\hbar}{k_b T} \quad (2.25)$$

[42]. For zero temperature the system maps then to a fully 2D classical theory when $L_\tau \rightarrow \infty$. The HXY is essentially the XY model with an additional frustration in the \hat{x} direction analog to Villain's model. For small pitch angles θ of the chiral states, a full winding takes place over a distance $l \gg a$ much larger than the lattice constant. In that case we can move to a continuous $\phi_i \mapsto \phi(x, y)$ theory of the spin angles. In the case of isotropic NN interaction, i.e. $K_0 = K_1$, the resulting mesoscopic model ($a = 1$) was derived as

$$\beta\mathcal{H} = \frac{K_0}{2} \int_{\mathbf{x}} \left[\frac{1}{4}((\partial_x \phi)^2 - \theta^2)^2 + (\partial_y \phi)^2 + \frac{1}{4}(\partial_x^2 \phi)^2 \right]; \quad (2.26)$$

The derivation was done earlier by substituting $\phi_i \mapsto \phi(x, y)$ and $\phi_{i+\hat{x}} \mapsto \phi(x+a, y)$ and expanding the difference $\phi_i - \phi_{i+\hat{x}}$ in the $\cos(\dots)$ terms, similar to the expansion proposed by Hubert [46].

In the case of the frustrated XY chain for large spin, Kolezhuk [43] was able to map the system to a classical helimagnet with the action

$$\mathcal{A}[\varphi] = \frac{1}{2T_{\text{eff}}} \int dx \int dy \left[\frac{1}{4}((\partial_x \varphi)^2 - \theta^2)^2 + (\partial_y \varphi)^2 + \frac{1}{4}(\partial_x^2 \varphi)^2 \right], \quad (2.27)$$

where effective temperature T_{eff} is related to the spin S via $T_{\text{eff}} = \sqrt{\frac{3}{2}} \frac{1}{S}$, relating to the value K_0 used in our definition as

$$K_0 = \sqrt{\frac{2}{3}} S. \quad (2.28)$$

Even though we will be dealing with a purely classical system, this relation can be used to connect it to the large spin case of frustrated 1D quantum chains, [43]. The procedure is sketched out in more detail in the appendix A.2.

2.3 Landau–Ginzburg–Wilson Hamiltonian

A different approach to the chiral systems has been done by Bak and Mukamel, [44], using symmetry considerations to construct the Landau–Ginzburg–Wilson (LGW) Hamiltonian. For a system with a chiral wave vector \mathbf{q} in one direction, they constructed a 4-component order-parameter expansion. This model connects to the models we have discussed so far. A derivation starting from a microscopic model, followed by an expansion around its critical modes, was done by Kawamura, [49, 50], and leads to the same Hamiltonian. Both, the work done by Bak and Mukamel and the work done by Kawamura consider 3D systems. The derivation can be easily modified to suit the 2D case, but there are several disadvantages that make further study impractical. The critical dimension for the LGW system is $d_c = 4$, making a renormalization-group approach for $d = 2$ impossible. Also, we will see that splitting the order parameters into a right and left spiral state will be helpful. The coupling of these two different states will turn out to not be small in the chiral regime that we want to study. Both points render this line of attack on the problem unfruitful. The works are discussed here nevertheless, to give a sense of these approaches.

Bak and Mukamel approach

Let us start with the purely macroscopic approach used by Bak and Mukamel, [44]. They consider the spiral structures that emerge in the rare earth metals Ho, Tb and Dy, by looking at their underlying crystal symmetry. As mentioned in the introduction, they crystallize in the hexagonal closely-packed structure and in each hexagonal layer, their magnetic moments are aligned. Moving along the z -axis, perpendicular to the different layers, the magnetic moments form a helix, described by the wave vector $\mathbf{q} = (0, 0, \theta/a)$. As order parameter, they choose the Fourier coefficients of the magnetic moments around the wave vector \mathbf{q} of the chiral configuration, given as

$$\psi_{\pm q, P} = \phi_P \pm i\bar{\phi}_P = \sum_{\mathbf{r}} S_P(\mathbf{r})e^{\pm i\mathbf{q}\mathbf{r}}, \quad P = x, y. \quad (2.29)$$

In the case of a chiral structure around the \hat{z} -axis, the wave vector is given by $\mathbf{q} = (0, 0, q) = (0, 0, \theta/a)$, with XY spins $\mathbf{S} = (S_x, S_y, 0)$ in the plane perpendicular to \mathbf{q} . Writing down the symmetry invariants of these order parameters, Bak and Mukamel arrive at the following LGW-expansion

$$\begin{aligned} H_{BM} = \frac{1}{2} [& ((\nabla\phi_x)^2 + (\nabla\phi_y)^2 + (\nabla\bar{\phi}_x)^2 + (\nabla\bar{\phi}_y)^2 + r(\phi_x^2 + \phi_y^2 + \bar{\phi}_x^2 + \bar{\phi}_y^2)) \\ & + u_1(\phi_x^2 + \phi_y^2 + \bar{\phi}_x^2 + \bar{\phi}_y^2)^2 + u_2(\phi_x\bar{\phi}_y - \phi_y\bar{\phi}_x)^2 \end{aligned} \quad (2.30)$$

The gradient terms favor a homogeneous order parameter. The parameters r , u_1 and u_2 now determine the minimum configuration of the system. In the simple case when all of them are positive, the minimum is reached when all four order parameters vanish. For different parameter configurations, the order parameter can take on finite values, marking ferromagnetic or chiral structures. In the present notation, the system is not very transparent. A better understanding of this expansion can be obtained by introducing the parameters η_i and $\bar{\eta}_i$

$$\eta_1 = \frac{1}{\sqrt{2}}(\phi_x + \bar{\phi}_y), \quad \eta_2 = \frac{1}{\sqrt{2}}(\phi_x - \bar{\phi}_y), \quad (2.31)$$

$$\bar{\eta}_1 = \frac{1}{\sqrt{2}}(\bar{\phi}_x - \phi_y), \quad \bar{\eta}_2 = \frac{1}{\sqrt{2}}(\bar{\phi}_x + \phi_y). \quad (2.32)$$

in order to identify the left and right twisting spiral configurations. They describe the spiral parts of the magnetic structure as

$$\eta_{1,2} \propto \sum_{\mathbf{r}} S_x(\mathbf{r}) \cos(\mathbf{k}\mathbf{r}) \pm S_y(\mathbf{r}) \sin(\mathbf{k}\mathbf{r}), \quad (2.33)$$

$$\bar{\eta}_{1,2} \propto \sum_{\mathbf{r}} \pm S_x(\mathbf{r}) \cos(\mathbf{k}\mathbf{r}) + S_y(\mathbf{r}) \sin(\mathbf{k}\mathbf{r}), \quad (2.34)$$

[44]. Grouping the parameters corresponding to the different chiralities

$$\boldsymbol{\eta}_i = \begin{pmatrix} \eta_i \\ \bar{\eta}_i \end{pmatrix} \quad (2.35)$$

now makes the discussion clearer. Here $\boldsymbol{\eta}_1$ corresponding to the right-handed spiral and $\boldsymbol{\eta}_2$ corresponding to the left-handed case. The free energy now has the form

$$\begin{aligned} \bar{F} &= \frac{1}{2}r \sum_i \boldsymbol{\eta}_i^2 + 4u' \left(\sum_i \boldsymbol{\eta}_i^2 \right)^2 + 8u' \boldsymbol{\eta}_1^2 \boldsymbol{\eta}_2^2 \\ &= \frac{1}{2}r [\boldsymbol{\eta}_1^2 + \boldsymbol{\eta}_2^2] + u [(\boldsymbol{\eta}_1^2)^2 + (\boldsymbol{\eta}_2^2)^2] + 2v \boldsymbol{\eta}_1^2 \boldsymbol{\eta}_2^2. \end{aligned} \quad (2.36)$$

The coefficients u and v are related to the previous coefficients u_1 and u_2 via

$$u = u_1 - \frac{1}{4}u_2, \quad v = \frac{1}{2}u_2. \quad (2.37)$$

Ground state

In its form given in equation (2.36), the structure becomes clear. For $r < 0$ and $u > 0$, the system will favor non vanishing amplitudes $|\boldsymbol{\eta}_i|$ for the left- and right-handed chiral structures. Now the coupling parameter v determines if they both exist simultaneously and form a ferromagnetic (FM) structure or if only one is favored, describing a chiral state (Ch). For $r > 0$ and $u > 0$ both amplitudes vanish and the system is paramagnetic (P). These configurations are listed in table 2.1. Some special cases can be discussed before doing a direct minimization of the energy.

	P	Ch+	Ch-	FM
$ \eta_1 $	0	const	0	const
$ \eta_2 $	0	0	const	const

Table 2.1: Overview of the possible ground states. P being the paramagnetic state, Ch+ and Ch- corresponding to the right or left chiral structure and FM being the ferromagnetic configuration

Without a coupling between the two amplitudes, $v = 0$, we are dealing with two independent two-component systems. Both having the exact same structure and are determined by the parameters r and u , meaning that they will simultaneously be either 0 or non-vanishing. In the case of $r < 0$ and $u > 0$, the system will be in the FM state, since both amplitudes will not vanish. In the special case of $v = u$, the whole system can be written in terms of the 4-component vector $\mathbf{g} = \boldsymbol{\eta}_1 \oplus \boldsymbol{\eta}_2$, with

$$\bar{F} = \frac{1}{2}r\mathbf{g}^2 + u(\mathbf{g})^4.$$

The system only fixes the amplitude of \mathbf{g} and is invariant under rotation. For a fixed amplitude the direction $(1, 0, 0, 0)$, referring to $|\boldsymbol{\eta}_1| \neq 0$ and $|\boldsymbol{\eta}_2| = 0$, has the same energy as the direction $\frac{1}{\sqrt{2}}(1, 0, 1, 0)$, referring to both amplitudes being non-vanishing. The line $u = v$ therefore marks the transition from a ferromagnetic to a chiral state, because both will have the same energy for this parameter configuration.

Let us now exactly calculate the minimum of the energy. Minimizing the gradient terms is done by having spatially constant order parameters. The energy is then simply given as

$$E = \frac{1}{2}r [\boldsymbol{\eta}_1^2 + \boldsymbol{\eta}_2^2] + u [(\boldsymbol{\eta}_1^2)^2 + (\boldsymbol{\eta}_2^2)^2] + 2v\boldsymbol{\eta}_1^2\boldsymbol{\eta}_2^2 \quad (2.38)$$

and the minimum is determined by

$$\partial_{\eta_1^{x/y}} E = r\eta_1^{x/y} + 4u(\eta_1^{x/y})^3 + 4u\eta_1^{x/y}(\eta_1^{y/x})^2 + 4v\eta_1^{x/y}((\eta_2^{x/y})^2 + (\eta_2^{y/x})^2) = 0. \quad (2.39)$$

The different possible solutions and their respective energies for $r < 0$ can now be calculated.

$$\text{P} \quad |\boldsymbol{\eta}_1| = |\boldsymbol{\eta}_2| = 0 \quad E = 0 \quad (2.40)$$

$$\text{Ch} \quad |\boldsymbol{\eta}_1| = \sqrt{-\frac{r}{4u}}; \quad \boldsymbol{\eta}_2 = 0 \quad E = -\frac{1}{16} \frac{r^2}{u} \quad u > 0 \quad (2.41)$$

$$\text{FM} \quad |\boldsymbol{\eta}_1| = |\boldsymbol{\eta}_2| = \sqrt{\frac{-r}{4(u+v)}} \quad E = -\frac{1}{8} \frac{r^2}{(u+v)} \quad u+v > 0 \quad (2.42)$$

We see that the energy is not bounded from below for $u < 0$ and $v < -u$, and the system is unstable for those parameter configurations. The full mean-field phase diagram of the system is shown in figure 2.3. One can see that around $v \approx 0$, where the two chiralities $\boldsymbol{\eta}_{1/2}$ decouple,

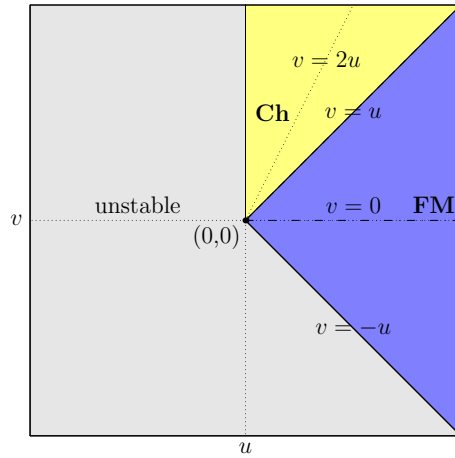


Figure 2.3: Mean-field solutions for the free energy expansion of the system.

the system is in the ferromagnetic state. In the chiral case that we are interested in, none of the parameters can be treated as a perturbation.

Kawamura expansion

The Landau–Ginzburg–Wilson (LGW) expansion of the microscopic HXY model has been studied by Kawamura in 1988, [49, 50], to calculate the critical behavior in 3D using the renormalization-group. Starting from the microscopic hard-spin model, using the Fourier transform and keeping

only near-critical modes, the effective system reads as

$$H_{LGW} = \frac{1}{2} [(\nabla \mathbf{a})^2 + (\nabla \mathbf{b})^2 + \bar{r}(\mathbf{a}^2 + \mathbf{b}^2) + \bar{u}(\mathbf{a}^2 + \mathbf{b}^2)^2 + \bar{v}\{(\mathbf{a}\mathbf{b})^2 - \mathbf{a}^2\mathbf{b}^2\}], \quad (2.43)$$

where \mathbf{a} and \mathbf{b} are the 2-component vector fields corresponding to the sine and cosine components of the non-collinear spin structure with the wave vector \mathbf{q} , [49, 50].

$$\langle \mathbf{S}(\mathbf{r}) \rangle = \mathbf{a}(\mathbf{r}) \cos(\mathbf{q}\mathbf{r}) + \mathbf{b}(\mathbf{r}) \sin(\mathbf{q}\mathbf{r}). \quad (2.44)$$

We see that the system favors $\mathbf{a} \perp \mathbf{b}$ for $\bar{v} > 0$, corresponding to the spiral structure. In the case of $\bar{v} < 0$ the vectors \mathbf{a} and \mathbf{b} tend to align and form linear polarized spin structure, [49]. The expansion derived from the microscopic model by Kawamura is actually identical to the one derived simply by symmetry considerations done by Bak and Mukamel. Looking at the near critical modes around \mathbf{q} we see the immediate connection between the order parameters used by Bak and Mukamel and the order parameter used by Kawamura, being

$$\phi_{x/y} \sim a_{x/y}, \quad \bar{\phi}_{x/y} \sim b_{x/y}. \quad (2.45)$$

The first three terms in the expansion by Bak and Mukamel, equation 2.30, can be easily recognized as being equal to the first three of the Kawamura expansion in equation 2.43 using the identified connection of the order parameters from equation 2.45. The last term can be checked by computing

$$(\mathbf{a}\mathbf{b})^2 - \mathbf{a}^2\mathbf{b}^2 = a_x^2 b_x^2 + 2a_x b_x a_y b_y + a_y^2 b_y^2 - a_x^2 b_x^2 - a_x^2 b_y^2 - a_y^2 b_x^2 - a_y^2 b_y^2 = -(a_x b_y - a_y b_x)^2 \quad (2.46)$$

and again using the identification $a_{x/y} \leftrightarrow \phi_{x/y}$ and $b_{x/y} \leftrightarrow \bar{\phi}_{x/y}$ from equation 2.45. The parameters are connected via

$$r = \bar{r}, \quad u_1 = \frac{1}{2}\bar{u}, \quad u_2 = -\frac{1}{2}\bar{v}, \quad (2.47)$$

$$r = \bar{r}, \quad u = \frac{1}{2}\bar{u} + \frac{1}{8}\bar{v}, \quad v = -\frac{1}{4}\bar{v}. \quad (2.48)$$

The connection to the microscopic parameters $\{J_0, J_1, J_2\}$ has been formally calculated by Kawamura, [45, 49], as

$$\bar{r} = \frac{1}{c_1} \left(\frac{1}{2} P_{ii} - \frac{1}{4} + c_0 \right), \quad \bar{u} = \frac{3}{256} \frac{1}{c_1^2}, \quad \bar{v} = \frac{1}{64c_1^2}, \quad (2.49)$$

where the the matrix P is given in relation to the interaction matrix of the HXY system written as $H = \sum_{ij} \mathbf{S}_i K_{ij} \mathbf{S}_j$ with

$$K_{ij} = J_0 \delta_{i,i+\hat{x}} + J_1 \delta_{i,i+\hat{y}} + J_2 \delta_{i,i+2\hat{x}}. \quad (2.50)$$

The matrix P is now the inverse defined as

$$P_{ij} = [P_0 \delta_{ij} + K_{ij}]^{-1}, \quad (2.51)$$

where the constant P_0 is chosen to make P positive definite. The constants c_0 and c_1 are the coefficients of the expansion of the Fourier transform $P(\mathbf{q})$ of P

$$P(\mathbf{q}) \approx c_0 + c_1 \mathbf{q}^2 + \mathcal{O}(\mathbf{q}^4), \quad (2.52)$$

[45, 49]. However, the elements P_{ii} and the coefficients c_0 and c_1 are never explicitly calculated. The calculation does not give explicit values for the microscopically determined coefficients r , u and v , but still connects the symmetry considerations to a microscopic model where the chirality is driven by frustrated interaction.

3. Chiral Transition

In this chapter we will focus on the chiral transition of the HXY model. The starting point is its continuous version, the Hamiltonian H

$$\beta H = \frac{K_0}{2} \int d^2x \left[\frac{1}{4} [(\partial_x \phi)^2 - \theta^2]^2 + (\partial_y \phi)^2 + \frac{1}{4} (\partial_x^2 \phi)^2 \right] \quad (3.1)$$

which we discussed in chapter 2. The potential for the $\partial_x \phi$ terms has the form of a double well with the two minima at $\partial_x \phi = \pm \theta$. The term $(\partial_x \phi)^4$ complicates the system, a straight forward computation of the partition function and the thermodynamical properties is not possible. Instead we will approximate the system with a quadratic trial Hamiltonian H_T .

$$\beta H_T = \frac{K_0}{2} \int d^2x \left[r((\partial_x \phi) - Q)^2 + (\partial_y \phi)^2 + \frac{1}{4} (\partial_x^2 \phi)^2 \right] \quad (3.2)$$

with the parameters r and Q . The quadratic nature of H_T will make analytic computations possible. Now we have to find the optimal values for r and Q for a given K_0 , such that the approximation is closest to the original. So what is meant by “closest” approximation and how can the quality of the approximation be measured? This is done by constructing a functional with certain properties, whose minimum is determined by the original Hamiltonian. This so called variational approach is used in order to determine the best possible parameters approximating the original system, [51].

3.1 The variational approach

We will start by constructing the above mentioned functional $\mathcal{V}[H_T]$. All thermodynamic properties of the system are encoded in its thermodynamical potential, the free energy

$$F = -T \ln(Z) \quad (3.3)$$

and the partition function Z of the system. The partition functions of the system are given by

$$Z = \int \mathcal{D}[\phi] e^{-\beta H} \quad Z_T = \int \mathcal{D}[\phi] e^{-\beta H_T}$$

where the integration $\int \mathcal{D}[\phi]$ is over all field configurations. Starting from the partition function of the original system, we can insert $0 = \beta H_T - \beta H_T$ without changing the result

$$Z = \int \mathcal{D}[\phi] e^{-\beta H} = \int \mathcal{D}[\phi] e^{-\beta H + \beta H_T - \beta H_T} \quad (3.4)$$

By multiplying the expression with $1 = Z_T/Z_T$, we can define the average $\langle \dots \rangle_T$

$$\langle \dots \rangle_T = \frac{1}{Z_T} \int \mathcal{D}[\phi] e^{-\beta H_T} (\dots) \quad (3.5)$$

in the expression. The partition function Z can now be written as the averaged function of the difference between the original and the trial Hamiltonian.

$$Z = Z_T \left\langle e^{-\beta(H - H_T)} \right\rangle_T \quad (3.6)$$

In order to compute the average of a function $\exp(\dots)$, we would need to compute the average of all powers of the argument. This is not feasible. But it is possible put a lower limit on the partition function using Jensens inequality $\langle e^{-A} \rangle \geq e^{-\langle A \rangle}$, [51].

$$Z \geq Z_T e^{\langle -\beta(H-H_T) \rangle_T} \quad (3.7)$$

Taking the logarithm on both sides we get

$$-\ln(Z) \leq -\ln(Z_T) + \langle \beta H - \beta H_T \rangle_T$$

So the minimum of the functional

$$\mathcal{V}[H_T] = -\ln(Z_T) + \langle \beta H - \beta H_T \rangle_T \stackrel{!}{=} \min \quad (3.8)$$

now determines the best or “closest” approximation of the system.

Computing the derivatives

The minimum condition $\partial_\alpha \mathcal{V} \stackrel{!}{=} 0$ now determines the optimal parameters $\alpha = \{r, Q\}$. The calculation is done in two parts. First the equation is reduced to simple averages which will be evaluated in the second part.

Reducing the minimum condition to simple averages

Starting with the first term $\ln Z_T$ from equation (3.8) we immediately get

$$-\partial_\alpha \ln(Z_T) = -\frac{1}{Z_T} \int \mathcal{D}[\phi] e^{-\beta H_T} (\partial_\alpha (-\beta H_T)) = \langle (\partial_\alpha \beta H_T) \rangle_T \quad (3.9)$$

This reduces the problem to the simple average of the derivatives of the trial Hamiltonain. When dealing with the second part, it is convenient to introduce $\Delta = \beta H - \beta H_T$ and $\langle \dots \rangle \equiv \langle \dots \rangle_T$ to clear up the notation. Then we get

$$\begin{aligned} \partial_\alpha \langle \Delta \rangle &= \partial_\alpha \left(\frac{1}{Z_T} \int \mathcal{D}[\phi] e^{-\beta H_T} \Delta \right) \\ &= -\frac{1}{Z_T^2} (\partial_\alpha Z_T) \int \mathcal{D}[\phi] e^{-\beta H_T} \Delta + \frac{1}{Z_T} \int \mathcal{D}[\phi] e^{-\beta H_T} (\partial_\alpha (-\beta H_T)) \Delta \\ &\quad + \frac{1}{Z_T} \int \mathcal{D}[\phi] e^{-\beta H_T} \partial_\alpha \Delta \\ &= \langle (\partial_\alpha \beta H_T) \rangle \langle \Delta \rangle - \langle (\partial_\alpha \beta H_T) \Delta \rangle + \langle \partial_\alpha \Delta \rangle \end{aligned} \quad (3.10)$$

Note that $\partial_\alpha \Delta = -\partial_\alpha \beta H_T$, since H is independent of r and Q . The derivative $\partial_\alpha \mathcal{V}$ can now be computed by combining the two previous results

$$\begin{aligned} \partial_\alpha \mathcal{V}[H_T] &= \partial_\alpha [-\ln Z_T + \langle \Delta \rangle] \\ &= \langle \partial_\alpha \beta H_T \rangle + \langle \partial_\alpha \beta H_T \rangle \langle \Delta \rangle - \langle (\partial_\alpha \beta H_T) \Delta \rangle + \langle \partial_\alpha \Delta \rangle \\ &= [\langle \partial_\alpha \beta H_T \rangle \langle \Delta \rangle - \langle (\partial_\alpha \beta H_T) \Delta \rangle] \end{aligned} \quad (3.11)$$

This leaves us with the equation for the minimum of the functional as

$$\langle \partial_\alpha \beta H_T \rangle \langle \Delta \rangle - \langle (\partial_\alpha \beta H_T) \Delta \rangle = 0 \quad (3.12)$$

Computing the averages

Now when computing the averages in equation (3.12), it is useful to introduce the new fields $\partial_x \varphi = \partial_x \phi - Q$. The approximate Hamiltonian H_T is quadratic in $\partial_x \varphi$ with mean 0, turning the average $\langle \dots \rangle_T$ into a Gaussian average with zero mean. This makes the application of Wick's theorem for the $\partial_x \varphi$ possible. Now we will compute the derivatives $\partial_r H_T$ and $\partial_Q H_T$ and then write the results in the new fields $\partial_x \varphi$. The $\partial_r \beta H_T$ derivative is simply

$$\partial_r \beta H_T = \frac{K_0}{2} \int d^2x [(\partial_x \phi - Q)^2] = \frac{K_0}{2} \int d^2x (\partial_x \varphi)^2 \quad (3.13)$$

Writing it as a power series in $(\partial_x \varphi)^n$ where all the coefficients h_n^r are zero except for $h_2^r = 1$ with

$$\partial_r \beta H_T = \frac{K_0}{2} \int d^2x \left[\sum_n h_n^r (\partial_x \varphi)^n \right] \quad (3.14)$$

This will help later on when applying Wick's theorem. The $\partial_Q \beta H_T$ will be treated in the same way.

$$\partial_Q \beta H_T = \frac{K_0}{2} \int d^2x [-2Qr(\partial_x \phi - Q)] = \frac{K_0}{2} \int d^2x [-2Qr\partial_x \varphi] \quad (3.15)$$

The coefficients h_n^Q of the power series are zero except for $h_1^Q = -2Qr$ with

$$\partial_Q \beta H_T = \frac{K_0}{2} \int d^2x \left[\sum_n h_n^Q (\partial_x \varphi)^n \right] \quad (3.16)$$

The coefficients can be summarized as

$$h_n^r = \delta_{n,2} \quad h_n^Q = -2Qr \delta_{n,1} \quad (3.17)$$

The same variable transformations are applied to Δ with the expansion coefficients f_n

$$\Delta = \frac{K_0}{2} \int d^2x \left[\frac{1}{4} [(\partial_x \varphi + Q)^2 - \theta^2]^2 - r(\partial_x \varphi)^2 \right] = \frac{K_0}{2} \int d^2x \left[\sum_n f_n (\partial_x \varphi)^n \right] \quad (3.18)$$

Expanding the powers after we have switched to $\partial_x \varphi$

$$\begin{aligned} \frac{1}{4} [(\partial_x \varphi + Q)^2 - \theta^2]^2 &= \frac{1}{4} (\partial_x \varphi + Q)^4 - \frac{\theta^2}{2} (\partial_x \varphi + Q)^2 + \frac{\theta^4}{4} \\ &= \frac{1}{4} (\partial_x \varphi)^4 + Q(\partial_x \varphi)^3 + \frac{1}{4} (6Q^2 - 2\theta^2) (\partial_x \varphi)^2 \\ &\quad + (Q^3 - \theta^2 Q) (\partial_x \varphi) + \frac{1}{4} (Q^4 - 2\theta^2 Q^2 + \theta^4) \end{aligned}$$

we can now identify the non-vanishing coefficients f_n as listed in table 3.1. The minimum equation (3.12) for the functional $\partial_\alpha \mathcal{V}[H_T] = 0$ then takes on the general form

$$\sum_{n,m} h_n^\alpha f_m [\langle (\partial_x \tilde{\varphi})^n \rangle \langle (\partial_x \tilde{\varphi})^m \rangle - \langle (\partial_x \tilde{\varphi})^n (\partial_x \tilde{\varphi})^m \rangle] = 0 \quad (3.19)$$

f_n	Value
f_0	$\frac{1}{4}(Q^2 - \theta^2)^2$
f_1	$Q(Q^2 - \theta^2)$
f_2	$\frac{1}{4}(6Q^2 - 2\theta^2) - r$
f_3	Q
f_4	$\frac{1}{4}$
$f_{n>4}$	0

Table 3.1: The coefficients for the expansion of Δ in powers of $(\partial_x \varphi)^n$.

Applying Wick's theorem

Now the task is to simplify and finally solve the equation (3.19). So far we have reduced it to averages over finite powers of the fields $\partial_x \varphi$. As we discussed earlier, the average is Gaussian and we can use Wick's theorem, as e.g. derived in [52], to reduce the average of higher powers to functions of the variance. First we will write equation (3.19) in a compact form by introducing $A = \partial_x \varphi$ and $B = \partial_{x'} \varphi$. We can also see that all the terms with either $n = 0$ or $m = 0$ cancel. In the first term, only even n or m survive because odd powers of ∂_φ average to zero, i.e. $\langle A^{2k+1} \rangle = 0$. In the second term only $m + n = \text{even}$ terms survive due to Wick's theorem, resulting in

$$h_2^\alpha f_2 (\langle A^2 \rangle \langle B^2 \rangle - \langle A^2 B^2 \rangle) + h_2^\alpha f_4 (\langle A^2 \rangle \langle B^4 \rangle - \langle A^2 B^4 \rangle) - h_1^\alpha f_3 \langle AB^3 \rangle - h_1^\alpha f_1 \langle AB \rangle = 0$$

Applying Wick's theorem again, we see that only connected parts survive. For each term $h_n^\alpha f_n$ the results of applying the Wick theorem are listed in table 3.1. The minimum condition for the

$h_n^\alpha f_n$	$\langle \dots \rangle \langle \dots \rangle$	$\langle \dots \rangle$
$h_2^\alpha f_2$	$\langle A^2 \rangle \langle B^2 \rangle = \langle A^2 \rangle^2$	$\langle A^2 B^2 \rangle = \langle A^2 \rangle^2 + 2\langle AB \rangle^2$
$h_2^\alpha f_4$	$\langle A^2 \rangle \langle B^4 \rangle = 3\langle A^2 \rangle^3$	$\langle A^2 B^4 \rangle = 3\langle A^2 \rangle^3 + 12\langle A^2 \rangle \langle AB \rangle^2$
$h_1^\alpha f_1$	$\langle A \rangle \langle B \rangle = 0$	$\langle AB \rangle = \langle AB \rangle$
$h_1^\alpha f_3$	$\langle A \rangle \langle B^3 \rangle = 0$	$\langle AB^3 \rangle = 3\langle A^2 \rangle \langle AB \rangle$

Table 3.2: Wick's theorem applied to the averages, with $A \equiv \partial_x \varphi$ and $B \equiv \partial_{x'} \varphi$

functional can now be reduced to

$$-2h_2^\alpha \langle AB \rangle^2 (f_2 + 6f_4 \langle A^2 \rangle) - h_1^\alpha \langle AB \rangle (f_1 + 3f_3 \langle A^2 \rangle) = 0 \quad (3.20)$$

Plugging in the concrete values for h_n^α and f_n from equation (3.17) and table 3.1, minimization in respect to r and Q results in the two following equations

$$\partial_Q \mathcal{V} \stackrel{!}{=} 0 \quad \Rightarrow \quad Q \{Q^2 - \theta^2 + 3\langle (\partial_x \varphi)^2 \rangle\} = 0 \quad (3.21)$$

$$\partial_r \mathcal{V} \stackrel{!}{=} 0 \quad \Rightarrow \quad 3Q^2 - \theta^2 - 2r + 3\langle (\partial_x \varphi)^2 \rangle = 0 \quad (3.22)$$

with the two solutions

$$\textcircled{1} \quad r = \theta^2 - 3\langle (\partial_x \varphi)^2 \rangle \quad Q^2 = r \quad (3.23)$$

$$\textcircled{2} \quad 2r = -\theta^2 + 3\langle (\partial_x \varphi)^2 \rangle \quad Q = 0 \quad (3.24)$$

3.2 The solutions

The solution ① from equation (3.23), has a finite $Q \neq 0$ and represents the chiral case. The second solution ② with $Q = 0$ is the non-chiral case. When the system switches from one solution to the other, we will have pin-pointed the chiral transition. For $T \rightarrow 0$ the fluctuation term $\langle(\partial_x\varphi)^2\rangle$ vanishes and the system goes to $r = \theta^2$ and $Q = \pm\theta$. This is the chiral ground state, as expected. For high temperatures the fluctuations increase to a point where $3\langle(\partial_x\varphi)^2\rangle > \theta^2$. A negative r in solution ① corresponds to an imaginary Q and is non-physical. The selected solution is ② with $Q = 0$, where the chiral order is lost.

To investigate the solution, we will start with a closer look at the fluctuations $\langle(\partial_x\varphi)^2\rangle$ given as

$$\langle(\partial_x\varphi)^2\rangle = \frac{1}{K_0} \int_{-\pi}^{\pi} \frac{d^2k}{(2\pi)^2} \frac{k_x^2}{rk_x^2 + k_y^2 + \frac{1}{4}k_x^4} \equiv \frac{1}{K_0} \sigma^2(r) \quad (3.25)$$

Here we introduced the a cutoff $\Lambda = \pi$, restricting the momentum-space integrals to the first Brillouin zone of the system. The function $\sigma^2(r)$ can be calculated analytically, for example with a computer algebra system, and has the form

$$\begin{aligned} \sigma^2(r) = & \frac{2}{\pi^2} \left(\sqrt{2} \sqrt{\sqrt{r^2 - \pi^2} + r} \tan^{-1} \left(\frac{\pi}{\sqrt{2} \sqrt{r - \sqrt{r^2 - \pi^2}}} \right) \right. \\ & + \sqrt{2} \sqrt{r - \sqrt{r^2 - \pi^2}} \tan^{-1} \left(\frac{\pi}{\sqrt{2} \sqrt{\sqrt{r^2 - \pi^2} + r}} \right) \\ & \left. - \pi \sqrt{r} + \sqrt{4r + \pi^2} \tan^{-1} \left(\frac{2}{\sqrt{4r + \pi^2}} \right) \right) \end{aligned} \quad (3.26)$$

The function $\sigma^2(r)$ cannot be inverted. Self-consistent solutions to the two equations 3.23 and 3.24 will have to be found numerically.

Low temperatures

Let us start with the low temperature solution ①. The equation (3.23) describing the solution can be written as

$$K_0(r - \theta^2) = -3\sigma^2(r) \quad (3.27)$$

The left hand side of the equation is a line going through $r = \theta^2$ with a slope K_0 . The function $\sigma^2(r)$ is convex. We can see this fact by computing the second derivative

$$\partial_r^2 \sigma^2(r) = \frac{1}{2\pi^2} \int d^2k \frac{k_x^6}{(rk_x^2 + k_y^2 + \frac{1}{4}k_x^4)^3} > 0 \quad (3.28)$$

Since the second derivative of $\sigma^2(r)$ in respect to r is always positive, $\sigma^2(r)$ is convex. The right hand side of equation (3.27), $-3\sigma^2(r)$, is therefore a concave function with the lowest value $-3\sigma^2(0) \approx -3.5794$. We can now plot $-3\sigma^2(r)$ and the line $K_0(r - \theta^2)$ and look for intersecting points in order to solve the equation (3.27). For small θ the features in the plots are hard to make out, so we use a schematic plot with $\theta^2 = 1$ in figure 3.1 to illustrate the discussion. Shown is the concave function $-3\sigma^2(r)$ and the line for three different temperatures. For low temperature T the parameter $K_0 = \beta J_0$ becomes large. In this region we find one solution to r . then for a certain temperature range there will be two different solutions for r that will meet for a finite r_c at T_c and than the equation will produce no solution for r for higher $T > T_c$.

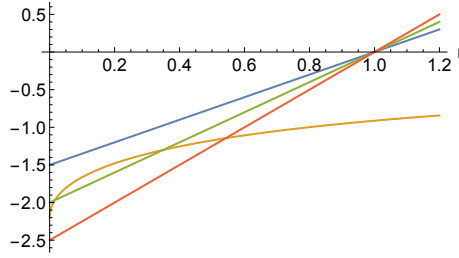


Figure 3.1: Illustration of the low-T equations for r . Drawn is the concave function $-3\sigma^2(r)$ (right hand side of equation (3.27)) and the left hand side of the same equation for different temperatures T . One can easily see how the equation goes from one solution (small T , large slope) over to produce two solutions and finally no solution at all for r

The second solution to the equation (3.23) emerges once the line $K_0(r - \theta^2)$ allows the solution $r = 0$ by passing through the point $-3\sigma^2(0)$. The temperature K_c , that marks this emergence of the second solution is determined to be

$$K_c^{-1} = \frac{\theta^2}{3\sigma^2(0)} \quad (3.29)$$

with $\sigma^2(0) \approx 0.732805$. The other special point r_d is reached, when both solutions merge. The critical temperature K_d^{-1} is reached once the line $K_d(r_d - \theta^2)$ with the slope K_d is a tangent to the function $-3\sigma^2(r)$, which is the case when

$$K_d = -3\partial_r \sigma^2(r) \Big|_{r=r_d} = -3\sigma^{2'}(r_d) \quad (3.30)$$

The prime denotes the derivative in respect to r . The value r_d , where the two solutions merge is determined by the equation

$$r_d - \theta^2 = \frac{\sigma^2(r_d)}{\sigma^{2'}(r_d)} \quad (3.31)$$

Since $\sigma^2(r)$ and $\sigma^{2'}(r)$ are known, the equation can be solved numerically. Once the value r_d is known, the critical temperature marking this point is then given by

$$K_d^{-1} = \frac{1}{3} \frac{1}{|\sigma^{2'}(r_d)|} \quad (3.32)$$

Both critical temperatures $K_c^{-1}(\theta)$ and $K_d^{-1}(\theta)$ are shown in figure 3.2. As one can see, the difference between the two solutions starts to vanish for small θ . In the regime of small $\theta \ll 1$ for which our model was expanded, there is only one solution for a given θ .

High temperatures

The case for high temperatures is less complicated. The equation we have to solve can be written as

$$K_0(2r + \theta^2) = 3\sigma^2(r) \quad (3.33)$$

Here we have a straight line going through $-\frac{1}{2}\theta^2$ with the slope $2K_0$. As we discussed earlier, the function on the right hand side $3\sigma^2(r)$ is convex. For all slopes $2K_0$ there is only one point of intersection.

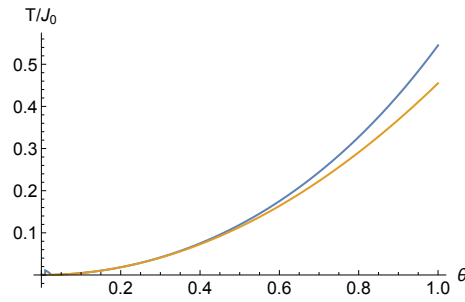


Figure 3.2: The critical temperatures $K_c^{-1}(\theta)$ and $K_d^{-1}(\theta)$ as functions of θ with $K_c^{-1} < K_d^{-1}$. The region between the two temperatures marks the temperature window where two solutions to the equation (3.27) for r exist. As we see this window vanishes for small θ .

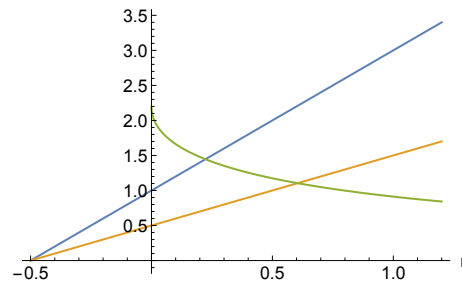


Figure 3.3: Illustration of the high-T equations for r . Drawn is the convex function $3\sigma^2(r)$ (right hand side of equation (3.33)) and the left hand side of the same equation for different temperatures T . One can easily see how there is only one solution for r for a given temperature.

3.3 Discussion

Now, using a computer algebra system like Mathematica, the equations (3.23) and (3.24) can be solved numerically. All solutions for r/θ^2 for $\theta = 1$ are shown in figure 3.4 For $\theta = 1$ the region

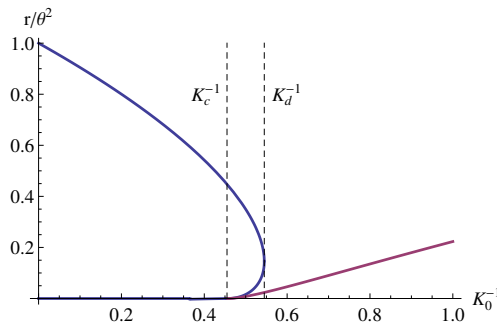


Figure 3.4: The found solutions for $\theta = 1$. The dashed lines mark K_d^{-1} and K_c^{-1} with $K_c^{-1} < K_d^{-1}$.

between K_c^{-1} and K_d^{-1} is pretty pronounced and would indicate a first order transition due to

the jump in order parameter. As we discussed earlier, this window decreases rapidly for small θ , approaching a continuous change in the order parameter. The variational approach is known to wrongly capture a second order transition as a first order one.

A prominent example is the variational study of the XY model discussed by Patashinskii and Pokrovskii in [53]. Here the continuous phase transition, will lead to a jump in the fitted order parameter. Without further knowledge this would cause one to believe the transition to be first order, which is clearly wrong. In a similar model, the same effect has been discussed by Pytte, [54]. The transition is believed to be continuous and the jump in order parameter is an artifact of the variational method.

The chiral transition is indicated by a vanishing $r = 0$. For the critical temperature K_c^{-1} of the chiral transition we then simply find

$$K_c^{-1} = \frac{\theta^2}{3\sigma^2(0)} \propto \theta^2 \quad (3.34)$$

4. Renormalization Group

In the previous chapter we focused on the chiral transition using a variational approach. Here the compact nature of the angles $\phi(\mathbf{x})$ was ignored and in extension vortices. Now we will focus on the vortices in the system and their influence on the magnetic phase transition in order to obtain a complete picture. As we saw when discussing the model in section 2.1, the system is described by

$$\beta H = \frac{K_0}{2} \int d^2x \left[\frac{1}{4}(\phi_x^2 - \theta^2)^2 + \phi_y^2 + \frac{1}{4}\phi_{xx}^2 \right]. \quad (4.1)$$

To shorten the equations, we have introduced the short hand notation for the derivatives as $\phi_x \equiv \partial_x \phi$. Each subscript marks one derivative, so ϕ_{xx} is the second derivative of ϕ in respect to x . Without the constant energy offset $\frac{1}{2}\theta^4$, the model is simply

$$\beta H = \frac{K_0}{2} \int d^2x \left[-\frac{1}{2}\theta^2\phi_x^2 + \phi_y^2 + \frac{1}{4}\phi_{xx}^2 + \frac{1}{4}\phi_x^4 \right] \quad (4.2)$$

and can be substituted by the effective model

$$\beta \mathcal{H} = \frac{K_0}{2} \int_{\mathbf{x}} \left[r\phi_x^2 + \phi_y^2 + \frac{1}{4}\phi_{xx}^2 + \frac{u}{4}N[\phi_x^4] \right] \quad (4.3)$$

with the parameters r and u . Here $N[\phi_x^4] = \phi_x^4 - 6\sigma^2\phi_x^2 + \sigma^4$ is the normal ordering and $\sigma^2 = \langle \phi_x^2 \rangle$ is the same fluctuation term as used in the previous chapter, [40]. In this model,

$$\xi_x = \frac{1}{\sqrt{r}} \qquad \xi_y = \frac{1}{r} \quad (4.4)$$

can be directly identified as playing the role of the correlation length in x - and y -direction.

4.1 Vortices

Now, in order to focus on vortices, let us consider a region of the dimensions L_x and L_y . We can rescale the system with $x/L_x \mapsto x$ and $y/L_y \mapsto y$ and introduce the parameters $\lambda_\alpha = \xi_\alpha/L_\alpha$. The linearized saddle point equation for the system after this rescaling is

$$\lambda_x^2\phi_{xx} - \frac{1}{4}\lambda_x^4\phi_{xxxx} + \lambda_y^2\phi_{yy} = 0 \quad (4.5)$$

[40]. Analogous to the classical XY model, the angle ϕ can be split into a spin-wave part ϕ_s and vortex part ϕ_v . Both do not interact. The spin wave part ϕ_s , which carries the chiral order, will be treated using the RG method later in this chapter.

The saddle-point equation (4.5) with an additional inhomogeneous part $\delta(\mathbf{x})$ on the right-hand side describes a vortex. This equation cannot be solved analytically. On small scales, large momenta, the ϕ_{xx} can be ignored compared to the ϕ_{xxxx} term. This is equivalent to setting $r = 0$. In this case the scaling between length in y -direction and x -direction is easily identified

as $L_y \sim L_x^2$. One way of estimating the core energy of the vortex is by choosing an appropriate anisotropic ansatz for the vortex

$$\phi_v(x, y) = \arcsin(\zeta)\theta(x) + [\pi - \arcsin(\zeta)]\theta(-x) \quad (4.6)$$

where $\zeta = y/\sqrt{\kappa^2 x^4 + y^2}$ and $\theta(x)$ is the Heaviside step function. κ is a numerical parameter that we can now vary to minimize the energy. The powers x^4 and y^2 in the denominator reflect the scaling law for small scales. The Ansatz is plotted in figure 4.1. Now we can minimize the core energy ($r = 0$)

$$E_{\text{core}}(\kappa) = \frac{K_0}{2} \int d^2x \left[\phi_y^2 + \frac{1}{4}(\phi_{xx}^2 + \phi_x^4) \right] \quad (4.7)$$

with respect to κ . When introducing a cutoff on the scales of the lattice constant $a = 1$, these integrals can be solved analytically. This is summarized in the appendix B.1. The function

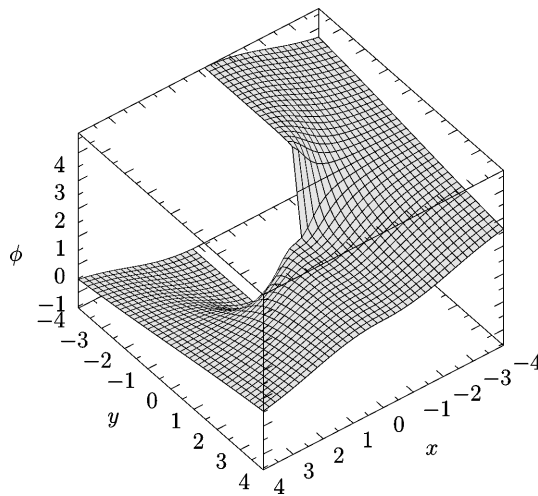


Figure 4.1: Anisotropic Vortex Ansatz plotted for $\kappa = 0.42$.

$E_{\text{core}}(\kappa)$ can now be minimized using standard numerical methods and we obtain the results

$$\bar{E}_{\text{core}} = 2.38K_0 \quad \kappa = 0.42 \quad (4.8)$$

The vortices are dominated by short length scales as is their interaction. In the regular BKT scenario the long range interactions are screened by the appearance of vortex–antivortex pairs on shorter scales. In the case of an already small scale of the interaction length, this screening mechanism will not take place. There is simply no space for additional vortex–antivortex pairs to form and screen the interaction. On large scales the ϕ_{xxxx} term in the saddle point equation can be ignored and we obtain the standard Berezinskii–Kosterlitz–Thouless vortices for $\lambda_x = \lambda_y = 1$.

4.2 Long-range interaction in Ising order parameter model

On small scales, when the correlation length exceed the vortex size, $\xi_\alpha \ll L_\alpha$, ϕ_x acts as the order parameter of the system. As we will see now, introducing this Ising like order parameter $\psi = \phi_x$ in our system will lead to a long range interaction. This is profoundly different from the classical soft spin $\lambda\psi^4$ theory for the Ising model. The transition should therefore not lie in the

Onsager universality class. Later, after doing more rigorous calculations, we will indeed see that the critical exponents are different from the Onsager ones.

Starting with the effective Hamiltonian \mathcal{H} , equation (4.3), we switch to the order parameter $\psi \equiv \phi_x$. The only non-trivial part of the Hamiltonian will be due to the ϕ_y^2 -proportional term

$$\mathcal{H}_y = \frac{K_0}{2} \int d^2x \phi_y^2 \quad (4.9)$$

Using the Fourier transform, as e.g. discussed in [5]

$$f(\mathbf{x}) = \frac{1}{L^d} \sum_{\mathbf{k}} e^{i\mathbf{k}\mathbf{x}} f_{\mathbf{k}} \quad f_{\mathbf{k}} = \int d^d x e^{-i\mathbf{k}\mathbf{x}} f(\mathbf{x}) \quad (4.10)$$

this interaction transforms to

$$\tilde{\mathcal{H}}_y = \frac{K_0}{2} \sum_{\mathbf{k}} k_y^2 |\phi_{\mathbf{k}}|^2 = \frac{K_0}{2} \sum_{\mathbf{k}} \frac{k_y^2}{k_x^2} |\psi_{\mathbf{k}}|^2 \quad (4.11)$$

In the last step we already switched to our new order parameter ψ by using $\psi_{\mathbf{k}} \equiv i k_x \phi_{\mathbf{k}}$. Now we want to transform this expression back into position space. The back transformation of the k_y^2 part is simple and returns the partial derivatives ∂_y in y . The complicated and therefore interesting term revolves around the back transformation of the $1/k_x^2$ interaction.

$$A = \int \frac{dk_x}{2\pi} \frac{e^{ik_x x}}{k_x^2} = -\frac{1}{2}|x| \quad (4.12)$$

The Fourier transform can be solved by a computer algebra system, e.g. Mathematica. Another approach is to realize that the second derivative of this function is $\partial_x^2 A = -\delta(x)$. In this case the integral can be written as $A = -1/2(x\theta(x) - x\theta(-x))$ with

$$\partial_x^2 A = -\partial_x \left[\frac{1}{2} (\theta(x) - \theta(-x) + 2x\delta(x)) \right] = -\delta(x) \quad (4.13)$$

Combining the result with the y -back transform, we have the following long range interaction in position space.

$$-\frac{1}{2} \int d^2x \int dx' \psi_y(x, y) |x - x'| \psi_y(x', y) \quad (4.14)$$

4.3 RG - small scales

The consideration of different length scales that we did for the vortices, is also important when doing the renormalization group approach. We will be starting with small scales, where the correlation length ξ exceeds the system size in each direction. Following the standard approach from [5], we can write down the RG flow equations for the parameters r , K , u and the vortex fugacity y . The initial values for these parameters are given by $r_0 \ll 1$, $u_0 = 1$, K_0 and $y_0 = \exp(-E_{\text{core}})$, with the vortex core energy as we have estimated earlier. As will be discussed in more detail later, when focusing on the anomalous scaling dimension of the system, the u term is not marginal in $d = 2$. The critical dimension of the system is $d_c = 5/2$. We will extend the y -dimension into a $(d-1)$ -dimensional vector and perform the flow calculations as perturbations in the small parameter $\epsilon = 5/2 - d$. The RG procedure starts by integrating out the fluctuation in $\phi_{\mathbf{k}}$ limited by the momentum shell

$$\pi^2 > \frac{1}{4} k_x^4 + k_y^2 > \pi^2 e^{-2l} \quad (4.15)$$

with the small scale parameter l , and finally rescaling the parameters according to

$$x = x' e^{l/2} \quad y = y' e^l \quad r' = r e^l \quad (4.16)$$

We do not rescale ϕ as it is a compact variable and we want to treat it as such. u is not rescaled as well. The flow equations that we obtain as a result are

$$\frac{d \ln u}{dl} = -\frac{9}{2\pi^3} \frac{u}{K} \quad \frac{d \ln r}{dl} = 1 - \frac{9}{6\pi^3} \frac{u}{K} \quad (4.17)$$

We discussed earlier, that on the small scales there is no screening due to vortices. Consequently the vortex fugacity $y = \exp(-K)$ and K only change via rescaling, meaning

$$\frac{dK}{dl} = -\epsilon \quad \frac{d \ln y}{dl} = \frac{3}{2} \quad (4.18)$$

The rescaling of the vortex fugacity $y = \exp(-E_{\text{core}} + S)$ is due to the entropy S , corresponding to the change in area

$$S = \ln \left(\frac{xy}{x'y'} \right) = \frac{3}{2} l \quad (4.19)$$

The RG procedure stops when we reach $r_{l_c} \approx 1$ with $e^{l_c} \equiv \xi_y$. Integrating the flow equations (4.17) produces

$$\xi_y = \frac{2}{t\theta^2} \mathcal{P} \quad (4.20)$$

$$t = \frac{K_0}{K} - 1 \quad (4.21)$$

$$\mathcal{P}(\xi_y) = 1 + \frac{9}{2\pi^3} \frac{1}{\epsilon K_0} (\xi_y^\epsilon - 1) \quad (4.22)$$

The critical region of the chiral transition marked by

$$\frac{9}{2\pi^3} \frac{1}{\epsilon K_0} \xi_y^\epsilon \gg 1 \quad (4.23)$$

we find for the correlation length ξ_y and the correlation length exponent ν_y

$$\xi_y \sim \frac{1}{\theta^2} |t|^{-\nu_y} \quad \nu_y^{-1} = 1 - \frac{\epsilon}{3} \quad (4.24)$$

From the general scaling for the correlation lengths we see $\nu_y^{-1} = (2\nu_x)^{-1}$. Systems with an anisotropic Lifshitz point, such as the one discussed here, were also studied by Hornreich et al. using a Ginzburg–Landau expansion, [55]. They found the anisotropic scaling law

$$\nu_x(d-1)\nu_y = 2 - \alpha \quad (4.25)$$

which is satisfied for $\alpha = \nu_y \epsilon / 3$.

4.4 RG - large scales

On large scales $l > l_c$ the non-linear terms of our system can be ignored. In this case, the vortices are just the standard BKT vortices and for $d = 2$ the flow equations are just the standard BKT equations

$$\frac{d}{dl} \tilde{K}^{-1} = 4\pi^3 y^2 \quad \frac{dy}{dl} = (2 - \pi \tilde{K}) y \quad (4.26)$$

as can be found in [5]. Unlike the flow equations for the small scales, these equations cannot be easily integrated.

Numerical solution

There is no known solution to these coupled differential equations for $K(l)$ and $y(l)$. We have to resort to other means in order to obtain something feasible. Taking the second derivative of \tilde{K}^{-1} in respect to the length scale l for example leads to

$$\frac{d^2}{dl^2} \tilde{K}^{-1} = 8\pi^3 y \frac{dy}{dl} = 8\pi^3 y^2 (2 - \pi \tilde{K}) = 2(2 - \pi \tilde{K}) \frac{d}{dl} \tilde{K}^{-1} \quad (4.27)$$

which is now just a differential equation for $\tilde{K}^{-1}(l)$, independent of $y(l)$. This can be now be solved numerically. Taking l to be a large value, we can even hope to approximate the critical value $\tilde{K}_\infty^{-1} = \tilde{K}^{-1}(l \rightarrow \infty)$. A fairly good approximation is $l = 100$ in the numerics. Given the starting values $\tilde{K}^{-1}(l = 0) = K_0^{-1}$ and $\frac{d}{dl} \tilde{K}^{-1}(l = 0) = 4\pi^3 y_0^2$, the simple Mathematica code from listing 4.1

```

1 KInf[k0_, g0_] := Module[{numerik, f, x},
2   numerik[x_] =
3     f[x] /. NDSolve[{f'[x] == 2 f[x] (2 - Pi/f[x]), f[0] == 1/k0,
4     f'[0] == g0}, f[x], {x, 0, 100}][[1]];
5   1/numerik[100]
6 ]

```

Listing 4.1: Mathematica Code used to numerically solve for $\tilde{K}_\infty(\tilde{K}_0, y_0)$

produces the numeric solution $\tilde{K}_\infty(K_0, y_0)$. The results of the Mathematica code using the starting value $y_0 = \exp(-K_0)$ and the length cutoff $l = 100$ are shown in figure 4.2.

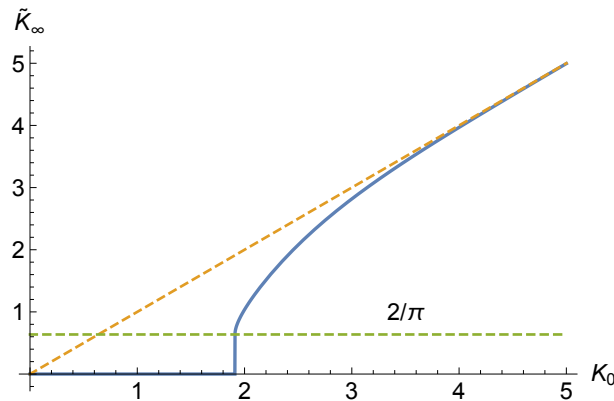


Figure 4.2: Shown is the function $\tilde{K}_\infty(K_0, y_0)$ with $y_0 = \exp(-K_0)$. For reference the value $\tilde{K}_\infty = 2/\pi$ and the line $\tilde{K}_\infty = K_0$ have been drawn (dashed lines).

Analytical solution

It turns out that the function $\tilde{K}_\infty(K_0)$ can be obtained analytically. For this we divide the differential equations to obtain the ODE of the critical line

$$\frac{d}{dy} \tilde{K}^{-1} = \frac{4\pi^3 y}{2 - \pi \tilde{K}} \quad (4.28)$$

This equation is separable

$$d\tilde{K}^{-1} \left(2 - \frac{\pi}{\tilde{K}^{-1}} \right) = dy(4\pi^3 y) \quad (4.29)$$

and we can integrate both sides, using the starting values K_0^{-1} and y_0 .

$$2 \left(\frac{1}{\tilde{K}} - \frac{1}{K_0} \right) - \pi \ln \left(\frac{K_0}{\tilde{K}} \right) = 2\pi^3 (y^2 - y_0^2) \quad (4.30)$$

Taking the $\exp(\dots)$ on both sides leaves us with

$$\frac{\tilde{K}}{K_0} \exp\left(\frac{2}{\pi}(\tilde{K}^{-1} - K_0^{-1})\right) = \exp(2\pi^2(y^2 - y_0^2)) \quad (4.31)$$

This equation can be solved for \tilde{K} , where the solution is related to the Lambert W function. To make this connection more clear, we will introduce the constants c_1 and c_2 to contain everything but the \tilde{K} dependency leading to

$$\tilde{K} \exp\left(\frac{c_1}{\tilde{K}}\right) = c_2 \quad (4.32)$$

$$c_1 = 2/\pi \quad (4.33)$$

$$c_2 = K_0 \exp\left(2\pi^2(y^2 - y_0^2) + \frac{2}{\pi} \frac{1}{K_0}\right) \quad (4.34)$$

The Lambert W function is defined as the inverse to $xe^x = y$, so the function $W(y)$ satisfies the identity

$$W(y) \exp(W(y)) = y \quad (4.35)$$

The defining equation for $W(y)$ looks very similar to our equation (4.32). Indeed we can use the knowledge of $W(y)$ ¹ to solve for $\tilde{K}(y)$ as

$$\tilde{K}(y) = -\frac{c_1}{W(-c_1/c_2)} \quad (4.36)$$

$$\tilde{K}^{-1}(y) = -\frac{1}{c_1} W(-c_1/c_2) \quad (4.37)$$

Combined with $y_0 = \exp(-K_0)$ this leads to the expressions

$$\tilde{K}_\infty(K_0) = -\frac{2}{\pi W\left(-\frac{2}{\pi K_0} \exp\left(2\pi^2 e^{-2K_0} - \frac{2}{\pi K_0}\right)\right)} \quad (4.38)$$

$$\tilde{K}_\infty^{-1}(K_0) = -\frac{\pi}{2} W\left(-\frac{2}{\pi K_0} \exp\left(2\pi^2 e^{-2K_0} - \frac{2}{\pi K_0}\right)\right) \quad (4.39)$$

We can now compare this analytic solution to the one obtained earlier by numerically integrating the equations for \tilde{K} . The results are pictured in figure 4.3 and show excellent agreement. The equation for $\tilde{K}(y)$ can also be inverted to

$$y = \pm \frac{1}{\sqrt{2\pi}} \sqrt{\ln\left(\frac{c_0 e^{2\tilde{K}^{-1}/\pi}}{\tilde{K}^{-1}}\right)} \quad (4.40)$$

$$c_0 = K_0 \exp\left(\frac{2}{\pi K_0} - 2\pi^2 y_0^2\right) \quad (4.41)$$

¹The Lambert W function is referred to as ProductLog in Mathematica

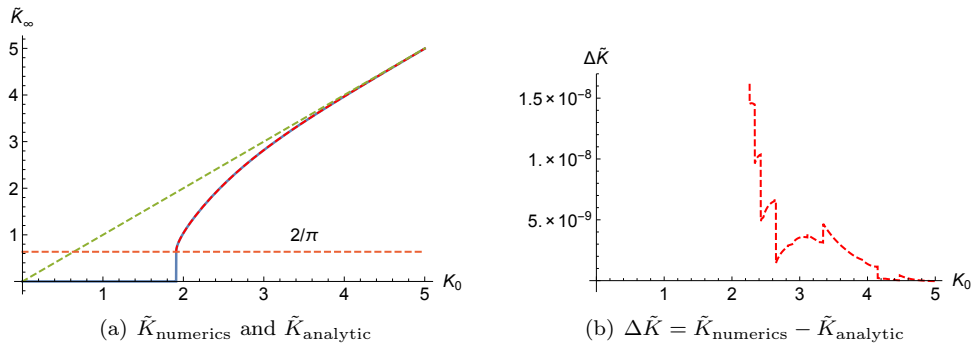


Figure 4.3: The plots show the difference between the numerically obtained result for $\tilde{K}_\infty(K_0)$ with the analytic solution. We see that the difference is of the order of $\sim 10^{-9}$. Both results are in excellent agreement.

The figure 4.4 shows $y(K^{-1})$ for different starting values K_0 and $y_0 = \exp(-K_0)$, similar to e.g. the one depicted in [10]. We can also see that the critical value $\tilde{K}_\infty = 2/\pi$ is reached for

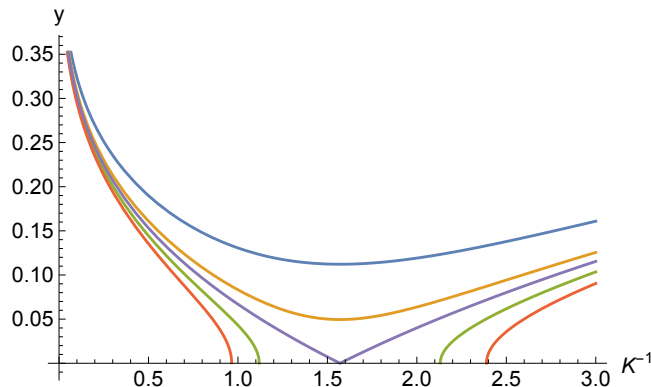


Figure 4.4: Flow diagram for Kosterlitz recursion relations as derived from the known set of differential equations.

$W(x) = -1$. With $W(-1/e) = -1$ this gives the condition $c_1/c_2 = 1/e$. The critical equation describing the points (K_0, y_0) that lead to a critical \tilde{K}_∞ is given by

$$\frac{1}{K_0} \exp\left(2\pi^2 y_0^2 - \frac{2}{\pi K_0}\right) = \frac{\pi}{2e} \quad (4.42)$$

We arrive at the same condition by looking at the values that produce $y = 0$ in equation (4.40).

Taking the $\ln(\dots)$ on both sides of the critical equation (4.42) we get

$$\frac{2}{\pi K} = 1 + \ln(2) + 2\pi^2 y^2 - \ln(\pi K) \quad (4.43)$$

describing the values belonging to the BKT transition.

4.5 Anomalous dimension of chiral transition

Now let us focus specifically on the anomalous scaling dimension of the chiral system.

$$\beta H = \int dx \int d^{d-1}y \left[\frac{1}{2}r\phi_x^2 + \frac{1}{2}\phi_y^2 + \frac{1}{8}\phi_{xx}^2 + u\phi_x^4 \right] \quad (4.44)$$

where we extended $d \rightarrow 5/2$ to make the interaction term $u\phi_x^4$ marginal and enable a RG calculation. Using the following rescaling

$$\begin{aligned} x \mapsto x' = x/b & & r \mapsto r' = b^{\Delta_r} r & & \phi \mapsto \phi' = b^{\Delta_\phi} \phi \\ y \mapsto y' = y/b^z & & u \mapsto u' = b^{\Delta_u} u & & \end{aligned}$$

Fixing the scaling of the two gradient terms ϕ_y^2 and ϕ_{xx}^2 fixes the dynamical exponent $z = 2$, leaving the integral to scale as

$$\int dx d^{d-1}y \mapsto b^{1+2(d-1)} \int dx' d^{d-1}y' \quad (4.45)$$

With the condition that the gradients should not scale with b , we get $\Delta_\phi = d - 5/2$. The other scaling exponents follow leaving us with

$$\Delta_r = 2 \quad \Delta_\phi = d - \frac{5}{2} = -\epsilon \quad \Delta_u = 5 - 2d = 2\epsilon \quad z = 2$$

Now we will consider the perturbation around the dimension $d_c = 5/2$ in the small parameter $\epsilon = 5/2 - d$.

Fix point u^* to first order in ϵ

In order to compute the first order correction to the scaling in u we have to write down the first loop corrections due to

$$\begin{aligned} \text{Diagram} & = -36u^2 \int_{\Lambda/b}^{\Lambda} \frac{dk_x}{2\pi} \frac{d^{3/2}k_\perp}{(2\pi)^{3/2}} \frac{k_x^4}{(k_\perp^2 + \frac{1}{4}k_x^2)^2} = -36u^2 \frac{K_{3/2}}{(2\pi)^{5/2}} \ln(b) \quad (4.46) \end{aligned}$$

where the combinatorial pre-factor consists of $\frac{1}{2} * \binom{4}{2} * 2 * \binom{4}{2} = 36$ and the vertices giving a $(-1)(-u)^2$ contribution. We used the general change to spherical coordinates $\int d^d x = K_d \int dr r^{d-1}$ with $K_d = 2\pi^{d/2}/\Gamma(d/2)$. This leads to the one-loop rescaling of u as

$$\begin{aligned} u' & = b^{2\epsilon} \left[u - 36u^2 \frac{K_{3/2}}{(2\pi)^{5/2}} \ln(b) \right] \\ \Rightarrow u^* & = \frac{(2\pi)^{5/2} (1 - b^{2\epsilon})}{36K_{3/2} \ln(b)} \approx \frac{(2\pi)^{5/2}}{18K_{3/2}} \epsilon + \mathcal{O}(\epsilon^2) \quad (4.47) \end{aligned}$$

with the non-trivial fix point u^* .

2-loop correction to the self energy

Looking at the scaling relations, the full propagator $G = \langle \partial_x \phi \partial_x \phi \rangle \propto x^{-2-2\tilde{\Delta}_\phi} \propto k_x^{2-2\tilde{\Delta}_\phi}$ with $\tilde{\Delta}_\phi = \Delta_\phi + \Delta_\phi^{(\epsilon)}$. With $d = 5/2$ as we saw before, $\Delta_\phi = 0$ and the full propagator scaling can be

where the constant c_x can be numerically evaluated to be $c_x = -0.000281769$. The calculation is done in appendix B.7. The anomalous dimension then works out to be

$$\begin{aligned}\Delta_\phi^{(\epsilon)} &= 2 * 24u^{*2}K_{3/2}c_x = 48 \left(\frac{(2\pi)^{5/2}}{18K_{3/2}}\epsilon \right)^2 K_{3/2}c_x = \frac{4}{27} \frac{(2\pi)^5}{K_{3/2}} c_x \epsilon^2 \\ &\approx -0.10614 \epsilon^2\end{aligned}\tag{4.54}$$

An expansion in k_y with $k_x = 0$ in order to obtain the anomalous scaling dimension in y direction leads to

$$\begin{aligned}\int dx d^{3/2}y G^3(x, \mathbf{y}) (e^{i\mathbf{k}_\perp \cdot \mathbf{y}} - 1) &\approx \frac{2}{3} K_{3/2} k_\perp^2 \int dx \int dy \sqrt{y} y^2 G^3(x, \mathbf{y}) \\ &= \frac{2}{3} K_{3/2} k_\perp^2 \int dx \int dy \frac{1}{\sqrt{y}} f^3(x^2/y) \\ &= \frac{2}{3} K_{3/2} k_\perp^2 \underbrace{\int dy}_{\text{linear divergent}} \underbrace{\int dz \frac{1}{2\sqrt{z}} f^3(z)}_{\equiv c_y}\end{aligned}$$

There is no logarithmic divergence present, so no rescaling in the y direction takes place. The critical exponent in y direction therefor does not have any two-loop corrections. With $\eta = 2\Delta_\phi$ we get for the critical exponents

$$\eta_x = -0.212\epsilon^2 + \mathcal{O}(\epsilon^3) \qquad \eta_y = 0 + \mathcal{O}(\epsilon^3)\tag{4.55}$$

in two loop correction. Indeed, they are different from the Onsager exponents $\eta = \frac{1}{4}$, [40].

4.6 Comparison to numerics

The HXY model has been investigated numerically by Sorokin et al. [56]. They find different critical exponents than the ones discussed here. However, in their study they failed to properly account for the anisotropy of the system, [57]. We can read out the data from the plots and find the exponents ourselves, by fitting the obtained data. The data for the heat capacity C from figure 7 from [56] as it was read out graphically is listed in table B.1 in appendix B.8. Data was read out from the paper and can be found in table B.1 in appendix B.8.

The critical exponent α can now be obtained by fitting the power-law behavior close to the critical transition. The fit is shown in 4.5 and produces $\alpha \approx 0.32$. The chiral order parameter κ can be read out from figure 19 from [56]. Here, only a few data point are available. They are listed in table B.2. Determining the critical exponent β is done by manually fitting a line to the data in a double logarithmic plot, as shown in figure 4.6. This results in $\beta \approx 0.30$. The chiral susceptibility χ_k data is taken from figure 17 from [56] and is listed in table B.3. The fit is again done in the double logarithmic plot and is shown in figure 4.7. The result is $\gamma \approx 1.08$.

$$\alpha \approx 0.32 \qquad \beta \approx 0.30 \qquad \gamma \approx 1.08\tag{4.56}$$

The fitted exponents, equation (4.56), are in reasonable agreement with the found exponents,

$$\alpha = \frac{1}{6} \qquad \beta = \frac{1}{3} \qquad \gamma = \frac{7}{6}\tag{4.57}$$

for the first order in $\epsilon = 1/2$.

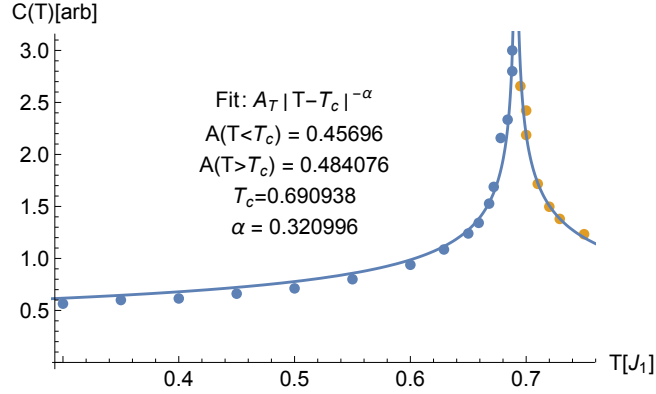


Figure 4.5: α exponent fit from simulated heat capacity data in Sorokin et al. [56], listed in table B.1.

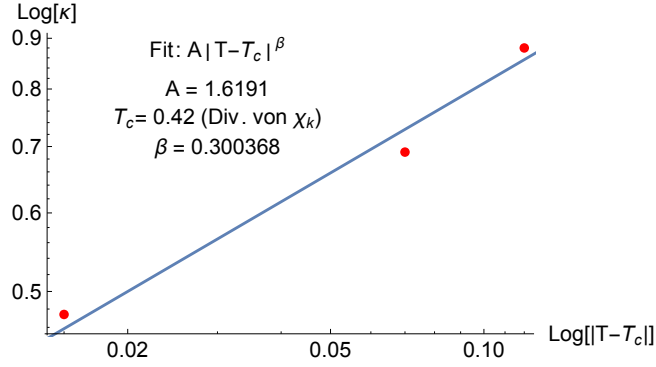


Figure 4.6: β exponent fit from simulated chiral order parameter data in Sorokin et al. [56], listed in table B.2.

4.7 Phase diagram

Now we have to solve the equation (4.43). We started from small scales up to the length scale l_c in section 4.3. Leading to the values

$$K_{l_c} = K \exp(-\epsilon l_c) \quad y_c \approx \exp(3l_c/2 - \bar{E}_{\text{core}}) \quad (4.58)$$

where the core energy was estimated earlier as $\bar{E}_{\text{core}} = 2.38K$. Once the length scale l_c is reached, such that

$$e^{l_c} \approx \xi_y \quad (4.59)$$

the system is essentially governed by the KT flow equations.

$$\frac{2}{\pi K_{l_c}} = 1 + \ln(2) + 2\pi^2 y_{l_c}^2 - \ln(\pi K_{l_c}) \quad (4.60)$$

For the correlation length we identified $\xi_y = \frac{1}{r}$ when looking at the effective Hamiltonian. This $r(K)$ dependent effective constant can be approximated with the variational method used for

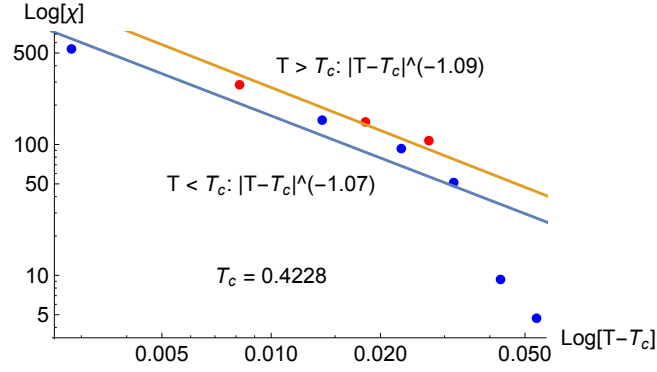


Figure 4.7: γ exponent fit from simulated chiral susceptibility χ_k data in Sorokin et al. [56], listed in table B.3.

the chiral transition, done in chapter 3. As discussed earlier, for temperatures above the chiral transition, r satisfies the self consistent equation

$$r + \frac{1}{2}\theta^2 = \frac{3}{2K}\sigma^2(r) \quad (4.61)$$

where $\sigma^2(r)$ was defined in equation (3.25) as

$$\sigma^2(r) = \int_{-\pi}^{\pi} \frac{d^2k}{(2\pi)^2} \frac{k_x^2}{rk_x^2 + k_y^2 + \frac{1}{4}k_x^4} \quad (4.62)$$

which could be solved analytically. The solution is given in equation (3.26). Given the form of $\sigma^2(r)$, we can numerically solve equation (4.61) to find $r(K)$, using the simple Mathematica code from listing 4.2.

```

1 s2[m_] :=
2 1/\[Pi]^2 2 (-Sqrt[m] \[Pi] +
3 Sqrt[4 m + \[Pi]^2] ArcTan[2/Sqrt[4 m + \[Pi]^2]] +
4 Sqrt[2] Sqrt[m + Sqrt[m^2 - \[Pi]^2]]
5 ArcTan[\[Pi]/(Sqrt[2] Sqrt[m - Sqrt[m^2 - \[Pi]^2]])] +
6 Sqrt[2] Sqrt[m - Sqrt[m^2 - \[Pi]^2]]
7 ArcTan[\[Pi]/(Sqrt[2] Sqrt[m + Sqrt[m^2 - \[Pi]^2]])])
8 rk[\[Theta]_, kinv_] := Module[{x},
9 x /. FindRoot[x + (1/2) \[Theta]^2 - 3 kinv/2 s2[x], {x, 1}] // Chop
10 ]

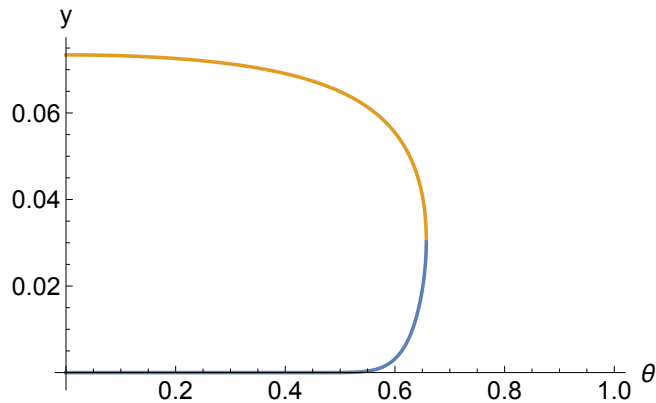
```

Listing 4.2: Mathematica Code used to numerically solve for $r(K^{-1})$

Plugging everything in equation (4.60) for $\epsilon = \frac{1}{2}$, get the self consistent equation

$$\frac{2}{\pi K_{BKT} \sqrt{r(K_{BKT})}} = 1 + \ln(2) + \frac{2\pi^2 e^{-4.76K_{BKT}}}{r^3(K_{BKT})} - \ln\left(\pi K_{BKT} \sqrt{r(K_{BKT})}\right) \quad (4.63)$$

for the critical temperature K_{BKT} of the BKT transition. This equation can be solved numerically with Mathematica using the FindRoot-Method similar to listing 4.2 and produces the re-entrance part of the phase diagram, figure 4.9, above the chiral transition line. The flow equations work under the assumption of small fugacity y for the vortices. Once the numerical solution is found, one can compute the fugacity for these lines to see if they are small compared

Figure 4.8: Fugacity y

to one. The results are shown in figure 4.8. As one can see, the condition $y < 1$ is satisfied for all the solutions and our method is self-consistent. Below the chiral transition we saw that the variational approach produced a non-physical artifact, which leads to the appearance of a jump in order parameter and the accompanied parameter r . This effect vanishes for small θ but is pronounced once we approach $\theta \sim 1$. To avoid non-physical artifacts in the phase diagram, we have to approximate the correlation length without using the self-consistent equation for r for low temperatures. Introducing the reduced temperature t as

$$t = \frac{K_c}{K_{BKT}} - 1 \quad (4.64)$$

with the chiral transition temperature K_c^{-1} , we can estimate the correlation length as

$$\xi_y \propto \frac{|t|^{-\nu_y}}{\theta^2} \quad (4.65)$$

with $\nu_y^{-1} = 1 - \epsilon/3$ which for $\epsilon = 1/2$ is $\nu_y = 6/5$, as we discussed in section 4.3. The numerical solution of the equation for K_{BKT} below the chiral transition produces just one simple transition line close, but not identical, to the chiral transition. The resulting full phase diagram is shown in figure 4.9. For low temperatures the system exhibits chiral order and magnetic quasi-long range order (QLRO), indicated by an algebraic decay in spin-spin correlations. Increasing the effective temperature K_0^{-1} for a fixed θ leads to a BKT transition. As our numerical solution has shown, the BKT transition occurs before the chiral transition, leading to an exponential decay in spin-spin correlations while still exhibiting chiral order. This is the helical spin liquid phase. For large $\theta > \theta_c \approx 0.66$, an increase in K_0^{-1} leads to the loss of chiral order at the chiral transition and the system enters the paramagnetic phase. In the case of small $\theta < \theta_c$ a re-entrance in the magnetic phase was found, after the chirality was lost. Now the system only exhibits QLRO in the absence of chirality in the quasi ferromagnetic phase (quasi FM). As we will discuss in the next section, experimental systems are usually classified by the ratio α of the NN and NNN interaction, instead of the pitch angle θ . To be able to better compare our results to those systems, figure 4.10 shows the phase diagram with K_2/K_0 as the x -axis instead of the angle θ . The results for the phase diagram have been published in Physical Review Letters, [40].

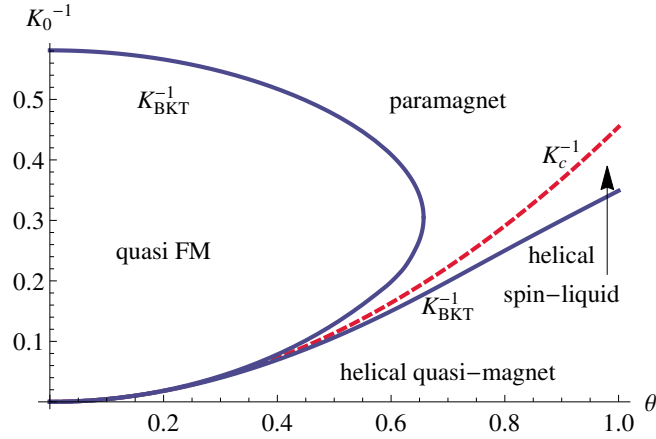


Figure 4.9: Phase Diagram of the helical XY model as a function of the chiral pitch angle $\theta = \arccos(-\frac{K_0}{4K_2})$. The diagram was calculated by numerically solving equation (4.60). The BKT transition (K_{BKT}^{-1}) is marked by the solid lines, the chiral transition K_c^{-1} by the dashed ones.

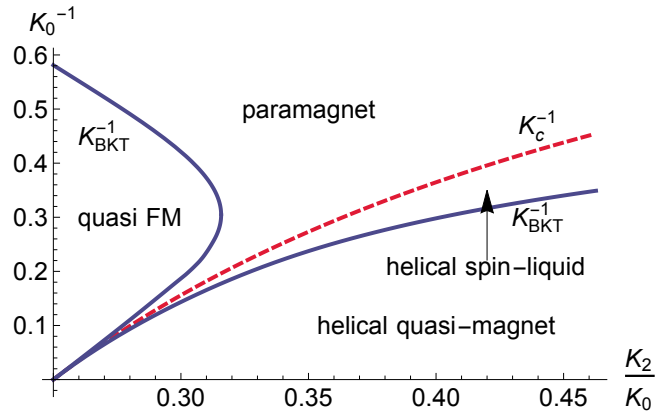


Figure 4.10: Phase diagram of the helical XY model as a function of the parameter ratio K_2/K_0 . The diagram was calculated by numerically solving equation (4.60). The BKT transition (K_{BKT}^{-1}) is marked by the solid lines, the chiral transition K_c^{-1} by the dashed ones. This figure is depicted in [40] with slightly different labels, fitting the notation of the publication.

4.8 Discussion

Experiments

We already discussed several possible materials offering experimental realizations of chiral order in the introduction. Finding materials to experimentally check the phase diagram 4.10 however is difficult. There is a whole class of rare earth metals exhibiting helical magnetic phases like Tb, Dy and Ho,[24]. Experiments on thin films have only been done on films perpendicular to the vector chirality, [58].

One-dimensional frustrated quantum chains

The best chance of finding an experimental system that would fit our model is the class of one-dimensional quantum chains of the form

$$H = \sum_i (J_1 \hat{s}_i \hat{s}_{i+1} + J_2 \hat{s}_i \hat{s}_{i+2})$$

The experimental convention has $J_n > 0$ as antiferromagnetic interaction. Instead of using the pitch angle θ to classify the chiral order, the parameter $\alpha = J_2/J_1$ is used in experimental classification. As we discussed when introducing the model, the phase diagram is symmetric under the change in sign of J_1 , see chapter 2. To find suitable parameters only the absolute value $|\alpha|$ is important and relates directly to our parameter K_2/K_0 that we used in the phase diagram 4.10.

$$\alpha = -\frac{K_2}{K_0} \quad (4.66)$$

There are several challenges in finding suitable systems. First one needs to identify compounds that contain special chains where the intra-chain interactions are frustrated and are by several orders of magnitude larger than the inter-chain interactions. Once the ratio between inter- and intra-chain interaction strength is sufficiently small, the system can be treated as a collection of one-dimensional chains. Since we are dealing with low temperature systems, one still has to make sure that there are no inter-chain effects that would change the system to behave like a 3D one close to the phase transition.

Finding these systems that satisfies just these criteria is already difficult. A good overview was assembled by Hase et al. in [59]. The table presented by them is shown here as table 4.1. What we need is a ratio α in the parameter window of $0.25 < |\alpha| < 0.361$ to study the re-entrance

Material	J_1 [K]	J_2 [K]	α	Source
CuGeO ₃	150-160	36-57.6	0.24-0.36	[60, 61]
Cu(ampy)Br ₂	17	3.4	0.2	[62]
(N ₂ H ₅)CuCl ₃	4.1	16.3	4	[63]
Cu ₆ Ge ₆ O ₁₈ ·6H ₂ O	222	60	0.27	[64, 65]
Cu ₆ Ge ₆ O ₁₈ ·0H ₂ O	451	131	0.29	[64, 65]
Li _{1.16} Cu _{1.84} O _{2.01}	67	19	0.29	[66]
Pb[Cu(SO ₄)(OH ₂)]	-30	15	-0.5	[67]
La ₆ Ca ₈ Cu ₂₄ O ₄₁	-215	78	-0.36	[68]
Li ₂ CuO ₂	-100	62	-0.62	[68]
Ca ₂ Y ₂ Cu ₅ O ₁₀	-25	55	-2.2	[68]
Rb ₂ Cu ₂ Mo ₃ O ₁₂	-138	51	-0.37	[59]
SrCuO ₂	1-100	1800	18-1800	[69, 70]

Table 4.1: Several different compounds being frustrated quantum spin chains. This table is taken from Hase et al. [59], where an overview of these systems was given.

part of the phase diagram and values $|\alpha| < 0.46$ for the small θ approximation to hold. One material in which two nearby transitions have been found is LiCu₂O₂, that has been thoroughly studied by Masuda et al., [66, 68, 71, 72], with a value $\alpha = -0.62$. The study of these materials is new, so conclusive phase diagrams and extensive measurements are rare. Additionally the

above mentioned systems are all $S = 1/2$ Heisenberg chains. Finding systems with larger spin that justify the large spin approximation when doing the mapping to a classical system is rare.

One compound containing 1D quantum spin chains with higher spins is the spin $S = 1$ chain in CaV_2O_4 , studied by Kikuchi et al. It is suspected of exhibiting a spin gap [73], but it has not been conclusively shown yet. But still $S = 1$ is still too small to justify the large spin limit approximation discussed by Kolezhuk [43], needed to map the quantum model to our classical one.

The best candidate found so far is the material $\text{Gd}(\text{hfac})_3\text{NiTiPr}$, [39, 74]. In this molecular-based system, isoPropyl organic radicals iPr with spin $s = 1/2$ are alternated with the rare-earth Gd^{3+} magnetic ions with spin $S = 7/2$ along the quasi one-dimensional chain, [74]. Along the chain, the spins interact ferromagnetically with their nearest neighbor and antiferromagnetically with their next nearest ones, causing a frustrated interaction similar to the basis of our model. Additionally, anisotropy of the system causes the spins to favor the restriction to the plane perpendicular to the chain axis, effectively making it a XY spin system. The effective spin of the system is $\sqrt{sS} = \sqrt{7}/2 > 1$ and the frustrated interaction results in a pitch angle $\theta \approx 0.358\pi$, [75]. Even though the spin is not quite large enough and the pitch angle not small enough to completely justify our approximations, given the circumstances, this is a very good experimental candidate. Heat capacity measurements of this system revealed two peaks at $T_c \approx 2.19\text{K}$ and $T_N \approx 1.88\text{K}$, identified as chiral and magnetic phase transitions respectively, [39]. The mapping discussed in the chapter 2 identified the parameter $K_0 = \sqrt{2/3}S$. As discussed earlier, the mapping from the quantum to the classical system introduces a new dimension, with the extension

$$L_\tau = \frac{\hbar}{k_b T} \quad (4.67)$$

related to the temperature, [42]. In our case the system is truly 2D in the case of $T = 0$. One idea put forward by Nattermann, [40, 76] was to relate the found phase transition in our model via finite size scaling in the temperature. The model presented here would explain these peaks as the result of a quantum phase transition.

Josephson–Junction arrays

Theoretically, there is also a way of directly fabricating an experimental realization of our system as a Josephson-Junction (JJ) array, based on the idea of [77, 78]. The local phases of the complex order parameter can be mapped to classical XY spins as used in our model. Engineering so called 0- and π - couplings in the array will model ferromagnetic- and antiferromagnetic interaction. The ferro- and antiferromagnetic couplings can be achieved with Superconductor-Insulator-Superconductor (SIS) junctions and superconductor-ferromagnet-superconductor (SFS) junctions respectively, [79, 80]. As an insulator, Al_2O_3 is often used, while Gd (Gadolinium) can be used as a ferromagnet [81].

Producing a zig-zag chain would be a simple way of producing a classical one-dimensional chain with frustration. In this case one could try to make the interactions tunable using an applied magnetic field, as theorized in [82]. Deciding beforehand on the coupling-strength, one could stack these Josephson chains to introduce couplings in the y -direction. One can also start from a 2D array with ferromagnetic coupling in y -direction and an antiferromagnetic on in x -direction. Stacking a second, identical layer on top, shifted by have a lattice spacing in the x -direction and coupling it ferromagnetic to the lower half, one can produce the same zig-zag layer. Two-dimensional JJ arrays have already been build, [83], and even 3D JJ structures have been realized, as shown in [84].

Other theoretical work

Starting in 1978 with Villain, [85], there have been several analytical studies of the same or similar models with vastly different predictions for the phase diagram. Villain used a mean field study to first predict the existence of an intermediate phase, where QLRO order was broken, but the system was still exhibiting chiral order. Similar to what will be discussed here, the transitions take place at two distinct temperatures, with the magnetic one T_{BKT} laying below the chiral T_c . In 1980 the model as used here has been analytically studied by Garel and Doniach, [86]. Introducing two component order parameters for each chirality, they propose a simple coupling between them, to study the system. What they find is an inverse sequence of the transitions where first the chiral order breaks down, lying in the Onsager universality class, followed by the loss of QLRO in form of a classical BKT transition. We saw that the system can be written in terms of the chiral Ising order parameter that will produce a non-local interaction, indicating that the transition is not in the Onsager universality class. Additionally, the simple coupling proposed in [86] does not appear as part of the Ginzburg–Landau expansion. A later study by Okwamoto in 1984, [87], uses a self-consistent harmonic approximation (SCHA), that, similar to the phase diagram here, produces a re-entrance phase, but differs in the sequence of transitions. The BKT transition destroying QLRO happens before the chiral order is destroyed, similar to the picture by Garel and Doniach. In 1998 Kawamura showed that the system in three dimension exhibits both transitions simultaneously, [50]. This was done using the Ginzburg–Landau expansion of the system and the renormalization group.

It is easy to see that this topic has been very controversial with vastly different results where no consensus has been reached even concerning just the sequence of transitions. Most recent analytic work focuses on one-dimensional quantum chains and in that context mainly on low spin systems such as $S = 1/2$, [47, 88], where the mapping to the classical system with XY spins becomes a stretch. Recently, numerical work by Sorokin et al. dealing with our model has been published, [56]. They also find a different universality class. However, they neglected the anisotropic nature of the system when performing their finite size scaling analysis, [57]. As we saw, a direct analysis of their published data, leads to reasonable agreement with the critical exponents as discussed here. The region where we expect the re-entrance phase to appear is small and falls in between data points of the numerics. The fact that it does not appear in the phase diagram discussed in [56] is due to its coarse grained resolution. Parts of this work are

Author(s)	System	Parameter Regime	Source
Okwamoto	classical HXY model	$\theta \approx 0$	[87]
Kawamura	3D-RG of classical HXY model	$\theta \approx 0$	[50]
Nersesyan et al.	zig-zag Heisenberg spin ladder $S = \frac{1}{2}$	$\theta \approx \frac{\pi}{2}$	[47]
Lecheminant et al.	frustrated XY quantum chain $S = \frac{1}{2}$	$\theta \approx \frac{\pi}{2}$ and $\theta \approx \pi$	[88]
Hikihara et al.	frustrated XY quantum chain $S = \frac{1}{2}, \frac{3}{2}, 1, 2$	$\theta \approx \pi$	[89]
Kolezhuk	frustrated XXZ quantum chain	$\theta \approx \pi$	[43]
Sorokin et al.	classical HXY model (numerics)	$\theta \approx \pi$	[56]

Table 4.2: Parameter regime of different analytical and numerical works on frustrated spin chains.

published in Physical Review Letters (PRL), [40]. In between the publication of the letter and this dissertation, the work by Dimitrova, [90], on the same system was published. The presented phase diagram agrees qualitatively with our, i.e. it exhibits the same the sequence of transitions and a re-entrance to a QLRO phase without chiral order is present, [40, 90]. The main differences are a more pronounced re-entrance phase in the work of Dimitrova and different universality class

for the chiral transition. As we discussed, we expect that the strong anisotropy of the system is reflected in the critical exponents, leading to $\nu_x \neq \nu_y$ and $\eta_x \neq \eta_y$ in our case. The necessity of replacing each of the simple exponents η and ν by a respective pair in an anisotropic system with chiral ground state is also discussed by Hornreich et al., [55]. However the exponents found by Dimitrova are isotropic, [90]. The procedure used in [90] is based on rewriting the system as a ϕ^4 theory non-trivially coupled to a free auxiliary field followed by the RG-procedure. For reasons not quite clear, this is done for $dydx^{2-\epsilon}$ around $d = 3 - \epsilon$ as apposed to an expansion around the upper critical dimension $d_c = 4$ of the ϕ^4 theory, [90, 91].

5. Multiferroics

In this chapter we will take a closer look at the relation between chiral order and polarization in multiferroic systems. Different mechanisms for the coupling of magnetic and electric order are discussed and, starting from a symmetry argument, the HXY model will be extended by an interaction with the electric field. The effect of the polarization on the domain walls of the system will be studied. The resulting saddle-point equations will be solved perturbatively and are compared to numerical results.

In the previous chapters we discussed the HXY model where a frustrated interaction of the XY spins in x -direction leads to a chiral ground state with wave vector $\pm\mathbf{q} = \pm(\theta/a, 0, 0)$. The energy of the system in terms of the magnetization can be written as

$$\mathcal{H} = \frac{J}{2a} \int d^2x \left[-\frac{\theta^2}{2} (\partial_x \mathbf{m})^2 + \frac{a^2}{4} (\partial_x^2 \mathbf{m})^2 + (\partial_y \mathbf{m})^2 \right] \quad (5.1)$$

similar to [18]. When we are only focusing on the phase fluctuations, as is typical for 2D systems, we obtain

$$\mathcal{H} = \frac{J}{2a} \int d^2x \left[-\frac{\theta^2}{2} (\partial_x \phi)^2 + \frac{a^2}{4} ((\partial_x \phi)^4 + (\partial_x^2 \phi)^2) + (\partial_y \phi)^2 \right] \quad (5.2)$$

the same model as derived in chapter 2 equation (2.19) from a microscopic system where ferromagnetic nearest neighbor interaction competes with an antiferromagnetic next-nearest neighbor interaction, [40]. From this on out we will set the lattice constant $a = 1$ for convenience. By shifting the ground state energy by $\frac{1}{4}\theta^4$, we can give the system a form that makes the double minimum nature of the $\partial_x \phi$ terms clear

$$\mathcal{H} = \frac{J}{2} \int d^2x \left[\frac{1}{4} ((\partial_x \phi)^2 - \theta^2)^2 + (\partial_y \phi)^2 + \frac{1}{4} (\partial_x^2 \phi)^2 \right] \quad (5.3)$$

As discussed in the previous chapters and partially published in [40], this model exhibits sequential phase transitions by increasing βJ where first the magnetic order is lost by a BKT transition followed by the loss of chiral order. Additionally a re-entrance to a quasi ferromagnetic state was found for small angles θ . The phase of interest in the small region of no magnetic order while still exhibiting chiral order is referred to as the helical spin liquid, [40]. The experimental measurement of this phase is complicated when only looking at the magnetic orientation as pointed out by Villain [85], because a 4-point correlator is needed to identify the chiral correlations in two different chains in the absence of magnetic ordering. One possible idea to circumvent this complicated measurement is to look at multiferroic materials where the vector chiral order parameter

$$\boldsymbol{\kappa} = \langle \mathbf{S}_i \times \mathbf{S}_{i+1} \rangle = \langle \sin(\partial_x \phi) \rangle \hat{\kappa} \approx \langle \partial_x \phi \rangle \hat{\kappa} \quad (5.4)$$

can couple to the polarization \mathbf{P} of the system. Here the unit vector $\hat{\kappa}$ points in the direction perpendicular to the rotation plane of the XY spins \mathbf{S}_i . In the following sections we will discuss multiferroic materials and the connection of the chiral order and the polarization. With the proper coupling identified we can examine the effect of the polarization on chiral domain walls. We will see that polarization and chiral domains are in one-to-one correspondence.

5.1 Connection between chiral order and polarization

Multiferroics are materials that exhibit both electric and magnetic order at the same time. They are of special interest since they allow for electric manipulation of magnetic domains and vice versa the control of polarization via magnetic fields. Generally one can distinguish between two classes of multiferroics, referred to as Type I and Type II, [30]. Type I multiferroics are materials where the coupling between ferroelectricity and magnetism are rather weak and both phenomena occur largely independent. BiFeO₃ and YMnO₃ are examples of this category, [30]. For us Type II multiferroics are of interest. Here magnetic order causes ferroelectricity. Compared to Type I multiferroics, the strength of the resulting polarization is however weaker. [30–32]

So far we have not explicitly chosen the rotation plane of our XY spins, since for any plane we arrive at the Hamiltonian of equation (5.3). For the coupling to the polarization the rotation plane of the spins in respect to the propagation vector $\mathbf{q} \parallel \hat{x}$ is important. We have to distinguish the cases of \mathbf{q} lying in or being perpendicular to the rotation plane, as shown in figure 5.1.

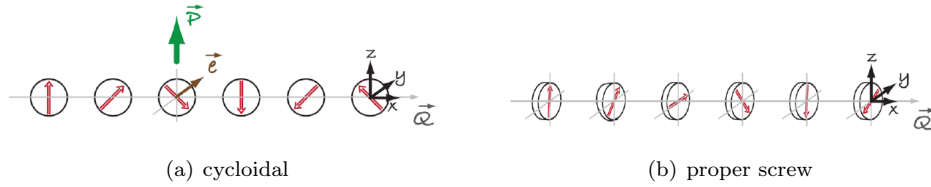


Figure 5.1: Pictured are the a) cycloidal spiral structure and b) the proper screw structure. Illustrations taken from [30].

First we will consider the cycloidal chiral structure, where \mathbf{q} lies in the rotation plane of the spins, e.g. the XY plane, figure 5.1(a). We will see that in this case the chiral order is directly connected to the polarization. Afterward we will discuss the case of the proper screw structure, where \mathbf{q} is perpendicular to the rotation plane, figure 5.1(b). Here, no polarization is induced except for some special cases as discussed by Arima, [92].

Cycloidal spin structures

The cycloidal spin structure, with \mathbf{q} lying in the rotation plane of the spin, has been examined microscopically by Katsura, Nagaosa and Balatsky, [33] and phenomenologically by Mostovoy, [19]. Both show that this spin structure results in an electric dipole moment

$$\mathbf{p} \propto \hat{e}_{ij} \times (\mathbf{S}_i \times \mathbf{S}_j) \propto \mathbf{q} \times (\mathbf{S}_i \times \mathbf{S}_j) \quad (5.5)$$

Here i and j mark neighboring sites and the vector \hat{e}_{ij} points in the direction connecting those sites. The expression is closely related to the spin-current, [19, 30, 33]. For the cycloidal case let us assume the rotation plane of the spins to be the XY plane. The cross product $\mathbf{S}_i \times \mathbf{S}_j$ will then be parallel to the z -axis and the resulting dipole moment parallel to the y -axis. We can also see that for proper screws $\mathbf{S}_i \times \mathbf{S}_j \parallel \hat{x}$, therefore no dipole moment is generated for $\mathbf{q} = q\hat{x}$.

Equation (5.5) also shows the direct connection to the vector chiral order parameter

$$\boldsymbol{\kappa} = \langle \mathbf{S}_i \times \mathbf{S}_{i+1} \rangle \quad (5.6)$$

making the link between the chiral order to the polarization in the cycloidal system rather obvious. The microscopic origin is due to spin-orbit coupling of the canted spins, referred to as inverse Dzyaloshinskii–Moriya (DM) term, [32, 93, 94].

In order to extend the phenomenological theory from Hamiltonian (5.3) to include this coupling, let us follow the phenomenological arguments by Mosotvoy, [19]. Discussing the coupling between magnetization \mathbf{m} and polarization \mathbf{P} purely via symmetry considerations.

Symmetry	\mathbf{m}	\mathbf{P}
Time Reversal	odd	even
Spatial Inversion	even	odd

Table 5.1: Transformation of magnetic order \mathbf{m} and polarization \mathbf{P} under time reversal and spatial inversion, [19].

Considered are the transformation properties of \mathbf{m} and \mathbf{P} under time reversal and spatial inversion symmetry as listed in table 5.1. Only allowing couplings that are invariant under both transformations, the following invariant to lowest order in \mathbf{m} and \mathbf{P} is found

$$\mathcal{H}_P = \gamma \mathbf{P} [(\mathbf{m} \nabla) \mathbf{m} - \mathbf{m}(\nabla \mathbf{m})] \quad (5.7)$$

For the parametrization of the cycloidal configuration as pictured in figure 5.1(a), we choose the spins lying in the XY plane with the wave vector $\mathbf{q} \parallel \hat{e}_x$. Ignoring amplitude fluctuations we can write for the magnetization

$$\mathbf{m} = \cos(\phi(x, y)) \hat{x} + \sin(\phi(x, y)) \hat{y} \quad (5.8)$$

The coupling term from equation (5.7) then computes to

$$(\mathbf{m} \nabla) \mathbf{m} - \mathbf{m}(\nabla \mathbf{m}) = -\partial_y \phi \hat{x} + \partial_x \phi \hat{y} \quad (5.9)$$

leading to a coupling of the x -component of the polarization to $\partial_y \phi$ and the y -component coupling to $\partial_x \phi$ via

$$\mathcal{H}_P = -\gamma P_x (\partial_y \phi) + \gamma P_y (\partial_x \phi) \quad (5.10)$$

Proper screw structure

In the case of the proper screw structure the spins rotate in a plane perpendicular to the propagation vector \mathbf{q} . As already discussed, the inverse DM type interaction cannot produce a polarization, since \hat{e}_{ij} is parallel to $\mathbf{S}_i \times \mathbf{S}_{i+1}$. With

$$\mathbf{m} = \cos(\phi(x, y)) \hat{y} + \sin(\phi(x, y)) \hat{z} \quad (5.11)$$

we can also see that the phenomenological term derived by Mostovoy

$$(\mathbf{m} \nabla) \mathbf{m} - \mathbf{m}(\nabla \mathbf{m}) = \partial_y \phi \hat{z} \quad (5.12)$$

vanishes for $\mathbf{q} \parallel \hat{x}$ where $\partial_y \phi = 0$. The system does not feature any polarization.

This is certainly true for simple geometries such as cubic or tetragonal crystals, [30]. Interestingly, Arima showed that for certain symmetries a proper screw structure can produce a non-vanishing polarization, [92].

Effective theory

Assuming a cycloidal chiral ground state, we already derived the coupling to the polarization as

$$\mathcal{H}_P = \gamma P_y (\partial_x \phi) - \gamma P_x (\partial_y \phi) \quad (5.13)$$

with the coupling constant γ . Together with the coupling \mathbf{EP} to the electric field we get the effective phenomenological theory

$$\begin{aligned} \mathcal{H} = & \frac{J}{2} \int d^2x \left[\frac{1}{4} ((\partial_x \phi)^2 - \theta^2)^2 + \frac{1}{4} (\partial_x^2 \phi)^2 + (\partial_y \phi)^2 \right] \\ & + \int d^2x \left[\gamma P_y (\partial_x \phi) - \gamma P_x (\partial_y \phi) - \mathbf{EP} + \frac{\mathbf{P}^2}{2\chi} + \frac{g}{2} (\nabla \mathbf{P})^2 \right] \end{aligned} \quad (5.14)$$

where χ is the dielectric susceptibility. Included is also a gradient term in $(\nabla \mathbf{P})^2 \equiv \sum_i (\nabla P_i)^2$, allowed by the symmetry considerations.

Simple variation of the energy in respect to the polarization leads to

$$P_y = \chi E_y - \chi \gamma (\partial_x \phi) + g \nabla^2 P_y \quad P_x = \chi E_x + \chi \gamma (\partial_y \phi) + g \nabla^2 P_x \quad (5.15)$$

Connecting this to the vector order parameter

$$\boldsymbol{\kappa} = \langle \mathbf{S}_i \times \mathbf{S}_{i+1} \rangle = \langle \sin(\partial_x \phi) \rangle \hat{\kappa} \quad (5.16)$$

where $\hat{\kappa}$ is perpendicular to the plane of rotation of the spins. For small \mathbf{q} , i.e. small gradients, we can expand the $\sin(\partial_x \phi) \approx \partial_x \phi$ to see the direct connection to the polarization. Since $\langle \partial_y \phi \rangle$ vanishes as can be easily seen from the Hamiltonian, $\langle \mathbf{P} \rangle$ and $\boldsymbol{\kappa}$ only differ in their orientation. The polarization in the absence of an external electric field is therefore directly related to the order parameter of the chiral order. The helical spin liquid can therefore be identified via the absence of magnetic order with a non vanishing polarization.

Measurement of polarization

Let us give some small notes on experimental methods to measure polarization. The measurement of a polarization perpendicular to the surface can be done by means of dielectric spectroscopy. This is achieved by placing the sample between two conducting layers forming a capacitor and applying an alternating voltage, generating an electric field parallel to the polarization. The polarization of the sample changes its dielectric properties which changes the impedance of the capacitor, leaving a measurable signature. A more elaborate technique even able to give spatial resolution of the domain walls in the system is the method of piezoresponse force microscopy (PFM), similar to atomic force microscopy with a electrically charged tip, described in detail in [95]. Using vertical or lateral movement of the tip allows the measurement of a polarization perpendicular or parallel to the surface.

5.2 One-dimensional domain wall

Let us study the effect of the polarization and the coupling to the electric field on the ground state and domain walls of the system in the x -direction. The effective one dimensional model of the chain in x -direction is then given by

$$\mathcal{H}_x = \frac{J}{2} \int dx \left[\frac{1}{4} ((\partial_x \phi)^2 - \theta^2)^2 + \frac{1}{4} (\partial_x^2 \phi)^2 \right] + \int dx \left[\gamma P_y (\partial_x \phi) - E_y P_y + \frac{P_y^2}{2\chi} + \frac{g}{2} (\partial_x P_y)^2 \right] \quad (5.17)$$

where we are only interested in electric fields that couple to the gradient in x -direction.

Ground state

The two functions of interest in the one-dimensional model are the pitch angle $\phi(x)$ of the spins and the polarization profile $P_y(x)$ that minimize the energy \mathcal{H}_x . Variation in respect to ϕ and P_y leads to the two saddle point equations

$$\frac{\delta\mathcal{H}_x}{\delta\phi} = \frac{J}{2} \left((-3\partial_x\phi)^2 \partial_x^2\phi + \theta^2 \partial_x^2\phi + \frac{1}{2} \partial_x^4\phi \right) - \gamma \partial_x P_y = 0 \quad (5.18)$$

$$\frac{\delta\mathcal{H}_x}{\delta P_y} = \frac{1}{\chi} P_y - E_y + \gamma \partial_x\phi - g \partial_x^2 P_y = 0 \quad (5.19)$$

that can be simplified to

$$\partial_x \left[\frac{J}{2} \left((\partial_x\phi)^3 - \theta^2 \partial_x\phi - \frac{1}{2} \partial_x^3\phi \right) + \gamma P_y \right] = 0 \quad P_y = \chi E_y - \chi\gamma \partial_x\phi + g\chi \partial_x^2 P_y \quad (5.20)$$

Noting that these equations only depend on the gradients $\partial_x\phi$, we can use the substitution $\Psi = \partial_x\phi$ and drop the index in P_y for convenience,

$$2\Psi^3 - 2\theta^2\Psi - \partial_x^2\Psi + \frac{4\gamma}{J}P = C \quad P = \chi E_y - \chi\gamma\Psi + g\chi \partial_x^2 P \quad (5.21)$$

The integration constant C from the saddle point equations has the meaning of an applied electric field. It can be absorbed by rescaling $P \rightarrow P + JC/(4\gamma)$ and $E_y \rightarrow E_y + JC/(4\gamma\chi)$. After absorbing the integration constant we can look at minimum configuration of $\Psi = \Psi_0 = \text{const}$ and $P = P_0 = \text{const}$ with

$$2\Psi_0^3 - 2\theta^2\Psi_0 + \frac{4\gamma}{J}P_0 = 0 \quad P_0 = \chi E_y - \chi\gamma\Psi_0 \quad (5.22)$$

leading to

$$2\Psi_0^3 - 2 \left(\theta^2 + \frac{2\gamma^2\chi}{J} \right) \Psi_0 + \frac{4\gamma\chi}{J} E_y = 0 \quad (5.23)$$

For $E_y = 0$, this equation has two minima given by

$$\Psi_0(E_y = 0) = \pm \sqrt{\theta^2 + \frac{2\gamma^2\chi}{J}} \equiv \pm\tilde{\theta} \quad (5.24)$$

The ground state solution $\Psi_0 = \partial_x\phi = \text{const}$ corresponds to a spiral with a fixed pitch angle $\tilde{\theta}$. Here we can already see some effects of the coupling to the polarization via the constant γ . One is the new pitch angle $\tilde{\theta} > \theta$ for $\gamma \neq 0$. The ground state value $\tilde{\theta}$ can be used to simplify the equations by rescaling $\tilde{\theta}\tilde{\Psi}_0 = \Psi_0$ for $E_y \neq 0$. This leads to

$$\tilde{\Psi}_0^3 - \tilde{\Psi}_0 = \frac{c}{2} \quad c = -\frac{4\chi\gamma E_y}{J(\theta^2 + 2\chi\gamma^2/J)^{3/2}} \quad (5.25)$$

This cubic equation can be solved. We see (figure 5.2) that for $|c| < c_{\max} = \frac{4}{3\sqrt{3}}$ we have two different minima, while for $|c| > c_{\max}$ only one minimum is selected due to the electric field. The critical field is given by

$$E_y^{(c)} = \frac{J}{\chi\gamma} (3(\theta^2 + 2\frac{\chi\gamma^2}{J}))^{3/2} \quad (5.26)$$

and the minimum values can be obtained by using a computer algebra system (such as Mathematica) to yield

$$\tilde{\Psi}_+ = \frac{2\sqrt[3]{-6} - (-1)^{2/3} (\sqrt{81c^2 - 48} - 9c)^{2/3}}{6^{2/3} \sqrt[3]{\sqrt{81c^2 - 48} - 9c}} \quad (5.27)$$

$$\tilde{\Psi}_- = -\frac{(\sqrt{81c^2 - 48} - 9c)^{2/3} + 26^{1/3}}{6^{2/3} \sqrt[3]{\sqrt{81c^2 - 48} - 9c}} \quad (5.28)$$

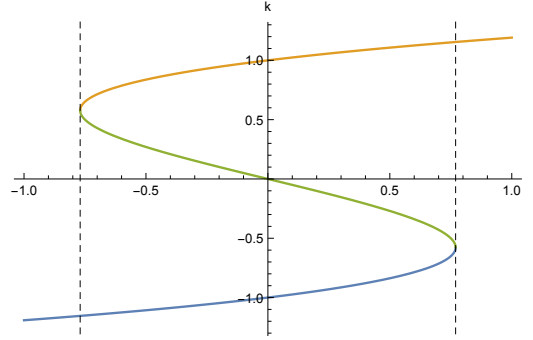


Figure 5.2: Different solutions for the ground state. The dashed lines mark $|c| = c_{\max} = 4/(3\sqrt{3})$ and the green curve marks the maximum. The yellow curve plot $\tilde{\Psi}_+(c)$ and blue marks $\tilde{\Psi}_-(c)$.

As a test, one can compute the case for $c = 0$ to verify that the solutions are indeed $\tilde{\Psi}_\pm = \pm 1$. We can see that the effect of the coupling to the polarization is the change in the pitch angle θ of the ground state to $\tilde{\theta}$ effectively increasing its value. As expected the ground state $\Psi = \theta$ is obtained for $\gamma = 0$.

The effect of the electric field now changes the minima so that $|\tilde{\Psi}_+| \neq |\tilde{\Psi}_-|$. The energy E_\pm of the configuration per length is given as

$$E_\pm = \frac{J}{8}(\Psi_\pm^2 - \theta^2)^2 - \frac{1}{2}\chi(E_y - \gamma\Psi_\pm)^2 \quad (5.29)$$

For the case of $E_y = 0$ we see that the minimum is given with

$$E_+ = E_- = -\frac{1}{2}\gamma^2\theta^2\chi - \frac{\gamma^4\chi^2}{2J} \quad (5.30)$$

which vanishes for $\gamma = 0$. For $E_y \neq 0$ the situation is different, here $E_+ \neq E_-$ and the two minima have different energies.

Domain wall equations

The domain wall separating the region of solution Ψ_- from a region Ψ_+ is a solution to the differential equation with the boundary conditions

$$\lim_{x \rightarrow \infty} \Psi_{DW}(x) = \Psi_+ \quad \lim_{x \rightarrow -\infty} \Psi_{DW}(x) = \Psi_- \quad (5.31)$$

In the absence of an electric field, we know $\Psi_+ = -\Psi_- = \tilde{\theta}$ and $P_{\pm} = -\gamma\chi\Psi_{\pm}$. The typical length scale in this problem is given by the pitch angle $\tilde{\theta}$. Using this information we can make the saddle point equations

$$2\Psi^3 - 2\theta^2\Psi - \partial_x^2\Psi + \frac{4\gamma}{J}P = 0 \quad P = -\gamma\chi\Psi + g\chi\partial_x^2P \quad (5.32)$$

dimensionless, by introducing the rescaled functions $\psi(x)$ and $p(x)$ via

$$\Psi(x) = \tilde{\theta}\psi(\tilde{\theta}x) \quad P(x) = -\gamma\chi\tilde{\theta}p(\tilde{\theta}x) \quad (5.33)$$

The first equation transforms as

$$\begin{aligned} 2\tilde{\theta}^3\psi^3(\tilde{\theta}x) - 2\theta^2\tilde{\theta}\psi(\tilde{\theta}x) - \tilde{\theta}^3\partial_x^2\psi(\tilde{\theta}x) - \frac{4\gamma^2\chi\tilde{\theta}}{J}p(\tilde{\theta}x) &= 0 \\ 2\tilde{\theta}^3\psi^3(\tilde{\theta}x) - 2\left(\theta^2 + \frac{2\gamma^2\chi}{J}\right)\tilde{\theta}\psi(\tilde{\theta}x) - \tilde{\theta}^3\partial_x^2\psi(\tilde{\theta}x) + \frac{4\gamma^2\chi\tilde{\theta}}{J}(\psi(\tilde{\theta}x) - p(\tilde{\theta}x)) &= 0 \\ 2\psi^3(\tilde{\theta}x) - 2\psi(\tilde{\theta}x) - \partial_x^2\psi(\tilde{\theta}x) + \frac{4\gamma^2\chi}{J\tilde{\theta}^2}(\psi(\tilde{\theta}x) - p(\tilde{\theta}x)) &= 0 \end{aligned}$$

The second equation can be written as

$$\begin{aligned} -\gamma\chi\tilde{\theta}p(\tilde{\theta}x) &= -\gamma\chi\tilde{\theta}\psi(\tilde{\theta}x) - g\chi^2\gamma\tilde{\theta}^3\partial_x^2p(\tilde{\theta}x) \\ \frac{4\gamma^2\chi}{J\tilde{\theta}^2}(\psi(\tilde{\theta}x) - p(\tilde{\theta}x)) &= -\frac{4g\gamma^2\chi^2}{J}\partial_x^2p(\tilde{\theta}x) \end{aligned}$$

After rescaling $\tilde{\theta}x \rightarrow x$ we obtain the new saddle point equations

$$2\psi(x)^3 - 2\psi(x) - \psi''(x) + k(\psi(x) - p(x)) = 0 \quad (5.34)$$

$$lp''(x) + k(\psi(x) - p(x)) = 0 \quad (5.35)$$

making the saddle point equations only dependent on the parameters

$$k = \frac{4\gamma^2\chi}{J\tilde{\theta}^2} \quad \text{and} \quad (5.36)$$

$$l = 4g\gamma^2\chi^2/J. \quad (5.37)$$

The energy in terms of $\psi(x)$ and $p(x)$ can be written as

$$\begin{aligned} \mathcal{H}_x &= \frac{J}{8\tilde{\theta}} \int dx \left[(\tilde{\theta}^2\psi(x)^2 - \theta^2)^2 + \tilde{\theta}^4(\partial_x\psi(x))^2 + \frac{4\gamma^2\chi}{J}\tilde{\theta}^2(p(x)^2 - 2p(x)\psi(x)) \right. \\ &\quad \left. + \frac{4g\tilde{\theta}^4\gamma^2\chi^2}{J}(\partial_x p(x))^2 \right] \\ &= \frac{J\tilde{\theta}^3}{8} \int dx \left[(\psi(x)^2 - 1)^2 + (\partial_x\psi(x))^2 + \frac{4\gamma^2\chi}{J\tilde{\theta}^2}(p(x) - \psi(x))^2 + \frac{4g\gamma^2\chi^2}{J}(\partial_x p(x))^2 \right] + \text{const} \end{aligned}$$

Dropping the constant by shifting the ground state energy to zero and measuring the energy in units of $J\tilde{\theta}^3/8$ we obtain the dimensionless energy Hamiltonian of the form

$$\tilde{\mathcal{H}} = \int dx \left[(\psi(x)^2 - 1)^2 + (\psi'(x))^2 + k(p(x) - \psi(x))^2 + l(p'(x))^2 \right] \quad (5.38)$$

Domain wall solutions

Now that we rescaled the saddle point equations and the Hamiltonian, we can look at the solutions. Without coupling the solution for the polarization is simply $p(x) = 0$ while the solution for the domain wall is already known as $\psi(x) = \tanh(x)$, [18].

$$\psi(x) = \tanh(x) \qquad p(x) = 0 \qquad \text{for } \gamma = 0 \qquad (5.39)$$

The simplest case is $g = l = 0$ when the gradient term in the polarization vanishes. In this case the solution is given by

$$\psi(x) = p(x) = \tanh(x) \qquad \text{for } g = 0 \qquad (5.40)$$

However for a non vanishing gradient $g \neq 0$ we will find that $\psi(x) \neq p(x)$ since $p''(x) \neq 0$ in this case. For $g \ll k$, when the effect of the gradient in the polarization is small the two profiles should be well approximated by $\tanh(x)$ profile. The ansatz

$$\psi(x) = \tanh(c_\psi x) \qquad p(x) = \tanh(c_p x) \qquad (5.41)$$

with c_ψ and c_p being constants of order one, should be a good approximation. One can plug these profiles in the dimensionless variational and obtain

$$\tilde{\mathcal{H}} = \frac{4}{3c_\psi} + \frac{4c_\psi}{3} + \frac{4c_p}{3}l + k \int dx (\tanh(c_\psi x) - \tanh(c_p x))^2 \qquad (5.42)$$

where the last integral could not be solved analytically, but a good approximation for $c_p \approx 1$ and $c_\psi \approx 1$ could be found (details see appendix C.1), leading to

$$\tilde{\mathcal{H}} \approx \frac{4}{3} \left(\frac{1}{c_\psi} + c_\psi \right) + \frac{4c_p}{3}l + k \left[-2 \left(\frac{1}{c_p} + \frac{1}{c_\psi} \right) + 2 \frac{a_0(c_p^2 + c_\psi^2) + a_1 c_p c_\psi}{c_p c_\psi^2 + c_\psi c_p^2} \right] \qquad (5.43)$$

with $a_0 = 2 \ln(2)$ and $a_1 = 4 - 4 \ln(2)$. We can now determine the minimum of $\tilde{\mathcal{H}}$ in respect to c_p and c_ψ .

Numerics

In this subsection we want to find the exact solution of the domain wall profile by numerically minimizing the dimensionless Hamiltonian from equation (5.38). Numerically solving the saddle point equations is problematic, because we would need some information about the initial conditions. For these two second order differential equations one would need to know the value and the first derivative at one point for both functions. However only the boundary conditions $\psi(x \rightarrow \pm\infty) = \pm 1$ and $p(x \rightarrow \pm\infty) = \pm 1$ are known.

In order to calculate the profile without the knowledge of any initial conditions, we minimize the functional \mathcal{H} directly, using Chernous'ko's algorithm, [96]. On a finite interval $[-a, a]$ we describe the functions $\psi(x)$ and $p(x)$ by two sets $\{\psi_i\}$ and $\{p_i\}$ of equidistant points with spacing Δx . The integral in equation (5.38) can then be written as the discrete sum

$$\mathcal{H} \approx \Delta x \sum_i \Phi(\psi_i, \psi_{i+1}, p_i, p_{i+1}) \qquad (5.44)$$

with

$$\begin{aligned}\Phi(\psi_i, \psi_{i+1}, p_i, p_{i+1}) &= \frac{1}{2}(\psi_i^2 - 1)^2 + \frac{1}{2}(\psi_{i+1}^2 - 1)^2 + \left(\frac{\psi_{i+1} - \psi_i}{\Delta x}\right)^2 \\ &\quad + \frac{1}{2}k \left((\psi_i - p_i)^2 + (\psi_{i+1} - p_{i+1})^2\right) \\ &\quad + g \left(\frac{p_{i+1} - p_i}{\Delta x}\right)^2\end{aligned}\quad (5.45)$$

The solution is obtained by performing successive approximations. Going from the n -th approximation $\{\psi_i^{(n)}, p_i^{(n)}\}$ to the next is done by computing the 5 energies

$$F^0 = \Phi(\psi_{i-1}^{(n+1)}, \psi_i^{(n)}, p_{i-1}^{(n+1)}, p_i^{(n)}) + \Phi(\psi_i^{(n)}, \psi_{i+1}^{(n)}, p_i^{(n)}, p_{i+1}^{(n)}) \quad (5.46)$$

$$F_\psi^\pm = \Phi(\psi_{i-1}^{(n+1)}, \psi_i^{(n)} \pm h, p_{i-1}^{(n+1)}, p_i^{(n)}) + \Phi(\psi_i^{(n)} \pm h, \psi_{i+1}^{(n)}, p_i^{(n)}, p_{i+1}^{(n)}) \quad (5.47)$$

$$F_p^\pm = \Phi(\psi_{i-1}^{(n+1)}, \psi_i^{(n)}, p_{i-1}^{(n+1)}, p_i^{(n)} \pm h) + \Phi(\psi_i^{(n)}, \psi_{i+1}^{(n)}, p_i^{(n)} \pm h, p_{i+1}^{(n)}) \quad (5.48)$$

assuming the first $i - 1$ points of the $n + 1$ approximation have already been found. The new values at site i are then chosen according to the minimal energy $F_{min} = \min(F^0, F_\psi^\pm, F_p^\pm)$ as

$$(\psi_i^{(n+1)}, p_i^{(n+1)}) = \begin{cases} (\psi_i^{(n)}, p_i^{(n)}) & F^0 = F_{min} \\ (\psi_i^{(n)} \pm h, p_i^{(n)}) & F_\psi^\pm = F_{min} \\ (\psi_i^{(n)}, p_i^{(n)} \pm h) & F_p^\pm = F_{min} \end{cases} \quad (5.49)$$

For the starting point $i = 0$ we do the same by comparing the energies

$$\bar{F}^0 = \Phi(\psi_0^{(n)}, \psi_1^{(n)}, p_0^{(n)}, p_1^{(n)}) \quad (5.50)$$

$$\bar{F}_\psi^\pm = \Phi(\psi_0^{(n)} \pm h, \psi_1^{(n)}, p_0^{(n)}, p_1^{(n)}) \quad (5.51)$$

$$\bar{F}_p^\pm = \Phi(\psi_0^{(n)}, \psi_1^{(n)}, p_0^{(n)} \pm h, p_1^{(n)}) \quad (5.52)$$

The boundary conditions are enforced by only allowing negative values in the first half of the interval and positive values in the second half. To keep the center of the domain from moving, the value of ψ is fixed as zero at that particular point. The value h is chosen to be of the order Δx . The process is iterated until no more improvements to the previous approximation occur. In that case h is cut in half and the process is repeated. If there is still no improvement the number of points for the approximation is doubled, i.e. Δx is cut in half. The process ends once Δx reaches a pre-determined threshold. The algorithm is implemented in python and the code is listed in listing C.1 in the appendix. For a more detailed description of the algorithm see the original publication of Chernous'ko, [96].

As we can see in figure 5.3 and table 5.2, the test profiles used reveal a very good agreement with the numerics for $k < 1$ and $l < 1$. We see the main effect of the gradient term, i.e. parameter l , is the widening of the polarization profile compared to the chiral domain wall. For $l \sim 1$ and greater even the shape becomes modified enough so that the simple $\tanh(x)$ profile is not adequate enough.

Improvements

As we could see from the numerics, in the case of weak coupling $k < 1$ but strong gradients in the polarization $l > 1$ the $\tanh(x)$ profile is still a very good approximation for $\psi(x)$ but the

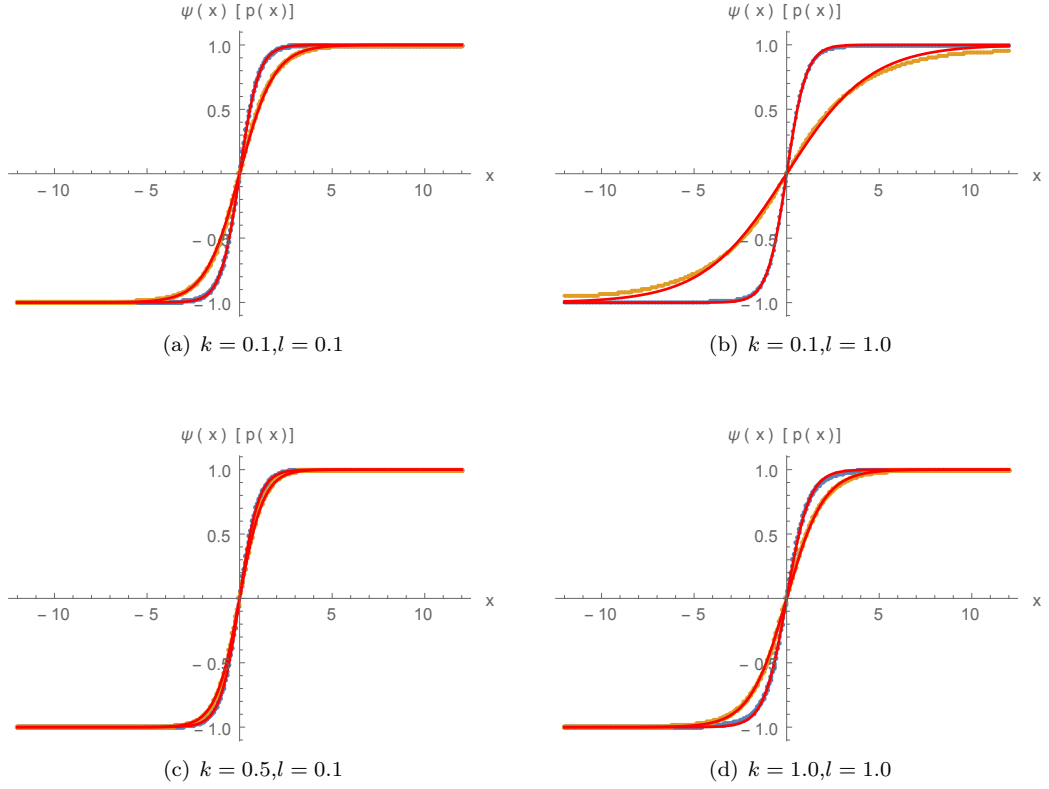


Figure 5.3: Comparison of the numerical solutions to the variational ansatz. The blue dots mark the numerical data for the gradient profile $\psi(x)$ and the yellow dots represent the polarization $p(x)$. The red lines correspond to the $\tanh(c_{\psi}/p x)$ profiles where the coefficients c_{ψ} and c_p are determined via a variational ansatz. A list of determined coefficients is given in table 5.2.

polarization becomes more spread out and changes shape. One can refine the approximations by taking $\psi(x) = \tanh(c_{\psi} x)$ and solve the saddle point equation for $p(x)$ treating $\psi(x)$ as a fixed inhomogeneous part. The equation to solve becomes then

$$lp''(x) + k(\psi(x) - p(x)) = 0 \quad (5.53)$$

After rescaling and introducing $a^2 = \frac{1}{k} c_{\psi}^2$ we get

$$a^2 p''(x) - p(x) = -\tanh(x) \quad (5.54)$$

which is solved by

$$p(x) = {}_2F_1\left(1, \frac{1}{2a}; 1 + \frac{1}{2a}; -e^{-2x}\right) - {}_2F_1\left(1, \frac{1}{2a}; 1 + \frac{1}{2a}; -e^{2x}\right) \quad (5.55)$$

where ${}_2F_1(a, b; c; x)$ is the hypergeometric function. This can be checked by using the following relation for the hypergeometric function and its derivative

$$\partial_z {}_2F_1(a, b; c; z) = \frac{ab}{c} {}_2F_1(a+1, b+1; c+1; z) \quad (5.56)$$

k	l	c_ψ		c_p	
		fit	var.	fit	var.
0.1	0.1	0.979559	0.980431	0.546640	0.537453
0.1	0.2	0.970731	0.972602	0.428703	0.426606
0.1	0.3	0.965441	0.967535	0.365188	0.367031
0.1	0.5	0.958978	0.960853	0.293586	0.299516
0.1	1.0	0.950317	0.951705	0.211803	0.222729
0.2	0.1	0.972431	0.973995	0.660808	0.647669
0.3	0.1	0.968537	0.970254	0.721541	0.707875
0.5	0.1	0.964362	0.965904	0.787305	0.774988
0.2	0.2	0.958425	0.961309	0.541039	0.533266
0.3	0.3	0.938395	0.942641	0.535595	0.529064
0.5	0.5	0.901068	0.906687	0.525113	0.520633
1.0	1.0	0.816935	0.824908	0.500415	0.499642

Table 5.2: Effective parameters c_ψ and c_p for the phase profile and polarization respectively. Compared are the results from fitting the $\tanh(c_\psi/p x)$ profiles to the numerical solutions to the parameters determined via the variational ansatz for different parameters l and k . k is the rescaled coupling parameter and l the rescaled gradient coefficient of the polarization profile $p(x)$.

found in [97] to compute

$$\partial_x {}_2F_1(\pm) \equiv \partial_x {}_2F_1\left(1, \frac{1}{2a}; 1 + \frac{1}{2a}; z_\pm\right) = \frac{1}{1+2a} {}_2F_1\left(2, 1 + \frac{1}{2a}; 2 + \frac{1}{2a}; z_\pm\right) (\pm 2z_\pm) \quad (5.57)$$

where we introduced $z_\pm = -\exp[\pm 2x]$ with $\partial_x z_\pm = 2\pm z_\pm$. Now we can use the relations between contiguous hypergeometric series to simplify the result. We know from [97] that the following general relations holds

$$(a-b)z {}_2F_1(a, b; c+1; z) = c {}_2F_1(a-1, b; c; z) - c {}_2F_1(a, b-1; c; z) \quad (5.58)$$

This transforms our result to

$$\partial_x {}_2F_1(\pm) = \pm \frac{1}{a} \frac{1}{1-\frac{1}{2a}} \left({}_2F_1\left(1, 1 + \frac{1}{2a}; 1 + \frac{1}{2a}; z_\pm\right) - {}_2F_1\left(2, \frac{1}{2a}; 1 + \frac{1}{2a}; z_\pm\right) \right) \quad (5.59)$$

Now we can already simplify the result by using the special function

$${}_2F_1(1, a; a; z) = \frac{1}{1-z} \quad (5.60)$$

Transforming our function to

$$\partial_x {}_2F_1(\pm) = \pm \frac{1}{a} \frac{1}{1-\frac{1}{2a}} \left(\frac{1}{1-z_\pm} - {}_2F_1\left(2, \frac{1}{2a}; 1 + \frac{1}{2a}; z_\pm\right) \right) \quad (5.61)$$

For the second term in the derivative we can use the relation

$$(b-a) {}_2F_1(a, b; c; z) + a {}_2F_1(a+1, b; c; z) - b {}_2F_1(a, b+1; c; z) = 0 \quad (5.62)$$

also found in [97], leading to

$$\begin{aligned} {}_2F_1\left(2, \frac{1}{2a}; 1 + \frac{1}{2a}; z_{\pm}\right) &= \left(1 - \frac{1}{2a}\right) {}_2F_1\left(1, \frac{1}{2a}; 1 + \frac{1}{2a}; z_{\pm}\right) + \frac{1}{2a} {}_2F_1\left(1, 1 + \frac{1}{2a}; 1 + \frac{1}{2a}; z_{\pm}\right) \\ &= \frac{1}{2a} \frac{1}{1 - z_{\pm}} + \left(1 - \frac{1}{2a}\right) {}_2F_1\left(1, \frac{1}{2a}; 1 + \frac{1}{2a}; z_{\pm}\right) \end{aligned} \quad (5.63)$$

The derivative can then be written simply as

$$\partial_x {}_2F_1(\pm) = \pm \frac{1}{a} \left(\frac{1}{1 - z_{\pm}} - {}_2F_1\left(1, \frac{1}{2a}; 1 + \frac{1}{2a}; z_{\pm}\right) \right) \quad (5.64)$$

The second derivative can now be performed easily and yields

$$\partial_x^2 {}_2F_1(\pm) = \frac{1}{a} \frac{-z_{\pm}}{(1 - z_{\pm})^2} - \frac{1}{a^2} \frac{1}{1 - z_{\pm}} + \frac{1}{a^2} {}_2F_1(\pm) \quad (5.65)$$

Plugging this into the differential equation we get

$$\begin{aligned} (a^2 \partial_x^2 - 1)({}_2F_1(-) - {}_2F_1(+)) &= \frac{1}{1 - z_+} - \frac{1}{1 - z_-} + \frac{az_+}{(1 - z_+)^2} - \frac{az_-}{(1 - z_-)^2} \\ &= \frac{1}{1 + e^{2x}} - \frac{1}{1 + e^{-2x}} - \frac{ae^{2x}}{(1 - e^{2x})^2} + \frac{ae^{-2x}}{(1 - e^{-2x})^2} \\ &= \frac{1 - e^{2x}}{1 + e^{2x}} = -\tanh(x) \end{aligned} \quad (5.66)$$

So we have shown that the hypergeometric function is the solution to the inhomogeneous differential equation.

The solution after beck transformation of the parameters is then

$$p(x) = {}_2F_1\left(1, \frac{1}{2c_{\psi}} \sqrt{\frac{k}{l}}; 1 + \frac{1}{2c_{\psi}} \sqrt{\frac{k}{l}}; -e^{-2xc_{\psi}}\right) - {}_2F_1\left(1, \frac{1}{2c_{\psi}} \sqrt{\frac{k}{l}}; 1 + \frac{1}{2c_{\psi}} \sqrt{\frac{k}{l}}; -e^{2xc_{\psi}}\right) \quad (5.67)$$

Interaction potential of chiral domain wall and polarization domain wall

So far in the numerics we saw that $\psi(x)$ and $p(x)$ share the same center and thus are physically located on top of each other. We now want to investigate this apparent one-to-one correspondence a bit further. As discussed above, the domain wall configuration is only stable in the absence of an applied electric field. In the case of $E_y = c = 0$ and small parameters k and l the solution is given by

$$\psi(x) = \tanh(c_{\psi}x) \qquad p(x) = \tanh(c_p x) \quad (5.68)$$

Now we look at the case where the profile of the phase gradient and the polarization are not at the same position but separated by the distance Δx by introducing

$$p(x - \Delta x) = \tanh(c_p(x - \Delta x)) \quad (5.69)$$

Now we can compute an effective interaction potential $V(\Delta x)$ for the two profiles as

$$V(\Delta x) = \mathcal{H}_x[p(\Delta x)] - \mathcal{H}_x[p(\Delta x = 0)] = 2k \int dx \psi(x)(p(x) - p(x - \Delta x)) \quad (5.70)$$

For the simple case of $l = 0$ we know the exact result as $c_p = c_\psi = 1$. In this case the interaction potential is of the form

$$V(\Delta x) = 2k \int dx \tanh(x)(\tanh(x) - \tanh(x - \Delta x)) = 4k(\Delta x \coth(\Delta x) - 1) \quad (c_\psi = c_p = 1) \quad (5.71)$$

which is illustrated in figure 5.4. The interaction potential favors $\Delta x = 0$ so that the polarization

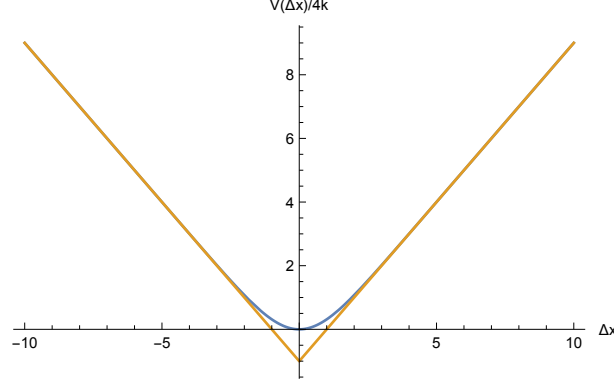


Figure 5.4: Interaction potential of gradient profile and polarization with $|x| - 1$ as comparison.

is identical to the gradient profile. For separations greater than the size of the domain walls, $\Delta x \gg 1$, the potential is linear. Both profiles have reached their respective ground state value of ± 1 and the profiles can be replaced by step functions. The integral then simplifies to $4k \int_0^{\Delta x} dx = 4k\Delta x$ for $\Delta x > 0$.

5.3 Two-dimensional domain wall

Focusing now on the two-dimensional model where the ground state is described by the wave vector $\mathbf{q} = \pm(q, 0, 0)$, [40]. As described earlier the energy for $\mathbf{E} = 0$ is given by

$$\mathcal{H} = \frac{J}{2} \int d^2x \left[\frac{1}{4}((\partial_x \phi)^2 - \theta^2)^2 + \frac{1}{4}(\partial_x^2 \phi)^2 + (\partial_y \phi)^2 \right] + \int d^2x \left[\gamma P_y (\partial_x \phi) - \gamma P_x (\partial_y \phi) + \frac{\mathbf{P}^2}{2\chi} \right] \quad (5.72)$$

where we dropped the gradient terms in the polarization. We have seen that its main effect is a widening in the polarization profile, but no strong change for the domain wall profile for the assumed small coupling. The term is dropped to make calculations easier, since we can now use the known exact solutions to study the effect of small rotations of the domain wall. The resulting saddle point equations are

$$-\partial_x (\partial_x \phi)^3 + \theta^2 \partial_x^2 \phi + \frac{1}{2} \partial_x^4 \phi - 2\partial_y^2 \phi - \frac{2\gamma}{J} \partial_x P_y + \frac{2\gamma}{J} \partial_y P_x = 0 \quad (5.73)$$

$$P_y = -\gamma \chi \partial_x \phi \quad (5.74)$$

$$P_x = \gamma \chi \partial_y \phi \quad (5.75)$$

Leading to the combined saddle point equation for ϕ

$$-\partial_x (\partial_x \phi)^3 + \left(\theta^2 + \frac{2\gamma^2 \chi}{J} \right) \partial_x^2 \phi + \frac{1}{2} \partial_x^4 \phi - 2 \left(1 - \frac{\gamma^2 \chi}{J} \right) \partial_y^2 \phi = 0 \quad (5.76)$$

where $J > \gamma^2\chi$ otherwise the gradient in $\partial_y\phi$ contribution will diverge in the energy as we will also see later when comparing the energies of different DW configurations. We can try to find solutions of the form $\phi = f(z)$ with $z = ax + by$ reducing the equation to

$$-\partial_z(\partial_z f)^3 + \frac{1}{a^4} \left[a^2(\theta^2 + \frac{2\gamma^2\chi}{J}) - 2b^2(1 - \frac{\gamma^2\chi}{J}) \right] \partial_z^2 f + \frac{1}{2} \partial_z^4 f = 0 \quad (5.77)$$

Finally, we apply the rescaling

$$z \mapsto dz \quad (5.78)$$

$$d = \frac{1}{a^2} \sqrt{a^2(\theta^2 + \frac{2\gamma^2\chi}{J}) - 2b^2(1 - \frac{\gamma^2\chi}{J})} \quad (5.79)$$

$$a^2 > b^2 \frac{2(J - \gamma^2\chi)}{J\theta^2 + 2\gamma^2\chi} \quad (5.80)$$

where the inequality between the coefficients a and b ensures that we are still dealing with a chiral minimum. A violation of that inequality removes the double minimum structure and we end up with the trivial $\phi = \text{const}$ ground state. After the rescaling we find

$$\partial_z \left[-(\partial_z f)^3 + \partial_z f + \frac{1}{2} \partial_z^2(\partial_z f) \right] = 0 \quad (5.81)$$

which we already encountered and is solved by $f(z) = \ln(\cosh(z)) + \text{const}$ leading to

$$\phi = \ln \cosh \left(\frac{1}{a^2} \sqrt{a^2(\theta^2 + \frac{2\gamma^2\chi}{J}) - 2b^2(1 - \frac{\gamma^2\chi}{J})} (ax + by) \right) + \text{const} \quad (5.82)$$

The energy of the saddle point is given by

$$\mathcal{H} = \frac{J}{2} \int d^2x \left[\frac{1}{4} ((\partial_x \phi)^2 - \theta^2)^2 + \frac{1}{4} (\partial_x^2 \phi)^2 - \frac{1}{J} \gamma^2 \chi (\partial_x \phi)^2 + (1 - \frac{1}{J} \gamma^2 \chi) (\partial_y \phi)^2 - E_{\min} \right] \quad (5.83)$$

where the last term shifts the ground state energy to zero. Plugging the profile $\phi(a, b)$ in the equation we get an integral of the form

$$\int dx \int dy f(ax + by) \quad (5.84)$$

where a rotation by $\alpha = \arctan(b/a)$ transforms the integral to

$$\int d\tilde{x} \int d\tilde{y} f(\sqrt{a^2 + b^2} \tilde{x}) = L_{\tilde{y}} \int d\tilde{x} f(\sqrt{a^2 + b^2} \tilde{x}) \quad (5.85)$$

The domain wall energy is therefor proportional to its length. Doing the transformation after plugging in $\phi(a, b)$ yields

$$\begin{aligned} \mathcal{H}(a, b) &= L_{\tilde{x}} L_{\tilde{y}} \frac{b^2}{2a^4 J} [(J - \gamma^2\chi) (a^2 (2\gamma^2\chi + \theta^2 J) + (\gamma^2\chi - J))] \\ &+ L_{\tilde{y}} \frac{1}{4a^4 J} \int dx (a^2 (2\gamma^2\chi + \theta^2 J) - 2b^2 (J - \gamma^2\chi))^2 \times \\ &\text{sech}^4 \left(\frac{x \sqrt{(a^2 + b^2)(a^2(2\gamma^2\chi + \theta^2 J) - 2b^2(J - \gamma^2\chi))}}{a^2} \right) \end{aligned} \quad (5.86)$$

where one can easily see that any tilt in the domain wall, i.e. $b \neq 0$, is punished by an energy term proportional to the area. The minimum solution is therefore $b = 0$ with

$$H(a, b = 0) = \frac{J\tilde{\theta}^3}{3} L_y \quad (5.87)$$

5.4 Domain wall in “four-state” model

Let us now consider a system where chiral order can also appear in the y -direction, leading to 4 possible ground states of the form $\pm(q, q, 0)$ and $\pm(q, -q, 0)$. An easy way of constructing such a model is by introducing a frustrated interaction in the y -direction, which leads to a simple Hamiltonian of the form

$$\mathcal{H}^{(4)} = \frac{J}{8} \int d^2x [((\partial_x \phi)^2 - \theta^2)^2 + (\partial_x^2 \phi)^2 + ((\partial_y \phi)^2 - \theta^2)^2 + (\partial_y^2 \phi)^2] \quad (5.88)$$

with the saddle point equation

$$-\partial_x(\partial_x \phi)^3 + \theta^2 \partial_x^2 \phi + \frac{1}{2} \partial_x^4 \phi - \partial_y(\partial_y \phi)^3 + \theta^2 \partial_y^2 \phi + \frac{1}{2} \partial_y^4 \phi = 0 \quad (5.89)$$

Simple domain walls

To find solutions of single domain walls, i.e. walls separating two different domains, we use the ansatz $\phi = f(z)$ with $z = ax + by$ again, transforming the partial differential saddle point equation to an ordinary differential equation in z as

$$-\partial_z(\partial_z f)^3 + \theta^2 \frac{a^2 + b^2}{a^4 + b^4} \partial_z^2 f + \frac{1}{2} \partial_z^4 f = 0 \quad (5.90)$$

yielding the solution

$$\phi = \ln(\cosh(\theta \sqrt{\frac{a^2 + b^2}{a^4 + b^4}}(ax + by))) \quad (5.91)$$

where the energy is given by

$$\begin{aligned} \mathcal{H} = & L_x L_y \frac{J\theta^4}{8} \frac{(a^2 - b^2)^2}{(a^4 + b^4)} \\ & + \frac{J\theta^4}{4} \frac{(a^2 + b^2)^2}{(a^4 + b^4)} \int dx \int dy \operatorname{sech}^4 \left(\theta \sqrt{\frac{a^2 + b^2}{a^4 + b^4}}(ax + by) \right) \end{aligned} \quad (5.92)$$

Showing an area dependent part scaling with $(a^2 - b^2)$ vanishing for $a = \pm b$, minimizing the energy with $E = \frac{1}{3} J\theta^3 L$ with L being the length of the domain wall. So the minimal energy solution for the domain wall configurations separating two different domains is

$$\phi^{xy} = \pm \ln(\cosh(\theta(x \pm y))) \quad (5.93)$$

Domain walls separating 4 states

A simple extension to domain walls separating 4 domains can be found as

$$\phi_V = \ln(\cosh(\theta x)) + \ln(\cosh(\theta y)) \quad (5.94)$$

$$\phi_A = \ln(\cosh(\theta x)) - \ln(\cosh(\theta y)) \quad (5.95)$$

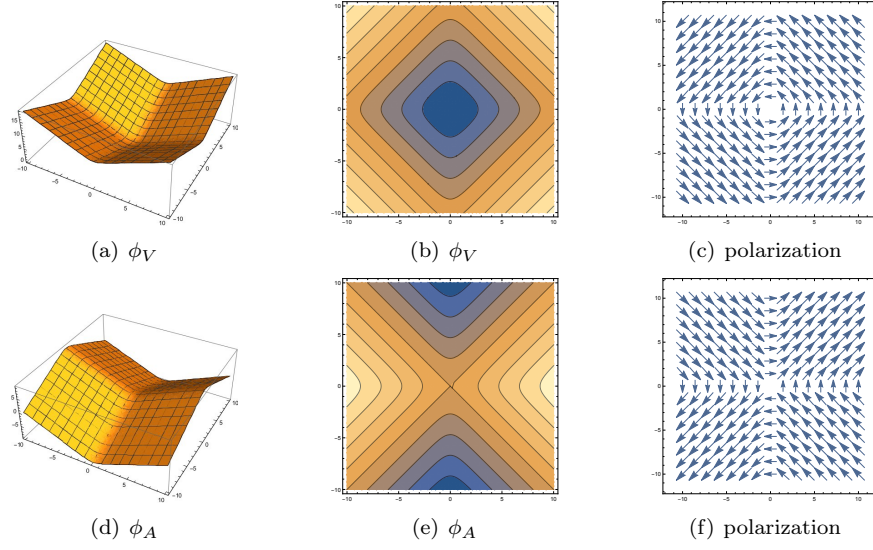


Figure 5.5: Polarization vortex and anti-vortex configuration

with an energy of $E = \frac{1}{3}J\theta^3(L_x + L_y)$ illustrated in figure 5.5.

The polarization plotted in figure 5.5 is calculated for in plane spins where the coupling is given as

$$\mathbf{P} \propto \begin{pmatrix} -\partial_y \phi \\ \partial_x \phi \\ 0 \end{pmatrix} \quad (5.96)$$

As can be seen the domain wall forms a vortex in the polarization. Interestingly when rotating the vortex structure, only the anti-vortex rotated by $\pi/4$ is a solution to the saddle point equation while the vortex configuration is not. The rotated solution is

$$\phi = \ln(\cosh(\frac{1}{2}\theta(x+y))) - \ln(\cosh(\frac{1}{2}\theta(x-y))) \quad (5.97)$$

with the energy given as

$$\mathcal{H} = \int dx dy \left[\frac{1}{32}\theta^4 J \left(\frac{8}{(\cosh(\theta x) + \cosh(\theta y))^2} + \operatorname{sech}^4\left(\frac{\theta}{2}(x-y)\right) + \operatorname{sech}^4\left(\frac{\theta}{2}(x+y)\right) + 4 \right) \right] \quad (5.98)$$

again with a part proportional to the area and therefore more expensive energy-wise compared to ϕ_V or ϕ_A .

Stretched vortices

Taking e.g. the vortex configuration ϕ_V and stitching it to a domain wall along the diagonal ϕ^{xy} one can create a “stretched” vortex of the form

$$\begin{aligned} \phi_{V_s} = & \theta(x+y-2d)(\ln(\cosh(\theta(x-d))) + \ln(\cosh(\theta(y-d)))) \\ & + (1-\theta(x+y-2d))\theta(x+y+2d)(2\ln(\cosh(\frac{\theta}{2}(x-y)))) \\ & + (1-\theta(x+y+2d))(\ln(\cosh(\theta(x+d))) + \ln(\cosh(\theta(y+d)))) \end{aligned} \quad (5.99)$$

shown in figure 5.6. In order to match the phase on the boundaries of the different profiles one has to adjust the “stretch” part from $\ln(\cosh(\theta(x-y))) \rightarrow 2 \ln(\cosh((1/2)\theta(x-y)))$ which is then no longer a solution to the saddle-point equations and is therefore punished by higher energy cost compared to the normal profile. The energy cost of the fitted single domain wall that has been

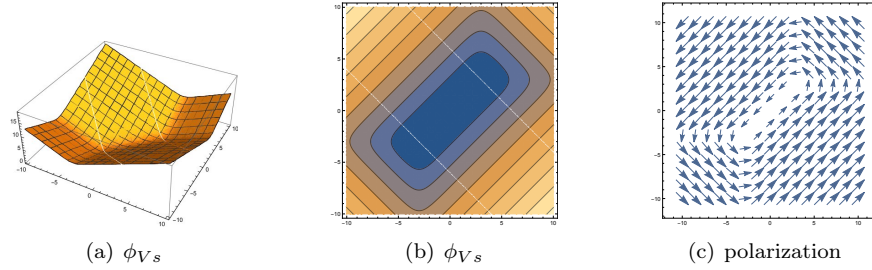


Figure 5.6: Stretched vortex

stitched in is

$$\mathcal{H} = \frac{5}{16} \theta^4 J \int dx dy \operatorname{sech}^4 \left(\frac{1}{2} \theta (x - y) \right) = \frac{5\sqrt{2}}{12} J \theta^3 L \quad (5.100)$$

Now, if we compare the energy cost in a square of area L^2 where the vortex itself has the energy cost $2LE_v = L^2 \frac{2}{3} J \theta^3$ and the modified diagonal domain wall over the whole diagonal $\sqrt{2}LE_d = \frac{5}{3} J \theta^3$. Measuring both in units of $J \theta^3$ we see that the vortex with $\frac{2}{3}$ cost less energy than the diagonal part with $\frac{5}{3}$ meaning that the stretched part is punished and the vortex configuration is stable.

6. MnWO₄

In this chapter we will focus on the multiferroic material MnWO₄. Here the chiral order couples to the polarization, as indicated by a magnetic phase transition with an accompanied onset of polarization. In collaboration with D. Niermann and the group of Prof. J. Hemberger, the critical behavior of the phase transition was studied. First the different phase transitions in MnWO₄ are described and the crystal symmetry is discussed. Starting from the Ginzburg–Landau free energy expansion done by Tolédano, the phase transitions will be classified and the critical dynamical behavior described. The resulting critical exponents are then compared to the experimental work of the group of Prof. J. Hemberger.

6.1 Material properties and observed phase transitions

MnWO₄ crystallizes in the P2/c space group and shows three consecutive phase transitions. Starting from a paramagnetic phase **P** the system undergoes its first transition to an incommensurate magnetic phase **AF3** at $T_N = 13.4\text{K}$ over to an incommensurate elliptical spiral phase **AF2** at $T_2 = 12.6\text{K}$ featuring an electric polarization.

$$\mathbf{P} \xrightarrow{T_N} \mathbf{AF3} \xrightarrow{T_2} \mathbf{AF2} \xrightarrow{T_1} \mathbf{COM}$$

In the last transition the system goes over to a commensurate magnetic phase **COM** without electric polarization **AF1** at $T_1 = 6.8\text{K}$, [37, 98, 99].

6.2 Group theory construction of Ginzburg–Landau free energy

The description of the phase transitions via the Ginzburg–Landau free energy has been done in [100]. Here we like to sketch the group theoretical method used to construct the free energy before moving on to the classifications of the different phase transitions.

Group theory and symmetries

Concerned with the symmetry analysis of MnWO₄, we start with the point group symmetry of the underlying Bravais lattice and will move on to the space group describing the crystal structure afterward. The Bravais lattice of MnWO₄ is monoclinic, [98], with the lattice constants $a \neq b \neq c$ and an easy axis b ($\beta = 91.075^\circ$)

$$a = 4.8226(3)\text{\AA} \qquad b = 5.7533(6)\text{\AA} \qquad c = 4.9923(5)\text{\AA}$$

according to [98].

The point group \mathcal{P} for the monoclinic lattice of MnWO₄ is $\mathcal{P} = C_{2h} = 2/m$ and contains all lattice symmetries leaving at least one point invariant. It consists of the identity $\mathbb{1}$, the 180° degree rotation C_2 around the easy-axis b (index $n = 2$ for $2\pi/n$ rotation), the mirror symmetry σ perpendicular to the rotation axis and the Inversion symmetry \mathbf{I} .

$$\mathcal{P} = \{\mathbb{1}, C_2, \sigma, \mathbf{I}\} \tag{6.1}$$

creating the 4 equivalent points

$$(x, y, z) \quad (\bar{x}, y, \bar{z}) \quad (x, \bar{y}, z) \quad (\bar{x}, \bar{y}, \bar{z})$$

Moving to the space group \mathcal{S} of the actual crystal structure we add the translation operators T_a , T_b and T_c allowing for glide reflections (reflections followed by a translation) and screw axis (rotations followed by a translation along the rotation axis) in the crystal. As reported e.g. in [98] the space group of $MnWO_4$ is $P2/c$ which means that the mirror operation σ from the point group is followed by a displacement of half a lattice constant in c ($T_{\frac{c}{2}}$) while the rotation symmetry is left unchanged [101], leaving

$$\mathcal{S} = \{\mathbf{1}, C_2, T_{\frac{c}{2}}\sigma, C_2T_{\frac{c}{2}}\sigma\} \quad (6.2)$$

with the 4 equivalent points

$$(x, y, z) \quad (\bar{x}, y, \bar{z}) \quad (x, \bar{y}, z + 1/2) \quad (\bar{x}, \bar{y}, \bar{z} - 1/2)$$

We see that the operator $C_2T_{\frac{c}{2}}(x, y, z) = (\bar{x}, \bar{y}, \bar{z}) - (0, 0, 1/2)$ is actually an inversion symmetry with its center half way between the two points at $-(0, 0, 1/4)$. The lattice is centrosymmetric (i.e. $\mathbf{I} \in \mathcal{P}$) and if we want to write the crystal structure as centrosymmetric it is convenient to shift the system by $(0, 0, 1/4)$ to make the new inversion center $(0, 0, 0)$. The glide reflection $\sigma_c = T_{\frac{c}{2}}\sigma$ is not affected by this, but the rotation axis of C_2 moves now through $(0, 0, 1/4)$ denoted by \tilde{C}_2 . The $P2/c$ space group consists of

$$P2/c = \{\mathbf{1}, \tilde{C}_2, \sigma_c, \mathbf{I}\} \quad (6.3)$$

producing the 4 equivalent points

$$(x, y, z) \quad (\bar{x}, y, \bar{z} + 1/2) \quad (x, \bar{y}, z + 1/2) \quad (\bar{x}, \bar{y}, \bar{z}) \quad (6.4)$$

which is the standard form of $P2/c$, [98].

Now we have classified the crystal symmetry of $MnWO_4$. For the study of the magnetic phase transitions however, we are interested in all magnetic symmetries, classified by the so called magnetic group. The magnetic group or Shubnikov group describes all the symmetries that leave magnetic structures invariant. Magnetic moments are inverted under time reversal symmetry R . When classifying magnetic symmetries one has to include the time reversal operator. Obviously the magnetic group cannot contain R itself. A magnetic structure that is symmetric in R would require that for each magnetic moment \mathbf{m}_i

$$\mathbf{m}_i = R\mathbf{m}_i = -\mathbf{m}_i$$

holds. This is only satisfied vanishing magnetic moments $\mathbf{m}_i = 0$ in the system, describing a non-magnetic state. Group theoretically speaking we cannot just take the direct product of the space group with the time reversal group $\{\mathbf{1}, R\}$. It is constructed as the direct product of the space group $P2/c$ with the time reversal symmetry R . There are 3 possible magnetic groups based on the point group $P2/c$, [101]. The magnetic group realized in $MnWO_4$ is $P2/c1'$, [100]. The prime indicates that the inversion symmetry is multiplied with the time reversal, while the 2-rotation is not, meaning that

$$P2/c1' = \{\mathbf{1}, \tilde{C}_2, R\sigma_c, R\mathbf{I}\} \quad (6.5)$$

A formal construction is done via the subgroup $\mathcal{H} = \{\mathbf{1}, \tilde{C}_2\}$ of index $2 = |P2/c|/|\mathcal{H}|$. It is known from group theory that the construction

$$P2/c1' = \mathcal{H} + R(P2/c - \mathcal{H}) \quad (6.6)$$

forms a group, [101].

Construction of free energy

In order to construct the free energy of the system, we have to identify the order parameters associated with the group and then construct the invariants of the group. To do so we first determine the irreducible representation of the magnetic space group P2/c1'. They can be found in [102] or we can use Olbrychski's method, [103], to determine the representation. For this we identify the generators G of the space group, i.e. set of elements that form all elements in the group through multiplication.

$$G = \{\sigma_c, \mathbf{I}, R, T_a, T_b, T_c\} \quad (6.7)$$

where R is time reversal symmetry and T_i is the translation in i -direction according to the incommensurable wave-vector $\mathbf{k}_{\text{inc}} = (k_x, 1/2, k_z)$ of the **AF2** phase. Now we write down the abstract definition of the generators by writing down the relations between the generators. The sequence of lattice translation is not important, so the operators T_i all commute with each other. Also it is not important if we first perform the translation to a certain lattice vector and then apply time reversal or reverse time before doing the translation. Therefor we have

$$[T_i, T_j] = 0 \quad [R, T_i] = 0 \quad i, j \in \{a, b, c\}. \quad (6.8)$$

Additionally space inversion \mathbf{I} and time reversal are their own inverse, leading to the two relations

$$\mathbf{I}^2 = \mathbf{1} \quad R^2 = \mathbf{1} \quad (6.9)$$

Now we consider the relations between inversion \mathbf{I} and translation T_i . Moving in one basis direction T_i , inverting the crystal around its inversion center (000) is equivalent to moving in the opposite direction T_i^{-1} after inversion, i.e.

$$\mathbf{I}T_i = T_i^{-1}\mathbf{I} \quad \Rightarrow \quad T_i\mathbf{I}T_i = \mathbf{I}. \quad (6.10)$$

For the glide reflection σ_c only the translation in b -direction is effected, leading to

$$\sigma_c T_{a/c} = T_{a/c} \sigma_c \quad \sigma_c T_b = T_b^{-1} \sigma_c \quad (6.11)$$

Taking the combination of $\mathbf{I}\sigma_c$ leading to the point $(\bar{x}, y, \bar{z}-1/2)$ and $\sigma_c\mathbf{I}$ leading to $(\bar{x}, y, \bar{y}+1/2)$ shows that they differ by a translation T_c leading to their defining relation

$$\sigma_c\mathbf{I} = T_c\mathbf{I}\sigma_c \quad (6.12)$$

Now that the equations (6.8)-(6.12) define the generators, we can solve these equation and find the two irreducible representations as listed in table 6.1, where we also used the knowledge about the translation subgroup discussed e.g. in [103–105].

The irreducible representation Γ^{k_1} and Γ^{k_2} have the two complex order parameters $\tilde{S}_1 = S_1 e^{i\theta_1}$ and $\tilde{S}_2 = S_2 e^{i\theta_2}$ associated with them. The transformations lead to the invariants $\mathcal{I}_1 = S_1^2$, $\mathcal{I}_2 = S_2^2$ and $\mathcal{I}_3 = \tilde{S}_1 \tilde{S}_1^* \tilde{S}_2^* \tilde{S}_2 + \tilde{S}_1^* \tilde{S}_1^* \tilde{S}_2 \tilde{S}_2 \propto S_1^2 S_2^2 \cos(2\varphi)$ with $\varphi = \theta_1 - \theta_2$, [100]. See appendix D.1 for more details.

The construction of the free energy from the invariants is straight forward

$$\Phi(T, S_1, S_2, \varphi) = \Phi_{10}(T) + \frac{\alpha_1}{2} S_1^2 + \frac{\beta_1}{4} S_1^4 + \frac{\alpha_2}{2} S_2^2 + \frac{\beta_2}{4} S_2^4 + \frac{\gamma_1}{2} S_1^2 S_2^2 \cos(2\varphi) + \frac{\gamma_2}{4} S_1^4 S_2^4 \cos^2(2\varphi) + \dots \quad (6.13)$$

Now we have to consider the coupling to the polarization P_y , following the notation of Tolédano, [100]. As discussed in [19] time inversion leaves the polarization invariant $RP = P$ while space inversion changes its sign, $\mathbf{I}P = -P$. With this it is easy to see that $P_y(\tilde{S}_1 \tilde{S}_2^* - \tilde{S}_1^* \tilde{S}_2) \propto$

$P2/c1'$		σ_y	\mathbf{I}	R	T_a	T_b	T_c
Γ^{k_1}	\tilde{S}_1	$\begin{pmatrix} e^{i\gamma} & 0 \\ 0 & e^{-i\gamma} \end{pmatrix}$	$\begin{pmatrix} 0 & 1 \\ 1 & 0 \end{pmatrix}$	$\begin{pmatrix} \bar{1} & 0 \\ 0 & \bar{1} \end{pmatrix}$	$\begin{pmatrix} e^{i\alpha} & 0 \\ 0 & e^{-i\alpha} \end{pmatrix}$	$\begin{pmatrix} \bar{1} & 0 \\ 0 & \bar{1} \end{pmatrix}$	$\begin{pmatrix} e^{i\gamma_2} & 0 \\ 0 & e^{-i\gamma_2} \end{pmatrix}$
	\tilde{S}_1^*	$\begin{pmatrix} 0 & e^{-i\gamma} \\ -e^{i\gamma} & 0 \end{pmatrix}$	$\begin{pmatrix} 0 & 1 \\ 1 & 0 \end{pmatrix}$	$\begin{pmatrix} \bar{1} & 0 \\ 0 & \bar{1} \end{pmatrix}$	$\begin{pmatrix} e^{i\alpha} & 0 \\ 0 & e^{-i\alpha} \end{pmatrix}$	$\begin{pmatrix} \bar{1} & 0 \\ 0 & \bar{1} \end{pmatrix}$	$\begin{pmatrix} e^{i\gamma_2} & 0 \\ 0 & e^{-i\gamma_2} \end{pmatrix}$
Γ^{k_2}	\tilde{S}_2	$\begin{pmatrix} -e^{i\gamma} & 0 \\ 0 & -e^{-i\gamma} \end{pmatrix}$	$\begin{pmatrix} 0 & 1 \\ 1 & 0 \end{pmatrix}$	$\begin{pmatrix} \bar{1} & 0 \\ 0 & \bar{1} \end{pmatrix}$	$\begin{pmatrix} e^{i\alpha} & 0 \\ 0 & e^{-i\alpha} \end{pmatrix}$	$\begin{pmatrix} \bar{1} & 0 \\ 0 & \bar{1} \end{pmatrix}$	$\begin{pmatrix} e^{i\gamma_2} & 0 \\ 0 & e^{-i\gamma_2} \end{pmatrix}$
	\tilde{S}_2^*	$\begin{pmatrix} 0 & -e^{-i\gamma} \\ e^{i\gamma} & 0 \end{pmatrix}$	$\begin{pmatrix} 0 & 1 \\ 1 & 0 \end{pmatrix}$	$\begin{pmatrix} \bar{1} & 0 \\ 0 & \bar{1} \end{pmatrix}$	$\begin{pmatrix} e^{i\alpha} & 0 \\ 0 & e^{-i\alpha} \end{pmatrix}$	$\begin{pmatrix} \bar{1} & 0 \\ 0 & \bar{1} \end{pmatrix}$	$\begin{pmatrix} e^{i\gamma_2} & 0 \\ 0 & e^{-i\gamma_2} \end{pmatrix}$

Table 6.1: The representation of the generators for the magnetic space group $P2/c1'$. Here we used the notation $\alpha = 2\pi k_x$ and $\gamma_2 = 2\gamma = 2\pi k_z$ to shorten the notation. This list can be found in [100].

$P_y S_1 S_2 \sin(\varphi)$ is then invariant under both R and \mathbf{I} . The coupling to the polarization is then described by

$$\Phi_D + \delta P_y S_1 S_2 \sin(\varphi) + \frac{P_y^2}{2\epsilon_{yy}^0} \quad (6.14)$$

[100]. The same structural form of the free energy has been derived starting from a microscopic description by [106].

6.3 Classification of phase transitions and critical dynamics

Now that the free energy for the system is obtained we can review the occurring phase transitions. Staying within the notation of Tolédano et al., the paramagnetic \mathbf{P} phase corresponds to $\alpha_1 > 0$ and $\alpha_2 > 0$, where the minimum of Φ is realized by $S_1 = S_2 = 0$. At the $\mathbf{P} \rightarrow \mathbf{AF3}$ transition at T_N , \tilde{S}_2 will become critical which will be frozen out once the $\mathbf{AF3} \rightarrow \mathbf{AF2}$ transition is reached at T_2 , giving us the sequence

$$\begin{array}{ccccccc} \mathbf{P} & & \mathbf{AF3} & & \mathbf{AF2} & & \mathbf{COM} \\ \tilde{S}_1 = 0, \tilde{S}_2 = 0 & \xrightarrow{T_N} & \tilde{S}_1 = 0, \tilde{S}_2 \neq 0 & \xrightarrow{T_2} & \tilde{S}_1 \neq 0, \tilde{S}_2 \neq 0 & \xrightarrow{T_1} & \tilde{S}_1 \neq 0, \tilde{S}_2 \neq 0 \end{array}$$

The mean field result for the equilibrium polarization $P_y^e(T) \propto \sqrt{T_2 - T}$ found by Tolédano et al. is in excellent agreement with polarization measurements done by Taniguchi et al. [99, 100]. In order to classify the types of transitions for $\mathbf{P} \rightarrow \mathbf{AF3}$ and $\mathbf{AF3} \rightarrow \mathbf{AF1}$ it is more convenient to introduce the real and imaginary parts of the order parameters via

$$\tilde{S}_1 = s_1 + i\bar{s}_1 \quad \tilde{S}_2 = s_2 + i\bar{s}_2 \quad (6.15)$$

with $s_1, \bar{s}_1, s_2, \bar{s}_2$ being real, leading to

$$\begin{aligned} \Phi = & \Phi_0(T) + \frac{\alpha_1}{2}(s_1^2 + \bar{s}_1^2) + \frac{\beta_1}{4}(s_1^2 + \bar{s}_1^2)^2 + \frac{\alpha_2}{2}(s_2^2 + \bar{s}_2^2) + \frac{\beta_2}{4}(s_2^2 + \bar{s}_2^2)^2 \\ & + \frac{\gamma_1}{2}((s_1^2 - \bar{s}_1^2)(s_2^2 - \bar{s}_2^2) + 4s_1\bar{s}_1s_2\bar{s}_2) + \frac{\gamma_2}{4}((s_1^2 - \bar{s}_1^2)(s_2^2 - \bar{s}_2^2) + 4s_1\bar{s}_1s_2\bar{s}_2)^2 \\ & + \delta P_y(\bar{s}_1s_2 - s_1\bar{s}_2) + \frac{P_y^2}{2\epsilon_{yy}^0} \end{aligned} \quad (6.16)$$

The details for these calculations can be found in the appendix D.1.

Transition from paramagnetic to commensurate phase ($\mathbf{P} \rightarrow \mathbf{AF3}$)

At the transition $\mathbf{P} \rightarrow \mathbf{AF3}$ at T_N , the order parameter \tilde{S}_2 is critical, i.e. $\alpha_2 \rightarrow 0$ while $\alpha_1 > 0$. In this case the free energy in \tilde{S}_1 is dominated by the quadratic part. Denoting the thermal average as $\langle \dots \rangle$ we substitute the terms in s_1 and \bar{s}_1 with their thermal averages. Assuming that the components are not correlated and fluctuating according to the same distribution, after integrating out the polarization we get the resulting effective free energy

$$\langle \Phi \rangle = \Phi'_0(T) + \frac{\alpha'_2}{2}(s_2^2 + \bar{s}_2^2) + \frac{\beta'_2}{4}(s_2^2 + \bar{s}_2^2)^2 + \zeta s_2^2 \bar{s}_2^2 \quad (6.17)$$

with

$$\alpha'_2 = \alpha_2 - \delta^2 \epsilon_{yy}^0 \langle s_1^2 \rangle \quad \beta'_2 = \beta_2 + 2\gamma_2(\langle s_1^4 \rangle - \langle s_1^2 \rangle^2) \quad \zeta = 4\gamma_2(3\langle s_1^2 \rangle^2 - \langle s_1^4 \rangle) \quad (6.18)$$

where we see the correction to the transition temperature T_N in $\alpha_2 = a_2(T - T_N)$ is of order $\mathcal{O}(\delta^2)$ which is neglect able for small couplings δ as assumed by Tolédano et al., [100], and later estimated by Matityahu et al. [106].

The model can be written as an $O(N)$ model with cubic anisotropy with $\phi_1 = s_2$ and $\phi_2 = \bar{s}_2$ and $N = 2$.

$$\langle \Phi \rangle = g(T) + \frac{m_0^2}{2} \sum_{i=1}^N \phi_i^2 + \frac{u_0}{4!} \left(\sum_{i=1}^N \phi_i^2 \right)^2 + \frac{v_0}{4!} \sum_{i=1}^N (\phi_i^2)^2 \quad (6.19)$$

with the parameters

$$m_0^2 = \alpha'_2 = \alpha_2 - \delta^2 \epsilon_{yy}^0 \langle s_1^2 \rangle \quad u_0 = 6\beta'_2 + 6\gamma'_2 \left(1 + \frac{\zeta}{2} \right) \quad v_0 = -3\zeta\gamma'_2 \quad \gamma'_2 = 2\gamma_2(\langle s_1^4 \rangle - \langle s_1^2 \rangle^2) \quad (6.20)$$

An extended version of the calculation is done in section D.2. Assuming Gaussian fluctuations we can use Wick's theorem

$$\langle s_1^4 \rangle = 3\langle s_1^2 \rangle^2 \quad (6.21)$$

which leads to

$$\zeta = 0 \quad \Rightarrow \quad v_0 = 0 \quad (6.22)$$

a vanishing anisotropy term. The model is then identical to the $O(2)$ model and the transition lies in the 3D-XY universality class with the symmetric fixpoint being the stable one.

In the case of non-Gaussian fluctuations, we get a $\zeta \neq 0$ and therefor an anisotropic term in the $O(2)$ model. This model has been studied for a sub critical $N < N_c$, where it has been found that the symmetric Heisenberg fixpoint is still the stable fixpoint for the system. There is still some debate on the exact value of N_c for $d = 3$, [107], which is in the order of $N_c \sim 3$, however calculations by Aharony, [108, 109] and Brézin et.al [110] show that for $N = 2$ in $d = 3$ the symmetric fix point is the stable one. The transition is then in the $O(2)$ -symmetric universality class. The exponents up to $\mathcal{O}(\epsilon^5)$ and a discussion on the stability of the Heisenberg fix point in the presents of cubic anisotropy is given in [91]. The same type of universality class for the $\mathbf{P} \rightarrow \mathbf{AF3}$ transition has been discussed by Matityahu et al., [106] and the reference therein, Harris et al. [111].

Transition to the elliptical phase ($\mathbf{AF3} \rightarrow \mathbf{AF2}$)

For $T < T_N$ the order parameter \tilde{S}_2 is frozen out, [100], and can be considered constant when approaching the second transition with $\alpha_1 = a_1(T - T_2)$. The equilibrium value in \tilde{S}_2 is given

by $S_2 = s = \sqrt{-\alpha'_2/\beta'_2}$ with an arbitrary phase θ_2 so that

$$s_2 = s \cos(\theta_2) \qquad \bar{s}_2 = s \sin(\theta_2) \qquad (6.23)$$

Introducing the vector $\mathbf{p} = (s_1, \bar{s}_1, P_y)$ the quadratic part Φ_M of the free energy with constant s_2 and \bar{s}_2 can be written as

$$\Phi_M = \frac{1}{2} \mathbf{p}^T \underline{\underline{M}} \mathbf{p} \qquad (6.24)$$

with

$$\underline{\underline{M}} = \begin{pmatrix} \alpha_1 + \gamma_1 s^2 \cos(2\theta_2) & \gamma_1 s^2 \sin(2\theta_2) & -\delta s \sin(\theta_2) \\ \gamma_1 s^2 \sin(2\theta_2) & \alpha_1 - \gamma_1 s^2 \cos(2\theta_2) & \delta s \cos(\theta_2) \\ -\delta s \sin(\theta_2) & \delta s \cos(\theta_2) & \frac{1}{\epsilon_{yy}^0} \end{pmatrix} \qquad (6.25)$$

using $\cos^2(\theta_2) - \sin^2(\theta_2) = \cos(2\theta_2)$ and $\cos(\theta_2) \sin(\theta_2) = \frac{1}{2} \sin(2\theta_2)$. Even in the case of no coupling to the polarization, i.e. $\delta = 0$ we will see that only one component is becoming critical at this transition, making it a member of the 3D-Ising universality class. For $\delta = 0$ the eigenvalues $\{\lambda_i\}$ and eigenvectors $\{\mathbf{v}_i\}$ of $\underline{\underline{M}}$ can be obtained as

$$\lambda_1 = \alpha_1 - \gamma_1 s^2 \qquad \lambda_2 = \alpha_1 + \gamma_1 s^2 \qquad \lambda_3 = \frac{1}{\epsilon_{yy}^0} \qquad (6.26)$$

and

$$\mathbf{v}_1 = \begin{pmatrix} -\sin(\theta_2) \\ \cos(\theta_2) \\ 0 \end{pmatrix} \qquad \mathbf{v}_2 = \begin{pmatrix} \cos(\theta_2) \\ \sin(\theta_2) \\ 0 \end{pmatrix} \qquad \mathbf{v}_3 = \begin{pmatrix} 0 \\ 0 \\ 1 \end{pmatrix} \qquad (6.27)$$

As discussed in [100] the physical realized transition takes place for $\gamma_1 > 0$. In that case λ_1 is the first eigenvalue to vanish, while the other two are still positive, so that only one component becomes critical. The phase transition is therefor in the $O(1)$ 3D-Ising universality class, agreeing with [106, 111]. A more detailed discussion is done in section D.3.

6.4 Dynamical exponent at $\mathbf{AF3} \rightarrow \mathbf{AF2}$

As seen in the previous section the transition at T_2 lies in the 3D-Ising $O(1)$ universality class. Using the vectors $\mathbf{p} = (s_1, \bar{s}_1, P_y)$ and the matrix $\underline{\underline{M}}$ from equation (6.25) we could write the quadratic part of the free energy as $\mathbf{p}^T \underline{\underline{M}} \mathbf{p}$. Now we want to rotate the system in its diagonal form with the new vector $\mathbf{u} = (u_1, u_2, u_3)$ where only u_1 becomes critical at T_2 . We determine the eigenvalues and the corresponding eigenvectors leading to the construction of the rotation matrix $\underline{\underline{R}}$ that gives us the correspondence $\mathbf{u} \leftrightarrow \mathbf{p}$. We will order the eigenvalues in a way so that λ_1 corresponding to u_1 is the first one to vanish, making u_1 the critical field at T_2 . We get

$$\lambda_{1/2} = \frac{\alpha_1}{2} - \frac{\gamma_1 s^2}{2} + \frac{1}{2\epsilon_{yy}^0} \mp \frac{1}{2\epsilon_{yy}^0} \sqrt{4\epsilon_{yy}^0 (s^2 (\gamma_1 + \delta^2 \epsilon_{yy}^0) - \alpha_1) + (\alpha_1 \epsilon_{yy}^0 - \gamma_1 s^2 \epsilon_{yy}^0 + 1)^2}$$

$$\lambda_3 = \alpha_1 + \gamma_1 s^2$$

Here, the eigenvalues vanish at

$$\alpha_1^{(1)} = \gamma_1 s^2 + \delta^2 \epsilon_{yy}^0 \qquad \Rightarrow \qquad \lambda_1 = 0 \qquad (6.28)$$

$$\alpha_1^{(2)} = -\gamma_1 s^2 \qquad \Rightarrow \qquad \lambda_3 = 0 \qquad (6.29)$$

and λ_2 never goes to zero. Expanding the eigenvalues around $\alpha_1^{(1)}$ via $\alpha_1 = \alpha_1^{(1)} + x$ for small deviation x around the critical value of α_1 we get

$$\lambda_1 = \frac{1}{1 + s^2 \delta^2 \epsilon_{yy}^0} x + \mathcal{O}(x^2) \quad (6.30)$$

$$\lambda_2 = \frac{1}{\epsilon_{yy}^0} + s^2 \delta^2 \epsilon_{yy}^0 + x \left(1 - \frac{1}{1 + s^2 \delta^2 \epsilon_{yy}^0} \right) + \mathcal{O}(x^2) \approx \frac{1}{\epsilon_{yy}^0} + s^2 \delta^2 \epsilon_{yy}^0 \quad (6.31)$$

$$\lambda_3 = 2\gamma_1 s^2 + \delta^2 \epsilon_{yy}^0 + x + \mathcal{O}(x^2) \approx 2\gamma_1 s^2 + \delta^2 \epsilon_{yy}^0 \quad (6.32)$$

The eigenvectors $\{\mathbf{v}_i\}$ can be written as

$$\mathbf{v}_1 = \frac{1}{\sqrt{B^2 + 1}} \begin{pmatrix} -B \sin(\theta_1) \\ B \cos(\theta_1) \\ 1 \end{pmatrix} \quad \mathbf{v}_2 = \frac{1}{\sqrt{B^2 + 1}} \begin{pmatrix} \sin(\theta_1) \\ -\cos(\theta_1) \\ B \end{pmatrix} \quad \mathbf{v}_3 = \begin{pmatrix} \cos(\theta_1) \\ \sin(\theta_1) \\ 0 \end{pmatrix} \quad (6.33)$$

Neither the rotated free energy nor the mapping $P_y(\mathbf{u})$ depends on the angle θ_1 (as can be seen either by doing the full calculations or by noting that the free energy is only dependent on the angle difference $\varphi = \theta_1 - \theta_2$). We can therefore choose $\theta_1 = 0$ to make the representations more convenient, leading to

$$\mathbf{v}_1 = \frac{1}{\sqrt{B^2 + 1}} \begin{pmatrix} 0 \\ B \\ 1 \end{pmatrix} \quad \mathbf{v}_2 = \frac{1}{\sqrt{B^2 + 1}} \begin{pmatrix} 0 \\ -1 \\ B \end{pmatrix} \quad \mathbf{v}_3 = \begin{pmatrix} 1 \\ 0 \\ 0 \end{pmatrix} \quad (6.34)$$

with

$$\begin{aligned} B &= \frac{1}{2\delta s \epsilon_{yy}^0} \sqrt{1 + \epsilon \left(-2\alpha_1 + \epsilon_{yy}^0 \left((\alpha_1 - \gamma_1 s^2)^2 + 4\delta^2 s^2 \right) + 2\gamma_1 s^2 \right)} - \frac{\alpha_1}{2\delta s} + \frac{\gamma_1 s}{2\delta} + \frac{1}{2\delta s \epsilon_{yy}^0} \\ &= \frac{1}{s\delta \epsilon_{yy}^0} - \frac{x}{s\delta + s^3 \delta^3 \epsilon_{yy}^0} + \mathcal{O}(x^2) \approx \frac{1}{s\delta \epsilon_{yy}^0} \end{aligned} \quad (6.35)$$

where we expanded around $\alpha_1 = \alpha_1^{(1)} + x$ and assumed small δ and temperatures close to the transition. With this the rotation matrix becomes

$$\underline{\underline{R}} = \frac{1}{\sqrt{1 + B^2}} \begin{pmatrix} 0 & B & 1 \\ 0 & -1 & B \\ \sqrt{1 + B^2} & 0 & 0 \end{pmatrix} \quad (6.36)$$

And the relation for $\mathbf{p} \leftrightarrow \mathbf{u}$

$$\mathbf{p} = \begin{pmatrix} s_1 \\ \bar{s}_1 \\ P_y \end{pmatrix} = \underline{\underline{R}}^T \mathbf{u} = \frac{1}{\sqrt{1 + B^2}} \begin{pmatrix} u_3 \sqrt{1 + B^2} \\ B u_1 - u_2 \\ u_1 + B u_2 \end{pmatrix} \quad (6.37)$$

leading to the polarization

$$P_y = \frac{1}{\sqrt{1 + B^2}} (u_1 + B u_2) \quad (6.38)$$

For a spatial and time dependent polarization the fluctuations are

$$\langle P_y(\mathbf{x}, t) P_y(0) \rangle = \frac{1}{1 + B^2} (\langle u_1(\mathbf{x}, t) u_1(0) \rangle + 2\langle u_1(\mathbf{x}, t) u_2(0) \rangle + \langle u_2(\mathbf{x}, t) u_2(0) \rangle) \quad (6.39)$$

At the transition point the fluctuations in u_2 are still finite, so that the divergence in the polarization is determined by the divergence in $\langle u_1(\mathbf{x}, t)u_1(0) \rangle$, making their dynamical exponents identical. It is therefor sufficient to calculate the exponents for u_1 in order to predict the exponents in the polarization fluctuation. Diagonalizing the free energy leads to

$$\Phi = \frac{1}{2}\lambda_1 u_1^2 + \frac{1}{2}\lambda_2 u_2^2 + \frac{1}{2}\lambda_3 u_3^2 + \frac{\beta_2^+}{4} \frac{B^4}{(1+B^2)^2} u_1^4 + \frac{\beta_2^+}{4} \frac{1}{(1+B^2)^2} u_2^4 + \frac{\beta_2^+}{4} u_3^4 + A_{ij} u_1^i u_2^j u_3^{(4-i-j)} \quad (6.40)$$

with $\beta_2^\pm = \beta_2 \pm \gamma_2 s^4$ and $\{A_{2,0}, A_{1,1}, A_{3,1}, A_{0,2}, A_{2,2}, A_{1,3}\}$ being non-zero and the sum over double appearing indicies is applied.

$$\underline{A} = \frac{1}{1+B^2} \begin{pmatrix} 0 & 0 & \frac{B^2}{2}\beta_2^- & 0 \\ 0 & -B\beta_2^- & 0 & -\frac{B^3\beta_2^+}{1+B^2} \\ \frac{1}{2}\beta_2^- & 0 & \frac{3B^2\beta_2^+}{2(1+B^2)} & 0 \\ 0 & -\frac{B\beta_2^+}{1+B^2} & 0 & 0 \end{pmatrix} \quad (6.41)$$

Close to $\lambda_1 = 0$ the eigenvalues $\lambda_2 > 0$ and $\lambda_3 > 0$ with the quadratic terms in u_2 and u_3 dominate the behavior in these components. Substituting the values of u_2 and u_3 with their thermal averages, one obtains a simple one-loop correction to the eigenvalue λ_1 in an otherwise simple ϕ^4 -theory model, Φ_u .

$$\Phi_u = h(T) + \frac{1}{2}\lambda_1' u_1^2 + \frac{\beta_2^+}{4} \frac{B^4}{(1+B^2)^2} u_1^4 \quad \lambda_1' = \lambda_1 + A_{2,0}\langle u_3^2 \rangle + A_{2,2}\langle u_2^2 \rangle \quad (6.42)$$

Leaving us with a simple ϕ^4 theory at the transition T_2 . So now we want to consider the dynamical scaling of an Ising order parameter. Assuming an overdamped dynamics with a dampening coefficient Γ_0 our model is identical to the Model A discussed in [112]. The dynamical exponent z for the inverse relaxation time $\omega = \tau^{-1}$ is

$$\omega \propto \xi^{-z} \propto t^{\nu z} = \left[\frac{T - T_2}{T_2} \right]^{\nu z} \quad (6.43)$$

where νz is the experimentally measured exponent, at the reduced temperature $t = (T - T_2)/T_2$. Here ν is the critical exponent of the correlation length ξ of the 3D-Ising universality class. A good overview of the calculated exponents z for the 3D-Ising model is contained in Folk et al. [113], where the highest expansion is done by Prudnikov et al. [114] in terms of a 4-loop ϵ expansion with Padé-Borel summation leading to

$$z = 2.017 \quad (6.44)$$

which is very good agreement with the numerically found values around $z \approx 2.02$ found by [115–117]. With the value of ν found using resummation techniques (for $d = 3$) done by Guida and Zinn-Justin [118]

$$\nu = 0.6304 \pm 0.0013 \quad (6.45)$$

we get for the dynamical exponent of the relaxation time

$$\nu z \approx 1.272 \quad (6.46)$$

which is in agreement with the measured value $\nu z \approx 1.3$, [41]. In accordance with the experimental observations this paints the picture that the critical dynamics of the polarization are determined by an overdamped magnetic 3D-Ising order parameter.

6.5 Discussion

Using Bertraut's group theoretical consideration, [104, 105] the Landau expansion of the free energy of $MnWO_4$ was calculated. This was done following Tolédano et al., [100] for the incommensurable phase $\mathbf{k}_{inc} = (-0.214, 1/2, 0.457)$, [98, 100]. This theory could be used to classify the universality classes of the occurring transitions. The first transition from the paramagnetic **P** phase to the incommensurable phase **AF3** at T_N was found to be in the 3D-XY universality class, in agreement with [106, 111]. The main interest however lies on the second transition at T_2 , where the incommensurable phase switches to the spiral phase AF2 with a non-vanishing polarization $P_y \neq 0$. The transition was found to be in the 3D-Ising universality class, agreeing with [106, 111]. Describing the dynamics of the order parameter at the transition as overdamped leads to the so called Model A description, [112] and to a dynamical exponent $\nu z \approx 1.272$ for $MnWO_4$, agreeing with the measurements done by Niermann et al., [41]. The results of this chapter have been partially published in [41].

Part II

Vortices in Supraconducting Thin Films

7. Introduction

Helium was first liquified by H. K. Onnes in 1908. For the first time temperatures as low as a few degrees of Kelvin could be reached. Only 3 years later he was able to discover superconductivity in mercury in 1911, [119–121]. Two distinct features characterize the superconducting state. The onset of perfect conductivity below a critical temperature T_c was what Onnes discovered in 1911. The next distinct feature is perfect diamagnetism, discovered in 1933 by Meissner and Ochsenfeld, [122]. An applied magnetic field is prevented from entering the superconductor and actively expelled while cooling a superconductor through T_c in an external field, [123]. It can only penetrate a small surface layer and is exponentially suppressed, characterized by the penetration length λ . While the first effect can be explained by perfect conductance alone via an induced shielding current, the latter effect is unique to superconductors. A perfect conductor would trap a flux when being cooled in an external field.

In general, superconductors fall into two groups. Type I superconductors, e.g. lead (Pb), are characterized by their critical field H_c , next to the critical temperature T_c . Once the applied field reaches H_c , the energy needed to expel it is greater than the energy gained by entering the superconducting state and the superconductivity breaks down, [123]. In type II superconductors, the breakdown of superconductivity due to an applied field is not discontinuous like it is for type I superconductors, but continuous. After reaching the first critical field H_{c1} , the surface energy of magnetic domains becomes negative. The resulting division of domains proceeds to the microscopic length scale marked by the correlation length ξ of the system. This behavior was first discussed in 1957 by Abrikosov, [124], who also discovered that these microscopic subdomains, or vortices, repel each other and form regular lattices. This mixed state of superconductivity and vortices with normal conducting cores is referred to as the *Shubnikov phase*, [123]. These vortices move due to an applied current and their normal conducting core dissipates energy, leading to a small resistance. This can be stopped by e.g. pinning these vortices. The study of these vortices and their dynamics is important in order to produce superconducting materials that can withstand high magnetic fields.

In thin films with a thickness d of the order of the penetration length λ , vortices also appear in type I superconductors, [123]. The analytic solution for these type of vortices was found by Pearl in 1964, [125, 126], and are consequently named after him. Vortices in thin films are interesting for several reasons. The magnetic structure on the surface can be revealed by sprinkling it with a finely powdered ferromagnet that will settle at points with magnetic flux, i.e. vortices, [127]. This techniques called Bitter decoration is used to visualize the vortices on the surface and to study the lattice structures and the effect of impurities. Newer approaches using a nano-SQUID on the tip of a scanning microscope, [128], are able to produce images with high spatial resolutions. On top of that they are able to produce multiple scans of the same area, allowing the study of the dynamics of the vortices as well. The thin films offer experimental setups to study the melting of a 2D lattice, lattice deformation due to impurities and, since the vortices can be moved by a current, vortex and lattice dynamics.

This second part summarizes the work done on superconducting thin films. The experimental data used here was provided by the group of Prof. E. Zeldov. The group is known for its high resolution measurements of the surface magnetic field on superconducting thin films. Their technique using a SQUID placed on a small tip of a scanning microscope allows them to study magnetic vortices and their dynamics with spatial resolutions of $\sim 100\text{nm}$. Their aim is to study

the movement of vortex lattices in order to study the moving Bragg-glass phase experimentally, [129–131]. The Bragg-glass phase is characterized by a power-law decay in the density correlations.

At the beginning of the collaboration, the experiments were in their early stages. The main idea was to focus on thin strips with differently sized constrictions. These constrictions introduce some inhomogeneities in the current profile and consequently cause inhomogeneous deformations of the lattice. The deformed lattices with destroyed long-range correlation (no fixed lattice structure), are then moved by applying a direct current to the sample. When moving vortices through the setup, several effects have to be taken into account. Vortices can enter the sample from the borders of the strip and impurities can pin them.

We tried to contribute to the explanation of two different observed effects in their setups. Once a certain critical current I_c was surpassed, the vortices were observed to be moving, causing a measurable resistance. The measured $V(I)$ curve on these strip setups was characterized by a power law behavior

$$V(I) \sim I^\alpha, \quad \alpha \sim 10. \quad (7.1)$$

We tried to understand the origin of the exponent α as an effect of vortices trying to overcome a surface barrier. The results and details are discussed in chapter 10. The second effect the group observed concerned the dynamics of the vortices. They noticed that the moving vortices formed lines, effectively following each other. Additionally, around the inhomogeneities caused by the constrictions in the superconducting strip, these flow lines bifurcated. Both, the line formation and the origin of the bifurcation points are discussed in chapter 11.

Outline

We start by presenting the experimental setup and measurements that are the basis for the analytic work in chapter 8. Here, the two different observed effects are described in detail. After an introduction to superconductivity, thin films and vortices in chapter 9, the work done on the observed $V(I)$ curves is discussed in chapter 10. This is followed by the presentation of the work done on the vortex dynamics in chapter 11. The two projects are fairly separate, so an individual discussion is done at the end of each chapter.

8. Experimental Data

In this chapter we will focus on the experimental setup used by our collaborators L. Embon and E. Zeldov and the data they provided. There are two distinct features that we try to explain in the following chapters and we want to set the stage for them here. The first section will cover the setup and measurement techniques to give a general overview of the setup we are dealing with. They use a technique called nanoSQUID microscopy to track superconducting vortices in thin films exposed to an applied current and measure the resulting voltage drop along the strips. First, we will present the current–voltage curves and their power–law behavior. Later, in chapter 10, we will try and give an analytic explanation for this behavior. The moving vortices are also observed to move in lines. This second feature will be presented here discussed in detail later in chapter 11.

8.1 Experimental setup

The dynamic properties of superconducting vortices in a thin type I superconductor are studied experimentally by our collaborators. The material used is a thin lead (Pb) film of thickness $d = 50\text{nm}$ that is capped by a thin $\sim 10\text{nm}$ Germanium (Ge) layer, to prevent oxidation. A list of material properties of lead assembled from literature is found in table E.1 in appendix E.1. The mask used is shown in figure 8.1, where the light gray areas resemble the lead film. It contains 6 different strip setups, each with a different width for the hour-glass shaped constriction, [132]. The strip width is $w = 10\mu\text{m}$ for all setups, while the hourglass constriction can be as narrow as $5 - 6\mu\text{m}$. All measurements are done at $T = 4.2\text{K}$ in a liquid Helium cryostat. The magnetic field H is applied perpendicular to the film. Gold contacts on the film are used to connect the wiring, schematically shown in figure 8.2. There are two contributions to the current that is fed into the strip. The DC current is generated by applying a voltage U_{DC} over an $R_{\text{DC}} = 566\Omega$ resistor in series with the strip. Additionally a fixed AC contribution is added via a square wave U_{AC} applied over a $R_{\text{AC}} = 10\text{k}\Omega$. The AC voltage signal is a square wave at 1.137kHz with a constant 1.2V amplitude. DC and AC part of the resulting voltage drop are measured by a simple voltmeter and a lock-in amplifier respectively, [132]. The small structures one can see in figure 8.1 and even better in figure 8.2 (circular pattern), are present for engineering reasons only. They do not influence the measurements done on the thin strips.

The measurements of the magnetic fields are done with a technique referred to as scanning SQUID microscopy. A small hollow quartz tube with an opening diameter of $\sim 200\text{nm}$ is used and aluminum is evaporated on two opposing sides and on the circular opening, as illustrated in 8.3. The aluminum on the two sides form superconducting leads connected to the nanoSQUID ring formed on the opening of the quartz tube. This structure is referred to as a SQUID on top (SOT), [128]. The SOT is used as the tip on a scanning microscope. This setup allows for a high spatial resolution when imaging the magnetic field on the surface of the superconducting thin films. With this it is possible to see the vortex distribution and even dynamics in the thin films.

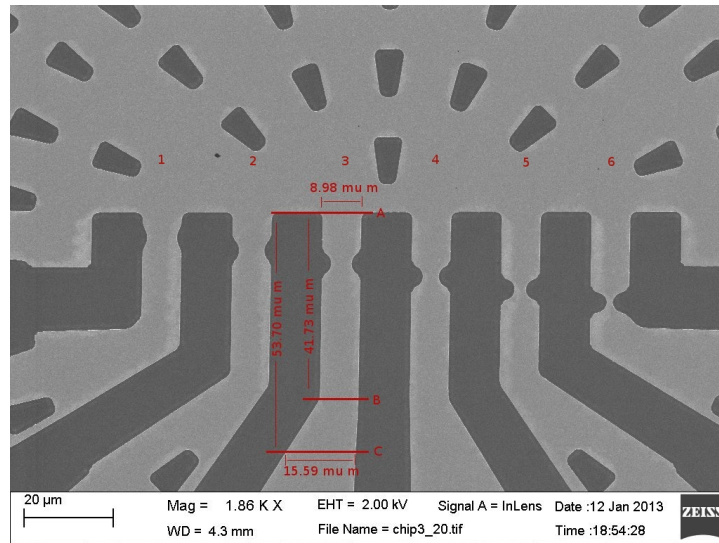


Figure 8.1: Top view of the constricted bridge setup. Light gray areas mark the lead film. The 6 different hour-glass shaped constrictions are easily visible. The graphics were kindly provided by L. Embon and E. Zeldov, private communication [132]. A wider view of the mask is shown in figure 8.2 including the gold contacts and schematic wiring for the voltage measurements and the application of currents to the system.

Experimental parameters

The parameters at $T = 4.2K$ for the correlation length ξ and penetration length λ for the discussed setup as reported by L. Embon and E. Zeldov, [132], are

$$\xi = 40 - 50\text{nm} \quad (8.1)$$

$$\lambda = 80 - 100\text{nm} \quad (8.2)$$

resulting in an effective penetration length

$$\Lambda_P = \frac{2\lambda^2}{d} = 170 - 330\text{nm} \quad (8.3)$$

The measurements were taken using the 3 strip in the constricted bridge setup shown in figure 8.1, where the bridge is $w_{\max} = 10\mu\text{m}$ at its widest and $w_{\min} = 5 - 6\mu\text{m}$ at its closest point. An example measurement done with an applied field of $H = 54\text{G}$ is shown in figure 8.4(a). One can see the constricted hour-glass bridge and the penetrating vortices quite clearly.

Magnetization First, let us get an idea of the resulting penetrating field due to the applied field, i.e. the flux trapped in the vortices. Starting point for this analysis is the measurement taken at $H = 54\text{G}$ with a direct current of $I = 12.2\text{mA}$ shown in figure 8.4(a). The vortices are not moving and the vortex structure is fixed. Taking the gray scale image of the vortices as a height profile, vortices can be easily detected by a simple hill-climber algorithm or, given the manageable number, even by hand. The results before and after detection are shown figure 8.4. The scale of the images is known to be 40nm per pixel. One can therefore mark an area and count the contained vortices to calculate the trapped flux and resulting trapped field B . In

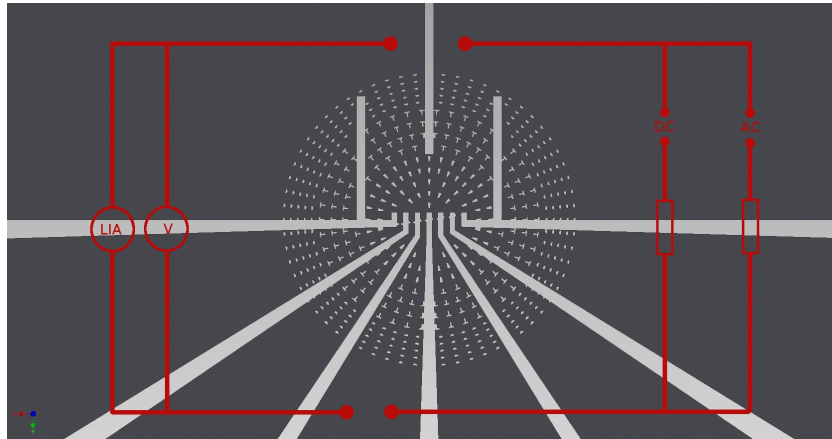


Figure 8.2: Top view of the masked used for the thin film setup. This is a wider view of the structure shown in figure 8.1. Note that in this schematic, the dark gray areas represent the lead film. Additionally the gold contacts and schematic wiring for the setup is shown (exemplified on strip no 3). A current is fed into the system so that it flows from bottom to top through the strip. The figure was kindly provided by L. Embon and E. Zeldov, private communication [132].

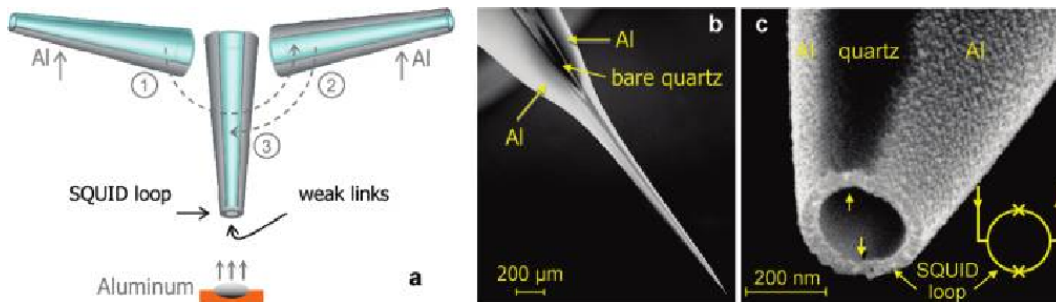


Figure 8.3: Figure taken from [128] illustrating the process of fabricating a SQUID on top (SOT) on a small hollow quartz tube.

figure 8.4(b) the detected vortices are shown. Red marks the vortices inside the selected area used to calculate the magnetization, blue marks the remaining vortices. The 80 vortices in an $3.6\mu\text{m} \times 10.6\mu\text{m}$ correspond to

$$B = \frac{80 * \phi_0}{3.6\mu\text{m} \times 10.6\mu\text{m}} \approx 43\text{G} \quad (8.4)$$

at an applied field of $H = 54\text{G}$.

A second approach can be used after the vortices have been detected. Once their coordinates are extracted, one employ the Delauny triangulation algorithm to find the next-neighbors. The algorithm first computes the Voronoi diagram, analog to constructing the Wigner–Seitz cell around each point. Its dual graph is the desired information, similar to connecting neighboring cells. The algorithm is not perfect and to prevent it from connecting vortices too far apart, which happens at the boundaries, a cutoff of $l_{\text{cutoff}} = 1.4\mu\text{m}$ (35pixel) was introduced. In figure 8.4(c) the result is shown, vortices with exactly 6 next-neighbors are colored red, while the once

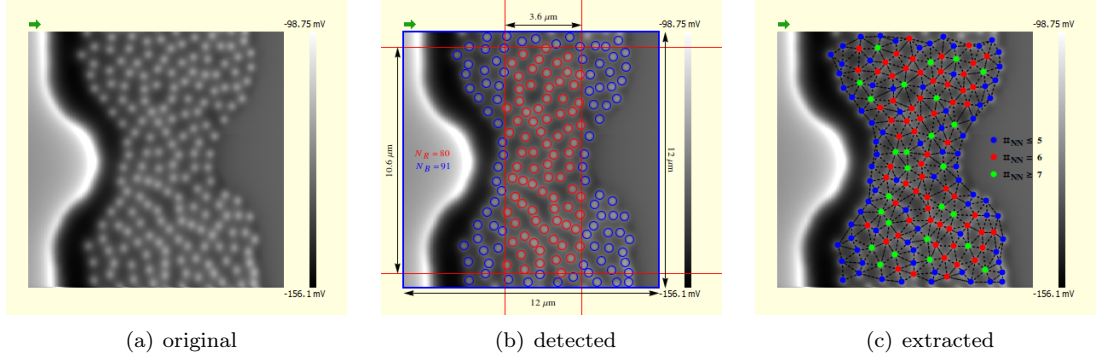


Figure 8.4: Measurements taken for $I = 12.2\text{mA}$ at $T = 4.2\text{K}$ in a magnetic field of $H = 54\text{G}$. Next to it are the images run through a vortex detection script. Plot 8.4(b) a square of $3.6\mu\text{m} \times 10.6\mu\text{m}$ was selected (being as big as possible while at the same time not including boundary effects) which contains 80 vortices. Summing up the magnetic flux of the vortices in that area results in a magnetic field $B \approx 43\text{G}$ at an applied field $H = 54\text{G}$. Plot 8.4(c) connects every vortex to its nearest neighbor (determined via Delaunay triangulation). The number of next neighbors $\#_{NN}$ determines their color as to highlight dislocations. This extracted map can be used to determine the average vortex distance. Shown is the non-moving vortex lattice, the case of moving vortices at higher current is shown in figure 8.6(b).

with less are blue and the once with more colored green. Notice the amount of dislocations (ignoring the boundaries). This gives a first impression of how far away the structure is from a normal hexagonal lattices that one would expect in a thin film sample without constrictions. The statistics give an average vortex–vortex distance (core to core) of

$$a_v = (0.76 \pm 0.16)\mu\text{m} > \Lambda_P > \lambda > \xi. \quad (8.5)$$

As an estimate we used Abrikosov’s lattice spacing formula $a_\Delta = (2/\sqrt{3})^{(1/2)}\sqrt{\phi_0/B}$, with $\phi_0 = 2.067833758(46) \times 10^{-15}\text{Wb}$ being the magnetic flux quantum and B the magnetic field.

$$B = \frac{2}{\sqrt{3}}\frac{\phi_0}{a_v^2} = (41 \pm 17)\text{G} \quad (8.6)$$

with an error bar that makes this value agree with previously determined value using the vortex density. The error bar is so high, since the lattice quite strongly deviates from the triangular lattice assumed by Abrikosov.

Pearl Vortices The rough size of a vortex as marked by circles in figure 8.4(b) (radius of 5 pixel, with $40\text{nm}/\text{pixel}$) can be read out as

$$r_v \approx 0.2\mu\text{m} \approx \Lambda_P \quad (8.7)$$

which is consistent with the expected value for the Pearl length. Indeed we are dealing with Pearl vortices in the Type I superconducting thin film.

8.2 Current–Voltage curves

The measured voltage as a function of the applied direct current for different magnetic fields is shown in figure 8.5. There are several features I want to point out. First, for currents below

a critical value $I_c(H)$ the measured voltage is of the order of the detection limit of the voltage measurements. The samples in this case are still in the superconducting phase. The vortices that entered the strips are still pinned, as can be seen by comparing the microscopic scan of the sample at $I = 12.2\text{mA}$ and $H = 54\text{G}$ from figure 8.4(a) to the measurement at a similar field 10.1. The current is well below the critical current, indicating no resistivity of the probe.

For currents above the critical current I_c we observe a non-vanishing voltage. The strip exhibits some measurable resistivity. As a reference, power-laws are plotted for the different data curves. One can see that the measurement for $H = 42\text{G}$, figure 8.5(a), exhibits a different power-law behavior than the rest. The curve for $H = 120\text{G}$ has a small “dip” and seems to follow a I^5 law right after the jump and then moves up to an I^{10} behavior. In general the behavior for $I > I_c$ is characterized by a power-law with an exponent $\alpha \gg 1$. We will try to give a plausible

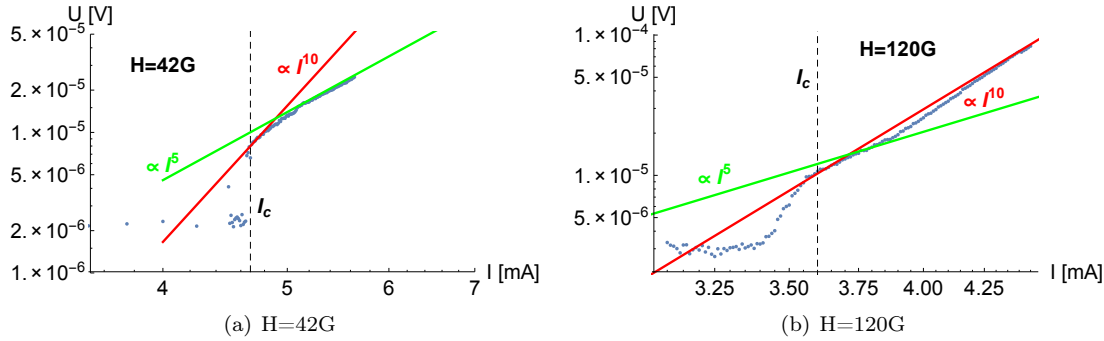


Figure 8.5: Measurements for the I–V curve for different magnetic fields. The red lines show a power-law with exponent 10, the green line a power-law with exponent 5.

model for such a power-law behavior in chapter 10.

8.3 Vortex dynamics

In chapter 11 we analytically discuss the problem of vortex line flow. Applying a current to the strip (running from bottom to top in the figure 8.6) applies a Lorentz force \mathbf{f}_l (per unit length) on the vortices perpendicular to the magnetic field and the current density $\mathbf{j}(\mathbf{r})$

$$\mathbf{f}_l = \frac{1}{c} \mathbf{j}(\mathbf{r}) \times \hat{\phi} \quad (8.8)$$

with the flux of the vortex $\hat{\phi} = \phi_0 \hat{z}$ and the flux quantum $\phi_0 = \frac{hc}{2e}$ in cgs units as discussed in, e.g. [123]. In the experiment shown in figure 8.6 this causes a force pushing the vortices from left to right, [132]. In the experiments several things can be observed. Below a certain critical current I_c the vortices form a fixed, non-moving state as can be seen in figure 8.6(a). If not explicitly stated otherwise we will use cgs units throughout this chapter. In a clean, disorder-free system, they form a triangular lattice, as first discussed by Abrikosov [124]. Deformations of the lattice can be due to the presence of disorder in form of impurities and an inhomogeneous force due to the current flowing through the constriction. The inhomogeneous current would cause a non-uniform compressing force on the lattice, which would in response reorganize in a non-trivial way, leading to the deformations. Taking the gray-scale image of the vortices as a height profile, a hill-climber algorithm can easily detect the vortices. Using Delaunay triangulation we can identify the next-neighbors of the vortices, illustrated in 8.6(a). Vortices with 6 next-neighbors, as expected in

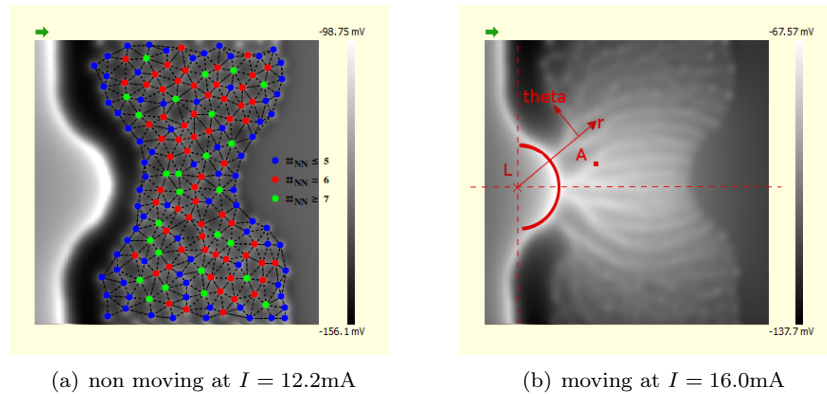


Figure 8.6: Experimental measurements of vortices, in a non moving 8.6(a) and moving 8.6(b) state. The applied current flows from bottom to top and the magnetic field is applied perpendicular to the image plane causing the vortices to experience a force from left to right [132]. In figure 8.6(a), vortices with 6 next-neighbors are colored in red. Blue marks vortices with less NN and green indicates vortices with more NN. Identification of the NN was done using the Delauny triangulation algorithm. Figure 8.6(a) is identical to figure 8.4(c) and is shown here for a better comparison to the moving case.

the triangular Abrikosov lattice, are colored in red. Blue indicated vortices with less and green marks vortices with more next-neighbors. With this coloring scheme it is easy to see that the observed static vortex configuration is strongly deformed compared to a plain triangular lattice.

Once the critical current I_c is exceeded, the vortices start to move from left to right as seen in figure 8.6(b). Two distinct features stand out. The vortices start to move in lines and bifurcation points such as the point labeled A in figure 8.6(b) appear. These are the two features we want to focus on in chapter 11.

9. Superconductivity

This chapter will give a brief introduction into the theoretical description of superconductivity with the focus on superconducting vortices. A successful microscopic theory for superconductivity was developed by Bardeen, Cooper and Schrieffer in 1957, [133], commonly referred to as the BCS theory of superconductivity. The basic idea behind the theory is that electrons form so called Cooper-pairs due to an attractive interaction caused by lattice deformations (phonons). These pairs of electrons are now of bosonic nature and can all occupy the same groundstate, forming the quantum state that is superconductivity. Despite its importance, we will not focus on the microscopic picture since the work done on superconductors in this part is based on the earlier macroscopic and phenomenological description by the Ginzburg–Landau theory and the London equations.

London–Equations

One of the first phenomenological descriptions of superconductivity was done by F. and H. London, [134], by proposing the two equations

$$\mathbf{E} = \tilde{\Lambda} \frac{\partial}{\partial t} \mathbf{j}_s \quad (9.1)$$

$$\mathbf{B} = -c\tilde{\Lambda} \nabla \times \mathbf{j}_s \quad (9.2)$$

for the microscopic electric field \mathbf{E} , magnetic field \mathbf{B} and the superconducting current \mathbf{j}_s . Here

$$\tilde{\Lambda} = \frac{4\pi\lambda^2}{c^2} = \frac{m}{n_s e^2} \quad (9.3)$$

was introduced as a phenomenological parameter, with λ being the penetration length, n_s the number density of superconducting electrons, the speed of light c and the electron mass m , [123]. In the discussion of superconductivity, we will use the cgs system. In combination with the Maxwell equation $\nabla \times \mathbf{B} = 4\pi\mathbf{j}/c$ we immediately get

$$\nabla^2 \mathbf{B} = \frac{1}{\lambda^2} \mathbf{B} \quad (9.4)$$

showing the exponential screening of the magnetic field inside the superconductor with the penetration depth λ , describing the Meissner effect, [123]. A simple derivation of these equations can be done based on the Drude model. This simple model explains resistance in a conductor via scattering of electrons, characterized by the scattering time-scale τ . The equations of motion for the electrons with mass m traveling with the speed \mathbf{v} in an external electric field \mathbf{E} is then phenomenologically described by

$$m \frac{d\mathbf{v}}{dt} = e\mathbf{E} - \frac{m}{\tau} \mathbf{v} \quad (9.5)$$

For the number of superconducting electrons, density n_s , the time between scattering events τ will go to infinity, $\tau \rightarrow \infty$. The superconducting current

$$\mathbf{j}_s = n_s e \mathbf{v} \quad (9.6)$$

can then be related to the electric field, using the Drude equation (9.5), resulting in the first London equation

$$\frac{d\mathbf{j}_s}{dt} = n_s e \frac{d\mathbf{v}}{dt} = \frac{n_s e^2}{m} \mathbf{E}, \quad (9.7)$$

as found in [123]. Another way to approach the derivation is by looking at the canonical momentum \mathbf{p} of the electrons in the presents of a magnetic field characterized by its vector potential \mathbf{A} via $\mathbf{B} = \nabla \times \mathbf{A}$ given as

$$\mathbf{p} = m\mathbf{v} + \frac{e}{c} \mathbf{A} \quad (9.8)$$

Without an electric field, the net momentum should be zero leading to

$$\langle \mathbf{v} \rangle = -\frac{e}{mc} \mathbf{A}. \quad (9.9)$$

The resulting relationship for the superconducting current density then becomes

$$\mathbf{j}_s = -\frac{1}{\Lambda c} \mathbf{A} \quad (9.10)$$

as, e.g. shown in [123]. Performing either the time derivative or the curl on equation (9.10), results in the two London equations. This compact form of the equations will be used throughout this work.

Ginzburg–Landau theory

Before the BCS–theory, in 1950 Ginzburg and Landau proposed a description of superconductivity based on the second order phase transition theory by Landau. For the order parameter of the system, they introduced a complex pseudo–wave function ψ , [123, 135]. The order parameter describes the density of the superconducting electrons n_s via

$$n_s = |\psi(x)|^2. \quad (9.11)$$

n_s is identical to the notation used for the London equations, [123]. The free energy f expanded in this order parameter in the framework of second order transitions

$$f = f_{n0} + \alpha |\psi|^2 + \frac{\beta}{2} |\psi|^4 + \frac{1}{2m^*} \left| \left(\frac{\hbar}{i} \nabla - \frac{e^*}{c} \right) \psi \right|^2 + \frac{1}{8\pi} \mathbf{B}^2 \quad (9.12)$$

yields the so called Ginzburg–Landau (GL) free energy for superconductivity, [123]. For $\psi = 0$ the theory reduces to the free energy of the normal conducting state $f_{n0} + \mathbf{B}^2/8\pi$. The gradient–term stems from the analogy of the pseudo-wave function ψ to an electron of charge e^* and mass m^* in a magnetic field. The GL–theory is a great success in describing the macroscopic phenomenon of the superconductivity including non-linear effects in the presents of strong fields, something the linear London–equations are not able to.

The connection to a microscopic picture came in 1959, when Gor’kov derived the phenomenological GL–free energy from the microscopic BCS–theory, [123, 136]. Initially it was expected that the parameters e^* and m^* were identical to the charge and mass of a single electron. Experimental data however suggested $e^* \approx 2e$. Once the microscopic connection to the BCS–theory was established the ambiguity could be removed and the values were connected to the charge and mass of the Cooper–pairs with $e^* = 2e$.

Varying the free energy we obtain the Ginzburg–Landau differential equations as

$$\alpha\psi + \beta|\psi|^2\psi + \frac{1}{2m^*} \left(\frac{\hbar}{i}\nabla - \frac{e^*}{c}\mathbf{A} \right)^2 \psi = 0 \quad (9.13)$$

$$\mathbf{j}_s = \frac{c}{4\pi}\nabla \times \mathbf{B} = \frac{e^*\hbar}{2m^*i}(\psi^*\nabla\psi - \psi\nabla\psi^*) - \frac{e^{*2}}{m^*c}\psi^*\psi\mathbf{A} \quad (9.14)$$

For a spatial constant order parameter $\psi(x) = \psi_{const}$, we see that the equation for the current density \mathbf{j}_s reduces to the London–equation, [123]. We will take the minimum value $\psi_{const}^2 = -\alpha/\beta > 0$ to rescale the first GL–differential equation (9.13) via $g = \psi/\psi_{const}$. In the absence of an applied field we have $\mathbf{A} = 0$ and the equation reduces to

$$\frac{\hbar^2}{2m^*|\alpha|} \frac{d^2g}{dx^2} + g - g^3 = 0. \quad (9.15)$$

We can now define a natural length scale ξ for the problem, being

$$\xi^2(T) = \frac{\hbar^2}{2m^*|\alpha(T)|}. \quad (9.16)$$

Generally ξ is referred to as the GL coherence length, [123]. Combined with the penetration length λ characterizing the system, we can define the dimensionless quantity

$$\kappa = \frac{\lambda}{\xi} \quad (9.17)$$

known as the Ginzburg–Landau parameter, [123]. The GL parameter was used by Abrikosov to classify superconductors in Type I and Type II separated by $\kappa = 1/\sqrt{2}$. The two different types of superconductors are further explained in the context of vortices in the following section.

9.1 Vortices

At a certain critical field H_c the energy gain from being in the superconducting state is less than the energy needed to exclude the field. Superconductivity breaks down and the sample becomes normal conducting. One distinguishes between two different types of superconductors. **Type I** superconductors are characterized by a simple critical field H_c , that marks the abrupt destruction of the superconducting field. Superconductors of **Type II** exhibit an intermediate phase. For $\kappa > 1/\sqrt{2}$ the surface energy of the domain walls separating normal and superconducting state is negative leading to a subdivision of the domains until the microscopic length scale ξ is reached, [123, 124]. Once a critical field H_{c1} is surpassed making the formation of small domains feasible, the magnetic field can partially enter the superconductor in form of vortices. With increasing magnetic field, the vortices will move closer and closer together. Once full field penetration is reached at H_{c2} superconductivity breaks down completely.

These vortices can form a lattice and, as we will discuss below, can be manipulated by an external current. In thin films they can be e.g. used to study melting and dynamical properties of 2D lattices and the absence and presence of disorder.

Bulk - Abrikosov vortices

In a Type II bulk superconductor the magnetic profile of a single vortex has been calculated by Abrikosov, [124]. For $\kappa \gg 1$ the order parameter ψ approaches ψ_{const} already at length scales

ξ away from the vortex core, [123]. Outside the vortex the superconductor is described by the London-equation, since $\psi \approx \psi_{const}$. They have to be modified in order to account for the normal conducting core of the vortex, carrying the magnetic flux quantum ϕ_0 , [123]. This can be done by modeling the vortex via a delta function $\delta_2(\mathbf{r}) = \delta(x)\delta(y)$ in the XY plane. The final equation is

$$\frac{4\pi\lambda^2}{c}\nabla \times \mathbf{j}_s + \mathbf{B} = \hat{z}\phi_0\delta_2(\mathbf{r}) \quad (9.18)$$

where \hat{z} is a unit vector pointing in the z -direction. Combined with Maxwell's equations $\nabla \times \mathbf{B} = 4\pi/c\mathbf{j}_s$ and $\nabla \cdot \mathbf{B} = 0$ we get the equation

$$\nabla^2 \mathbf{B} - \frac{1}{\lambda^2} \mathbf{B} = -\frac{\phi_0}{\lambda^2} \hat{z} \delta(\mathbf{r}) \quad (9.19)$$

describing the magnetic field of the vortex. The equation can be analytically solved with

$$\mathbf{B} = \frac{\phi_0}{2\pi\lambda^2} K_0\left(\frac{r}{\lambda}\right) \hat{z} \quad (9.20)$$

with K_0 being the Hankel function of imaginary argument, [123, 124]. The function $K_0(r/\lambda)$ cuts off exponentially for large distances, similar to the screening on the surface in the Meissner state.

$$B(r) \rightarrow \frac{\phi_0}{2\pi\lambda^2} \left(\frac{\pi\lambda}{2r}\right)^{1/2} e^{-r/\lambda} \quad r \rightarrow \infty \quad (9.21)$$

$$B(r) \approx \frac{\phi_0}{2\pi\lambda^2} \left[\ln \frac{\lambda}{r} + 0.12 \right] \quad \xi \ll r \ll \lambda \quad (9.22)$$

This makes the vortices and their current profile localized. When computing the vortex-vortex interaction, we will see that this leads to short range interaction that can be well approximated by just an interaction to the nearest vortex.

Thin film - Pearl vortices

In thin films of thickness $d \sim \lambda$, even Type I superconductors develop an intermediate phase with vortices. The magnetic profile of these vortices was calculated by Pearl in 1964, [125, 126]. This type of vortex is of main interest for us, the experiments by our collaborators were done on thin lead (Pb) films, which is a Type I superconductor. There are no immediate simplifications for the thin film systems, so we start from the full GL-theory

$$f = \int_{\mathbf{r}} \alpha |\psi(\mathbf{r})|^2 + \frac{\beta}{2} |\psi(\mathbf{r})|^4 + \frac{1}{2m^*} \left| \left(\frac{\hbar\nabla}{i} - \frac{e^*}{c} \mathbf{A}(\mathbf{r}) \right) \psi(\mathbf{r}) \right|^2 + \frac{1}{8\pi} \int_{\mathbf{r}} (\nabla \times (\mathbf{A}(\mathbf{r})))^2 \quad (9.23)$$

For an infinitely thin disk, the super current density is restricted to the $z = 0$ layer. This means that the superconducting order parameter $\psi(\mathbf{r})$ is zero outside the disk and can be written as

$$\psi(\mathbf{x}) = d\delta(z)\psi(r, \theta) \quad (9.24)$$

A variation with respect to $\mathbf{A}(\mathbf{r})$ leads to the differential equations

$$-\frac{1}{4\pi} \nabla \times (\nabla \times \mathbf{A}(\mathbf{r})) = \frac{d\delta(z)}{2m^*} \left\{ -\frac{e^*}{c} \left[\psi^* \frac{\hbar\nabla}{i} \psi - \psi \frac{\hbar\nabla}{i} \psi^* \right] + 2 \frac{e^{*2}}{c^2} \mathbf{A}(\mathbf{r}) |\psi|^2 \right\} \quad (9.25)$$

where the left-hand side is connected to the current density \mathbf{j} via the Maxwell equation

$$\nabla \times (\nabla \times \mathbf{A}) = \nabla \times \mathbf{B} = \frac{4\pi}{c} \mathbf{j} \quad (9.26)$$

Assuming a constant order parameter throughout the sample (analog to Pearl [125] or Fetter and Hohenberg [137]) we write

$$\psi(r, \theta) = \psi_0 e^{i\theta} \quad (9.27)$$

with $|\psi_0|^2 = n_s$ where n_s is the density of superconducting electrons. Now we can introduce the London penetration length λ and the flux quantum ϕ_0 according to [123] as well as the effective penetration length Λ

$$\lambda = \sqrt{\frac{m^* c^2}{4\pi n_s e^{*2}}} \quad \phi_0 = \frac{hc}{e^*} \quad \Lambda = \frac{2\lambda^2}{d} \quad (9.28)$$

With $\nabla = \hat{r}\partial_r + \frac{1}{r}\hat{\theta}\partial_\theta + \hat{z}\partial_z$ we can evaluate

$$\psi^* \frac{\nabla}{i} \psi - \psi \frac{\nabla}{i} \psi^* = 2|\psi_0|^2 \frac{1}{r} \hat{\theta} = 2n_s \frac{1}{r} \hat{\theta} \quad (9.29)$$

and the differential equation for the vector potential then reads as

$$-\nabla \times (\nabla \times \mathbf{A}(\mathbf{r})) = \frac{2}{\Lambda} \delta(z) \left\{ -\frac{n\phi_0}{2\pi r} \hat{\theta} + \mathbf{A}(\mathbf{r}) \right\} \quad (9.30)$$

The problem is rotational symmetric so the vector potential only has a $\hat{\theta}$ component and can be written as

$$\mathbf{A}(\mathbf{r}) = g(r, z) \hat{\theta} \quad (9.31)$$

with the reduced vector potential $g(r, z)$. This leads to a differential equation for $g(r, z)$ of the form

$$\left[\frac{\partial^2}{\partial z^2} + \frac{\partial}{\partial r} \frac{1}{r} \frac{\partial}{\partial r} r \right] g(r, z) = -\frac{4\pi}{c} j(r) \delta(z) = \frac{2}{\Lambda} \delta(z) \left[g(r, z) - \frac{\phi_0}{2\pi r} \right] \quad (9.32)$$

The differential equation can be solved using the Hankel transform and has the solution

$$g(r, z) = \frac{\phi_0}{2\pi} \int_0^\infty d\gamma \frac{J_1(\gamma r)}{1 + \Lambda\gamma} e^{-\gamma|z|} \quad (9.33)$$

and the current distribution

$$\mathbf{j}(r, z) = \frac{\phi_0 c}{4\pi} \hat{\theta} \delta(z) \int_0^\infty d\gamma \frac{\gamma}{1 + \Lambda\gamma} J_1(\gamma r) = \frac{\phi_0 c}{8\pi \Lambda^2} \delta(z) \hat{\theta} \left[H_1\left(\frac{r}{\Lambda}\right) - Y_1\left(\frac{r}{\Lambda}\right) - \frac{2}{\pi} \right] \quad (9.34)$$

as done by Pearl, [125, 126], with the Struve function H_n and the modified Bessel function Y_n .

9.2 Vortex interaction

Vortices are interacting with each other throughout the superconductor. Assuming that the order parameter approaches ψ_{const} fast outside the vortex-core, the governing equations can be taken as linear. In this case the magnetic field due to two vortices $\mathbf{B}(\mathbf{r})$ at the positions \mathbf{r}_1 and \mathbf{r}_2 is just the superposition of the simple vortex profile $\mathbf{B}_v(\mathbf{r})$. This can be written as

$$\mathbf{B}(\mathbf{r}) = \mathbf{B}_v(|\mathbf{r} - \mathbf{r}_1|) + \mathbf{B}_v(|\mathbf{r} - \mathbf{r}_2|). \quad (9.35)$$

Calculating the free energy per unit length f of the magnetic field

$$f = \frac{1}{8\pi} \int dS (\mathbf{B}^2 + \lambda^2 |\nabla \times \mathbf{B}|^2) \quad (9.36)$$

by integrating over the XY plane, [123]. Calculating the change in free energy Δf compared to just twice the field energy of a single vortex f_s is

$$\Delta f = f - 2f_s = \frac{\phi_0}{4\pi} B(|\mathbf{r}_1 - \mathbf{r}_2|) \quad (9.37)$$

a calculation done in detail e.g. by Tinkham [123]. We see that the interaction is repulsive. In the case of Abrikosov vortices, it is exponentially decaying like the magnetic profile of the vortices themselves, leading to a short range interaction. In the case of Pearl vortices, we are dealing with a long range interaction. Taking the vortices to be aligned on the x axis, we can compute the force per line in the x -direction acting on vortex 1 from vortex 2 as

$$\tilde{f}_x = -\frac{\partial \Delta f}{\partial x_2} = -\frac{\phi_0}{4\pi} \frac{\partial B(|\mathbf{r}_1 - \mathbf{r}_2|)}{\partial x_2} = \frac{\phi_0}{c} j_y(|\mathbf{r}_1 - \mathbf{r}_2|) \quad (9.38)$$

where the Maxwell equation $\nabla \times \mathbf{B} = 4\pi/c \mathbf{j}$ was used in the last step. The current density of the second vortex then applies a force on the first. In full vector form this is

$$\tilde{\mathbf{f}} = \frac{1}{c} \mathbf{j}(|\mathbf{r}_1 - \mathbf{r}_2|) \times (\phi_0 \hat{z}) \quad (9.39)$$

which can easily be extended to general current densities. The force per unit length on a vortex due to a current density \mathbf{j}_s is

$$\tilde{\mathbf{f}} = \frac{1}{c} \mathbf{j}_s \times \hat{\phi}_0 \quad (9.40)$$

with $\hat{\phi}_0 = \phi_0 \hat{z}$, [123].

10. Current–Voltage Curves

In this chapter we will explain the power–law behavior in the I–V curves that we saw in chapter 8 when presenting the data we are working with. In that chapter we saw that

$$V(I) \propto I^\alpha, \quad (10.1)$$

with $\alpha \sim 10$. We tried to understand the origin of the exponent α as an effect of vortices trying to overcome a surface barrier.

Breakdown of superconductivity

Before tackling the problem of the observed power–law behavior, we want to focus on the jump in voltage towards the end of the measurements. This can be seen in figure 10.1. The jump

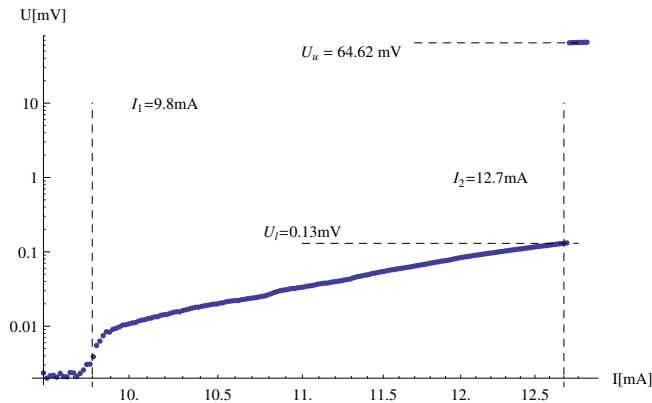


Figure 10.1: I–V curve for $H=57\text{G}$ on a constricted bridge shown in figure 8.1. Dashed lines mark $I_1 = 9.8\text{mA}$ and $I_2 = 12.7\text{mA}$

occurs over several orders of magnitude. As we will discuss in the next subsection, it is due to the break down of superconductivity due to high current densities. The strip enters the normal conducting state and heats up, changing its resistivity even more.

The critical temperature of lead (Pb) is $T_c = 7.2\text{K}$, [138]. Let us now calculate the resistance of the little lead strip on the break-down of superconductivity so we get a sense for the order of magnitude of the expected measured voltage. The resistivity for Pb at $T = 7.2\text{K}$ is $\rho_n(T = 7.2\text{K}) = 0.20\text{n}\Omega\text{m}$, as given in Landolt–Börnstein [139]. A picture of the bridge is shown in figure 8.1 with its measurements highlighted. The measured width is $w = 8.89\mu\text{m}$ and its length $\overline{AB} = 41.73\mu\text{m}$, $\overline{AC} = 53.70\mu\text{m}$ and a thickness of $d = 50\text{nm}$.

The geometric measurements and the important voltages from figure 10.1 are listed in table 10.1. The current density on the upper end of the bridge (above line A) drops rapidly since the Pb film widens immensely, so even if the critical current density is reached inside the bridge (causing the system to be normal conducting) the Pb film above line A will still be superconducting, therefore not contributing to the resistance.

The lower end (below line B) opens up rather quick, so that the current density inside the bridge drops to $8.98/15.59 \approx 0.58$ of its value. The I–V data with proper axis is shown in figure 10.1. Here, the current $I_1 = I_c = 9.8\text{mA}$ marks the first increase in voltage and $I_2 = 12.7\text{mA}$ marks a big jump of 3 orders of magnitude in the voltage. These correspond to the current densities $j_1 = 2.18 * 10^{10} \text{Am}^{-2}$ and $j_2 = 2.82 * 10^{10} \text{Am}^{-2}$ inside the bridge with the cross section $A = wd = 4.49 * 10^{-13} \text{m}^2$. A decrease by a factor of 0.58 puts the current-density j_2 below j_1 , $0.58 * j_2 < j_1$. There is no important contribution to the resistance after the line C.

SYMBOL	VALUE
d	50 nm
w	8.98 μm
w_2 (line C)	15.59 μm
$l = \overline{AB}$	41.73 μm
$l_2 = \overline{AC}$	53.70 μm
$n_v(H = 54\text{G})$	$2.096 * 10^{12} \text{m}^{-2}$
$B(H = 54\text{G}) = n_v \phi_0$	43 G
$\rho_n(T_c = 7.2\text{K})$	0.20 n Ωm
I_2	12.7 mA
U_d	0.13 mV
U_u	64.62 mV
$H_{c_2}^m(d = 90\text{nm}, T = 4.2\text{K}), [140]$	539 G

Table 10.1: Measurements for the constricted bridge as shown in figure 8.1.

The upper critical field H_{c_2} has been measured for a 90nm thick lead film with $T = 7.26\text{K}$ and $\kappa = 0.51$ and a $H_{c_2}^m = 539\text{G}$, [140]. As a first estimate, we ignore the hour-glass constriction. The resistance R_n at $T = 7.2\text{K}$ for the strip is then simply

$$R_n = \frac{l\rho_n}{dw} = \frac{41.73\mu\text{m} * 0.2\text{n}\Omega\text{m}}{8.98\mu\text{m} * 50\text{nm}} = 0.0186\Omega \quad (10.2)$$

At the current I_2 this would cause a Voltage

$$U_n = R_n I_2 = 0.236\text{mV} \quad (10.3)$$

The observed voltages are $U_l = 0.13\text{mV}$ for the lower end jumping to a value of $U_u = 64.62\text{mV}$ and we have

$$U_l < U_n < U_u. \quad (10.4)$$

This is consistent with the breakdown scenario. Once the superconductivity vanishes the strip will heat up, causing the resistivity of lead to increase above its $T = 7.2\text{K}$ value.

Simple scaling approach

In the previous subsections we have seen that the Voltage data for currents below the critical value I_c can be understood as pinned vortices that do not affect the conductivity of the system. There is a second critical current, where the voltage jumps up to an order of magnitude. We gave plausible indication that this is due to a breakdown of the superconductive state, leading to a normal resistance of the strip. The main focus of the following sections will be the power-law behavior of the Voltage in between these two critical values for the current.

The first approach is a simple dimensional analysis in order to make the experimental data dimensionless. We start by using Buckingham’s theorem to deduce some scaling relations for the experimental data. The simplest Ansatz is to assume that for fixed temperature, geometry and material properties each curve is just determined by the parameters $\{H, \phi_0, c, I, I_c\}$. ϕ_0 is the magnetic flux quantum and c the speed of light. For the V–I curves we get the simple form of

$$U \propto c\sqrt{\phi_0 H} f\left(\frac{I}{I_c}\right) \quad (10.5)$$

with a dimensionless function $f(x)$. The rescaled data is shown in figure 10.2(a). In figure 10.2(b) the curve for $H = 42\text{G}$ is lowered by an extra-factor of 0.8, so all the zero lines are aligned. In this case the curves for $H = 42\text{G}$ and $H = 120\text{G}$ align perfect in the region behind the critical current. The curves are not identical, but close. Adding the vortex density n_v as an

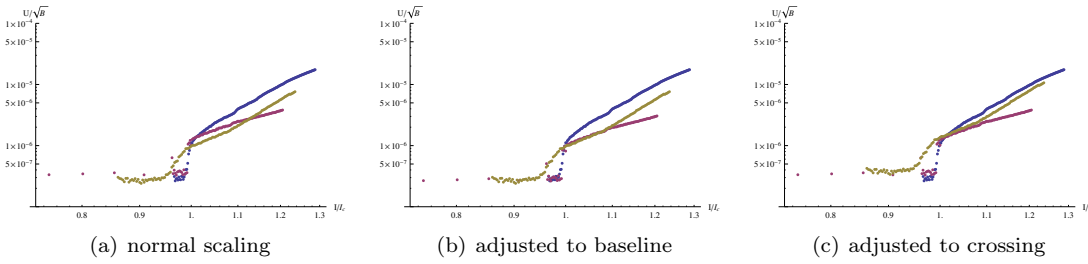


Figure 10.2: I–V measurements for different magnetic fields. Blue shows $H = 57\text{G}$, violet $H = 42\text{G}$ and beige $H = 120\text{G}$.

additional parameter (or likewise the magnetic induction B) will introduce another dimensionless quantity. The data should then match on a dimensionless function $f(x, y)$ dependent on two dimensionless parameters. However there is not enough data available thoroughly follow up on that advanced scaling approach. The simple scaling however is fairly good and shows that the data follows a similar pattern as

$$U \propto c\sqrt{\phi_0 H} \left(\frac{I}{I_c}\right)^\alpha \quad (10.6)$$

with an exponent $\alpha \sim 10$. Explaining the critical current is a difficult task, that we will not attempt here. One can see that it is different for every curve. Since all other characteristic parameters for the setup (length scales, possible impurity densities, temperature) are identical, the critical current is dependent on the applied magnetic field H and the magnetic induction B . The three data points cannot be connected by a simple power-law and a complex relation is to be expected.

We will focus on explaining the $\alpha \sim 10$ exponent.

10.1 Bardeen–Stephen flow

A superconducting vortex exposed to an external current feels a Lorentz force perpendicular to both the current and the applied field responsible for the vortices, [123]. The moving normal conducting core of the vortex will lead to energy dissipation just as in a regular conductor. The vortex itself will experience a resulting drag famously discussed by Bardeen and Stephen, [141].

The system can be described by three relations, describing the force \mathbf{F}_L acting on a single vortex due to the external current density \mathbf{j} , the relation of the vortex velocity \mathbf{v} as a function of

the force \mathbf{F}_L acting on it and the total electric field \mathbf{E} due to the movement of all vortices. We will chose the coordinate system such that the magnetic field $\mathbf{B} \parallel \hat{\phi}_0 \parallel \hat{z}$ and the current $\mathbf{j} \parallel \hat{y}$. The resulting vortex-movement $\mathbf{v} \parallel \hat{x}$ assuming that $\mathbf{v} \parallel \mathbf{F}_L$ for all $\mathbf{v}(\mathbf{F}_L)$. Using the cgs system we have the following equations describing the situation

$$\mathbf{F}_L = \frac{\phi_0 d}{c} \mathbf{j} \times \hat{z}, \quad \mathbf{v} = \mathbf{v}(\mathbf{F}_L), \quad \mathbf{E} = \frac{1}{c} \mathbf{B} \times \mathbf{v}. \quad (10.7)$$

The relation between the electric field and the velocity of the vortices can be explained by the Josephson relation $U = (1/c)\phi_0/(2\pi)\dot{\phi}$ relating the change in phase difference ϕ between two points P_1 and P_2 to a voltage difference. A vortex passing between the points separated by a distance l leads to an increase in the phase difference by 2π . The situation is as illustrated in figure 10.3. With a vortex density $n = B/\phi_0$ and the vortices traveling with \mathbf{v} perpendicular to

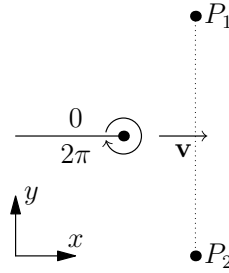


Figure 10.3: Schematic drawing of a vortex passing through the line between the points P_1 and P_2 causing a phase difference $\Delta\phi = 2\pi$ resulting in a voltage drop between P_1 and P_2 according to the Josephson relation $U = (1/c)\phi_0/(2\pi)\dot{\phi}$

the line $\overline{P_1 P_2}$ the average change in phase is $\delta\phi = 2\pi(B/\phi_0)lv\delta t$ leading to generated voltage of

$$U = \frac{\phi_0}{2\pi} \frac{\delta\phi}{\delta t} = Blv \quad (10.8)$$

The physics lays in the “reaction“ of the vortex velocity \mathbf{v} to the applied force \mathbf{F}_L on the vortex. In a clean sample this relationship is linear with a drag coefficient η as discussed by Bardeen and Stephen [141]

$$\eta = \phi_0 H_{c2}(0) \sigma_n / c^2 \quad (cgs) \quad (10.9)$$

$$\eta = \mu_0 \phi_0 H_{c2}(0) \sigma_n \quad (SI) \quad (10.10)$$

with the normal conductivity σ_n and the areal current density $j = I/(dw)$ with the thickness d , the width w of the system and area $A = dw$.

$$U = \mu_0 \phi_0 B \frac{Il}{A\eta} \quad \Rightarrow \quad \frac{U}{I} = \frac{B}{H_{c2}} \frac{l}{A} \sigma_n^{-1} = R_n \frac{B}{H_{c2}} \quad (10.11)$$

giving the $V(I)$ curve for free moving vortices in a magnetic field. Here the vortex density $n = B/\phi_0$ and the normal resistance of the strip $R_n = (l/A)\sigma_n^{-1}$. The simple free moving vortices lead to a linear V – I relation, i.e. $\alpha = 1$. In our case there obviously is a different mechanism at work that leads to $\alpha \sim 10$.

10.2 Surface barrier

We saw that simple free moving vortices lead to a linear relation between the measured voltage and the applied current, i.e. $\alpha = 1$. This theory however only looks at free moving vortices inside the sample. In the present experimental setup we are dealing with a small strip that has an hour–glass constriction. One effect that can produce the observed power–law behavior is due to vortices interacting with the boundary of the strip.

This type of surface barrier is known in the literature as the Bean–Livingston barrier, [142, 143]. The simple picture is the following. Close to the boundary of the strip the vortex will feel its mirror image or antivortex, similar to the mirror charges in electrostatic. There is no current flowing through the boundary, meaning that the normal component of the current density on the boundary vanishes. A condition that is satisfied by the vortex–antivortex pair construction. The applied current will try to push the vortex away from the boundary inside the sample. The antivortex counteracts and will push the vortex towards the boundary. The resulting potential barrier or activation energy E_A can be overcome by thermal fluctuations. Since the interaction between the vortex and its mirror image is logarithmic on short scales and the activation rate R being of Arrhenius form

$$R \propto \exp \left[-\frac{E_A}{k_b T} \right] \quad (10.12)$$

this will produce a power–law behavior for the resulting voltage. In this section, we will examine the resulting voltage response due to vortices entering the sample.

The vortex–vortex interaction for Pearl vortices has been calculated by Pearl [125] to be

$$V(r') = \frac{\phi_0^2}{2\Lambda\mu_0} \left[H_0 \left(\frac{r}{\Lambda} \right) - Y_0 \left(\frac{r}{\Lambda} \right) \right] \quad (10.13)$$

in SI units with the Struve function H_n and the modified Bessel function of the second kind Y_n . $\Lambda = 2\lambda^2/d$ is the effective penetration depth. The interaction force has the form

$$F_{12}(r') = -\frac{\phi_0^2}{2\Lambda^2\mu_0} \left[H_1 \left(\frac{r'}{\Lambda} \right) - Y_1 \left(\frac{r'}{\Lambda} \right) - \frac{2}{\pi} \right]. \quad (10.14)$$

The potential can be expanded around the limiting cases for $r \ll \Lambda$ and $r \gg \Lambda$, as shown in [144].

$$V(r) = \begin{cases} \frac{\phi_0^2}{\pi\mu_0\Lambda} \ln \left(1.135 \frac{\Lambda}{r} \right) & : \frac{r}{\Lambda} \ll 1 \\ \frac{\phi_0^2}{\mu_0\pi r} & : \frac{r}{\Lambda} \gg 1 \end{cases}$$

They can be combined into an interpolation formula

$$V(r) \approx \frac{\phi_0^2}{\pi\mu_0\Lambda} \ln \left(1.135 \frac{\Lambda}{r} - \frac{0.135\Lambda}{4.5\Lambda + r} + 1 \right). \quad (10.15)$$

as shown by Brandt, [144]. Note that the equation used by Brandt use a definition of the penetration length Λ without the factor of 2. The interpolation formula is very accurate and is used since it is easier to handle than the Struve and Bessel function. For later convenience, we will introduce the characteristic energy scale of the interaction

$$E_0 = \frac{\phi_0^2}{\pi\mu_0\Lambda} \quad (10.16)$$

As the coordinate system, we will choose the applied magnetic field perpendicular to the strip in the z -direction and the current moving in the y -direction as shown in figure 10.4. The Lorentz

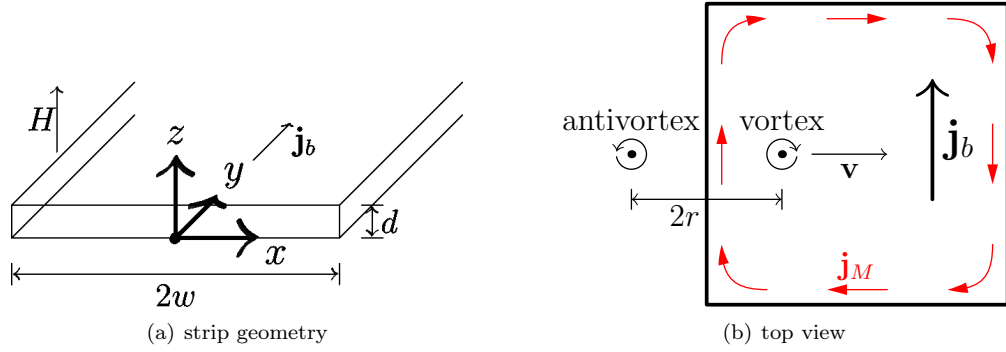


Figure 10.4: Schematic of the superconducting strip. The current flows in the y -direction \mathbf{j}_b pushing the vortices in the positive x -direction with the speed \mathbf{v} . The system reacts to the applied field \mathbf{H} by creating the Meissner current (red) to expel the magnetic field from the inside of the sample.

force $\mathbf{F}_L(\mathbf{x})$ acting on a vortex caused by the current density $\mathbf{j}(\mathbf{x})$ in this case leads to

$$\mathbf{F}_L(\mathbf{x}) = d\mathbf{j}(\mathbf{x}) \times \hat{\phi}_0 = dj(\mathbf{x})\phi_0 \hat{x}, \quad (10.17)$$

as previously discussed or derived in [123]. We will denote the distance from the surface to the vortex by r . The interaction with the antivortex is governed by the vortex–vortex interaction where the distance between them in this notation is $2r$. Additionally the current-distribution inside the sample $\mathbf{j}(r)$ pulls the vortex in the x -direction. The work done on the vortex W is

$$W = \int_0^r dr' F_L(r') = d\phi_0 \int_0^r dr' j(r') \quad (10.18)$$

The potential barrier for one vortex, dependent on the vortex position r is then given by

$$V_{\text{Barrier}}(r) = -V(2r) - \int_0^r dr' F_L(r') \quad (10.19)$$

Note that the interaction potential for the vortex–antivortex has the negative sign of the vortex–vortex interaction.

Simple current model

The current density $\mathbf{j}(r)$ consists of two contributions. First contribution is the applied current, fed in through the experiment. Second contribution comes from the Meissner current. The applied magnetic field induces a Meissner current oriented in a way to expel the applied field from the superconductor. Both effects and their internal distribution are important in determining the activation energy of the vortices. As we will later discuss in more detail, these profiles are non trivial and can complicate the calculation. To get a first idea of the order of magnitude of the resulting exponents let us start with a simple model for the current distribution. Neglecting the Meissner current completely we will assume a constant $\mathbf{j}(r) = j_0\hat{y}$ current density close to the surface. The resulting energy model for the surface barrier is similar to the one studied by Burlachkov et al. for pancake vortices in high T_c superconductors, [145], being

$$V_{\text{Barrier}}(r) = -E_0 \ln \left(1.135 \frac{\Lambda}{2r} - \frac{0.135\Lambda}{4.5\Lambda + 2r} + 1 \right) - dj_0\phi_0 r \quad (10.20)$$

The difference lies in the interaction strength of the logarithmic term, since we are dealing with Pearl vortices in this scenario. The current density flowing through the sample is assumed to be constant for the time being, identical to the profile used by Burlachkov et al. Later we will use a more realistic current profile for the thin films.

Looking at the interaction profile, we see that the stronger the applied current, the smaller the distance needed to achieve enough energy to separate the vortex from its mirror image. The equilibrium distance r_0 will therefore be smaller for higher applied current densities j_0 . Assuming a strong enough current, so that the separation process will happen close to the surface, i.e. $r_0 \sim \mathcal{O}(\Lambda)$ the surface barrier can be simplified to

$$V_{\text{Barrier}}(r) \approx -E_0 \ln \left(1.135 \frac{\Lambda}{2r} \right) - dj_0 \phi_0 r \quad (10.21)$$

The maximum of the potential is reached at the equilibrium distance r_0 of

$$r_0 = \frac{E_0}{dj_0 \phi_0} \quad (10.22)$$

leading to an activation energy

$$E_A = E_0 \ln \left(\frac{2E_0}{1.135\Lambda dj_0 \phi_0} \right) - E_0 \quad (10.23)$$

The Arrhenius type penetration rate R is then proportional to

$$R \propto \exp \left[-\frac{E_A}{k_b T} \right] = e^{E_0} \left(\frac{1.135\Lambda dj_0 \phi_0}{2E_0} \right)^{\frac{E_0}{k_b T}} \propto I^\alpha \quad (10.24)$$

with the exponent

$$\alpha = \frac{E_0}{k_b T} \quad (10.25)$$

Plugging in the values for Λ in our system we get

$$E_0 = \frac{\phi_0^2}{\mu_0 \pi \Lambda} = \begin{cases} 2.4 \times 10^5 \text{K} & : \Lambda = 330 \text{nm} \\ 4.6 \times 10^5 \text{K} & : \Lambda = 170 \text{nm} \end{cases}$$

The resulting exponent for the current dependency for temperatures around $T = 4.2\text{K}$ is

$$\alpha \sim 10^5 \quad (10.26)$$

several orders of magnitude larger than the observed $\alpha \approx 10$. To obtain an exponent of the observed magnitude the temperature would have to exceed the bulk melting temperature $T \approx 600\text{K}$ of Pb by orders of magnitude. For the material value see table E.1. The expected heating effects close to the second jump in voltage, as seen in figure 10.1 and discussed in the previous sections, will not change the discrepancy in the exponents. The large exponent is similar to the one for the theory of thermal activated flux creep as discussed in literature, [143, 145–147].

Current distribution inside the strip

In the previous part, we used a constant current profile, mainly for its simplicity. Let us now focus more on the actual current distribution inside the thin strip. In the absence of vortices and an applied current, only the Meissner current is present. We consider the strip thickness d to

be small enough so that the current distribution along the z -axis can be treated as homogenous. For a strip of width $2w$ going from $-w$ to w in the x -direction. The current profile is known to be

$$j_M(x) = -\frac{2Hx}{d\sqrt{w^2 - x^2}} \quad (10.27)$$

as can be found in e.g. [148–156]. The current profile exhibits a characteristic square-root divergence towards the surface of the film, when $x \rightarrow \pm w$. In the presence of vortices, magnetic flux was able to penetrate into the thin film. Averaged over scales larger than the vortex size, this leads to the magnetic induction B inside the sample. The Meissner current now only has to compensate the reduced field $H' = H - B/\mu_0$.

The total transport current I flowing through the strip is distributed as

$$j_T(x) = \frac{I}{\pi d\sqrt{w^2 - x^2}} \quad (10.28)$$

also discussed in [148]. The work W done by the current moving the vortex by the distance r away from the outer border at $-w$ is written as

$$W = d\phi_0 \int_{-w}^{-w+r} dr' (j_M(r') + j_T(r')) \quad (10.29)$$

As discussed earlier, the surface barrier is now written as

$$V_{\text{Barrier}}(r) = -V(2r) - W \quad (10.30)$$

In the case of strong enough currents, the equilibrium position r_0 will be small, i.e. of the order $\mathcal{O}(\Lambda)$ and the interaction potential can be simplified as $V(2r) \approx E_0 \ln(1.135 \frac{\Lambda}{2r})$. The condition for the equilibrium position $\partial_r V_{\text{Barrier}}(r)|_{r_0} = 0$ results in the equation

$$\frac{E_0}{r_0} = \frac{2H'(w - r_0)}{\sqrt{r_0(2w - r_0)}} + \frac{I}{\pi\sqrt{r_0(2w - r_0)}}. \quad (10.31)$$

Expanding the right hand side of the equation for small r_0 we obtain

$$\frac{E_0}{r_0} \approx \phi_0 \left(\frac{I}{\pi\sqrt{2w}} + \sqrt{2wH'} \right) \frac{1}{\sqrt{r_0}}, \quad (10.32)$$

with the equilibrium distance

$$r_0 \approx \left(\frac{E_0}{\frac{\phi_0 I}{\pi\sqrt{2w}} + \sqrt{2wH'} \phi_0} \right)^2. \quad (10.33)$$

The activation energy then works out to be

$$E_A = E_0 \ln \left(\frac{2r_0}{1.135\Lambda} \right) - \phi_0 I - 2\phi_0 H' \sqrt{r_0(2w - r_0)} + \phi_0 I \arccos \left(\frac{r_0}{w} - 1 \right). \quad (10.34)$$

The applied total currents are of the order of $\sim 10\text{mA}$. The energy of the current is of the same order as E_0 with

$$\phi_0 I \sim 1.5 \cdot 10^5 \text{K}. \quad (10.35)$$

For small equilibrium positions r_0 , we can expand the expression for E_A as

$$E_A = E_0 \ln \left(\frac{2r_0}{1.135\Lambda} \right) - 2\phi_0 H' \sqrt{2wr_0} - \frac{\phi_0 I \sqrt{r_0}}{\pi \sqrt{w}}, \quad (10.36)$$

leading to the simple form of

$$E_A = E_0 \ln \left(\frac{2r_0}{1.135\Lambda} \right) - 2E_0. \quad (10.37)$$

The penetration rate then yields

$$\begin{aligned} R &\propto \exp \left[-\frac{E_A}{k_b T} \right] = e^{2 \frac{E_0}{k_b T}} \left(\frac{1.135\Lambda}{2r_0} \right)^{\frac{E_0}{k_b T}} \\ &\propto \left(\frac{1.135\Lambda}{2E_0^2} \left(\frac{\phi_0 I}{\pi \sqrt{2w}} + \sqrt{2w} H' \phi_0 \right)^2 \right)^{\frac{E_0}{k_b T}} \end{aligned} \quad (10.38)$$

Interestingly enough the exponent $\propto I^\alpha$ in this case is larger by a factor of 2 compared to the constant current assumption

$$\alpha = 2 \frac{E_0}{k_b T} \quad (10.39)$$

The geometry of the setup makes the system even more sensitive to the current, which leads to a higher exponent α . A more accurate description of the current distribution actually increases the exponent. Additionally including geometric effects from the hour-glass construction will not reduce the exponent.

Possible screening of vortex–vortex interaction

The thermally activated entering of the vortices into the strip is able to produce a power-law response of the voltage to the applied current. However the theory predicts an exponent $\alpha = 2E_0/k_b T$ that is several orders of magnitude higher than the observed value of $\alpha \sim 10$. A process that can reduce the interaction strength E_0 would reduce the exponent. Screening effects due to spontaneously created vortex–antivortex pairs could be one possible mechanism to reduce E_0 . Thermally created pairs would screen the interaction, similar to the RG for the Coulomb–gas picture of the XY model, [10]. However there are two problems with this approach. Screening effects take place on large scales. On short distances $r \sim \Lambda$ the effects will be slim. Second, the energy cost to create a pair compared to the thermal energy is too large to be possible.

The core energy of a vortex has been calculated by Pearl, and according to [126, 157] is

$$E_v = E_0 \left[\ln \left(\frac{\Lambda}{r_c} \right) + \frac{1}{24} \left(\frac{r_c}{\xi} \right)^2 \right] \quad (10.40)$$

with E_0 being the energy-scale of the interaction, the size of the vortex core r_c and the correlation length ξ . We already computed the interaction strength to be

$$E_0 = \frac{\phi_0^2}{\mu_0 \pi \Lambda} = \begin{cases} 2.4 \times 10^5 \text{K} & : \Lambda = 330 \text{nm} \\ 4.6 \times 10^5 \text{K} & : \Lambda = 170 \text{nm} \end{cases}$$

Taking the vortex–size to be of the order of the correlation length ξ , we get a pre-factor

$$E_v = E_0 \times \begin{cases} 1.93 & : \Lambda = 330 \text{nm} \\ 1.27 & : \Lambda = 170 \text{nm} \end{cases}$$

Making the core energy several orders of magnitude larger than the thermal energy $T = 4.2\text{K}$. Screening effects due to thermal activated vortex–antivortex pairs is therefor impossible.

10.3 Discussion

In this chapter we have looked into the conductivity measurements done on the constricted bridge setup. The characteristic curve as shown in figure 10.1 features 3 distinct scenarios. For low currents we have no measurable voltage. The strip is still in the superconducting phase at $T = 4.2\text{K} < T_c = 7.2\text{K}$ and vortices are pinned, as seen in figure 8.4(a). After the vortices are depinned, a power–law behavior in the voltage of the form

$$U \propto I^\alpha \tag{10.41}$$

was observed, with an exponent of $\alpha \sim 10$. This was followed by a jump in the voltage that we could trace back to a thermal quench in the system, where the strip was becoming normal conducting again.

The main focus lay in finding an explanation for the power-law behavior with the exponent $\alpha \sim 10$. We saw that thermal activated vortices surmounting a surface barrier will lead to a power–law behavior. However the predicted exponent $\alpha \sim 10^5$ for this theory was several orders of magnitude larger than the observed one. Even including the internal distribution of the current inside the thin strip did not change the discrepancy. Quite the opposite. The internal current distribution makes the system more sensitive to the current than a simple constant distribution. The resulting exponent is even larger by a factor of 2.

The energy scale of the current $\phi_0 I \sim E_0$ is of the same order as the vortex interaction strength and core energy of the vortices. The next step would have been to look more detailed into the effect of possible pair creation inside the sample due to the current and its effect on the V–I curves. The geometry and local impurities in the surface itself can also reduce the surface barrier and change the power-law behavior compared to the simple model used so far. At this point however, the collaboration was focusing mainly on the vortex dynamics and we stopped exploring additional modifications to the surface barrier model. The data on the voltage measurements were too thin to extract more qualitative features other than the relative large exponent $\alpha \sim 10$. The experimental setup in general was geared towards the vortex dynamics. Especially the hour–glass constriction in the strips complicates the voltage curve analysis. The surface barrier model successfully explains the power–law, but due to time constraints we were not able to identify the missing contributions that produce the right order of magnitude for the exponent α .

11. Vortex Dynamics

In this chapter we will discuss the case of the moving vortices. Once the vortices start moving, they do so in lines, following each other. It is this line-formation that we want to focus on further. We will start with general symmetry considerations of the experimental setup. This will motivate the chosen Corbino disk setup introduced in the following section. The approach for the next sections will be as follows. First we will simplify the geometry to make a theoretical approach easier yet still contain the inhomogeneous current density we believe to play a crucial role. We will then try and solve the distribution of an applied current and the response to the setup to an external field. Once the current density profile is known we will try and combine this knowledge with the vortices in the sample and their effect on the current. To do so, we tried several different approaches, including the description as a non-local theory and a multitude of simplified analytic models.

11.1 The Corbino disk setup

Looking more closely at the measurements, especially figure 8.6(b), we can make several observations. The flow-line pattern is almost mirror-symmetric along the line through the narrowest parts of the constriction (dashed line in figure 8.6(b)), following the strip symmetry. To make a discussion easier, let us introduce polar coordinates on the left border (L) of the constriction with the radial vector \hat{r} and the tangential unit vector $\hat{\theta}$ as illustrated in figure 8.6(b). There is no current passing through the borders of the strip, meaning the current component perpendicular to the border in r -direction vanishes and the current is flowing parallel to them in the θ -direction. The vortices are pushed perpendicular to the current, equation (8.8), radially outwards in r -direction, with the separation between vortices in θ -direction growing. One mechanism contributing to the flow line pattern and the formation of the bifurcation points is obviously the inhomogeneous current density due to the sample geometry.

The constricted strip geometry used in the experiment (figure 8.6) is difficult to treat theoretically. We consider the simpler Corbino disk geometry as shown in figure 11.1, which is identical to the system considered by Ketchen et al. [158]. It consists of an annular superconducting ring of thickness d with an inner radius R_1 and an outer radius R_2 in the XY plane at $z = 0$ and its center at the origin. Its rotational symmetry simplifies the treatment and allows for a tangential current that will apply a radially force to the vortices.

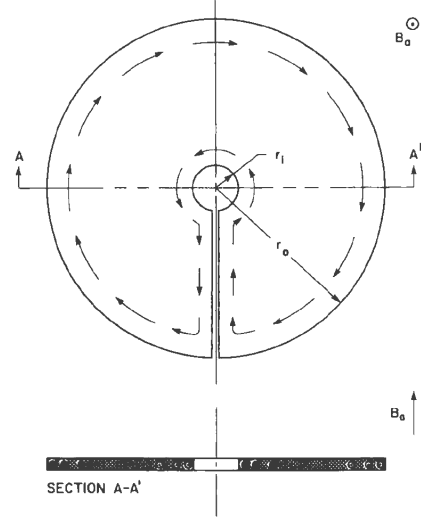
The additional modification suggested in [158], consists of a small (low inductance) slit connecting the inner hole with the outside. This makes it possible to feed a tangential current I into the system and additionally allows the magnetic field to enter the inner ring. The current will be applied to flow counter clockwise (mathematical positive direction). Beyond these effects, the slit will not be considered, i.e. the system will be treated as rotationally symmetric.

The disk is placed in a homogenous magnetic field $\mathbf{B}_a = B_a \hat{z}$ parallel to the \hat{z} direction, or in cylinder coordinates (with the unit vectors \hat{r} , \hat{z} and $\hat{\theta}$)

$$\mathbf{B}_a = B_a \hat{z} = \nabla \times \mathbf{A}_a \qquad \mathbf{A}_a(\mathbf{r}) = \frac{1}{2} r B_a \hat{\theta} \qquad (11.1)$$

In the Meissner state a shielding current is induced that flows counter clockwise around the inner hole and clockwise along the outer border as sketched in figure 11.1. The whole system is

Figure 11.1: Corbino disk configuration as considered in our calculations. The figure is taken from [158]. In our notation the inner radius is labeled with R_1 while the outer radius is R_2 . The disk lies in the XY plane at $z = 0$ with an applied magnetic field $\mathbf{B}_a = B_a \hat{z}$ parallel to the \hat{z} direction. The small slit allows the magnetic field to enter the hole and makes it possible to feed in an external tangential current I into the system. The direction of the shielding current induced by the magnetic field in the Meissner state is sketched by the black arrows.



rotationally symmetric and the resulting \mathbf{B} of the system has no $\hat{\theta}$ component nor a θ -dependency. This means we can write the magnetic field of the system \mathbf{B} as

$$\mathbf{B}(\mathbf{r}) = B_r(r, z)\hat{r} + B_z(r, z)\hat{z} \quad (11.2)$$

which is satisfied by the following ansatz for the vector potential

$$\mathbf{A}(\mathbf{r}) = A_\theta(r, z)\hat{\theta}. \quad (11.3)$$

In the limits far away from the sample, the field is equal to the applied field, which makes it convenient to introduce the reduced vector potential $f(r, z)$ as

$$A_\theta(r, z) = f(r, z) + \frac{1}{2} r B_a \quad (11.4)$$

with the condition that $f(r, z)$ vanishes far away from the sample, i.e.

$$\lim_{z \rightarrow \pm\infty} f(r, z) = 0, \quad \lim_{r \rightarrow \infty} f(r, z) = 0. \quad (11.5)$$

This reduces the whole discussion of the system to the determination of the vector potential $f(r, z)$, which is connected to the current distribution via the Maxwell equation

$$\nabla \times \mathbf{B} = \frac{4\pi}{c} \mathbf{j}(\mathbf{r}). \quad (11.6)$$

The current density $\mathbf{j}(\mathbf{r})$ of the system is made to flow counter clockwise and consists only of a tangential component in $\hat{\theta}$ -direction. Approximating the film by a $\delta(z)$ -thin sheet, it can be written as

$$\mathbf{j}(r, z) = j(r)\delta(z)\hat{\theta}. \quad (11.7)$$

The system itself is described by the Maxwell and London equations discussed in the previous chapter 9. This leads to a differential equation for the reduced vector potential $f(r, z)$

$$\left[\frac{\partial^2}{\partial z^2} + \frac{\partial}{\partial r} \frac{1}{r} \frac{\partial}{\partial r} r \right] f(r, z) = -\frac{4\pi}{c} j(r)\delta(z) = \begin{cases} \frac{2}{\Lambda} \delta(z) \left[f(r, z) + \frac{B_a r}{2} - \frac{n\phi_0}{2\pi r} \right], & R_1 \leq r \leq R_2, \\ 0, & \text{elsewhere.} \end{cases} \quad (11.8)$$

A detailed derivation of this equation is shown in appendix F.2.

11.2 The current distribution in the Corbino disk

The current density $j(r)$ is determined by the differential equation (11.8). Due to its linear nature, we can treat the inhomogeneous terms separately. Imagine the scenario where there is no applied field, $B_a = 0$, but a current $I \neq 0$ in the disk. The current circling the hole produces a net magnetic field inside it, which is identical to a trapped flux. Vice versa, a trapped flux inside the Corbino disk is accompanied with a current profile $j(r)$ around it and therefore a finite current I . We see that the two are equivalent and we can think of the current I fed into the system as a trapped flux $\phi_f = n\phi_0$ inside the ring. The other scenario we consider is an applied field $B_a \neq 0$ without a current, $I = 0$. Here, the superconducting disk, in its Meissner phase, tries to expel the magnetic field inducing a shielding current that flows around the outsides of the disk as shown in figure 11.1. No net current is present and no flux is trapped in the inner ring. The full current $j(r)$ then splits into the two contribution $j_\phi(r)$ and $j_B(r)$. The current $j_\phi(r)$ is due to the trapped flux ϕ_f in the hole of the disk and the current $j_B(r)$ due to the magnetic field without a trapped flux. The relation of the densities to the total current I is given as

$$I = \int_{R_1}^{R_2} dr j(r), \quad j(r) = j_\phi(r) + j_B(r). \quad (11.9)$$

It is easier to discuss the effects separately.

There are several known analytic results. One is the case of a superconducting sheet with a hole ($R_2 \rightarrow \infty$) in the perfect diamagnetic state, i.e. $\Lambda = 0$. Here, the current density $j_\phi(r)$ is given as

$$j_\phi(r) = \frac{\phi_f c}{4\pi^2} \frac{1}{r\sqrt{r^2 - R_1^2}} \Theta(r - R_1) \quad (11.10)$$

and as has been calculated by Ketchen et. al. [158] by mapping to an electrostatic problem. The second known case is that of a perfect diamagnetic disk in a magnetic field, [158], giving us

$$j_B(r) = -\frac{B_a c}{\pi^2} \frac{r}{\sqrt{R_2^2 - r^2}} \Theta(R_2 - r). \quad (11.11)$$

Lastly, we have the famous result by Pearl, which is equivalent to a trapped flux in a thin film ($R_1 \rightarrow 0$ and $R_2 \rightarrow \infty$) that results in the current density $j_P(r)$ for the Pearl vortex as

$$j_P(r) = \frac{\phi_0 c}{8\pi\Lambda^2} \left[H_1\left(\frac{r}{\Lambda}\right) - Y_1\left(\frac{r}{\Lambda}\right) - \frac{2}{\pi} \right] \approx \frac{\phi_f c}{4\pi^2} \frac{1}{r(r + \Lambda)}, \quad (11.12)$$

which can be found in [137]. Here $H_n(x)$ is the Struve function and $Y_n(x)$ the modified Bessel function. In appendix F.3 we show that all these known limiting cases are indeed analytic solutions to the differential equation (11.8). We do this by transforming the differential equation to an integral equation which can then be solved in aforementioned limits, see appendix F.2.

On the basis of the integral equations and the known limiting cases, we can construct an approximate profile of the current density. A more detailed discussion of the literature and the known approximate profiles is done in appendix F.1. The first approximate profile is with a set of free parameters $\{c_0, c_1, c_2\}$ can be written down as

$$j_\phi(r) = \frac{\phi_f c}{4\pi^2} \frac{c_0 + c_1 \frac{r}{R_2} + c_2 \frac{r^2}{R_2^2}}{r\sqrt{(r + R_1 + \Lambda)(r - R_1 + \Lambda)}\sqrt{(1 - \frac{r}{R_2} + \frac{\Lambda}{R_2})(1 + \frac{r}{R_2} + \frac{\Lambda}{R_2})}} \Theta(r - R_1) \Theta(R_2 - r). \quad (11.13)$$

It satisfies the known limiting cases. Computing

$$\lim_{R_1 \rightarrow 0} \lim_{R_2 \rightarrow \infty} j_\phi(r) = \frac{\phi_f c}{4\pi^2} \frac{c_0}{r(r + \Lambda)} \quad (11.14)$$

we see that it turns into the approximate Pearl solution for $c_1 = 1$ and for

$$\lim_{\Lambda \rightarrow 0} \lim_{R_2 \rightarrow \infty} j_\phi(r) = \frac{\phi_f c}{4\pi^2} \frac{c_0}{r\sqrt{r^2 - R_1^2}} \quad (11.15)$$

the solution becomes exact for $c_0 = 1$. The approximate current profile for the response to an magnetic field uses the free parameters $\{d_0, d_1, d_2, d_4\}$ and is given by

$$j_B(r) = -\frac{B_a c}{4\pi} \frac{R_2 \left(d_0 + d_1 \frac{r}{R_2} + d_2 \frac{r^2}{R_2^2} + d_4 \frac{r^4}{R_2^4} \right)}{\sqrt{(r + R_1 + \Lambda)(r - R_1 + \Lambda)} \sqrt{\left(1 - \frac{r}{R_2} + \frac{\Lambda}{R_2}\right) \left(1 + \frac{r}{R_2} + \frac{\Lambda}{R_2}\right)}} \Theta(r - R_1) \Theta(R_2 - r). \quad (11.16)$$

Computing again the the limiting case to verify that it indeed satisfies the known limiting conditions, we get

$$\lim_{\Lambda \rightarrow 0} \lim_{R_1 \rightarrow 0} j_B(r) = -\frac{B_a c R_2^2 \left(d_0 + d_1 \frac{r}{R_2} + d_2 \frac{r^2}{R_2^2} + d_4 \frac{r^4}{R_2^4} \right)}{4\pi r \sqrt{R_2^2 - r^2}}. \quad (11.17)$$

This is the exact solution of the problem for $d_0 = d_1 = d_4 = 0$ and $d_2 = 1$. The numerical procedure we use to determine the coefficients $\{c_0, c_1, c_2\}$ and $\{d_0, d_1, d_2, d_4\}$ is discussed at length in appendix F.4. Once the coefficients are determined, the condition for the total current in the system from equation (11.9) will be used to fix ϕ_f .

11.3 Non-local theory

Now that we have a very accurate model of the current distribution inside the disk, the next task is adding the superconducting vortices. On approach we followed is illustrated in this section. Outside the disk we are only dealing with free fields. The idea here is to take the full 3D Maxwell equation for the magnetic field and integrate out the part outside the disk. This will create a purely 2D theory with the trade off being non-local interactions in the fields. The calculation follows the procedure in reducing the dimensionality of the Hamiltonian as outlined by Radzihovsky, [159]. The hope is to use this 2D theory and use it as a more convenient jump off point in connecting the current distribution to the penetrating vortices.

Starting from a free-field system, we want to integrate out all the bulk degrees of freedom to obtain an effective system only with degrees of freedom in the $z = 0$ plane. Ignoring dynamical effects $\dot{\mathbf{A}} = 0$ the Hamiltonian reduces to

$$H = \frac{1}{8\pi} \int d^3x (\mathbf{B} - \mathbf{B}_a)^2 \quad (11.18)$$

in cgs units. Introducing the vector potential \mathbf{A} as

$$\mathbf{B} = \nabla \times \mathbf{A} \quad (11.19)$$

in order to write the theory simpler terms. Starting with the case of no applied field $\mathbf{B}_a = 0$, we are dealing with the simplified theory

$$H = \frac{1}{8\pi} \int d^3x (\nabla \times \mathbf{A})^2. \quad (11.20)$$

In order to perform the partial integration we need the following two identities

$$\begin{aligned} (\nabla \times \mathbf{A})^2 &= (\epsilon_{ijk} \partial_j A_k \hat{e}_i) (\epsilon_{lmn} \partial_m A_n \hat{e}_l) = \epsilon_{ijk} \epsilon_{lmn} (\partial_j A_k) (\partial_m A_n) \\ (\nabla \times \nabla \times \mathbf{A}) \mathbf{A} &= (\nabla \times \nabla \times \mathbf{A})_n A_n = \epsilon_{nmi} \partial_m (\nabla \times \mathbf{A})_i A_n = -\epsilon_{ijk} \epsilon_{imn} (\partial_m \partial_j A_k) A_n \end{aligned}$$

We can see that the two expressions can be made identical by partial integration. The theory for the free field can then be written as

$$H = \frac{1}{8\pi} \int d^3x (\nabla \times \mathbf{A})^2 = \frac{1}{8\pi} \int d^3x (\nabla \times \nabla \times \mathbf{A}) \mathbf{A} = -\frac{1}{8\pi} \int d^3x (\nabla^2 \mathbf{A}) \mathbf{A} \quad (11.21)$$

where we have used the Coulomb gauge $\nabla \cdot \mathbf{A} = 0$. Now we want to Fourier transform the system and afterward integrate out all degrees of freedom outside the $z = 0$ plane, leaving an effective 2D system. For this we want to introduce the following notation

$$\mathbf{x} = (\mathbf{r}, z) \quad \mathbf{q} = (\mathbf{k}, \omega) \quad \mathbf{A}_p(\mathbf{r}) = \mathbf{A}(\mathbf{r}, z = 0) \quad (11.22)$$

where \mathbf{x} and \mathbf{q} are related via the Fourier transform. The final system should only be \mathbf{r} dependent and is described by the 2D plane vector potential $\mathbf{A}_p(\mathbf{r})$. The Fourier transformed Hamiltonian reads as

$$\beta H = \frac{\beta}{8\pi} \int \frac{d^3q}{(2\pi)^3} \mathbf{q}^2 \mathbf{A}_q \mathbf{A}_{-\mathbf{q}} \quad (11.23)$$

$$= \frac{1}{2} \int_{\mathbf{q}} \int_{\mathbf{q}'} \mathbf{A}_q \mathcal{G}(\mathbf{q}, \mathbf{q}') \mathbf{A}_{\mathbf{q}'} \quad (11.24)$$

$$\mathcal{G}(\mathbf{q}, \mathbf{q}') = \frac{\beta}{4\pi} \frac{1}{(2\pi)^3} \mathbf{q}^2 \delta(\mathbf{q} + \mathbf{q}') \quad (11.25)$$

Here the integral notation $\int_{\mathbf{q}} = \int d^3q$ has been used. We already included the factor $\beta = 1/k_b T$, since we will be using βH in the partition function Z of the system.

$$Z = \int \mathcal{D}[\mathbf{A}] e^{-\beta H} \quad (11.26)$$

Introducing the degrees of freedom in the $z = 0$ plane, \mathbf{A}_p , via a delta distribution

$$Z = \int \mathcal{D}[\mathbf{A}] \int \mathcal{D}[\mathbf{A}_p] \delta(\mathbf{A}(\mathbf{r}, z = 0) - \mathbf{A}_p(\mathbf{r})) e^{-\beta H} = \int \mathcal{D}[\mathbf{A}_p] e^{-\beta H_p} \quad (11.27)$$

$$e^{-\beta H_p} = \int \mathcal{D}[\mathbf{A}] \delta(\mathbf{A}(\mathbf{r}, z = 0) - \mathbf{A}_p(\mathbf{r})) e^{-\beta H} \quad (11.28)$$

we can obtain our boundary Hamiltonian H_p . It will be living only in the $z = 0$ plane, once the integration over $\int \mathcal{D}[\mathbf{A}]$ is performed. This can be evaluated by using the Fourier representation of the δ -distribution for the Fourier components of the degrees of freedom.

$$\mathbf{A}_p(\mathbf{r}) \rightarrow \mathbf{A}_p(\mathbf{k}) \quad (11.29)$$

$$\mathbf{A}(\mathbf{x}) \rightarrow \mathbf{A}_q \quad (11.30)$$

$$\mathbf{A}(\mathbf{r}, z = 0) \rightarrow \int \frac{d\omega}{2\pi} \mathbf{A}_q \quad (11.31)$$

$$\delta(\mathbf{A}_p - \mathbf{A}(\mathbf{r}, z = 0)) \rightarrow \int \mathcal{D}[\lambda_{\mathbf{k}}] e^{i \int_{\mathbf{k}} \lambda_{\mathbf{k}} (\mathbf{A}_p(\mathbf{k}) - \int \frac{d\omega}{2\pi} \mathbf{A}_q)} \quad (11.32)$$

For the Boundary Hamiltonian we get the following relations based on the partition function

$$e^{-\beta H_p} = \int \mathcal{D}[\mathbf{A}] \int \mathcal{D}[\lambda_{\mathbf{k}}] \exp \left[-\frac{1}{2} \int_{\mathbf{q}} \int_{\mathbf{q}'} \mathbf{A}_{\mathbf{q}} \mathcal{G}(\mathbf{q}, \mathbf{q}') \mathbf{A}_{\mathbf{q}'} - i \int_{\mathbf{q}} \frac{\lambda_{\mathbf{k}}}{2\pi} \mathbf{A}_{\mathbf{q}} + i \int_{\mathbf{k}} \lambda_{\mathbf{k}} \mathbf{A}_p(\mathbf{k}) \right] \quad (11.33)$$

Here we can perform the integration over the $\mathbf{A}_{\mathbf{q}}$ components, since they form a quadratic theory.

$$e^{-\beta H_p} = \int \mathcal{D}[\lambda_{\mathbf{k}}] \exp \left[-\frac{1}{2} \int_{\mathbf{q}} \int_{\mathbf{q}'} \lambda_{\mathbf{k}} \frac{1}{(2\pi)^2} \mathcal{G}^{-1}(\mathbf{q}, \mathbf{q}') \lambda_{\mathbf{k}'} + i \int_{\mathbf{k}} \lambda_{\mathbf{k}} \mathbf{A}_p(\mathbf{k}) \right] \quad (11.34)$$

The inverse of \mathcal{G} can be calculated to be

$$\mathcal{G}^{-1}(\mathbf{q}, \mathbf{q}') = \frac{1}{\beta} 4\pi(2\pi)^3 \frac{1}{\mathbf{q}^2} \delta(\mathbf{q} - \mathbf{q}') \quad (11.35)$$

The new fields and therefore $\lambda_{\mathbf{k}}$ are not dependent on z (and equivalently ω). We can perform the integration over ω , effectively integrating out all degrees of freedom not in the $z = 0$ plane. Introducing the new effective Green's function $\tilde{\mathcal{G}}$ via

$$\tilde{\mathcal{G}}^{-1}(\mathbf{k}, \mathbf{k}') = \int_{\omega} \int_{\omega'} \frac{1}{(2\pi)^2} \mathcal{G}^{-1}(\mathbf{q}, \mathbf{q}') = \frac{1}{\beta} 8\pi^2 \int d\omega \frac{1}{\mathbf{k}^2 + \omega^2} \delta(\mathbf{k} + \mathbf{k}') \quad (11.36)$$

$$= \frac{(2\pi)^3}{\beta} \frac{1}{|\mathbf{k}|} \delta(\mathbf{k} + \mathbf{k}') \quad (11.37)$$

$$\tilde{\mathcal{G}}(\mathbf{k}, \mathbf{k}') = \frac{\beta}{(2\pi)^3} |\mathbf{k}| \delta(\mathbf{k} + \mathbf{k}') \quad (11.38)$$

Finally after integrating over $\lambda_{\mathbf{k}}$ we are left with

$$e^{-\beta H_p} = e^{-\frac{1}{2} \int_{\mathbf{k}} \int_{\mathbf{k}'} \mathbf{A}_p(\mathbf{k}) \tilde{\mathcal{G}}(\mathbf{k}, \mathbf{k}') \mathbf{A}_p(\mathbf{k}')} \quad (11.39)$$

$$H_p = \frac{1}{(4\pi)} \int \frac{d^2 k}{(2\pi)^2} |\mathbf{k}| \mathbf{A}_p(\mathbf{k}) \mathbf{A}_p(-\mathbf{k}) \quad (11.40)$$

Now all that is left is to perform the back transformation into position space. This results in a non-local interaction with a $|\mathbf{r}|^{-3}$ dependency, similar to the dipole-dipole interaction energy of two magnetic dipoles \mathbf{m}_1 and \mathbf{m}_2

$$E = \frac{\mathbf{m}_1 \mathbf{m}_2}{r^3} - \frac{3(\mathbf{m}_1 \hat{r})(\mathbf{m}_2 \hat{r})}{r^3} \quad (11.41)$$

Now we will connect the calculation done on the free field to the full Ginzburg-Landau theory for the superconductor. With the order parameter living only in the $z = 0$ plane, meaning $\psi(\mathbf{x}) = d\delta(z)\psi(\mathbf{r})$, the full Ginzburg-Landau Hamiltonian (see e.g. [123]) is of the form

$$H_f = \int_{\mathbf{r}} \frac{d}{2m^*} \left| \left(\frac{\hbar \nabla}{i} - \frac{e^*}{c} \mathbf{A}_p(\mathbf{r}) \right) \psi(\mathbf{r}) \right|^2 - \frac{1}{8\pi^2} \int_{\mathbf{r}} \int_{\mathbf{r}'} \frac{\mathbf{A}_p(\mathbf{r}) \mathbf{A}_p(\mathbf{r}')}{|\mathbf{r} - \mathbf{r}'|^3} \quad (11.42)$$

where $C = -\frac{1}{8\pi^2}$ is a numerical constant coming from the Fourier back-transform of the interaction $\sim |\mathbf{k}|$ and the system lives in the $z = 0$ plane with $\mathbf{r} = (x, y)$, coming from

$$\frac{1}{(4\pi)} \int \frac{d^2 k}{(2\pi)^2} |\mathbf{k}| e^{i\mathbf{k}\mathbf{r}} = \frac{1}{(4\pi)} \int_0^{2\pi} \frac{d\phi}{2\pi} \int_0^\infty \frac{dk}{2\pi} k^2 e^{ikr \cos(\phi)} = \frac{1}{8\pi^2} \int_0^\infty dk k^2 J_0(|kr|) \quad (11.43)$$

where we have to introduce a converging factor $e^{-\epsilon k}$ with $\epsilon > 0$ to force convergence, since the integral itself diverges.

$$\frac{1}{8\pi^2} \int_0^\infty dk k^2 J_0(|kr|) e^{-\epsilon k} = \frac{1}{8\pi^2} \frac{2\epsilon^2 - r^2}{(r^2 + \epsilon^2)^{5/2}} \quad (11.44)$$

$$\rightarrow -\frac{1}{8\pi^2} \frac{1}{r^3} \quad (11.45)$$

Thus the pre-factor $C = -\frac{1}{8\pi^2}$. A negative sign in front of the interaction energy seems strange and is due to the regularization via the converging factor. Using the radial symmetry of our problem $\mathbf{A}_p(\mathbf{r}) = A(r)\hat{\theta}$ one can reduce the interaction to

$$\int_{\mathbf{r}} \int_{\mathbf{r}'} \frac{\mathbf{A}_p(\mathbf{r})\mathbf{A}_p(\mathbf{r}')}{|\mathbf{r} - \mathbf{r}'|^3} = \int_r \int_{r'} A(r)K(r, r')A(r') \quad (11.46)$$

$$K(r, r') = \int_0^{2\pi} d\theta \frac{rr' \cos(\theta)}{\left(\sqrt{r^2 + r'^2 - 2rr' \cos(\theta)}\right)^3} \quad (11.47)$$

Since $K(\omega, \omega')$ or $K^{-1}(r, r')$ are not known, integrating out the parts of $r < R_1$ and $r > R_2$ to obtain our Corbino disk geometry, will not be possible.

Variation of Hamiltonian Now let us see what the effect of the integration procedure has on the saddle point equation of the Ginzburg–Landau theory. Taking the Hamiltonian from equation (11.42) and performing the variation in respect to ψ^* and \mathbf{A}_p leads to the equations

$$\left(\frac{\hbar\nabla}{i} - \frac{e^*}{c}\mathbf{A}_p(\mathbf{r})\right)^2 \psi(\mathbf{r}) = 0 \quad (11.48)$$

$$\frac{d}{2m^*} \left\{ -\frac{e^*}{c} \left[\psi^* \frac{\hbar\nabla}{i} \psi - \psi \frac{\hbar\nabla}{i} \psi^* \right] + 2\frac{e^{*2}}{c^2} \mathbf{A}_p(\mathbf{r}) |\psi|^2 \right\} = \frac{1}{4\pi^2} \int_{\mathbf{r}'} \frac{\mathbf{A}_p(\mathbf{r}')}{|\mathbf{r} - \mathbf{r}'|^3} \quad (11.49)$$

Following the standard assumptions, e.g. found in Tinkham, [123], we will assume a constant order parameter throughout the sample with $|\psi|^2 = n_s$. The London penetration depth is $\lambda = \sqrt{\frac{m^* c^2}{4\pi n_s e^{*2}}}$, the effective penetration-depth $\Lambda = \frac{2\lambda^2}{d}$ and the flux quantum $\phi_0 = \frac{hc}{e^*}$, [123]. Here the effective charge of the Cooper-pair is labeled by e^* . The saddle point equation for the vector potential transforms to

$$\left[\left\{ -\frac{1}{4\pi} \frac{2}{\Lambda} \frac{\phi_0}{4\pi} \left[\psi^* \frac{\nabla}{i} \psi - \psi \frac{\nabla}{i} \psi^* \right] \right\} + \frac{1}{4\pi} \frac{2}{\Lambda} \mathbf{A}_p(\mathbf{r}) \right] \Theta(r - R_1) \Theta(R_2 - r) = \frac{1}{4\pi^2} \int_{\mathbf{r}'} \frac{\mathbf{A}_p(\mathbf{r}')}{|\mathbf{r} - \mathbf{r}'|^3} \quad (11.50)$$

and can eventually be simplified to

$$\frac{2}{\Lambda} \left\{ -\frac{\phi_0}{4\pi} \left[\psi^* \frac{\nabla}{i} \psi - \psi \frac{\nabla}{i} \psi^* \right] + \mathbf{A}_p(\mathbf{r}) \right\} \Theta(r - R_1) \Theta(R_2 - r) = \frac{1}{\pi} \int_{\mathbf{r}'} \frac{\mathbf{A}_p(\mathbf{r}')}{|\mathbf{r} - \mathbf{r}'|^3} \quad (11.51)$$

The order parameter then takes on the form of

$$\psi(\mathbf{r}) = \psi(0) e^{i\theta} \quad (11.52)$$

and in polar coordinates with $\nabla = \hat{r}\partial_r + \frac{1}{r}\hat{\theta}\partial_\theta + \hat{z}\partial_z$ we can simplify the theory as

$$\frac{2}{\Lambda} \left\{ -\frac{\phi_0}{2\pi} \frac{1}{r} \hat{\theta} + \mathbf{A}_p(\mathbf{r}) \right\} \Theta(r - R_1) \Theta(R_2 - r) = \frac{1}{\pi} \int_{\mathbf{r}'} \frac{\mathbf{A}_p(\mathbf{r}')}{|\mathbf{r} - \mathbf{r}'|^3} \quad (11.53)$$

Note that the main result of the integration procedure is the non–local interaction. However its dipole like nature with the $\sim \frac{1}{r^3}$ dependency, makes it rather complicated. Additionally the divergence for $\mathbf{r} = \mathbf{r}'$ make a numerical treatment of this equation also very difficult to the point that this approach unfortunately did not turn out to be as fruitful as hoped.

11.4 Simple model for current–vortex interaction

The structure of the differential equations show the difficulties and complexity of the problem. In trying to get some insight into the problem of the moving vortices in a Corbino disk driven by a current I , we will now try and approach it by building a simplified model. We will start with a simple model trying to explore the competition between the current as a driving force and the interaction between the vortices in the disk.

With an applied field $H > H_{c1}$ and in the absence of a current, the vortices form a triangular lattice with the lattice spacing $a_B = \sqrt{\frac{\phi_0}{B}}$, with the flux quantum $\phi_0 = \frac{hc}{2e}$ (in cgs units). Averaging over distances larger than a_B , the magnetic induction due to the vortices in the the Corbino disk can be written as a smooth rotationally symmetric function $B(r) = \phi_0 n(r)$. According to the theory of vortex motion by Bardeen and Stephen the energy dissipation of a moving vortex leads to an overall resistivity $\rho = \rho_n \frac{B}{H_{c2}}$, [141]. For a varying vortex density $n(r)$ we can write

$$\rho(r) = \rho_n \frac{B(r)}{H_{c2}} = \rho_n \frac{\phi_0}{H_{c2}} n(r) \quad (11.54)$$

where ρ_n is the resistivity of the sample in the normal conducting state and H_{c2} the upper critical field when superconductivity breaks down. The idea now is to compute the resistivity of the full disk as a function of the vortex density to quantify the energy dissipation due to the vortices. To do so, we think of the Corbino disk as an assembly of small rings with width Δr in a parallel circuit. The conductance $g(r)$ for each ring is

$$g(r) = \sigma(r) \frac{d \Delta r}{2\pi r} = \sigma_n \frac{H_{c2}}{\phi_0} \frac{d \Delta r}{2\pi r n(r)} \quad (11.55)$$

with $\sigma_n^{-1} = \rho_n$ and d being the thickness of the disk. The total conductance G_{tot} in this case is the sum of conductance of each ring. For infinitesimal small rings the sum changes to an integration.

$$G_{\text{tot}} = \sum_r g(r) \rightarrow \sigma_n \frac{d H_{c2}}{2\pi \phi_0} \int_{R_1}^{R_2} dr \frac{1}{r n(r)} \quad (11.56)$$

The energy lost in the “circuit”, P , due to the applied current I is

$$P = UI = R_{\text{tot}} I^2 = G_{\text{tot}}^{-1} I^2 \quad (11.57)$$

which is energy dissipation of the resistor per time. Using cgs units, the resistivity $[\rho_n] = T$ is the time scale related to the electron phonon scattering. For a quasi static picture let us compare the energy lost in the resistor due to vortex motion to the overall energy in the lattice. We will use ρ_n as the appropriate time scale. This leads to the energy contribution of the current

$$H_I = R_{\text{tot}} I^2 \rho_n = \frac{2\pi \phi_0 \rho_n^2 I^2}{d H_{c2}} \frac{1}{\int_{R_1}^{R_2} dr \frac{1}{r n(r)}} \quad (11.58)$$

Measuring the length and density in terms of a_B we can introduce the dimensionless quantities

$$r = a_B \tilde{r} \qquad n(r) = \frac{1}{a_B^2} \tilde{n}(\tilde{r}) \qquad (11.59)$$

turning the energy due to the vortex motion into

$$H_I = \frac{E_I}{\int_{\tilde{R}_1}^{\tilde{R}_2} d\tilde{r} \frac{1}{\tilde{r}\tilde{n}(\tilde{r})}} \qquad E_I = \frac{2\pi\phi_0\rho_n^2 I^2}{dH_{c2}a_B^2} \qquad (11.60)$$

with E_I being the characteristic energy scale of the contribution.

Interaction energy Now we want to construct a simple model for the vortex–vortex interaction in order to compare it to the energy loss model. The interaction energy of the vortices with an interaction potential $V(r)$ dependent only on the distance between the vortices is

$$H_\phi = \int d^2r \int d^2r' n(\mathbf{r})V(|\mathbf{r} - \mathbf{r}'|)n(\mathbf{r}') \qquad (11.61)$$

in the most general case. The interaction between the vortices is logarithmic on small scales $r \sim \Lambda$, with Λ being the effective penetration depth of the system, and falls off with $\sim \frac{1}{r}$ for larger scales. The full repulsive interaction between two vortices and a good approximation are given by equation (10.15). The full interaction was found by Pearl [125, 137] and the approximate formula is due to Brandt [144]¹. For a first simple picture, let us ignore the long range nature of the interaction. The characteristic length scale for the interaction is then simply the vortex distance a_B . The vortex densities is assumed constant in the region of size πa_B^2 around the position \mathbf{r} . Using the Heaviside theta function $\theta(x)$ we can approximate the interaction potential with $V(r) = V(a_B)\theta(a_B - r)$. The most simple form of a short range interaction is therefore given by

$$H_\phi \approx V(a_B)\pi a_B^2 \int d^2r n^2(\mathbf{r}) = V(a_B)2\pi^2 a_B^2 \int_{R_1}^{R_2} dr r n^2(r) = 2\pi^2 V(a_B) \int_{\tilde{R}_1}^{\tilde{R}_2} d\tilde{r} \tilde{r} \tilde{n}^2(\tilde{r}) \qquad (11.62)$$

with $E_\phi = 2\pi^2 V(a_B)$ being the energy scale for the interaction. E_ϕ can be approximated as

$$E_\phi \approx \frac{1}{2} \frac{\phi_0^2}{a_B} \qquad a_B \gg \Lambda \qquad (11.63)$$

$$E_\phi \approx \frac{1}{2} \frac{\phi_0^2}{\Lambda} \ln\left(\frac{1.135\Lambda}{a_B}\right) \qquad a_B \ll \Lambda \qquad (11.64)$$

Ignoring the long–range nature of the interaction is a rather crude approximation. For thick disks or cylinders however, where we are dealing with Abrikosov vortices, the interaction is exponentially screened. In this case the approximation is expected to be much more accurate. It will however give us a first insight into the competition of interaction versus current contribution.

¹Brandt [144] works with SI units and the definition $\Lambda = \frac{\lambda^2}{d}$ is missing a factor of 2 as opposed to our definition of $\Lambda = \frac{2\lambda^2}{d}$

Interaction vs. Current Without entry or exit barriers in the system the total energy is simply the sum of the interaction energy and the loss due to the applied current

$$H[\tilde{n}(\tilde{r})] = \frac{E_I}{\int_{\tilde{R}_1}^{\tilde{R}_2} d\tilde{r} \frac{1}{\tilde{r}\tilde{n}(\tilde{r})}} + E_\phi \int_{\tilde{R}_1}^{\tilde{R}_2} d\tilde{r} \tilde{r}\tilde{n}^2(\tilde{r}) \quad (11.65)$$

with the following constraints

$$\int_{R_1}^{R_2} dr r n(r) = \frac{N}{2\pi} \quad n(r) \geq 0 \quad \forall R_1 \leq r \leq R_2 \quad (11.66)$$

N is the number of vortices in the sample. The first constraint can be added to the energy via a Lagrange multiplier γ . Varying the energy in respect to $\tilde{n}(\tilde{r})$ yields

$$\frac{\delta H}{\delta \tilde{n}(\tilde{r})} = E_I \frac{1}{\left(\int_{\tilde{R}_1}^{\tilde{R}_2} d\tilde{r} \frac{1}{\tilde{r}\tilde{n}(\tilde{r})}\right)^2} \frac{1}{\tilde{r}\tilde{n}^2(\tilde{r})} + 2E_\phi \tilde{r}\tilde{n}(\tilde{r}) + \gamma \tilde{r} = 0 \quad (11.67)$$

However finding a solution to this is quite difficult, especially with the additional restriction of $n(r) \geq 0$. In the cases for $E_I = 0$ or $E_\phi = 0$ the solutions are $n(r) \propto \frac{1}{r}$ and $n(r) = \text{const}$ respectively. Using these two cases we can construct a test profile

$$\tilde{n}_\alpha(\tilde{r}) = \alpha \frac{N}{\pi(\tilde{R}_2^2 - \tilde{R}_1^2)} + (1 - \alpha) \frac{N}{2\pi(\tilde{R}_2 - \tilde{R}_1)\tilde{r}} \quad (11.68)$$

with the free parameter α . The condition $n(r) \geq 0$ forces the monotonic profile to be greater or equal to zero at R_1 and R_2 resulting to the constriction on α as

$$-\frac{R_2 + R_1}{R_2 - R_1} \leq \alpha \leq \frac{R_2 + R_1}{R_2 - R_1} \quad (11.69)$$

Plugging the test profile $\tilde{n}_\alpha(\tilde{r})$ into our energy functional results in

$$H_\alpha = E_I f_I(\alpha) + E_\phi f_\phi(\alpha) \quad (11.70)$$

$$f_I(\alpha) = \left(\int_{\tilde{R}_1}^{\tilde{R}_2} d\tilde{r} \frac{1}{\tilde{r}\tilde{n}_\alpha(\tilde{r})} \right)^{-1} = \frac{\alpha N}{\pi(\tilde{R}_1 - \tilde{R}_2)(\tilde{R}_1 + \tilde{R}_2) \ln \left(\frac{\alpha\tilde{R}_1 + \tilde{R}_1 - \alpha\tilde{R}_2 + \tilde{R}_2}{-\alpha\tilde{R}_1 + \tilde{R}_1 + \alpha\tilde{R}_2 + \tilde{R}_2} \right)} \quad (11.71)$$

$$f_\phi(\alpha) = \int_{\tilde{R}_1}^{\tilde{R}_2} d\tilde{r} \tilde{r}\tilde{n}_\alpha^2(\tilde{r}) = \frac{N^2 \left(2(\alpha - 2)\alpha(\tilde{R}_1 - \tilde{R}_2) + (\alpha - 1)^2(\tilde{R}_1 + \tilde{R}_2) \ln \left(\frac{\tilde{R}_2}{\tilde{R}_1} \right) \right)}{4\pi^2(\tilde{R}_1 - \tilde{R}_2)^2(\tilde{R}_1 + \tilde{R}_2)} \quad (11.72)$$

To get an idea of the energy landscape and the minimum density configuration, different scenarios for $N = 200$, $\tilde{R}_1 = 10$, $\tilde{R}_2 = 1000$ are shown in figure 11.2. As we can see, when the interaction energy is bigger than the current energy $E_\phi > E_I$, figure 11.2(b), the minimum α is slightly above one, referring to a vortex distribution that decreases towards the inner ring R_1 and approaches a constant profile near R_2 , figure 11.2(a). Increasing the current shows the emergence of a second minimum, figure 11.2(c). If only the current is present, i.e. $E_\phi = 0$, we get an even more pronounced second minimum at negative α , figure 11.2(d). We can also see that $\alpha = 0$, referring to the $n(r) \sim 1/r$ case, is actually the maximum energy configuration of the system.

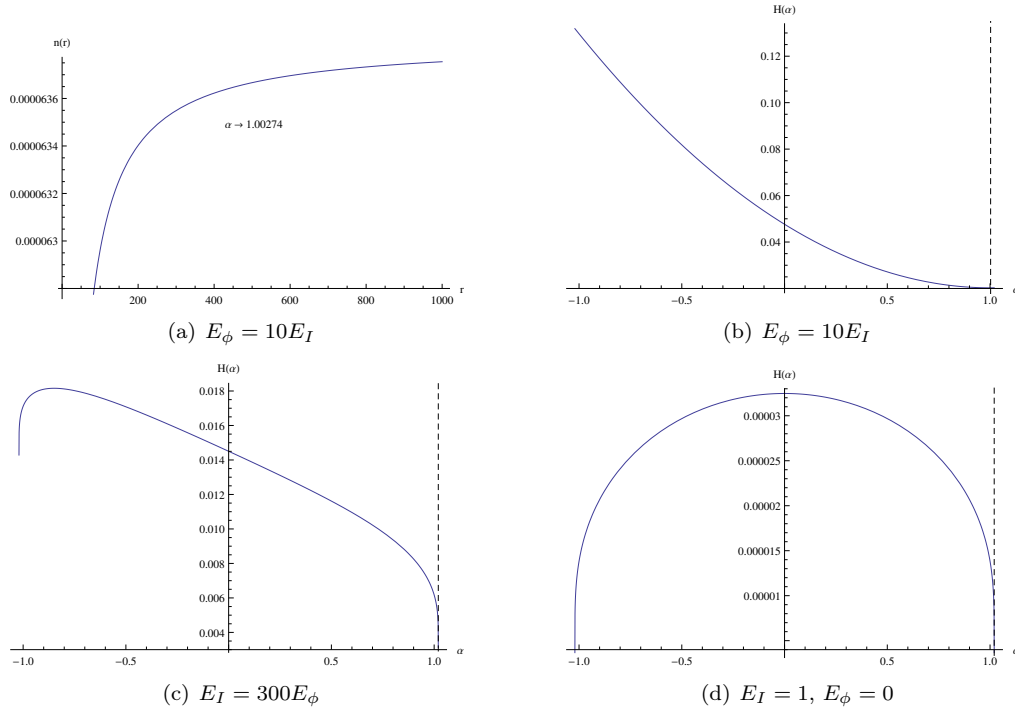


Figure 11.2: Figure 11.2(a) shows the vortex density profile for the case of $E_\phi = 10E_I$, determined by minimizing a test-function. The rest of the plots show the energy $H(\alpha)$ for different scenarios of energy ratios between E_I and E_ϕ for $N = 200$, $\tilde{R}_1 = 10$, $\tilde{R}_2 = 1000$. $H(\alpha)$ is a function of the free parameter α that characterizes the test-functions from equation (11.68)

11.5 Vortex–Current interaction - thin strip

In this section we want to move a bit away from the resistor model approach that we applied in the previous section. The applied current will move a vortex and apply work to the system. This was already discussed in the previous chapter 10 when we focused on the surface barriers. Additionally, the vortices all repel each other so each vortex configuration has an associated energy cost. Now we will try to look into the competition of these two effects. In this section we will ignore the geometric effects of the Corbino disk and revisit the strip setup.

The simplified geometry consist of a strip of width W in the x -direction and length L in the y -direction and thickness d in z -direction, illustrated in figure 11.3. The current density is applied so that $\mathbf{j} \parallel \hat{y}$ and the magnetic field $\mathbf{H} \parallel \hat{z}$, causing the vortices to move in x -direction. Taking the vortices to be straight line, i.e. no bending, and the current density averaged over the thickness $\mathbf{j}(x, z) = \frac{1}{d}j(x)\hat{y}$ the force per length \mathbf{f} on a vortex is

$$\mathbf{f} = \frac{\phi_0}{c} \mathbf{j}(x, y) \times \hat{z} \quad (11.73)$$

and the total force \mathbf{F} on a vortex

$$\mathbf{F} = \frac{\phi_0}{c} j(x) \hat{x} \quad (11.74)$$

We will work in the effective 2D system where the physical quantities are averaged over the z -direction. The notation we will be using for the coordinates are then two dimensional, given

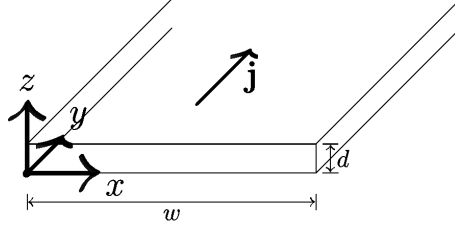


Figure 11.3: Illustration of the strip geometry used. The origin of the coordinate system is located on the left border of the strip. The magnetic field is applied in the z -direction and the current in the y -direction.

by $\mathbf{r} = (x, y)$. The work $E_j(\mathbf{r}_i)$ done by moving one vortex to the position \mathbf{r}_i due to the transport current is then just

$$E_j(\mathbf{r}_i) = \frac{\phi_0}{c} \int_0^{x_i} dx' j(x') \quad (11.75)$$

Summing over all vortices we will obtain the total energy E_j^t

$$E_j^t = \sum_{\{\mathbf{r}_i\}} E_j(\mathbf{r}_i) = \frac{\phi_0}{c} \sum_{\{\mathbf{r}_i\}} \int_0^{x_i} dx' j(x') = \frac{\phi_0}{c} \int d^2r \sum_{\{\mathbf{r}_i\}} \delta(\mathbf{r} - \mathbf{r}_i) \int_0^x dx' j(x') \quad (11.76)$$

$$= \frac{\phi_0}{c} \int d^2r n(\mathbf{r}) \int_0^x dx' j(x') \quad (11.77)$$

where we identified the vortex density $n(\mathbf{r})$ as

$$n(\mathbf{r}) = \sum_{\{\mathbf{r}_i\}} \delta(\mathbf{r} - \mathbf{r}_i) \quad (11.78)$$

Since the vortices move along the current, the system gains the energy E_j^t , meaning that $-E_j^t$ enters the total energy of the system. Each vortex in the sample cost a certain energy ϵ_1 and is favored by the applied field \mathbf{H} via $-\frac{dH}{4\pi} \int d^2r B(\mathbf{r})$, where $B(\mathbf{r})$ is the magnetic field due to the vortices

$$B(\mathbf{r}) = \sum_{\{\mathbf{r}_i\}} B_v(\mathbf{r} - \mathbf{r}_i) = \int d^2r' n(\mathbf{r}') B_v(\mathbf{r} - \mathbf{r}') \approx \phi_0 n(\mathbf{r}) \quad (11.79)$$

where $B_v(r)$ is the magnetic profile of a single vortex. Dealing with Pearl vortices and their algebraic decay of the current profile is very tricky. To get a first idea we deal with the case of exponentially decreasing currents, as they are the case for an Abrikosov vortex. Averaging over large scales compared to the vortex separation, the profile can be approximated by $\phi_0 \delta(r)$. Taking the line energy ϵ_1 into account, including the interaction between vortices via $V(r)$ and the energy gain $-E_j^t$ due to the transport current, we get

$$G = \left(\epsilon_1 - \frac{dH\phi_0}{4\pi} \right) \int d^2r n(\mathbf{r}) + \int d^2r \int d^2r' n(\mathbf{r}) V(|\mathbf{r} - \mathbf{r}'|) n(\mathbf{r}') - \frac{\phi_0}{c} \int d^2r n(\mathbf{r}) \int_0^x dx' j(x') \quad (11.80)$$

We will again assume short range interaction to simplify the calculations. The interaction energy can be written just as a potential $\Phi(n(\mathbf{r}))$

$$G = \left(\epsilon_1 - \frac{dH\phi_0}{4\pi} \right) \int d^2r n(\mathbf{r}) + \int d^2r \Phi(n(\mathbf{r})) - \frac{\phi_0}{c} \int d^2r n(\mathbf{r}) \int_0^x dx' j(x') \quad (11.81)$$

Variation leads to

$$\frac{\delta G}{\delta n(\mathbf{r})} = \left(\epsilon_1 - \frac{dH\phi_0}{4\pi} \right) + \Phi'(n(\mathbf{r})) - \frac{\phi_0}{c} \int_0^x dx' j(x') \stackrel{!}{=} 0 \quad (11.82)$$

The simplest form for the potential $\Phi(x) = \frac{c_0}{2}x^2$ leads to

$$n(\mathbf{r}) = \frac{1}{c_0} \left[\left(\frac{dH\phi_0}{4\pi} - \epsilon_1 \right) + \frac{\phi_0}{c} \int_0^x dx' j(x') \right] \quad (11.83)$$

The density is constant in the absence of a current and increases for $I > 0$. The current density of the system and the magnetic field due to the vortices are connected via Maxwell's equation

$$\nabla \times \mathbf{B} = \frac{4\pi}{c} \mathbf{j}(\mathbf{r}) \quad (11.84)$$

The current produced by an inhomogeneous vortex distribution can then be computed as

$$\phi_0 \nabla \times n(\mathbf{r}) \hat{z} = -\phi_0 \partial_x n(\mathbf{r}) \hat{y} = \frac{4\pi}{cd} j_v(x) \hat{y} \quad (11.85)$$

where we assumed no line deformation of the vortices, i.e. no x -component of the magnetic field. In the static case the vortices do not move. This means the total current at the center of each vortex, transport current $j(x)$ and the current from vortices $j_v(x)$ satisfy

$$j_v(x) + j(x) = 0 \quad (11.86)$$

giving us the connection of $n(x)$ and $j(x)$ as

$$j(x) = \frac{\phi_0 cd}{4\pi} \partial_x n(x) \quad (11.87)$$

This simple connection leads to

$$\frac{\phi_0}{c} \int_0^x dx' j(x') = \frac{\phi_0^2 d}{4\pi} (n(x) - n(0)) \quad (11.88)$$

leading to a constant vortex density as the solution to equation (11.83). Even for an arbitrary local interaction $\Phi(n(\mathbf{r}))$ the equation (11.82) can be written as

$$\Phi'(n(\mathbf{r})) - \frac{\phi_0^2 d}{4\pi} n(\mathbf{r}) = F(n(\mathbf{r})) = \left(\frac{dH\phi_0}{4\pi} - \epsilon_1 \right) - \frac{\phi_0^2 d}{4\pi} n(0) \quad (11.89)$$

where the right hand side is independent on the position, so the solution is just the constant profile $n(\mathbf{r}) = n(0)$ with

$$F(n(0)) = \left(\frac{dH\phi_0}{4\pi} - \epsilon_1 \right) - \frac{\phi_0^2 d}{4\pi} n(0) \quad (11.90)$$

So the vortex density does not seem to change due to a transport current. The constant density also means that there is no current $j_v = -\partial_x n(x) = 0$ and in order for the configuration to be static this means that also $j(x) = 0$ being in conflict with $\int_0^W dx j(x) = I > 0$. The only place left for the current would be the outer borders of the sample. In this very simplified picture the vortex lattice would stay constant for a non-vanishing current. The current itself would be pushed to the borders of the sample. Obviously this picture needs to be modified once the current densities at the borders reaches the critical density. The model itself has not included the effect of vortices entering or leaving the sample explicitly.

11.6 Vortex-Current interaction - Corbino disk

Now we are considering the case of vortices in a Corbino disk subject to a current, basically reformulating the theory for the previous section in polar coordinates. Without an external current present $I = 0$ the system is only subject to the vortex-vortex interaction $V(r)$ and produces (up to deformation effects close to the boundary) a constant distribution of vortices inside the sample. In this section we will be using polar coordinates for the disk setup, as illustrated in figure 11.4. Again we will calculate the force acting on a vortex due to the current

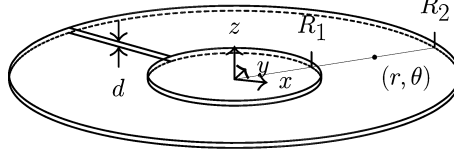


Figure 11.4: Polar coordinate system for the disk setup.

density $\mathbf{j}(\mathbf{r}) = \delta(z)j(r)\hat{\theta}$ is

$$F(r) = \frac{\phi_0}{c} j(r) \quad (11.91)$$

and the work E_v done to move one vortex to its position r from the inner Radius R_1 .

$$E_v = \frac{\phi_0}{c} \int_{R_1}^r dr' j(r') \quad (11.92)$$

The vortex density $n(r)$ is averaged over length scales larger than the vortex spacing $a_B = \sqrt{\phi_0/B}$. The work done on the whole system is

$$E_j = \frac{\phi_0}{c} \int d^2r n(r) \int_{R_1}^r dr' j(r') = \frac{2\pi\phi_0}{c} \int_{R_1}^{R_2} dr r n(r) \int_{R_1}^r dr' j(r') \quad (11.93)$$

Again we will consider the work done by the current and the general repulsion between the vortices as the main components. The interaction between vortices $V(r)$ in polar coordinates is given by

$$E_\phi = \int d^2r \int d^2r' n(r) V(|\mathbf{r} - \mathbf{r}'|) n(r') \quad (11.94)$$

As done in the previous section and in the case of the resistor model from section 11.4, we simplify the interaction to be local. This is not the complete picture, but should give a first insight into the nature of the configuration. The whole idea behind these approaches is finding a simple analytical model that will shed light on the complex problem of vortices entering and moving through the disk. We take $V(r) = V(a_B)\theta(a_B - r)$ leading to

$$E_\phi \approx 2\pi^2 a_B^2 V(a_B) \int_{R_1}^{R_2} dr r n^2(r) \quad (11.95)$$

Connection of $n(r)$ to $j(r)$: Now we have to connect the current density $j(r)$ to the averaged vortex density $n(r)$, so we can write the energy of the system as a functional of $n(r)$. We can do this by using Maxwell's equation

$$\nabla \times \mathbf{B} = \frac{4\pi}{c} \mathbf{j}(\mathbf{r}) = \frac{4\pi}{c} \delta(z) j(r) \hat{\phi} \quad (11.96)$$

and assuming that the magnetic field in the \hat{z} direction inside the sample ($z = 0$) is only determined by the vortex properties, meaning

$$B_z(z = 0) \approx \phi_0 n(r) \quad (11.97)$$

Using the rotational symmetry, we can introduce the vector potential $\mathbf{B} = \nabla \times \mathbf{A}$ with $\mathbf{A} = f(r, z)\hat{\theta}$. With the Coulomb gauge $\nabla \cdot \mathbf{A} = 0$ this results in the differential equation

$$\left[\frac{d^2}{dz^2} + \frac{d}{dr} \frac{1}{r} \frac{d}{dr} r \right] f(r, z) = -\frac{4\pi}{c} \delta(z) j(r) \quad (11.98)$$

Following Pearl [125, 137], we can use the Hankel transform and introduce $g(\gamma)$ via

$$f(r, z) = \int_0^\infty d\gamma g(\gamma) J_1(\gamma r) e^{-\gamma|z|} \quad (11.99)$$

which solves the homogeneous part $z > 0$ and for $z = 0$ reduces to

$$\int_0^\infty d\gamma \gamma g(\gamma) J_1(\gamma r) = \frac{2\pi}{c} j(r) \quad (11.100)$$

Using the inverse of the Hankel transform we can write the equation for $g(\gamma)$ as

$$g(\gamma) = \frac{2\pi}{c} \int_0^\infty dr r j(r) J_1(\gamma r) \quad (11.101)$$

Computing the z -component of the magnetic field via

$$(\nabla \times \mathbf{A})_z = \frac{1}{r} \frac{d}{dr} r A_\phi \approx \phi_0 n(r) \quad (11.102)$$

We can now use the fact that the Bessel-function $J_1(x)$ is the eigenfunction to the operator $\frac{1}{r} \frac{d}{dr} r$ with $\frac{1}{r} \frac{d}{dr} r J_1(\gamma r) = \gamma J_0(\gamma r)$ to get the relation

$$\phi_0 n(r) \approx \int_0^\infty d\gamma \gamma g(\gamma) J_0(\gamma r) \quad (11.103)$$

Again, using the properties of the Hankel transform of being its own inverse, we can now write $g(\gamma)$ dependent on $n(r)$ via

$$g(\gamma) \approx \phi_0 \int_0^\infty dr r n(r) J_0(\gamma r) \quad (11.104)$$

Plugging this into the relation for the current density we get

$$j(r) \approx \frac{c}{2\pi} \int_0^\infty d\gamma \gamma g(\gamma) J_1(\gamma r) = \frac{\phi_0 c}{2\pi} \int_0^\infty d\gamma \gamma J_1(\gamma r) \int_0^\infty dr' r' n(r') J_0(\gamma r') \quad (11.105)$$

Using the identity

$$\int_0^\infty d\gamma J_0(\gamma r') \gamma J_1(\gamma r) e^{-\gamma|z|} = \frac{k}{8\pi r^{\frac{5}{2}} r'^{\frac{3}{2}} (1 - k^2)} [k^2(r^2 - r'^2 - z^2)E(k) + 4rr'(1 - k^2)K(k)] \quad (11.106)$$

$$\equiv b_z(r', r, z) \quad (11.107)$$

$$k = \frac{2\sqrt{rr'}}{\sqrt{z^2 + (r + r')^2}} \quad (11.108)$$

(Prudnikov, Brychkov & Marichev Bd. II, p. 220, [160]), where the Elliptic integrals $E(k)$ and $K(k)$ are used in the Gradshteyn-Ryzhik definition, we can write

$$j(r) = \frac{\phi_0 c}{2\pi} \int_0^\infty dr' r' n(r') b_z(r', r, 0) \quad (11.109)$$

Now that we have derived a relation between the current density $j(r)$ and the vortex density $n(r)$ we can now combine The energy functional for $n(r)$ in the simplified form for the interaction then reads

$$H[n(r)] = 2\pi^2 V(a_B) \int_{R_1}^{R_2} dr r n^2(r) + \phi_0^2 \int_{R_1}^{R_2} dr r n(r) \int_{R_1}^r dr' \int_{R_1}^{R_2} dr'' r'' n(r'') b_z(r'', r', 0) \quad (11.110)$$

with the additional constrained that the number of vortices N in the sample stays fixed, meaning

$$\int_{R_1}^{R_2} dr r n(r) = \frac{N}{2\pi} \quad \int_{R_1}^{R_2} dr j(r) = I \quad (11.111)$$

Even after these simplifications the resulting energy functional in equation (11.110) is quite complicated due to the non-local nature of the current term. As we will see now, even a numerical approach using a test function will not be feasible due to the divergent nature of the integral kernel $b_z(r, r', z = 0)$ for $r = r'$.

Test functions: Using test functions that fulfill the constraints, we can try and get an idea of the shape of the vortex distribution. A simple distribution with only two parameters α and β can be constructed as

$$n_{\alpha,\beta}(r) = (1 - \alpha - \beta) \frac{N}{\pi(R_2^2 - R_1^2)} + \alpha \frac{N}{2\pi(R_2 - R_1)} \frac{1}{r} + \beta \frac{3N}{2\pi(R_2^3 - R_1^3)} r \quad (11.112)$$

consisting of a constant term, a $1/r$ decaying term and a linear increasing term. The expression satisfies the constrain $\int dr r n(r) = N/2\pi$ for all α and β . The second constrain

$$\int_{R_1}^{R_2} dr j(r) = \frac{\phi_0 c}{2\pi} \int_{R_1}^{R_2} dr \int_0^\infty dr' r' n(r') b_z(r', r, 0) = I \quad (11.113)$$

leads to the algebraic equation for the coefficients α and β as

$$(1 - \alpha - \beta)c_1 + \alpha c_2 + \beta c_3 = I \quad (11.114)$$

Here the numerical constants $\{c_i\}$ are given as

$$c_1 = \frac{N\phi_0 c}{2\pi^2(R_2^2 - R_1^2)} \int_{R_1}^{R_2} dr \int_{R_1}^{R_2} dr' r' b_z(r', r, 0) \quad (11.115)$$

$$c_2 = \frac{N\phi_0 c}{4\pi^2(R_2 - R_1)} \int_{R_1}^{R_2} dr \int_{R_1}^{R_2} dr' b_z(r', r, 0) \quad (11.116)$$

$$c_3 = \frac{3N\phi_0 c}{4\pi^2(R_2^3 - R_1^3)} \int_{R_1}^{R_2} dr \int_{R_1}^{R_2} dr' r'^2 b_z(r', r, 0) \quad (11.117)$$

The equation (11.114) can now be solved for β with

$$\beta = \frac{(1 - \alpha)c_1 + \alpha c_2 - I}{c_1 - c_3} \quad (11.118)$$

The test profile is now only dependent on the parameter α . In order to guarantee that $n_\alpha(r) \geq 0$ for all $R_1 \leq r \leq R_2$ we can calculate the critical values α_{c_1} and α_{c_2} where the vortex density actually vanishes

$$n_{\alpha_{c_1}}(R_1) = 0 \qquad n_{\alpha_{c_2}}(R_2) = 0 \qquad (11.119)$$

resulting in

$$\alpha_{c_1} = \frac{R_1 (3c_1 R_1 (R_1 + R_2) - 2c_3 (R_1^2 + R_1 R_2 + R_2^2) - I(R_1 - R_2)(R_1 + 2R_2))}{c_1 (R_1 - R_2)(R_1 + R_2)(2R_1 + R_2) - c_2 R_1 (R_1 - R_2)(R_1 + 2R_2) + c_3 (R_2^3 - R_1^3)} \qquad (11.120)$$

$$\alpha_{c_2} = \frac{R_2 (-3c_1 R_2 (R_1 + R_2) + 2c_3 (R_1^2 + R_1 R_2 + R_2^2) + I(-2R_1^2 + R_1 R_2 + R_2^2))}{c_1 (R_1 - R_2)(R_1 + R_2)(R_1 + 2R_2) + c_2 R_2 (-2R_1^2 + R_1 R_2 + R_2^2) + c_3 (R_2^3 - R_1^3)} \qquad (11.121)$$

Now plugging the test profile back into the energy functional, we will obtain the energy $H(\alpha)$ just as a function of the free parameter α . The first integral $\int dr' r' n^2(r')$ can be performed analytically for the test-profile. The current interaction part however has no known analytic form. The minimization has to be performed numerically. As already hinted at above, the function $b_z(r, r', z)$ is numerically not easy to tackle. The divergence in the integral kernel needs to be taken into account. Simple integration routines are not able to handle singularities in the integrand. Usually, the function gets divided into intervals which become increasingly finer. The sample points will get closer and closer to the singularity and will dominate the integral. One algorithm that can handle singularities is Monte-Carlo integration. Here the sample points are randomly chosen from the integration domain as apposed to being on a fixed or adapted grid. The main disadvantage is the high run time compared to the low accuracy of the routine. The run time for computing the energy for one fixed value α lies in the order of several hours. Several parameters have to be examined, like the interaction energy versus the current strength, without prior knowledge where interesting effects may lie. The high run time makes an exploratory approach unfeasible.

11.7 Discussion

In this chapter the focus was on the dynamics of superconducting vortices in thin films. Mainly the formation of flow lines and their bifurcation were of interest. In this chapter we examined a collection of attempts at a simple analytical picture for the problem, made during the collaboration via the German Israeli Foundation (GIF).

The problem itself is very complex. To simplify the geometry we have worked on either a simple strip configuration or with the Corbino disk setup. In the Meissner phase, i.e. in the absence of vortices, we could calculate a very good approximation to the current distribution in the disk. Both the contribution due to the Meissner effect and due to an external applied current. Once one tries to include vortices in trying to construct a simple picture of the system, things become complicated quick. We saw that integrating out the free magnetic fields outside the disk, lead to a non-local interaction of the currents. Different parts of the disk, e.g. vortices or more generally the current density, interact with each other via their generated and unshielded magnetic fields in the vacuum. Just analyzing the effect on the vortex density distribution due to the current in the disk turns out to be difficult in itself. Additionally one would have to account for the exit and entry of vortices into the system, much like the surface barriers discussed in the previous chapter 10.

Clean system In the clean system, i.e. ignoring disorder effects due to impurities in the system, our starting point was the construction of a simple picture for the vortex density distribution

and its interaction with the applied current density. In the Corbino disk setup the general flow of the vortices is radially outwards. The current is located at the borders of the disk and decreases towards the middle and with it the force acting on a vortex, as we calculated and illustrated in equation (11.13) and (11.16). The vortices close to the border will move faster than the vortices closer to the middle, effectively pushing them closer together in the r -direction. Starting with a dominant driving force, the vortices will move closer to each other until the force pushing them together is of the order of their respective repulsion. Now the system wants to maximize the distance between the vortices. Combined with the fact that the radial force in r -direction produces an increasing gap between vortices in the tangential direction θ between different lines. This was the general narrative we tried to explore analytically. It is plausible to expect a point where the creation of another flow line for the vortices will be favorable, being essentially a bifurcation point. For the strip geometry and small currents we saw that the vortex lattice is stable and the currents are pushed towards the boundary. Generally in order to minimize energy loss due to vortex movement, the system will try to separate vortex and current density. In the Corbino disk setup that means that the majority of the current is located towards the inner ring, while the majority of the vortices is located towards the outer ring. This radial change in vortex density, illustrated in figure 11.2(a), will lead to a reorganization of the lattice structure. A rearranging in a dynamical picture can be the basis for bifurcation points. Approaching this model analytically has proven to be very difficult. Even in a very simplified version, the resulting functional turned out to neither be analytically nor numerically accessible, as we saw in section 11.6

Disorder Additionally to the force of the current density and the interaction with the other vortices, a single vortex will also interact with a disorder background potential, e.g. due to impurities. The clean system alone turned out to be not accessible, so disorder has been ignored. The reason it is mentioned here is because it was one idea to explain the flow line formation of the moving vortices. Much like a drop of water going down a rough tilted surface, as discussed by Narayan and Fisher, [161], the vortex will see a disorder energy landscape. When moving through the landscape the vortex will choose the path of least resistance. The flow line will roughen. In the absence of interaction, a second vortex starting in the vicinity of the first will find the same path of low resistance following the first vortex. In case the driving force is much stronger than the repulsion from the nearest vortex, the vortices should start following the valleys of the disordered landscape.

Time dependent Ginzburg–Landau theory Some numerical work has been done by Braun et al., [162], solving the time dependent Ginzburg–Landau equations for small strips with an applied current. They see a change in the lattice density due to the current and the emergence of dislocations, predicting instabilities and “fault lines”. Abandoning the idea of a simple analytic model, the direct simulation of the constriction using the time dependent GL theory seems to be the most fruitful approach. However a simulation like this eludes the understanding of the mechanisms leading to the bifurcations.

Part III

Appendix

A. Appendix: Model

A.1 XY quantum chain

In the case of quantum XY spins without the z -component, the FM and AFM case can be mapped onto each other and are therefore identical, [42]. The model of quantum XY spins on a one-dimensional chain with nearest-neighbor interaction is often referred to as the XX chain given as

$$\hat{H}_{XX} = -\frac{J}{2} \sum_i \left(\hat{S}_i^+ \hat{S}_{i+1}^- + \hat{S}_i^- \hat{S}_{i+1}^+ \right) \quad (\text{A.1})$$

and has been solved analytically for $S = 1/2$ in 1961 by Lieb et al. [163]. Looking at the commutator relations for \hat{S}_i^\pm

$$[\hat{S}_i^z, \hat{S}_j^\pm] = \pm \delta_{ij} \hat{S}_i^\pm \quad [\hat{S}_i^+, \hat{S}_i^-] = 2\delta_{ij} \hat{S}_i^z \quad (\text{A.2})$$

we see that they have the meaning of raising \hat{S}_i^+ and lowering operators \hat{S}_i^- . In the case of $S = 1/2$ where the spin matrices are given by the Pauli matrices

$$\hat{\sigma}^x = \begin{pmatrix} 0 & 1 \\ 1 & 0 \end{pmatrix} \quad \hat{\sigma}^y = \begin{pmatrix} 0 & -i \\ i & 0 \end{pmatrix} \quad \hat{\sigma}^z = \begin{pmatrix} 1 & 0 \\ 0 & -1 \end{pmatrix} \quad (\text{A.3})$$

$\hat{S}_i^\alpha = \frac{1}{2} \hat{\sigma}_i^\alpha$ (setting $\hbar = 1$ for convenience), we see that \hat{S}_i^\pm behave both fermionic (on site)

$$\{\hat{S}_i^-, \hat{S}_i^+\} = 1 \quad (\hat{S}_i^\pm)^2 = 0 \quad (\text{A.4})$$

and bosonic (different sites)

$$[\hat{S}_i^+, \hat{S}_j^-] = [\hat{S}_i^+, \hat{S}_j^+] = [\hat{S}_i^-, \hat{S}_j^-] = 0 \quad i \neq j \quad (\text{A.5})$$

as pointed out in [163]. Using the Jordan-Wigner transformation, which introduces the operators

$$\hat{c}_i^+ = \hat{S}_i^+ \exp \left[-i\pi \sum_{j=1}^{i-1} \hat{S}_j^+ \hat{S}_j^- \right] \quad \hat{c}_i^- = \exp \left[i\pi \sum_{j=1}^{i-1} \hat{S}_j^+ \hat{S}_j^- \right] \hat{S}_i^- \quad (\text{A.6})$$

that behave fermionic on all sites, obeying the anti-commutator relations

$$\{\hat{c}_i^-, \hat{c}_j^+\} = \delta_{ij} \quad \{\hat{c}_i^\pm, \hat{c}_j^\pm\} = 0 \quad (\text{A.7})$$

The Hamiltonian for the XX chain in these new fermionic operators

$$\hat{H}_{XX} = -\frac{J}{2} \sum_i \left(\hat{c}_i^+ \hat{c}_{i+1}^- + \hat{c}_i^- \hat{c}_{i+1}^+ \right) \quad (\text{A.8})$$

as shown in [163]. The Hamiltonian is now quadratic in completely fermionic operators and describes the spectrum of spinless free fermions, [42, 163]. The model can be diagonalized by a simple Fourier transform

$$\hat{c}_k^- = \frac{1}{\sqrt{N}} \sum_i \hat{c}_i^- e^{-ikr_i} \quad (\text{A.9})$$

leading to

$$\hat{H}_{XX} = \sum_k \epsilon(k) \hat{c}_k^+ \hat{c}_k^- \quad (\text{A.10})$$

with $\epsilon(k) = -J \cos(ka)$ and the lattice constant a , [42]. Inside the first Brillouin zone $\pi/a \leq k \leq \pi/a$ the highest and lowest energies are $\pm J$ with the Fermi energy E_F laying in between at $E_F = 0$ at the Fermi vector $k_F = \pm \frac{\pi}{2a}$. In the absence of a chemical potential ($\mu = 0$) the system is half filled and the fermions at the Fermi energy, determine the relevant dynamics of the system at the momentum $k = k_F + q$. The moving fermions have therefor a linear dispersion relation with

$$\epsilon(k) = \epsilon(k_F + q) = -J \cos\left(\pm \frac{\pi}{2} + qa\right) \approx \pm Jqa \quad (\text{A.11})$$

Another way of approaching the system of spinless free fermions was done by Haldane, [164], by looking at the continuous version of the free fermions and mapping it to a Luttinger–Liquid. This results in a linear dispersion relation as well.

The Jordan–Wigner transformation does not work for $S \neq 1/2$. For large spin S the XX chain model has been studied, e.g. in [165], using the Holstein–Primakoff transformation, [10, 166–168]. Here the spin operators \hat{S}_i^α are represented via bosonic creation and annihilation operators \hat{a}^\dagger and \hat{a} measuring the deviation from the groundstate. Introducing a small magnetic field h in the x -direction to break the continuous symmetry, the groundstate lies in the x -direction. For spin S the deviation from the groundstate is measured by

$$\hat{S}_i^x = S - \hat{a}_i^\dagger \hat{a}_i \quad (\text{A.12})$$

$$-\hat{S}_i^z + \hat{S}_i^y = (2S - \hat{a}_i^\dagger \hat{a}_i)^{1/2} \hat{a}_i \quad (\text{A.13})$$

$$-\hat{S}_i^z - \hat{S}_i^y = \hat{a}_i^\dagger (2S - \hat{a}_i^\dagger \hat{a}_i)^{1/2} \quad (\text{A.14})$$

[165], which can be expanded in terms of $1/S$ for large spins resulting in the approximate expression for \hat{S}_i^y as

$$\hat{S}_i^y \simeq \frac{\sqrt{2S}}{2i} \left(\hat{a}_i - \hat{a}_i^\dagger \right) \quad (\text{A.15})$$

The XX chain Hamiltonian for large spin is then of the simple form

$$\hat{H}_{XX} = -J \sum_i \left(\hat{S}_i^x \hat{S}_{i+1}^x + \hat{S}_i^y \hat{S}_{i+1}^y \right) \quad (\text{A.16})$$

$$\simeq -JS^2 N + JS \sum_i \left(2\hat{a}_i^\dagger \hat{a}_i + \frac{1}{2} \left(\hat{a}_i \hat{a}_{i+1} + \hat{a}_i^\dagger \hat{a}_{i+1}^\dagger - \hat{a}_i^\dagger \hat{a}_{i+1} - \hat{a}_i \hat{a}_{i+1}^\dagger \right) \right) + \mathcal{O}(S^0) \quad (\text{A.17})$$

Resulting in a Hamiltonian that is quadratic in the bosonic operators \hat{a} , \hat{a}^\dagger and can be diagonalized via Fourier and Bogoliubov transformations leading to the new bosonic operators \hat{b}_k and \hat{b}_k^\dagger with

$$\hat{H} = \sum_k \epsilon(k) \hat{b}_k^\dagger \hat{b}_k \quad (\text{A.18})$$

where the new dispersion relation is

$$\epsilon(k) = 2JS \sqrt{1 - \cos(ka)} \approx \sqrt{2} JS |ka| \quad (\text{A.19})$$

[165], again leading to a linear dispersion relation for the excitations.

A.2 Kolezhuk mapping

In the case of the frustrated XY chain for large spin, Kolezhuk [43] was able to map the system to a classical helimagnet with the action

$$\mathcal{A}[\varphi] = \frac{1}{2T_{\text{eff}}} \int dx \int dy \left[\frac{1}{4} ((\partial_x \varphi)^2 - \theta^2)^2 + (\partial_y \varphi)^2 + \frac{1}{4} (\partial_x^2 \varphi)^2 \right] \quad (\text{A.20})$$

where effective temperature T_{eff} is related to the spin S via $T_{\text{eff}} = \sqrt{\frac{3}{2}} \frac{1}{S}$, relating to the value K_0 used in our definition as

$$K_0 = \sqrt{\frac{2}{3}} S \quad (\text{A.21})$$

Even though we will be dealing with a purely classical system, this relation can be used to connect it to the large spin case of frustrated one-dimensional quantum chains, [43].

Here we will reproduce the mapping procedure done by Kolezhuk in [43], with only slight deviations. In his case, the quantum chain has antiferromagnetic interaction for both nearest neighbors and next-nearest neighbors.

$$\hat{H} = \sum_n (\hat{\mathbf{S}}_n \hat{\mathbf{S}}_{n+1}) + j (\hat{\mathbf{S}}_n \hat{\mathbf{S}}_{n+2}) \quad (\text{A.22})$$

with the parameter spin operators $\hat{\mathbf{S}}_n = (\hat{S}_n^x, \hat{S}_n^y, \sqrt{\Delta} \hat{S}_n^z)$. In the case of XY spins ($\Delta = 0$), one can easily map the system to its ferromagnetic NN counterpart, by flipping every second spin along the x -axis. The expansion around $\theta \approx 0$ and $\theta \approx \pi$ show therefor the same critical behavior. We discussed this already in detail in chapter 2. Kolezhuk did the derivation for a finite Δ , we will here just focus on the $\Delta = 0$ case as it is the important one for this work.

Nonlinear sigma model

The first step is moving to coherent states, as described e.g. in [169, 170]. The Berry phase Φ_i for a single spin is written in terms of the vector \mathbf{n}_i parametrizing the coherent state at the site i

$$\Phi_i = S \int dt \frac{\partial_t \mathbf{n}_i (\mathbf{n}_i \times \mathbf{e}_i)}{1 + \mathbf{n}_i \mathbf{e}_i} \quad (\text{A.23})$$

Here \mathbf{e} describes an arbitrary unit vector, [43]. Choosing $\mathbf{e}_1 = -\mathbf{n}_2$ and $\mathbf{e}_2 = -\mathbf{n}_1$, the sum of the Berry phases of two neighboring spins works out to be

$$\Phi_{12} = S \int dt \frac{\mathbf{n}_1 \times \mathbf{n}_2}{1 - \mathbf{n}_1 \cdot \mathbf{n}_2} \partial_t (\mathbf{n}_2 - \mathbf{n}_1) \quad (\text{A.24})$$

Additionally Kolezhuk split the vector \mathbf{n}_i in a uniform magnetization \mathbf{m}_i and a staggered one \mathbf{l}_i via

$$\mathbf{n}_i = \mathbf{m}_i + (-1)^i \mathbf{l}_i \quad (\text{A.25})$$

Both \mathbf{m}_i and \mathbf{l}_i vary slowly close to the Lifshitz point $j = \frac{1}{4}$, making a continuum approximation possible. Resulting in the action \mathcal{A} as presented in [43].

$$\mathcal{A} = 2\pi S Q + S \int dx \int dt (\mathbf{1} \times \partial_t \mathbf{l}) - S^2 \int dx \int dt \left\{ \frac{3}{4} l_z^2 + 2f_\alpha m_\alpha^2 - 2\epsilon h_\alpha (\partial_x l_\alpha)^2 + \frac{1}{8} (\partial_{xx}^2 l_\alpha)^2 \right\}$$

with the topological charge $Q = \frac{1}{4\pi} \int dt \int dx \mathbf{l}(\partial_x \mathbf{l} \times \partial_t \mathbf{l})$. The notation used by Kolezhuk is

$$\epsilon = j - \frac{1}{4} \quad f_{x,y} = h_{x,y} = 1 \quad f_z = 1 \quad h_z = 0 \quad (\text{A.26})$$

In the chiral regime with $j > 1$ and $\epsilon > 0$ the pre-factor of $(\partial_x l_\alpha)^2$ is negative. When doing an expansion in the fields we then have to go up to at least the 4th order in the derivative in \mathbf{l} , [43]. The \mathbf{m} part can be integrated out and the imaginary time $\tau = 2iSt$ can be introduced to produce the Euclidean action

$$\mathcal{A}_E = \frac{1}{2g_0} \int dx \int d\tau \left\{ \frac{1}{f_\alpha} (\mathbf{l} \times \partial_\tau \mathbf{l})_\alpha^2 - 4\epsilon h_\alpha (\partial_x l_\alpha)^2 + \frac{1}{4} h_\alpha (\partial_{xx}^2 l_\alpha)^2 + \frac{3}{2} l_z^2 \right\} + i2\pi SQ \quad (\text{A.27})$$

as shown in [43], with the coupling constant $g_0 = 2/S$.

Helimagnet

Equation (A.27) will now be mapped to a helimagnet following [43, 171]. Kolezhuk switches to angular variables $l_x + il_y = \sin \theta e^{i\varphi}$ and $l_z = \cos(\theta)$. The field θ is massive and with $\theta = \frac{\pi}{2} + \vartheta$ we can expand the action in ϑ , [43].

$$\begin{aligned} \mathcal{A}_E = \mathcal{A}[\vartheta] + \frac{1}{2g_0} \int dx \int d\tau \left\{ \frac{1}{f_z} (\partial_\tau \varphi)^2 [1 + (f_z - 2)\vartheta^2] \right. \\ \left. + (1 - \vartheta^2) \left[-4\epsilon (\partial_x \varphi)^2 + \frac{1}{4} (\partial_x \varphi)^4 + \frac{1}{4} (\partial_{xx}^2 \varphi)^2 \right] \right\} + i2\pi SQ \end{aligned} \quad (\text{A.28})$$

$$\mathcal{A}[\vartheta] = \frac{1}{2g_0} \int dx \int d\tau \left\{ (\partial_\tau \vartheta)^2 - \frac{3}{2} \vartheta^2 \right\} \quad (\text{A.29})$$

Dealing with the special case $\Delta = 0$ simplifies equation (A.29) compared to the $\Delta \neq 0$ case in [43]. Here it is easy to see that ϑ is a massive field that will rescale the coupling parameters. Kolezhuk applied Polyakov-type RG to the $\Delta \neq 0$ model resulting to the planar helimagnet, dependent only on the in-plane angle φ , [43]. Setting $\Delta = 0$ afterward results in

$$\mathcal{A}[\varphi] = \frac{1}{2T_{eff}} \int dx \int dy \{ (\partial_y \varphi)^2 + V[\varphi] \} \quad (\text{A.30})$$

$$V[\varphi] = \frac{1}{4} [(\partial_x \varphi)^2 - 8\epsilon]^2 \quad (\text{A.31})$$

with the effective temperature $T_{eff} = \sqrt{3/2} \frac{1}{S}$ and the ‘‘spatial’’ dimension $y = \sqrt{3/2} \tau$. The topological charge Q is dropped when moving to the planar model.

B. Appendix: Renormalization Group

B.1 Vortex core energy integral

Here the analytic results for the core energy integrals are listed. The vortex profile ansatz

$$\phi_v(x, y) = \arcsin(\zeta)\theta(x) + [\pi - \arcsin(\zeta)]\theta(-x) \quad (\text{B.1})$$

where $\zeta = \lambda y / \sqrt{x^4 + \lambda^2 y^2}$ is used to approximate the core energy

$$E_{\text{core}}(\lambda) = \frac{K_0}{2} \int_{\mathbf{x}} \left[\phi_y^2 + \frac{1}{4}(\phi_{xx}^2 + \phi_x^4) \right] \quad (\text{B.2})$$

The diverge for small distances, so the small scale cutoff $a = 1$ is used, via $\int_{\mathbf{x}} \mapsto 4 \int_1^\infty d^2x$ The energy can be split into three different integrals as

$$E_{\text{core}} = 4 \frac{K_0}{2} \left[\underbrace{\int_1^\infty d^2x (\partial_y \phi_v)^2}_{=E_{\phi_y^2}} + \frac{1}{4} \underbrace{\int_1^\infty d^2x (\partial_x^2 \phi_v)^2}_{E_{\phi_{xx}^2}} + \frac{1}{4} \underbrace{\int_1^\infty d^2x (\partial_x \phi_v)^4}_{E_{\phi_x^4}} \right] \quad (\text{B.3})$$

The integrals can be solved analytically. The results are given in the equations (B.4), (B.5) and (B.6). They were obtained using Mathematica and checked by comparing the analytic expressions with their numeric counterparts.

$$\begin{aligned} E_{\phi_y^2} &= \int_1^\infty d^2x (\partial_y \phi_v)^2 \\ &= \frac{\lambda}{4} (\pi - 2 \arctan(\lambda)) \\ &\quad + \frac{\sqrt{\lambda}}{4\sqrt{2}} \left[\arctan \left(1 - \sqrt{\frac{2}{\lambda}} \right) - \arctan \left(\sqrt{\frac{2}{\lambda}} + 1 \right) - \operatorname{arccoth} \left(\frac{\lambda+1}{\sqrt{2\lambda}} \right) + \pi \right] \end{aligned} \quad (\text{B.4})$$

$$\begin{aligned} E_{\phi_{xx}^2} &= \int_1^\infty d^2x (\partial_x^2 \phi_v)^2 \\ &= \frac{5\pi}{2\sqrt{2}\lambda^{3/2}} + \frac{5}{4\sqrt{2}\lambda^{3/2}} \ln \left(\frac{\lambda - \sqrt{2\lambda} + 1}{\lambda + \sqrt{2\lambda} + 1} \right) + \frac{5}{2\sqrt{2}\lambda^{3/2}} \arctan \left(1 - \sqrt{\frac{2}{\lambda}} \right) \\ &\quad - \frac{5}{2\sqrt{2}\lambda^{3/2}} \arctan \left(1 + \sqrt{\frac{2}{\lambda}} \right) - \frac{4\lambda^2}{3(\lambda^2 + 1)^2} + \frac{1}{3(\lambda^2 + 1)} + \frac{\pi}{\lambda} - \frac{2}{\lambda} \arctan(\lambda) \end{aligned} \quad (\text{B.5})$$

$$\begin{aligned}
E_{\phi_x^4} &= \int_1^\infty d^2x (\partial_x \phi_v)^4 \\
&= \frac{3\lambda^2}{4(\lambda^2+1)^2} + \frac{\pi\sqrt{2\lambda}}{(\lambda^2+1)^2} + \frac{5}{12(\lambda^2+1)^2} + \frac{\sqrt{\lambda}}{4\sqrt{2}(\lambda^2+1)^2} \arctan(1-\sqrt{2\lambda}) \\
&\quad - \frac{\sqrt{\lambda}}{4\sqrt{2}(\lambda^2+1)^2} \arctan(1+\sqrt{2\lambda}) + \frac{2\lambda}{(\lambda^2+1)^2} \operatorname{arccot}(\lambda) + \frac{1}{\lambda(\lambda^2+1)^2} \operatorname{arccot}(\lambda) \\
&\quad + \frac{2(-1)^{3/4}\sqrt{\lambda}}{(\lambda^2+1)^2} \operatorname{arctanh}\left(\frac{\sqrt[4]{-1}}{\sqrt{\lambda}}\right) + \frac{2\sqrt[4]{-1}\sqrt{\lambda}}{(\lambda^2+1)^2} \operatorname{arctanh}\left(\frac{(-1)^{3/4}}{\sqrt{\lambda}}\right) \\
&\quad + \frac{\sqrt{\lambda}}{4\sqrt{2}(\lambda^2+1)^2} \operatorname{arccoth}\left(\frac{\lambda+1}{\sqrt{2\lambda}}\right) + \frac{\pi\lambda^{5/2}}{\sqrt{2}(\lambda^2+1)^2} + \frac{\pi}{\sqrt{2}\lambda^{3/2}(\lambda^2+1)^2} \\
&\quad + \frac{\lambda^{5/2}}{8\sqrt{2}(\lambda^2+1)^2} \arctan(1-\sqrt{2\lambda}) - \frac{\lambda^{5/2}}{8\sqrt{2}(\lambda^2+1)^2} \arctan(1+\sqrt{2\lambda}) \\
&\quad + \frac{1}{8\sqrt{2}\lambda^{3/2}(\lambda^2+1)^2} \arctan(1-\sqrt{2\lambda}) - \frac{1}{8\sqrt{2}\lambda^{3/2}(\lambda^2+1)^2} \arctan(1+\sqrt{2\lambda}) \\
&\quad + \frac{(-1)^{3/4}\lambda^{5/2}}{(\lambda^2+1)^2} \operatorname{arctanh}\left(\frac{\sqrt[4]{-1}}{\sqrt{\lambda}}\right) + \frac{\sqrt[4]{-1}\lambda^{5/2}}{(\lambda^2+1)^2} \operatorname{arctanh}\left(\frac{(-1)^{3/4}}{\sqrt{\lambda}}\right) \\
&\quad + \frac{(-1)^{3/4}}{\lambda^{3/2}(\lambda^2+1)^2} \operatorname{arctanh}\left(\frac{\sqrt[4]{-1}}{\sqrt{\lambda}}\right) + \frac{\sqrt[4]{-1}}{\lambda^{3/2}(\lambda^2+1)^2} \operatorname{arctanh}\left(\frac{(-1)^{3/4}}{\sqrt{\lambda}}\right) \\
&\quad + \frac{\lambda^{5/2}}{8\sqrt{2}(\lambda^2+1)^2} \operatorname{arccoth}\left(\frac{\lambda+1}{\sqrt{2\lambda}}\right) + \frac{1}{8\sqrt{2}\lambda^{3/2}(\lambda^2+1)^2} \operatorname{arccoth}\left(\frac{\lambda+1}{\sqrt{2\lambda}}\right) \\
&\quad + \frac{\lambda^3}{(1+\lambda^2)^2} \operatorname{arccot}(\lambda)
\end{aligned} \tag{B.6}$$

Here the convention introduced in the Software Mathematica is used, where

$$\sqrt[4]{-1} \equiv \frac{1}{\sqrt{2}} + \frac{i}{\sqrt{2}} \qquad (-1)^{3/4} \equiv -\frac{1}{\sqrt{2}} + \frac{i}{\sqrt{2}}. \tag{B.7}$$

This notation was adopted to shorten the already very lengthy expression.

The minimum of the function $E_{\text{core}}(\lambda)$ in respect to λ can then be determined numerically resulting in

$$E_{\text{core}} = 2.38K_0 \qquad \lambda = 2.38 \tag{B.8}$$

The nicer notation of $\kappa = 1/\lambda$ has been used in the main text and the publication [40].

B.2 Fourier transform in x -direction

Here the details concerning the computation of the correlator

$$\mathcal{G}(x, \mathbf{y}) = \int \frac{dk_x}{2\pi} \frac{d^{3/2}k_\perp}{(2\pi)^{3/2}} \frac{k_x^2}{k_\perp^2 + \frac{1}{4}k_x^4} e^{ik_x x} e^{i\mathbf{k}_\perp \mathbf{y}} = \frac{1}{y} f\left(\frac{x^2}{y}\right) \tag{B.9}$$

are presented.

We can perform the Fourier transform in the x -direction given by

$$M(k_\perp, x) = \int \frac{dk_x}{2\pi} \frac{k_x^2}{k_\perp^2 + \frac{1}{4}k_x^4} e^{ik_x x} \rightarrow \sqrt{8} \int \frac{dk'_x}{2\pi} \frac{k_x'^2}{k_\perp^2 + k_x'^4} e^{ik'_x x'} \tag{B.10}$$

where we used the scaling $k'_x = k_x/\sqrt{2}$ and $x' = \sqrt{2}x$ to remove the pre-factor of $1/4$ in front of the k_x^4 part.

$$\tilde{M}(k_\perp, x) = \int \frac{dk_x}{2\pi} \frac{k_x^2}{k_\perp^2 + k_x^4} e^{ik_x x} = \int \frac{dk_x}{2\pi} \frac{k_x^2}{\prod_i (k_x - k_i)} e^{ik_x x} = \oint \frac{k_x}{2\pi} \frac{k_x^2}{\prod_i (k_x - k_i)} e^{ik_x x}$$

where after identifying the roots $k_i = \{\pm e^{i\pi/4} \sqrt{k_\perp}, \pm e^{i3\pi/4} \sqrt{k_\perp}\}$ we switch to a contour integral for $x > 0$ by adding a circle path in the upper complex plane. The two roots in the upper plane are $k_1 = e^{i\pi/4} \sqrt{k_\perp} = 1/\sqrt{2}(1 + i)\sqrt{k_\perp}$ and $k_2 = e^{i3\pi/4} \sqrt{k_\perp} = 1/\sqrt{2}(-1 + i)\sqrt{k_\perp}$. Applying Cauchy's residual theorem, we can perform the contour integral

$$\begin{aligned} \tilde{M}(k_\perp, x) &= i \left[\frac{k_1^2}{\prod_{i \neq 1} (k_1 - k_i)} e^{ik_1 x} + \frac{k_2^2}{\prod_{i \neq 2} (k_2 - k_i)} e^{ik_2 x} \right] \\ &= \frac{1}{4} \sqrt{\frac{2}{k_\perp}} e^{-\sqrt{\frac{k_\perp}{2}} x} \left[\left(\frac{1}{2} + i\frac{1}{2}\right) e^{i\sqrt{\frac{k_\perp}{2}} x} - \left(-\frac{1}{2} + i\frac{1}{2}\right) e^{-i\sqrt{\frac{k_\perp}{2}} x} \right] \\ &= \frac{1}{4} \sqrt{\frac{2}{k_\perp}} e^{-\sqrt{\frac{k_\perp}{2}} x} \left[\cos\left(\sqrt{\frac{k_\perp}{2}} x\right) - \sin\left(\sqrt{\frac{k_\perp}{2}} x\right) \right] \end{aligned}$$

After scaling the variables back to their original, by multiplying with $\sqrt{8}$ and scaling $x \rightarrow \sqrt{2}x$ we arrive at the Fourier transform

$$M(k_\perp, x) = \frac{1}{\sqrt{k_\perp}} e^{-\sqrt{k_\perp} x} \left[\cos(\sqrt{k_\perp} x) - \sin(\sqrt{k_\perp} x) \right] \quad (\text{B.11})$$

B.3 Calculating the constant pre-factor $f(0)$

By looking at the scaling relations of the integral in equation (B.9), we can write our problem as

$$\int \frac{dk_x}{2\pi} \frac{d^{3/2} k_\perp}{(2\pi)^{3/2}} \frac{k_x^2}{k_\perp^2 + \frac{1}{4} k_x^4} e^{ik_x x} e^{i\mathbf{k}_\perp \mathbf{y}} = \int \frac{d^{3/2} k_\perp}{(2\pi)^{3/2}} M(k_\perp, x) e^{i\mathbf{k}_\perp \mathbf{y}} = \frac{1}{y} f\left(\frac{x^2}{y}\right) \quad (\text{B.12})$$

So with $M(k_\perp, 0) = 1/\sqrt{k_\perp}$ one can calculate the value for $f(0) = A = \text{const}$ with

$$\frac{f(0)}{y} = \int \frac{d^{3/2} k_\perp}{(2\pi)^{3/2}} \frac{1}{\sqrt{k_\perp}} e^{i\mathbf{k}_\perp \mathbf{y}} \quad (\text{B.13})$$

looking at the 3D and 4D polar coordinates for the integration we can generalize a relation for d -dimensions which can then be used for our fractional $d = 3/2$. We use the general pre-factor $K_d = 2\pi^{d/2}/\Gamma(d/2)$

$$\begin{aligned} 3D : \int d^3 x e^{i\mathbf{k}\mathbf{x}} &= \int_0^\infty dr \int_0^\pi d\phi_1 \int_0^{2\pi} d\phi_2 r^2 \sin(\phi_1) e^{ik_x \cos(\phi_1)} = K_2 \int_0^\infty dr \int_0^\pi d\phi_1 r^2 \sin(\phi_1) e^{ik_x \cos(\phi_1)} \\ 4D : \int d^4 x e^{i\mathbf{k}\mathbf{x}} &= K_3 \int_0^\infty dr \int_0^\pi d\phi_1 r^3 \sin^2(\phi_1) e^{ik_x \cos(\phi_1)} \\ d : \int d^d x e^{i\mathbf{k}\mathbf{x}} &= K_{d-1} \int_0^\infty dr \int_0^\pi \phi_1 r^{d-1} \sin^{d-2}(\phi_1) e^{ik_x \cos(\phi_1)} \end{aligned}$$

We can even perform the integration over the angular part (in general $d > 1$), where we will switch to $z = \cos(\phi)$ using $\sin(\arccos(z)) = \sqrt{1-z^2}$

$$\begin{aligned} \int_0^\pi d\phi \sin^{d-2}(\phi) e^{ik_\perp \cos(\phi)} &= \int_{-1}^1 dz (1-z^2)^{\frac{d-3}{2}} e^{ik_\perp z} = \sum_{n=0}^{\infty} \frac{(-1)^n k_\perp^{2n}}{(2n)!} \int_{-1}^1 dz z^{2n} (1-z^2)^{\frac{d-3}{2}} \\ &= \sum_{n=0}^{\infty} \frac{(-1)^n k_\perp^{2n}}{(2n)!} \int_0^1 dx x^{(n+\frac{1}{2})-1} (1-x)^{\frac{d-1}{2}-1} = \sum_{n=0}^{\infty} \frac{(-1)^n k_\perp^{2n}}{(2n)!} B\left(n + \frac{1}{2}, \frac{d-1}{2}\right) \end{aligned}$$

where, after switching to $x = z^2$, we identified the Beta function $B(x, y)$ with

$$B(x, y) = \int_0^1 dz z^{x-1} (1-z)^{y-1} = \frac{\Gamma(x)\Gamma(y)}{\Gamma(x+y)}$$

Using the doubling Formula for the Gamma function

$$\Gamma(2n+1) = \frac{1}{\sqrt{2\pi}} 2^{2n+\frac{1}{2}} \Gamma\left(n + \frac{1}{2}\right) \Gamma(n+1) = \frac{2^{2n}}{\sqrt{\pi}} \Gamma\left(n + \frac{1}{2}\right) n!$$

we can rewrite the sum

$$\begin{aligned} \sum_{n=0}^{\infty} \frac{(-1)^n k_\perp^{2n}}{(2n)!} B\left(n + \frac{1}{2}, \frac{d-1}{2}\right) &= \sum_{n=0}^{\infty} (-1)^n k_\perp^{2n} \frac{\Gamma\left(n + \frac{1}{2}\right) \Gamma\left(\frac{d-1}{2}\right)}{\Gamma(2n+1) \Gamma\left(n + \frac{d}{2}\right)} \\ &= \sqrt{\pi} \Gamma\left(\frac{d-1}{2}\right) \sum_n \left(-\frac{k_\perp^2}{4}\right)^n \frac{1}{n!} \frac{1}{\Gamma\left(n + \frac{d}{2}\right)} = \sqrt{\pi} \frac{\Gamma\left(\frac{d-1}{2}\right)}{\Gamma\left(\frac{d}{2}\right)} {}_0F_1\left(\frac{d}{2}, -\frac{k_\perp^2}{4}\right) \end{aligned}$$

Where we could identify the series representation of the confluent hypergeometric function ${}_0F_1(\alpha; x)$

$${}_0F_1(a; x) = \sum_{n=0}^{\infty} \frac{x^n}{n!} \frac{\Gamma(a)}{\Gamma(a+n)} \quad (\text{B.14})$$

giving us the general result

$$\int_0^\pi d\phi \sin^{d-2}(\phi) e^{ik_\perp \cos(\phi)} = \sqrt{\pi} \frac{\Gamma\left(\frac{d-1}{2}\right)}{\Gamma\left(\frac{d}{2}\right)} {}_0F_1\left(\frac{d}{2}, -\frac{k_\perp^2}{4}\right) \quad (\text{B.15})$$

So in our case we get

$$\begin{aligned} \frac{f(0)}{y} &= \frac{K_{1/2}}{(2\pi)^{3/2}} \int_0^\infty dk_\perp \int_0^\pi d\phi \frac{1}{\sqrt{\sin(\phi)}} e^{ik_\perp y \cos(\phi)} = \frac{1}{y} \frac{K_{1/2}}{(2\pi)^{3/2}} \int_0^\infty dk_\perp \int_0^\pi d\phi \frac{1}{\sqrt{\sin(\phi)}} e^{ik_\perp \cos(\phi)} \\ &= \frac{1}{y} \frac{K_{1/2}}{(2\pi)^{3/2}} \underbrace{\int_0^\infty dk_\perp \left\{ \sqrt{\pi} \frac{\Gamma\left(\frac{1}{4}\right)}{\Gamma\left(\frac{3}{4}\right)} {}_0F_1\left(\frac{3}{4}, -\frac{k_\perp^2}{4}\right) \right\}}_{=\pi} = \frac{1}{y} \frac{K_{1/2} \pi}{(2\pi)^{3/2}} = \frac{1}{y} \frac{2\pi^{5/4}}{(2\pi)^{3/2} \Gamma\left(\frac{1}{4}\right)} = \frac{1}{y} \frac{1}{\sqrt{2\pi^{1/4}} \Gamma\left(\frac{1}{4}\right)} \end{aligned}$$

Giving us the result $f(0)^{-1} = \sqrt{2\pi^{1/4}} \Gamma\left(\frac{1}{4}\right)$

$$f(0) = \frac{1}{\sqrt{2\pi^{1/4}} \Gamma\left(\frac{1}{4}\right)} \quad (\text{B.16})$$

B.4 Calculating the $f(z \rightarrow \infty)$ limit

One can even perform the $y \rightarrow 0$ limit of the function leading to the integral

$$I = \lim_{y \rightarrow 0} \frac{f(\frac{x^2}{y})}{y} = \int \frac{dk_x}{2\pi} \frac{d^{3/2}k_\perp}{(2\pi)^{3/2}} \frac{k_x^2}{k_\perp^2 + \frac{1}{4}k_x^4} e^{ik_x x} = \frac{K_{3/2}}{(2\pi)^{3/2}} \int_0^\infty dk_\perp \sqrt{k_\perp} M(k_\perp, x) \quad (\text{B.17})$$

Using the Fourier transformation in x -direction $M(k_\perp, x) = \frac{1}{\sqrt{k_\perp}} e^{-\sqrt{k_\perp} x} [\cos(\sqrt{k_\perp} x) - \sin(\sqrt{k_\perp} x)]$ from equation (B.11) the integral becomes

$$\begin{aligned} I &= \frac{K_{3/2}}{(2\pi)^{3/2}} \int_0^\infty dk_\perp e^{-\sqrt{k_\perp} x} [\cos(\sqrt{k_\perp} x) - \sin(\sqrt{k_\perp} x)] \\ &= \frac{1}{x^2} \frac{K_{3/2}}{(2\pi)^{3/2}} \int_0^\infty dk_\perp e^{-\sqrt{k_\perp}} [\cos(\sqrt{k_\perp}) - \sin(\sqrt{k_\perp})] \\ &= \frac{1}{x^2} \frac{K_{3/2}}{(2\pi)^{3/2}} \int_0^\infty dz (2z) e^{-z} [\cos(z) - \sin(z)] = \frac{1}{x^2} \frac{K_{3/2}}{(2\pi)^{3/2}} (-2\partial_a) \int_0^\infty dz e^{-az} [\cos(z) - \sin(z)] \Big|_{a=1} \\ &= \frac{1}{x^2} \frac{K_{3/2}}{(2\pi)^{3/2}} (-2\partial_a) \{ \mathcal{L}[\cos](a) - \mathcal{L}[\sin](a) \} \end{aligned}$$

where we introduced the variable transform $z = \sqrt{k_\perp}$. The Laplace transforms $\mathcal{L}[\dots]$ are given by

$$\begin{aligned} \mathcal{L}[\cos](a) &= \frac{a}{1+a^2} & \partial_a \mathcal{L}[\cos] \Big|_{a=1} &= \left[\frac{1}{1+a^2} - \frac{2a^2}{(1+a^2)^2} \right]_{a=1} = 0 \\ \mathcal{L}[\sin](a) &= \frac{1}{1+a^2} & \partial_a \mathcal{L}[\sin] \Big|_{a=1} &= -\frac{2a}{(1+a^2)^2} \Big|_{a=1} = -\frac{1}{2} \end{aligned}$$

leading to

$$\lim_{y \rightarrow 0} \frac{f(\frac{x^2}{y})}{y} = -\frac{1}{x^2} \frac{K_{3/2}}{(2\pi)^{3/2}} \quad f(z \rightarrow \infty) = -\frac{1}{z} \frac{K_{3/2}}{(2\pi)^{3/2}} \quad (\text{B.18})$$

B.5 Solving the full Fourier transform

Using the results for the Fourier transform $M(k_\perp, x)$ in x -direction from equation (B.11) and the general result for the angular integration of the \mathbf{k}_\perp integral from equation (B.15) the full

problem can be rewritten as

$$\begin{aligned}
\frac{f(z = \frac{x^2}{y})}{y} &= \int \frac{dk_x}{2\pi} \frac{d^{3/2}k_\perp}{(2\pi)^{3/2}} \frac{k_x^2}{k_\perp^2 + \frac{1}{4}k_x^4} e^{ik_x x} e^{i\mathbf{k}_\perp \mathbf{y}} \\
&= \frac{K_{1/2}}{(2\pi)^{3/2}} \sqrt{\pi} \frac{\Gamma(\frac{1}{4})}{\Gamma(\frac{3}{4})} \int_0^\infty dk_\perp \sqrt{k_\perp} M(k_\perp, x)_0 F_1\left(\frac{3}{4}, -\frac{(k_\perp y)^2}{4}\right) \\
&= \frac{K_{1/2}}{(2\pi)^{3/2}} \sqrt{\pi} \frac{\Gamma(\frac{1}{4})}{\Gamma(\frac{3}{4})} \int_0^\infty dk_\perp e^{-\sqrt{k_\perp} x} (\cos(\sqrt{k_\perp} x) - \sin(\sqrt{k_\perp} x))_0 F_1\left(\frac{3}{4}, -\frac{(k_\perp y)^2}{4}\right) \\
&= \frac{1}{y} \frac{K_{1/2}}{(2\pi)^{3/2}} \sqrt{\pi} \frac{\Gamma(\frac{1}{4})}{\Gamma(\frac{3}{4})} \int_0^\infty dk_\perp e^{-\sqrt{k_\perp} z} (\cos(\sqrt{k_\perp} z) - \sin(\sqrt{k_\perp} z))_0 F_1\left(\frac{3}{4}, -\frac{(k_\perp)^2}{4}\right) \\
&= \frac{1}{y} \frac{K_{1/2}}{(2\pi)^{3/2}} \sqrt{\pi} \frac{\Gamma(\frac{1}{4})}{\Gamma(\frac{3}{4})} \int_0^\infty dt (2t) e^{-t\sqrt{z}} (\cos(t\sqrt{z}) - \sin(t\sqrt{z}))_0 F_1\left(\frac{3}{4}, -\frac{t^4}{4}\right) \\
&= \frac{1}{y} \frac{z^{3/4}}{4\pi^{1/4}} \left(I_{-\frac{3}{4}}\left(\frac{z}{2}\right) - \mathbf{L}_{-\frac{3}{4}}\left(\frac{z}{2}\right) \right)
\end{aligned}$$

with $I_\nu(x)$ the modified Bessel function of the first kind and $\mathbf{L}_\nu(x)$ the modified Struve function.

B.6 Solving $f(z)$ via ODE

We can write down the differential equation for the correlator being the saddle point equations of the form

$$(\partial_x^4 - \Delta_\perp)G(x, y_\perp) = 0 \quad (\text{B.19})$$

The field correlator $G = \langle \phi \phi \rangle$ and the correlator of the derivatives $\mathcal{G} = \langle \partial_x \phi \partial_x \phi \rangle$ are related via the second derivative in x . Since ∂_x commutes with Δ_\perp , both functions are solutions to the differential equation above. So we can start looking for a function of the form $f(x^2/y)/y$ satisfying the above differential equation.

First we have to find a general form for the Laplace operator Δ_\perp which works in $d = 3/2$. In order to do so, we will look at the radial part of the Laplace operator in several known dimensions and generalize it for d -dimensions

$$\begin{aligned}
2D : \quad \Delta_r &= \frac{1}{r} \partial_r (r \partial_r f) & 3D : \quad \Delta_r &= \frac{1}{r^2} \partial_r (r^2 \partial_r f) \\
4D : \quad \Delta_r &= \frac{1}{r^3} \partial_r (r^3 \partial_r f) & d : \quad \Delta_r &= \frac{1}{r^{d-1}} \partial_r (r^{d-1} \partial_r f) = \left(\frac{d-1}{r} \partial_r + \partial_r^2 \right) f
\end{aligned}$$

With the ansatz $\mathcal{G}(x, r) = \frac{1}{r} f(\frac{x^2}{r})$ found by looking at the scaling relations in the integral from of \mathcal{G} , we can start to rewrite the differential equation

$$\left(\frac{1}{4} \partial_x^4 - \frac{1}{2r} \partial_r - \partial_r^2 \right) \frac{1}{r} f\left(\frac{x^2}{r}\right) = 0$$

using $z = x^2/r$ to compactify the notation, we can write the different parts of the partial

differential equation as

$$\begin{aligned}
\frac{1}{4}\partial_x^4 \left[\frac{1}{r}f(z) \right] &= \frac{1}{4r}\partial_x^3 \left[f'(z)\frac{2x}{r} \right] = \frac{1}{r}\partial_x^2 \left[f''(z)\left(\frac{2x}{r}\right)^2 + f'(z)\frac{2}{r} \right] \\
&= \frac{1}{4r}\partial_x \left[f'''(z)\left(\frac{2x}{r}\right)^3 + f''(z)\left(\frac{2}{r}\right)2x + f'(z)\frac{4x}{r^2} \right] \\
&= \frac{1}{r^3} [4z^2 f''''(z) + 12z f'''(z) + 3f''(z)] \\
\frac{1}{2r}\partial_r \left[\frac{1}{r}f(z) \right] &= \frac{1}{2r} \left[-\frac{1}{r^2}f(z) - \frac{x^2}{r^3}f'(z) \right] = \frac{1}{r^3} \left[-\frac{1}{2}f(z) - \frac{1}{2}zf'(z) \right] \\
\partial_r^2 \left[\frac{1}{r}f(z) \right] &= \partial_r \left[-\frac{1}{r^2}f(z) - \frac{x^2}{r^3}f'(z) \right] = \frac{1}{r^3} [z^2 f''(z) + 3zf'(z) + 2f(z)]
\end{aligned}$$

Leading to the ordinary differential equation for $f(z)$

$$4z^2 f''''(z) + 12z f'''(z) + (3 - z^2) f''(z) - \frac{7}{2} z f'(z) - \frac{3}{2} f(z) = 0 \quad (\text{B.20})$$

With the formal solution found by Mathematica

$$\begin{aligned}
f(z) &= \frac{1}{2} \sqrt[4]{-1} c_2 \sqrt{z} {}_1F_2 \left(1; \frac{1}{2}, \frac{5}{4}; \frac{z^2}{16} \right) \\
&+ \frac{1}{4} \sqrt{\frac{\pi}{2}} i c_3 z^{3/4} \Gamma \left(\frac{3}{4} \right) \mathbf{L}_{-\frac{3}{4}} \left(\frac{z}{2} \right) + \sqrt{2} c_1 z^{3/4} \Gamma \left(\frac{5}{4} \right) I_{-\frac{3}{4}} \left(\frac{z}{2} \right) \\
&+ \frac{(-1)^{3/4} c_4 z^{3/4} \Gamma \left(\frac{7}{4} \right) I_{\frac{3}{4}} \left(\frac{z}{2} \right)}{2\sqrt{2}}
\end{aligned}$$

Using the obtained limiting cases $f(0)^{-1} = \sqrt{2}\pi^{1/4}\Gamma(1/4)$ and $f(z \rightarrow \infty) = -B/x^2$ with $B = K_{3/2}/(2\pi)^{3/2}$ we can actually determine the constants $\{c_i\}$. Having $f(0) = \text{const}$ leaves $f(0) = c_1 = 1/(\sqrt{2}\pi^{1/4}\Gamma(1/4))$. In order to prevent divergence for $z \rightarrow \infty$ and have an overall $1/z$ decay we have to choose $c_2 = c_4 = 0$ and $c_3 = \frac{5i\sqrt{\frac{\pi}{2}}c_1\Gamma(-\frac{5}{4})}{4\Gamma(\frac{3}{4})^3}$, resulting in

$$f(z) = \frac{z^{3/4}}{4\pi^{1/4}} \left(I_{-\frac{3}{4}} \left(\frac{z}{2} \right) - \mathbf{L}_{-\frac{3}{4}} \left(\frac{z}{2} \right) \right) \quad (\text{B.21})$$

which agrees with the result obtained by the integration of the Fourier integral, with $I_\nu(x)$ being the modified Bessel function of the first kind and $\mathbf{L}_\nu(x)$ the modified Struve function.

B.7 Numerical calculation of the constant c_x

Calculating the constant

$$c_x = \int_0^\infty dz \sqrt{z} f^3(z) \quad (\text{B.22})$$

using a similar truncation procedure

$$\begin{aligned}
c_x \approx c_x^t &= c_{trunc} + c_{asym} & c_{trunc} &= \int_0^{50} dz \sqrt{z} f^3(z) = -0.000254197 \\
c_{asym} &= -B^3 \int_{50}^\infty dz \frac{1}{z^{5/2}} = \frac{16}{375\pi^{9/4}\Gamma(-\frac{1}{4})^3} = -0.0000275721
\end{aligned}$$

leading to

$$c_x^t = -0.000281769 \quad (\text{B.23})$$

B.8 Numerical data from Sorokin et al.

Sorokin et al., [56, 57], simulated the helical XY model numerically. Listed here in the tables B.1, B.2 and B.3 are the data points that were read out from their presented plots in [56]. This was done in order to extract the critical exponents.

$T[J_1]$	$C[T]$ [arb]
0.3	0.565
0.35	0.6
0.4	0.615
0.45	0.661
0.5	0.712
0.55	0.800
0.6	0.939
0.629	1.086
0.65	1.240
0.659	1.342
0.668	1.527
0.672	1.688
0.678	2.158
0.684	2.334
0.688	2.8
0.688	3
0.695	2.657
0.7	2.422
0.7	2.187
0.71	1.717
0.72	1.497
0.729	1.38
0.75	1.233

Table B.1: Numerical Data for the heat capacity C read out from the plots presented by Sorokin et al. in [56], obtained by numerical simulation of the HXY model

$T[J_1]$	κ [arb]
0.3	0.88
0.35	0.691
0.435	0.474

Table B.2: Numerical Data for the chiral order parameter κ read out from the plots presented by Sorokin et al. in [56], obtained by numerical simulation of the HXY model

$T[J_1]$	χ_k [arb]
0.369	4.7
0.38	9.3
0.391	51.2
0.4	93
0.409	153.5
0.42	537.2
0.431	286
0.441	148.8
0.45	107

Table B.3: Numerical Data for the chiral susceptibility χ_k read out from the plots presented by Sorokin et al. in [56], obtained by numerical simulation of the HXY model

C. Appendix: Multiferroics

C.1 Integral Approximation

Approximation of the integral

$$I(a, b) = \int dx (\tanh(ax) - \tanh(bx))^2 \quad (\text{C.1})$$

First of we can see the following symmetries and scaling relations

$$I(a, b) = I(b, a) = \frac{1}{a}I(1, b/a) = \frac{1}{a}I(b/a, 1) = \frac{1}{b}I(a/b, 1) \quad (\text{C.2})$$

so if one introduces the function $f(x) = I(1, x)$ it will have the property $f(x) = 1/x f(1/x)$ with

$$f(x) = \int dy (\tanh(y) - \tanh(xy))^2 = -2 \left(1 + \frac{1}{x}\right) + 2 \int_{-\infty}^{\infty} dy (1 - \tanh(y) \tanh(xy)) \quad (\text{C.3})$$

In the last integral we can introduce $z = \tanh(y)$ and simplify using $\operatorname{arctanh}(x) = \ln\left(\frac{1+x}{1-x}\right)$ leading to

$$g(x) = \int_{-\infty}^{\infty} dy (1 - \tanh(y) \tanh(xy)) = \int_{-1}^1 dz \frac{1 - z \frac{(1+z)^x - (1-z)^x}{(1+z)^x + (1-z)^x}}{1 - z^2} \quad (\text{C.4})$$

It is easy to see that $g(1) = 2$. For $x \rightarrow \infty$ we can write

$$g(x \rightarrow \infty) = 2 \lim_{x \rightarrow \infty} \int_0^1 dz \frac{1 - z \frac{(1+z)^x - (1-z)^x}{(1+z)^x + (1-z)^x}}{1 - z^2} = 2 \int_0^1 dz \frac{1 - z}{1 - z^2} = 2 \int_0^1 dz \frac{1}{1 + z} = 2 \ln(2) \quad (\text{C.5})$$

An ansatz for $g(x)$ that obeys the scaling $g(x) = 1/x g(1/x)$ and has the correct limits for $g(x \rightarrow \infty)$ and $g(x \rightarrow 0)$ is given by

$$g_a(x) = \frac{a_0 + a_1 x + a_0 x^2}{x + x^2} \quad (\text{C.6})$$

with $a_0 = 2 \ln(2)$ and the only free parameter a_1 . Fixing a_1 via $g_a(1) = 2$ we get

$$a_1 = 4 - 4 \ln(2) \quad (\text{C.7})$$

The difference $\Delta g = g(x) - g_a(x)$ is shown in figure C.1. The approximation around $x = 1$ is good up to 3 decimal places. For the approximation of $I(a, b)$ we can now write

$$I(x, y) = \frac{1}{x} f\left(\frac{y}{x}\right) = \frac{1}{x} \left[-2 \left(1 + \frac{x}{y}\right) + g\left(\frac{y}{x}\right) \right] \approx -2 \left(\frac{1}{x} + \frac{1}{y}\right) + 2 \frac{a_0(x^2 + y^2) + a_1 xy}{yx^2 + xy^2} \quad (\text{C.8})$$

Which is, as by construction, symmetric in x and y .

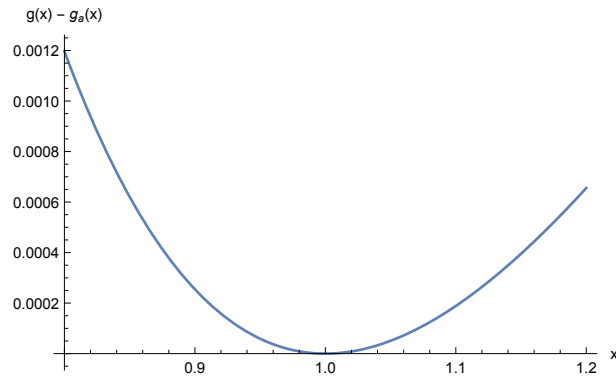


Figure C.1: Difference $\Delta g = g(x) - g_a(x)$ between the numerically evaluated integral $g(x)$ and the approximation $g_a(x)$. For small x the integration algorithm used by Mathematica starts to become less accurate and efficient due to the divergent nature of the integrand.

C.2 Python code for numerics

Shown in listing C.1 is the program code written in Python that was used to numerically find the minimum configuration of the variational given the boundary conditions of a domain wall.

```

1  #!/usr/bin/python
2
3  import numpy;
4  import random;
5
6
7  def simulation(couplingS, grad_coeffS):
8
9      max_x = 12.0;
10     points = 201;
11     special = (points - 1)/2;
12
13     coupling = couplingS;
14     grad_coeff = grad_coeffS;
15
16     name_grad = "Grad_" + str(coupling) + "_" + str(grad_coeff) + ".dat";
17     name_pol = "Pol_" + str(coupling) + "_" + str(grad_coeff) + ".dat";
18
19     deltaX = 2.0*max_x/(float(points-1));
20
21     def IK(xn, xnn, pn, pnn):
22         en = (0.5*(xn*xn - 1.0) * (xn*xn - 1.0) + 0.5*(xnn*xnn - 1.0) * (xnn*xnn -
23         1.0) + ((xnn - xn)*(xnn - xn))/(deltaX*deltaX));
24         en += 0.5*coupling*( (xn-pn)*(xn-pn) + (xnn-pnn)*(xnn-pnn) )
25         en += grad_coeff*(pn - pnn)*(pn - pnn)/(deltaX*deltaX);
26         return en;
27
28     def double_it(liste):
29         dummy = [];
30         print "vorher: ", len(liste);
31         for i in range(len(liste)-1):
32             dummy.append(liste[i]);
33             dummy.append((liste[i]+liste[i+1])/2.0);
34         dummy.append(liste[-1]);
35         print "nachher: ", len(dummy);

```

```

35     return list(dummy);
36
37     gradient = [];
38     polarization = [];
39
40     def save(name_g, name_p):
41         fg = open(name_g, "w");
42         fp = open(name_p, "w");
43         for i in range(len(gradient)):
44             fg.write(str(-max_x + float(i)*deltaX) + "\t" + str(gradient[i]) + "\n");
45             fp.write(str(-max_x + float(i)*deltaX) + "\t" + str(polarization[i]) + "\n");
46         ;
47         fg.close();
48         fp.close();
49
50     for i in range(points):
51         if (i < special):
52             gradient.append(1.0);# + random.uniform(-0.01,0.01));
53             polarization.append(-1.0);
54         else:
55             gradient.append(-1.0);# + random.uniform(-0.01,0.01));
56             polarization.append(1.0);
57
58     # Boundary conditions
59     gradient[special] = 0.0;
60     polarization[special] = 0.0;
61
62     h = 0.2;
63     changes = True;
64     dx_stop = 0.0001;
65     HdDx_stop = 0.0001;
66
67
68     while True:
69         #break;
70         print "DX: ", deltaX;
71         print "h: ", h;
72         print "h/DX: ", h/deltaX;
73         changes = True;
74         while changes:
75             changes = False;
76             grad_neu = list(gradient);
77             pol_neu = list(polarization);
78
79             # start and end point
80             f0 = IK(gradient[0], gradient[1], polarization[0], polarization[1]);
81             fp = IK(gradient[0]+h, gradient[1], polarization[0], polarization[1]);
82             fn = IK(gradient[0]-h, gradient[1], polarization[0], polarization[1]);
83             pp = IK(gradient[0], gradient[1], polarization[0]+h, polarization[1]);
84             pn = IK(gradient[0], gradient[1], polarization[0]-h, polarization[1]);
85
86             if fp <= fn and fp < f0 and fp <= pp and fp <= pn and (gradient[0] + h) >
87                 0.0:
88                 grad_neu[0] = gradient[0] + h;
89                 changes = True;
90                 elif fn < fp and fn < f0 and fn <= pp and fn <= pn and (gradient[0] - h) >
91                     0.0:
92                     grad_neu[0] = gradient[0] - h;
93                     changes = True;
94                 elif pp <= pn and pp < f0 and pp <= fp and pp <= fn:
95                     pol_neu[0] = polarization[0] + h;

```

```

94  changes = True;
95      elif pn < pp and pn < f0 and pn <= fp and pn <= fn:
96  pol_neu[0] = polarization[0] - h;
97  changes = True;
98      else:
99  #grad_neu[0] = gradient[0];
100 pass;
101
102      for i in range(1, points-1):
103
104  if i == special:
105      grad_neu[i] = 0.0;
106      pol_neu[i] = 0.0;
107      continue;
108
109  f0 = IK(grad_neu[i-1], gradient[i], pol_neu[i-1], polarization[i]) + IK(gradient[i
110 ], gradient[i+1], polarization[i], polarization[i+1]);
111  fp = IK(grad_neu[i-1], gradient[i]+h, pol_neu[i-1], polarization[i]) + IK(gradient[
112 i]+h, gradient[i+1], polarization[i], polarization[i+1]);
113  fn = IK(grad_neu[i-1], gradient[i]-h, pol_neu[i-1], polarization[i]) + IK(gradient[
114 i]-h, gradient[i+1], polarization[i], polarization[i+1]);
115  pp = IK(grad_neu[i-1], gradient[i], pol_neu[i-1], polarization[i] + h) + IK(
116 gradient[i], gradient[i+1], polarization[i]+h, polarization[i+1]);
117  pn = IK(grad_neu[i-1], gradient[i], pol_neu[i-1], polarization[i] - h) + IK(
118 gradient[i], gradient[i+1], polarization[i]-h, polarization[i+1]);
119
120 #print "f0: ", f0 , "\tfp: ", fp , "\tfn: ", fn;
121
122 if fp <= fn and fp < f0 and fp <= pp and fp <= pn:
123     grad_neu[i] = gradient[i] + h;
124     changes = True;
125 elif fn < fp and fn < f0 and fn <= pp and fn <= pn:
126     grad_neu[i] = gradient[i] - h;
127     changes = True;
128 elif pp <= pn and pp < f0 and pp <= fp and pp <= fn:
129     pol_neu[i] = polarization[i] + h;
130     changes = True;
131 elif pn < pp and pn < f0 and pn <= fp and pn <= fn:
132     pol_neu[i] = polarization[i] - h;
133     changes = True;
134 else:
135     #grad_neu[0] = gradient[0];
136     pass;
137
138     f0 = IK(grad_neu[-2], gradient[-1], pol_neu[-2], polarization[-1]);
139     fp = IK(grad_neu[-2], gradient[-1]+h, pol_neu[-2], polarization[-1]);
140     fn = IK(grad_neu[-2], gradient[-1]-h, pol_neu[-2], polarization[-1]);
141     pp = IK(grad_neu[-2], gradient[-1], pol_neu[-2], polarization[-1] + h);
142     pn = IK(grad_neu[-2], gradient[-1], pol_neu[-2], polarization[-1] - h);
143
144     if fp <= fn and fp < f0 and fp <= pp and fp <= pn and (gradient[-1] + h) <
145 0.0:
146 grad_neu[-1] = gradient[-1] + h;
147 changes = True;
148 elif fn < fp and fn < f0 and fn <= pp and fn <= pn and (gradient[-1] - h) <
149 0.0:
150 grad_neu[-1] = gradient[-1] - h;
151 changes = True;
152 elif pp <= pn and pp < f0 and pp <= fp and pp <= fn:
153 pol_neu[-1] = polarization[-1] + h;
154 changes = True;
155 elif pn < pp and pn < f0 and pn <= fp and pn <= fn:

```

```

149 pol_neu[-1] = polarization[-1] - h;
150 changes = True;
151     else:
152 #grad_neu[0] = gradient[0];
153 pass;
154
155
156     gradient = list(grad_neu);
157     polarization = list(pol_neu);
158
159 # save file:
160 print "Saved!";
161 save(name_grad, name_pol);
162
163     if h/deltaX < HdDx_stop:
164         if deltaX < dx_stop:
165 break;
166         # double x
167         gradient = list(double_it(gradient));
168         polarization = list(double_it(polarization));
169         points = len(gradient);
170         print "Points: ", points;
171         special = (points - 1)/2;
172         deltaX = 2.0*max_x/(float(points-1));
173         h = 2.0*deltaX;
174     else:
175         h = h/2.0;
176         #break;
177
178 save(name_grad,name_pol);
179
180 print "Finished";
181
182
183 print "Numerics";
184 # theta, coupling, grad_coeff;
185 # data = [ [1.0,0.0,1.0], [1.0,1.0,1.0],[0.3,0.1,1.0],[0.3,0.1,0.1] ];
186 #data = [[0.1,0.1],[0.1,0.2],[0.1,0.3],[0.1,0.5],[0.1,1.0],
187         [0.2,0.1],[0.3,0.1],[0.5,0.1],[1.0,0.1],[1.0,1.0]];
188 data = [[0.2,0.2],[0.3,0.3],[0.5,0.5]];
189
189 log = open("log_data.txt", "w");
190
191 for coef in data:
192     log.write("Start: [Coupling, " + str(coef[0]) + "], [Grad_Coeff, " + str(coef
193         [1]) + "]\n");
194     simulation(coef[0],coef[1]);
195     log.write("Finished!\n");
196
196 log.close();

```

Listing C.1: Python code used for the numerical calculations to obtain the minimum of the variational free energy given the boundary conditions for the domain walls. The program calculates the phase profile $\psi(x)$ and the polarization $p(x)$.

D. Appendix: MnWO₄

D.1 Different forms of order parameters

Here we write the invariant \mathfrak{J}_3 of the free energy ϕ in equation (6.13) in terms of the complex order parameters. Next to the trivial parts we have

$$\begin{aligned} \mathfrak{J}_3 &\propto \frac{1}{2} \left(\tilde{S}_1^* \tilde{S}_1^* \tilde{S}_2 \tilde{S}_2 + \tilde{S}_1 \tilde{S}_1 \tilde{S}_2^* \tilde{S}_2^* \right) = \frac{1}{2} \left(S_1^2 S_2^2 e^{i2\theta_1 - i2\theta_2} + S_1^2 S_2^2 e^{-i2\theta_1 + i2\theta_2} \right) \\ &= S_1^2 S_2^2 \cos(2(\theta_1 - \theta_2)) = S_1^2 S_2^2 \cos(2\varphi) \end{aligned} \quad (\text{D.1})$$

and for the order parameter part connected to the polarization we get

$$\frac{1}{2i} \left(\tilde{S}_1 \tilde{S}_2^* - \tilde{S}_1^* \tilde{S}_2 \right) = \frac{1}{2i} \left(S_1 S_2 e^{i\theta_1 - i\theta_2} - S_1 S_2 e^{-i\theta_1 + i\theta_2} \right) = S_1 S_2 \sin(\theta_1 - \theta_2) = S_1 S_2 \sin(\varphi) \quad (\text{D.2})$$

For the components we find

$$\begin{aligned} \frac{1}{2} \left(\tilde{S}_1^* \tilde{S}_1^* \tilde{S}_2 \tilde{S}_2 + \tilde{S}_1 \tilde{S}_1 \tilde{S}_2^* \tilde{S}_2^* \right) &= \frac{1}{2} \left((s_1 - i\bar{s}_1)^2 (s_2 + i\bar{s}_2)^2 + (s_1 + i\bar{s}_1)^2 (s_2 - i\bar{s}_2)^2 \right) \\ &= \frac{1}{2} \left((s_1^2 - 2is_1\bar{s}_1 - \bar{s}_1^2)(s_2^2 + 2is_2\bar{s}_2 - \bar{s}_2^2) \right) \\ &\quad + \frac{1}{2} \left((s_1^2 + 2is_1\bar{s}_1 - \bar{s}_1^2)(s_2^2 - 2is_2\bar{s}_2 - \bar{s}_2^2) \right) \\ &= \frac{1}{2} \left((A - iB)(C + iD) + (A + iB)(C - iD) \right) = AC + BD \\ &= (s_1^2 - \bar{s}_1^2)(s_2^2 - \bar{s}_2^2) + 4s_1\bar{s}_1s_2\bar{s}_2 \end{aligned} \quad (\text{D.3})$$

using

$$A = (s_1^2 - \bar{s}_1^2) \quad B = 2s_1\bar{s}_1 \quad C = (s_2^2 - \bar{s}_2^2) \quad D = 2s_2\bar{s}_2 \quad (\text{D.4})$$

and

$$(A - iB)(C + iD) + (A + iB)(C - iD) = AC + iAD - iBC + BD + AC - iAC + iBC + BD \quad (\text{D.5})$$

$$= 2(AC + BD) \quad (\text{D.6})$$

For the polarization part straight forward expansion shows

$$\begin{aligned} \frac{1}{2i} \left(\tilde{S}_1 \tilde{S}_2^* - \tilde{S}_1^* \tilde{S}_2 \right) &= \frac{1}{2i} \left((s_1 + i\bar{s}_1)(s_2 - i\bar{s}_2) - (s_1 - i\bar{s}_1)(s_2 + i\bar{s}_2) \right) \\ &= \frac{1}{2i} \left(s_1s_2 - is_1\bar{s}_2 + i\bar{s}_1s_2 + \bar{s}_1\bar{s}_2 - s_1s_2 - is_1\bar{s}_2 + i\bar{s}_1s_2 - \bar{s}_1\bar{s}_2 \right) \\ &= \bar{s}_1s_2 - s_1\bar{s}_2 \end{aligned} \quad (\text{D.7})$$

D.2 Transition at T_N : temperature fluctuations in \tilde{S}_1

Considering the phase transition at T_N where $\alpha_2 = a_2(T - T_N)$ is 0. Below T_N the order parameter \tilde{S}_2 is non-zero, and in the region $T_2 < T < T_N$: $\alpha_1 > 0$ and the order parameter \tilde{S}_1 is 0. Let us consider the effect of thermal fluctuations of \tilde{S}_1 around 0 (ignoring fluctuations in \tilde{S}_2 around its equilibrium value). Denoting the thermal average with $\langle \dots \rangle$ we make the following assumptions concerning the fluctuations. The order parameter fluctuates around 0

$$\langle \tilde{S}_1 \rangle = 0 \quad \Rightarrow \quad \langle s_1 \rangle = \langle \bar{s}_1 \rangle = 0 \quad (\text{D.8})$$

the fluctuations for the different components s_1 and \bar{s}_1 are uncorrelated

$$\langle f(s_1)g(\bar{s}_1) \rangle = \langle f(s_1) \rangle \langle g(\bar{s}_1) \rangle \quad (\text{D.9})$$

and the two components fluctuate according to the same distribution, meaning their moments are identical

$$\langle s_1^n \rangle = \langle \bar{s}_1^n \rangle \quad \forall n \in \mathbb{N} \quad (\text{D.10})$$

Averaging over the free energy Φ we get

$$\langle \Phi \rangle = \Phi_0(T) - f(T) + \frac{\alpha_2}{2}(s_2^2 + \bar{s}_2^2) + \frac{\beta_2}{4}(s_2^2 + \bar{s}_2^2)^2 + \underbrace{\alpha_1 \langle s_1^2 \rangle + \frac{\beta_1}{4} \langle (s_1^2 + \bar{s}_1^2)^2 \rangle}_{\equiv g(T)} \quad (\text{D.11})$$

$$+ \underbrace{\frac{\gamma_1}{2} ((s_2^2 - \bar{s}_2^2)(\langle s_1^2 \rangle - \langle \bar{s}_1^2 \rangle) + 4s_2\bar{s}_2 \langle s_1\bar{s}_1 \rangle)}_{=0} + \underbrace{\frac{\gamma_2}{4} \langle ((s_2^2 - \bar{s}_2^2)(s_1^2 - \bar{s}_1^2) + 4s_2\bar{s}_2 s_1\bar{s}_1)^2 \rangle}_{=A} \quad (\text{D.12})$$

$$- \frac{1}{2} \delta^2 \epsilon_{yy}^0 \underbrace{\langle (\bar{s}_1 s_2 - s_1 \bar{s}_2)^2 \rangle}_{=(s_1^2)(s_2^2 + \bar{s}_2^2)} \quad (\text{D.13})$$

The contribution A from the coupling γ_2 can be written as

$$A = \frac{\gamma_2}{4} ((s_2^2 - \bar{s}_2^2)^2 (\langle s_1^4 \rangle - 2\langle s_1^2 \bar{s}_1^2 \rangle + \langle \bar{s}_1^4 \rangle) + 16s_2^2 \bar{s}_2^2 \langle s_1^2 \bar{s}_1^2 \rangle) \\ = \frac{\gamma_2}{2} ((s_2^2 - \bar{s}_2^2)^2 (\langle s_1^4 \rangle - \langle s_1^2 \rangle^2) + 8s_2^2 \bar{s}_2^2 \langle s_1^2 \rangle^2) \quad (\text{D.14})$$

$$= \frac{\gamma_2}{2} ((s_2^4 - 2s_2^2 \bar{s}_2^2 + \bar{s}_2^4) (\langle s_1^4 \rangle - \langle s_1^2 \rangle^2) + 8s_2^2 \bar{s}_2^2 \langle s_1^2 \rangle^2) \quad (\text{D.15})$$

$$= \frac{\gamma_2}{2} ((s_2^2 + \bar{s}_2^2)^2 (\langle s_1^4 \rangle - \langle s_1^2 \rangle^2) - 4s_2^2 \bar{s}_2^2 (\langle s_1^4 \rangle - \langle s_1^2 \rangle^2) + 8s_2^2 \bar{s}_2^2 \langle s_1^2 \rangle^2) \quad (\text{D.16})$$

$$= \frac{\gamma_2'}{4} (s_2^2 + \bar{s}_2^2)^2 + \zeta s_2^2 \bar{s}_2^2 \quad (\text{D.17})$$

with

$$\gamma_2' = 2\gamma_2 (\langle s_1^4 \rangle - \langle s_1^2 \rangle^2) \quad \zeta = 4\gamma_2 (3\langle s_1^2 \rangle^2 - \langle s_1^4 \rangle) \quad (\text{D.18})$$

The changes to the free energy due to the fluctuations in \tilde{S}_2 are therefor

$$\phi_0(T) \rightarrow \phi_0'(T) = \phi_0(T) + g(T) \quad (\text{D.19})$$

$$\alpha_2 \rightarrow \alpha_2' = \alpha_2 - \delta^2 \epsilon_{yy}^0 \langle s_1^2 \rangle \quad (\text{D.20})$$

$$\beta_2 \rightarrow \beta_2' = \beta_2 + 2\gamma_2 (\langle s_1^4 \rangle - \langle s_1^2 \rangle^2) \quad (\text{D.21})$$

$$\zeta \rightarrow 4\gamma_2 (3\langle s_1^2 \rangle^2 - \langle s_1^4 \rangle) \quad (\text{D.22})$$

With the new free energy

$$\langle \Phi \rangle = \Phi'_0(T) - f(T) + \frac{\alpha'_2}{2}(s_2^2 + \bar{s}_2^2) + \frac{\beta'_2}{4}(s_2^2 + \bar{s}_2^2)^2 + \zeta s_2^2 \bar{s}_2^2 \quad (D.23)$$

The system can also be brought of the form of a N -component model with cubic anisotropy ($N = 2$)

$$\langle \Phi \rangle = g(T) + \frac{m_0^2}{2} \sum_{i=1}^N \phi_i^2 + \frac{u_0}{4!} \left(\sum_{i=1}^N \phi_i^2 \right)^2 + \frac{v_0}{4!} \sum_{i=1}^N (\phi_i^2)^2 \quad (D.24)$$

with $\phi_1 = s_2$, $\phi_2 = \bar{s}_2$ and

$$m_0^2 = \alpha'_2 = \alpha_2 - \delta^2 \epsilon_{yy}^0 \langle s_1^2 \rangle \quad u_0 = 6\beta'_2 + 6\gamma'_2 \left(1 + \frac{\zeta}{2}\right) \quad v_0 = -3\zeta\gamma'_2 \quad (D.25)$$

For spatial varying order parameters in d dimensions (here $d = 3$) the system is described by

$$H = \int d^d x \left[\frac{1}{2} \sum_{i=1}^N (m_0^2 \phi_i^2 + (\nabla \phi_i)^2) + \frac{u_0}{4!} \left(\sum_{i=1}^N \phi_i^2 \right)^2 + \frac{v_0}{4!} \sum_{i=1}^N (\phi_i^2)^2 \right] \quad (D.26)$$

This model has been studied in $\epsilon = 4 - d$ expansion and the stable fix point of the system corresponds to the $O(N)$ symmetrical Heisenberg fix point.

Gaussian fluctuations: In the special case of Gaussian fluctuations we can use Wicks theorem

$$\langle s_1^4 \rangle = 3 \langle s_1^2 \rangle^2 \quad (D.27)$$

which leads to

$$\zeta = 0 \quad \Rightarrow \quad v_0 = 0 \quad (D.28)$$

a vanishing anisotropy term. The model is then identical to the $O(2)$ model and the transition obviously in the 3D-XY universality class with the symmetric fixpoint being the stable one.

Mean-Field In the framework of the mean field study, the invariant corresponding to γ_2 is of $\mathcal{O}(S^8)$ and is not playing an important role stabilizing the phases. Since the anisotropy vanishes for $\gamma_2 = 0$ (ignoring said term in the Landau-expansion) it should not play an important role.

Non-Gaussian fluctuations In the case of non-Gaussian fluctuations and including the effect of γ_2 , we get a $\zeta \neq 0$ and therefor an anisotropic term in the $O(2)$ model. This model has been studied by and for a critical $N < N_c$ it has been found that the symmetric Heisenberg-fixpoint is still the stable fixpoint for the system. There is still some debate on the exact value of N_c for $d = 3$, [107], which is in the order of $N_c \sim 3$, however calculations by Aharony, [108, 109] and Brézin et al. [110] show that for $N = 2$ in $d = 3$ the symmetric fix point is the stable one. The transition is then in the $O(2)$ -symmetric universality class. The exponents up to $\mathcal{O}(\epsilon^5)$ and a discussion on the stability of the Heisenberg fix point in the presents of cubic anisotropy is given in [91], here we will only use the exponents up to $\mathcal{O}(\epsilon^3)$ being

$$\eta = \frac{N+2}{2(N+8)^2} \epsilon^2 \quad \nu^{-1} = 2 - \frac{N+2}{N+8} \epsilon - \frac{N+2}{2(N+8)^3} (13N+44) \epsilon^2 \quad (D.29)$$

$$= \frac{1}{50} \quad = \frac{73}{50} \quad (D.30)$$

where the numerical values are calculated for $N = 2$ and $\epsilon = 1$. Using the hyperscaling relations, we can compute the missing exponents

$$\alpha = 2 - \nu d \qquad \beta = \frac{\nu}{2}(d - 2 + \eta) \qquad \gamma = \nu(2 - \eta) \qquad \delta = \frac{d + 2 - \eta}{d - 2 + \eta} \quad (\text{D.31})$$

$$= -\frac{4}{73} \approx -0.055 \qquad = \frac{51}{146} \approx 0.349 \qquad = \frac{99}{73} \approx 1.356 \qquad = \frac{83}{17} \approx 4.882 \quad (\text{D.32})$$

Being the exponents of the 3D-XY ($O(2)$) universality class.

D.3 Transition at T_2 : Frozen \tilde{S}_1 order parameter

For $T < T_N$ we have $\alpha_2 < 0$ and the field in \tilde{S}_2 has reached a non-zero value. Approaching T_2 where $\alpha_1(T_2) = 0$, the field in \tilde{S}_1 will be critical. Compared to the fluctuations in \tilde{S}_1 the field in \tilde{S}_2 can be considered as frozen in first order. The values for s_2 and \bar{s}_2 can therefor be replaced by their equilibrium values $s_2^e = \langle s_2 \rangle$ and $\bar{s}_2^e = \langle \bar{s}_2 \rangle$. The theory left is only dependent on s_1 , \bar{s}_1 and the polarization P_y , which are coupled through bi-linear terms $\sim s_1 \bar{s}_1$, $\sim P_y s_1$ and $\sim P_y \bar{s}_1$. For a cleaner notation in the following section we switch $s_2^e \rightarrow s_2$ and $\bar{s}_2^e \rightarrow \bar{s}_2$. The free energy around T_0 under these considerations can be written as

$$\Phi = \tilde{g}(T) + \frac{\alpha_1}{2}(s_1^2 + \bar{s}_1^2) + \frac{\beta_1}{4}(s_1^2 + \bar{s}_1^2)^2 + \frac{1}{2\epsilon_{yy}^0} P_y^2 \quad (\text{D.33})$$

$$+ \frac{\gamma_1}{2} ((s_2^2 - \bar{s}_2^2)(s_1^2 - \bar{s}_1^2) + 4s_1 \bar{s}_1 s_2 \bar{s}_2) + \frac{\gamma_2}{4} ((s_1^2 - \bar{s}_1^2)(s_2^2 - \bar{s}_2^2) + 4s_1 \bar{s}_1 s_2 \bar{s}_2)^2 \quad (\text{D.34})$$

$$+ \delta P_y (\bar{s}_1 s_2 - s_1 \bar{s}_2) \quad (\text{D.35})$$

Introducing the vector $\mathbf{p} = (s_1, \bar{s}_1, P_y)$, the quadratic and bi-linear terms can be written as

$$\Phi_M = \frac{1}{2} \mathbf{p}^T \underline{\underline{M}} \mathbf{p} \quad (\text{D.36})$$

with the matrix $\underline{\underline{M}}$ given in equation (6.25). We can now rotate the system in its diagonal form in order to eliminate the bi-linear fields. The equilibrium case for the frozen out components s_2 and \bar{s}_2 is symmetric in the phase θ_2 and can be written as

$$s_2 = s \cos(\theta_2) \qquad \bar{s}_2 = s \sin(\theta_2) \qquad s = \sqrt{\frac{-\alpha'_2}{\beta'_2}} \quad (\text{D.37})$$

where θ_2 is arbitrary. With $\cos^2(\theta_2) - \sin^2(\theta_2) = \cos(2\theta_2)$ and $\cos(\theta_2) \sin(\theta_2) = \frac{1}{2} \sin(2\theta_2)$ the matrix $\underline{\underline{M}}$ can be simplified.

No coupling to polarization ($\delta = 0$): In the simple case of no coupling to the polarization P_y we have the following characteristic polynomial for the eigenvalues λ

$$(\alpha_1 + \gamma_1 s^2 \cos(2\theta_2) - \lambda)(\alpha_1 - \gamma_1 s^2 \cos(2\theta_2) - \lambda) \left(\frac{1}{\epsilon_{yy}^0} - \lambda \right) - \gamma_1^2 s^4 \sin^2(2\theta_2) \left(\frac{1}{\epsilon_{yy}^0} - \lambda \right) = 0 \quad (\text{D.38})$$

with $\lambda_3 = \frac{1}{\epsilon_{yy}^0}$ and

$$\lambda^2 - 2\alpha_1 \lambda + \alpha_1^2 - \gamma_1^2 s^4 = 0 \quad (\text{D.39})$$

giving

$$\lambda_{1/2} = \alpha_1 \pm \gamma_1 s^2 \quad (D.40)$$

So already in the absence of a coupling via the polarization the two components become critical at different temperatures. Calculating the eigenvectors corresponding to the eigenvalues we easily find

$$\lambda_3 = \frac{1}{\epsilon_{yy}^0} \quad \Rightarrow \quad \mathbf{v}_3 = \begin{pmatrix} 0 \\ 0 \\ 1 \end{pmatrix} \quad (D.41)$$

For λ_1 we find from $\underline{\underline{M}}\mathbf{v}_1 = \lambda_1\mathbf{v}_1$ with $\mathbf{v}_1 = (x, y, z)$ the following equations

$$\cos(2\theta_2)x + \sin(2\theta_2)y = -x \quad (D.42)$$

$$\sin(2\theta_2)x - \cos(2\theta_2)y = -y \quad (D.43)$$

$$\frac{1}{\epsilon_{yy}^0}z = (\alpha_1 - \gamma_1 s^2)z \quad (D.44)$$

with this we find $z = 0$ and the first two equations are identical and result in

$$\cos(\theta_2)x + \sin(\theta_2)y = 0 \quad (D.45)$$

which leads to the solution

$$\lambda_1 = \alpha_1 - \gamma_1 s^2 \quad \Rightarrow \quad \mathbf{v}_1 = \begin{pmatrix} -\sin(\theta_2) \\ \cos(\theta_2) \\ 0 \end{pmatrix} \quad (D.46)$$

and orthogonal to this (or by directly solving for λ_3) we find

$$\lambda_2 = \alpha_1 + \gamma_1 s^2 \quad \Rightarrow \quad \mathbf{v}_2 = \begin{pmatrix} \cos(\theta_2) \\ \sin(\theta_2) \\ 0 \end{pmatrix} \quad (D.47)$$

From the eigenvectors we can construct the rotation matrix $\underline{\underline{R}}$

$$\underline{\underline{R}} = \begin{pmatrix} -\sin(\theta_2) & \cos(\theta_2) & 0 \\ \cos(\theta_2) & \sin(\theta_2) & 0 \\ 0 & 0 & 1 \end{pmatrix} \quad (D.48)$$

and introduce the new fields

$$\mathbf{u} = \begin{pmatrix} u_1 \\ u_2 \\ u_3 \end{pmatrix} = \underline{\underline{R}}\mathbf{p} = \begin{pmatrix} -s_1 \sin(\theta_2) + \bar{s}_1 \cos(\theta_2) \\ s_1 \cos(\theta_2) + \bar{s}_1 \sin(\theta_2) \\ P_y \end{pmatrix} \quad (D.49)$$

so that

$$(\underline{\underline{R}}\mathbf{p})^T (\underline{\underline{R}} \cdot \underline{\underline{M}}(\delta = 0) \cdot \underline{\underline{R}}^T) (\underline{\underline{R}}\mathbf{p}) \quad \Rightarrow \quad \mathbf{u}^T \begin{pmatrix} \lambda_1 & 0 & 0 \\ 0 & \lambda_2 & 0 \\ 0 & 0 & \lambda_2 \end{pmatrix} \mathbf{u} \quad (D.50)$$

When u_1 becomes critical the equilibrium-values are

$$u_1 = c \quad u_2 = 0 \quad u_3 = 0 \quad (D.51)$$

with the constant c , leading to the equations for s_1 and \bar{s}_1

$$-s_1 \sin(\theta_2) + \bar{s}_1 \cos(\theta_2) = c \quad (\text{D.52})$$

$$s_1 \cos(\theta_2) + \bar{s}_1 \sin(\theta_2) = 0 \quad (\text{D.53})$$

leading to

$$\begin{pmatrix} s_1 \\ \bar{s}_1 \end{pmatrix} = c \begin{pmatrix} -\sin(\theta_2) \\ \cos(\theta_2) \end{pmatrix} \quad (\text{D.54})$$

which is perpendicular to the equilibrium vector $(s_2, \bar{s}_2) = s(\cos(\theta_2), \sin(\theta_2))$, in accordance with the calculations by Tolédano [100], who finds $\theta_1 - \theta_2 = (2n + 1)\frac{\pi}{2}$, corresponding to the chiral phase of the system, [98].

With coupling ($\delta \neq 0$): The condition that one of the eigenvalues vanishes (meaning that one field becomes critical) translates to the equation

$$\det(\underline{M}) = 0. \quad (\text{D.55})$$

In the case of a finite coupling $\delta \neq 0$, this leads to

$$\det(\underline{M}) = (\alpha_1 + \gamma_1(s_2^2 - \bar{s}_2^2))(\alpha_1 - \gamma_1(s_2^2 - \bar{s}_2^2))\frac{1}{\epsilon_{yy}^0} - (\alpha_1 + \gamma_1(s_2^2 - \bar{s}_2^2))\delta^2 s_2^2 \quad (\text{D.56})$$

$$- (2\gamma_1 s_2 \bar{s}_2)\delta^2 s_2 \bar{s}_2 - (2\gamma_1 s_2 \bar{s}_2)^2 \frac{1}{\epsilon_{yy}^0} \quad (\text{D.57})$$

$$- (2\gamma_1 s_2 \bar{s}_2)\delta^2 s_2 \bar{s}_2 - (\alpha_1 - \gamma_1(s_2^2 - \bar{s}_2^2))\delta^2 \bar{s}_1^2 \quad (\text{D.58})$$

$$= \frac{1}{\epsilon_{yy}^0} ((\alpha_1^2 - \gamma_1^2(s_2^2 + \bar{s}_2^2)^2 - \alpha_1 \epsilon_{yy}^0 \delta^2 (s_2^2 + \bar{s}_2^2) - \epsilon_{yy}^0 \delta^2 \gamma_1 (s_2^2 + \bar{s}_2^2)^2) \quad (\text{D.59})$$

$$= \frac{1}{\epsilon_{yy}^0} ((\alpha_1 + \gamma_1(s_2^2 + \bar{s}_2^2))(\alpha_1 - (s_2^2 + \bar{s}_2^2)(\gamma_1 + \epsilon_{yy}^0 \delta^2)) \quad (\text{D.60})$$

Giving the two conditions on α_1

$$\alpha_1 = -\gamma_1 s^2 \quad \alpha_1 = \gamma_1 s^2 + \delta^2 \epsilon_{yy}^0 \quad (\text{D.61})$$

yielding two fields becoming critical at different temperatures. For $\delta = 0$ the conditions agree with the obtained eigenvalues.

E. Appendix: Experiment

E.1 Material properties of lead

PROPERTY	SYMBOL	VALUE	SOURCE
lattice structure		fcc	[138]
lattice constant	a	4.95 Å	[138]
density	ρ	$11.34 * 10^3$ kg m ⁻³	[138]
mean atomic volume		30.3 Å ³	[138]
mean atomic radius	r_a	1.93 Å	[138]
ionic radius		0.84 Å (4+)	[138]
energy gap	$2\Delta(0)$	2.73 meV	[138]
critical temperature	T_c	7.2 K	[138]
Debye temperature	T_D	~ 100 K	[138]
melting temperature	T_M	600.7 K	[172]
critical field (bulk)	H_{c_0}	803 G	[138]
critical field (bulk)	$H_c(T)$	$H_c(T) = H_{c_0}(1 - T^2/T_c^2)$	[138]
critical field (thin film)	$H_{c_2} = \phi_0/(2\pi\xi^2)$	1300-2000 G	[132]
resistivity	$\rho_n(T = 295K)$	210 nΩm	[172]
conductivity	$\sigma_n(T = 295K)$	$0.48 * 10^5$ (Ωcm) ⁻¹	[172]
resistivity of thin film	$\rho_n(T = 77K, d = 100nm)$	~ 1 nΩm	[173]
resistivity (bulk)	$\rho_n(T = 50K)$	28 nΩm	[174]
resistivity (bulk)	$\rho_n(T = 25K)$	6.5 nΩm	[174]
resistivity (bulk)	$\rho_n(T = 7.2K)$	0.20 nΩm	[139]

Table E.1: Known properties of lead (Pb).

F. Appendix: Vortex Dynamics

In this appendix the current profile in the Corbino disk setup is discussed. There are some analytic results for the current distribution of the Corbino disk in different limits $R_1 \rightarrow 0$ or $R_2 \rightarrow \infty$, [158], in the case of $\Lambda \rightarrow 0$. A complete analytic picture for finite penetration length Λ is still missing. We distinguish two cases, the current profile due to an applied current I and the profile due to an applied field B_a . The applied current is equivalent to a trapped flux ϕ_f inside the inner ring of the Corbino disk.

An overview of the literature and the known features of the current profile is given in section F.1. Starting from the Ginzburg–Landau Hamiltonian describing superconductivity the differential equations describing the Corbino disk can be derived using the variational method in section F.2. The derivation is similar to the one done by Pearl, [125], but instead of just a thin film extended to infinity the derivation here is done for a finite Corbino disk with an inner and outer radius. In contrast to the thin film, the inhomogeneous differential equation can now not be solved by the Hankel transform that was employed by Pearl. However it can be used to transform the equation into a type II inhomogeneous Fredholm Integral equation. The limiting cases of the integral equation can be solved analytically and are shown in section F.3. Here the known features and limiting cases are reproduced using the integral equation. Finally in section F.4 we present a way to determine an approximate profile for the whole disk and finite Λ . Here, we want to avoid the complications involved in either numerically integrating the differential equations or numerically inverting the integration kernel in the integral equation. This can be done by finding an approximate parametrization of the full current profile. The problem can then be reduced in finding the optimal set of parameters describing the current profile as functions of the applied parameter I and B_a . The results are presented in section F.4.

F.1 Detailed overview of current distribution

In order to summarize the already known results and to get a feeling for the current distribution, it is sensible to split the ring into 5 regions according to their dominant length scales, as illustrated in figure F.1. Starting with the inner border where Λ is the important length scale and $|R_1 - r| \leq$

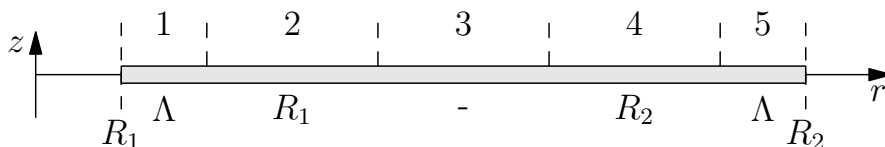


Figure F.1: Cross section of the Corbino disk illustrating the regions 1 to 5 and their respective dominant length scale.

Λ holds we have region 1, followed by region 2 which is close enough to the inner ring to make R_1 the dominant length scale but far enough from the border so that Λ is not important anymore. Region 3 is characterized by $R_1 \ll r \ll R_2$ so that neither R_1 , R_2 nor Λ are important. After this we are in region 5 close enough to the outer border that R_2 being the dominant length. Region 5 is similar to region 1 with Λ being the important length scale.

Response $j_\phi(r)$ to a trapped flux ϕ_f ($B_a = 0$)

An overview of the solution for the different regimes (regions) is given in table F.1. The total current I , that is fed into the system is described by an effective flux ϕ_f .

	1	2	3	4	5
region	$(r - R_1) \sim \Lambda$	$\Lambda < (r - R_1)$	$R_1 \ll r \ll R_2$	$(R_2 - r) > \Lambda$	$(R_2 - r) \sim \Lambda$
length scale	Λ	R_1	None	R_2	Λ
current	$j_\phi(R_1)e^{-2\frac{(r-R_1)}{a\Lambda}}$	$\frac{\phi_f c}{4\pi^2} \frac{1}{r\sqrt{r^2-R_1^2}}$	$\frac{\phi_f c}{4\pi^2} \frac{1}{r^2}$	$1/\sqrt{\dots}$ divergences close to R_2	$j_\phi(R_2)e^{-\frac{(R_2-r)}{b\Lambda}}$
SOURCE	Bowers (unpublished) as quoted by Glover [175] as part of the discussion of [176, 177]	$1/\sqrt{\dots}$ -profile thin film and edge (connection) [178, 179], for disks [158]	analog to Pearl profile for $r \gg \Lambda$ [125, 137], behaves like magnetic dipole	$1/\sqrt{\dots}$ profile (discussed by Brojeny, Clem, Brandt [152, 180]) numerically	analog to the edge of R_1 (Bowers)

Table F.1: The current density due to a trapped flux ϕ_f inside the inner ring R_1 approximated in different regions of the sample

Region 1 & 5: $|r - R_i| \sim \Lambda$ Close to the edges, the most important length scale is Λ . An approximate formula has been suggested by Bowers (unpublished) as quoted by Glover [175] as part of the discussion of [176, 177], for thin film strips. For small angles an angular segment can be approximated by a thin strip and close to the surface of length scale Λ , the inner radius R_1 is large enough so that the local curvature of the edge is not important. Therefor the solution given in the context of thin films also applies for the annular ring we are discussing. Close to the edge ($r - R_1 \ll \Lambda \sim d$) the magnetic field is exponentially screened leading to the suggested current density profile by Bowers

$$j_\phi(r) = j_\phi(R_1)e^{-2\frac{(r-R_1)}{a\Lambda}} \quad (\text{F.1})$$

where a is a numerical constant of order unity. Rhoderick et al. [178] suggest to join the solution to the analytically known solution inside the sample (Region 2) at a distance of $r = R_1 + \frac{\Lambda a}{4}$ leading to

$$j_\phi(R_1) = \frac{\phi_f c}{4\pi^2} \frac{16\sqrt{e}}{(a\Lambda + 4R_1)\sqrt{a\Lambda(a\Lambda + 8R_1)}} \quad (\text{F.2})$$

Region 2: $r - R_1 > \Lambda$ Away from the edge but near the inner hole (r of the order of R_1) the main length scale is R_1 . This approximation is equivalent to the situation of $\Lambda = 0$ and $R_2 \rightarrow \infty$ which has been solved analytically by Ketchen et al. [158] by relating it to an electrostatic problem.

$$j_\phi(r) = \frac{\phi_f c}{4\pi^2} \frac{1}{r\sqrt{r^2 - R_1^2}} \quad (\text{F.3})$$

Which has to be matched to the solution for Region 1 at a distance of $\sim \Lambda$, as done e.g. in [178, 179]. As we will see later, the approximation for Region 3 (no apparent length scale) is already included in this form.

Region 3: Deep inside the ring, far away from the inner and the outer radius, there is no direct external length scale and the problem is similar to an infinite film with a flux trapped at the origin. (Solved by Pearl [125])

$$j_\phi(r) \approx \frac{\phi_f c}{4\pi^2} \frac{1}{r^2} \quad (\text{F.4})$$

with a magnetic field decaying as $\frac{1}{r^3}$ (see discussion Fetter and Hohenberg, [137]) which behaves like a magnetic dipole with the magnetic dipole moment \mathbf{m}

$$\mathbf{m} = \frac{\phi_f c}{4\pi^2} \hat{z} \quad (\text{F.5})$$

This limit is already contained in the expression for Region 2, which can be used for both domains.

Region 4: $R_2 - r > \Lambda$ Close to the edge at R_2 but still far enough so that Λ is not important, the main length scale is R_2 . From the numerical work done by Brandt & Clem [180] we expect a $1/\sqrt{\dots}$ type divergence getting closer to the edge. In its vicinity we will have the exponential behavior as discussed earlier (Region 1) going back to Bowers, the divergence only appears in the formal $\Lambda \rightarrow 0$ case. (agreeing with the numerics for finite Λ , [180])

Response $j_B(r)$ to an applied field B_a (in the absence of a flux, $\phi_f = 0$)

This is a more artificial problem, since we force the flux inside the inner ring to be zero, in order to focus on the mathematical effects of the applied magnetic field. The final ring will have a small slit, that will make it easier to introduce an external current I . The slit will also lead to flux entering the the inner ring in order to compensate the effect due to only the magnetic field. The net current (without external current I) will then be zero.

	1	2	3	4	5
region	$(r - R_1) \sim \Lambda$	$\Lambda < (r - R_1)$	$R_1 \ll r \ll R_2$	$(R_2 - r) > \Lambda$	$(R_2 - r) \sim \Lambda$
length scale	Λ	R_1	None	R_2	Λ
current	$j_B(R_1)e^{-2\frac{(r-R_1)}{a\Lambda}}$	$1/\sqrt{\dots}$ divergence	vanishing current $\mathcal{O}(r/R_2)$ $-\frac{B_a c}{\pi^2} \frac{r}{R_2}$	$-\frac{B_a c}{\pi^2} \frac{r}{\sqrt{R_2^2 - r^2}}$	$j_B(R_2)e^{-\frac{(R_2-r)}{b\Lambda}}$
SOURCE	Bowers (unpublished) as quoted by Glover [175] as part of the discussion of [176, 177]	$1/\sqrt{\dots}$ numerically studied by Brandt et al. [180]	vanishing / homogeneous magnetic field in the middle of the sample	analytic result for disk by Ketchen et al. [158]	analog to the edge of R_1 (Bowers)

Table F.2: The current-density due to an applied field B_a . The slit in our geometry causes a flux ϕ_M to enter the inner ring R_1 so that the total current of the system is 0, approximated in different regions of the sample

Region 1 & 5: Close to the edges (dominant length scale Λ) the exponential screening suggested by Bowers should be dominant, as has been for the current density due to the trapped flux.

$$j_B(r) = j_B(R_2)e^{-2\frac{(R_2-r)}{b\Lambda}} \quad (\text{F.6})$$

Following the suggested form of Bowers. Here b is a numerical constant of order unity. For the width of the edge region $\frac{b\Lambda}{4}$ was suggested by Rhoderick and Wilson, [178], and was used for the trapped flux.

Region 2: For $|r - R_1| > \Lambda$ and $r \ll R_2$ the dominant length scale should be R_1 . Numerical work suggests a $1/\sqrt{\dots}$ divergence of the current density close to the edge for $\Lambda = 0$, which vanishes for finite Λ , [180]. An analytic expression is not known so far. However, for $R_1 = 0$ there is no current flowing in the center, so for vanishing R_1 the current density close to the edge needs to vanish as well. For small R_1 it is therefore reasonable to assume that the total current close to the edge is small, so it will not have a big effect on the total current I_m induced by the magnetic field.

Region 3: Deep inside the ring, when $R_1 \ll r \ll R_2$ there should be no length scale and therefor no real current. Extrapolation from the outer edge would give

$$j_B(r) = -\frac{B_a c}{\pi^2} \frac{r}{R_2}, \quad (\text{F.7})$$

which is vanishing for $r \ll R_2$. In the presents of a trapped flux, or if the ring has a small slit (washer with slit setup as discussed by Ketchen et al. [158]) where some flux ϕ_m can enter into the inner ring to counteract the applied magnetic field, the length scale of importance becomes the magnetic length $\sqrt{\frac{\phi_m}{B_a}}$ so that the current density would be of the form

$$j_B(r) = -\frac{B_a c}{\pi^2} f\left(\frac{r}{\sqrt{\frac{\phi_m}{B_a}}}\right) \quad (\text{F.8})$$

a linear form for $f(x) \sim x$ makes sense since it would produce a constant magnetic field analog to the extrapolation from the outer radius R_2 and since there is no other length scale in this region to justify a spatial inhomogeneous magnetic field.

Region 4: Away enough from the edge that the length Λ is not important anymore and so far away from the inner ring that R_1 does not play a role, the situation is equivalent to the one discussed by Ketchen et al. [158] ($\Lambda = 0$ and $R_1 = 0$), which they are able to solve analytically.

$$j_B(r) = -\frac{B_a c}{\pi^2} \frac{r}{\sqrt{R_2^2 - r^2}} \quad (\text{F.9})$$

close to the edge one expects the exponential shielding analog to the trapped flux, removing the singularity that would otherwise occur. The shielding current and the matching should be done similar to the previous section, resulting in

$$j_B(R_2) = \frac{\sqrt{e} B_a c (b\Lambda - 4R_2)}{\pi^2 \sqrt{b\Lambda(8R_2 - b\Lambda)}} \quad (\text{F.10})$$

Pearl's solution

In the special case of a trapped flux in a planar sheet (i.e. $R_1 \rightarrow 0$ and $R_2 \rightarrow \infty$) the current distribution is known to be that of the Pearl vortex, [125, 137]. The vector potential can be given as

$$f(r, z) = \frac{\phi_0}{2\pi} \int_0^\infty d\gamma \frac{1}{1 + \Lambda\gamma} J_1(\gamma r) e^{-\gamma|z|} \quad (\text{F.11})$$

resulting in a current density of

$$j(r) = \frac{\phi_0 c}{4\pi} \int_0^\infty d\gamma \frac{\gamma}{1 + \Lambda\gamma} J_1(\gamma r) = \frac{\phi_0 c}{8\pi\Lambda^2} \left[H_1\left(\frac{r}{\Lambda}\right) - Y_1\left(\frac{r}{\Lambda}\right) - \frac{2}{\pi} \right] \quad (\text{F.12})$$

with the Struve function $H_n(x)$ and the modified Bessel function $Y_n(x)$. The current density can be approximated by

$$j(r) \approx \frac{\phi_0 c}{4\pi^2} \frac{1}{r(r + \Lambda)} \quad (\text{F.13})$$

The approximation is also discussed in [137]. For distances much larger than Λ , the profile becomes that of a magnetic dipole with

$$j(r) \approx \frac{\phi_0 c}{4\pi^2} \frac{1}{r^2} \quad (\text{F.14})$$

F.2 Derivation of main equations

In this section, the derivation of the differential and integral equation describing the Corbino disk are presented in detail, starting from the Ginzburg–Landau Hamiltonian. The derivation of the differential equation is almost identical to the one presented by Fetter and Hohenberg, [137]. The difference to this work is, that here we consider a finite ring with an inner radius R_1 and an outer radius R_2 instead of just an infinite film. Once the differential equation is obtained, we will see that it cannot be solved by the Hankel transform anymore. This is due to the considered ring geometry. The Hankel transform can still be used to transform the differential equation into an integral equation. The integral equation will be the basis for the numerical procedure later on.

Derivation of differential equations

The basic equations describing the response of the superconducting disk in a magnetic field, are the Maxwell and London equations, which are conveniently combined in the Ginzburg–Landau Hamiltonian (see e.g. [123])

$$H = \int_{\mathbf{r}} \alpha |\Psi(\mathbf{r})|^2 + \frac{\beta}{2} |\Psi(\mathbf{r})|^4 + \frac{1}{2m^*} \left| \left(\frac{\hbar\nabla}{i} - \frac{e^*}{c} \mathbf{A}(\mathbf{r}) \right) \Psi(\mathbf{r}) \right|^2 + \frac{1}{8\pi} \int_{\mathbf{r}} (\nabla \times (\mathbf{A}(\mathbf{r}) - \mathbf{A}_a(\mathbf{r})))^2 \quad (\text{F.15})$$

for a particle of mass m^* and charge e^* (for a Cooper-pair we have $m^* = 2m_e$ and $e^* = 2e$). c denotes the speed of light and \mathbf{A}_a is the vector potential for the applied external field. For an infinitely thin disk, the super current density is restricted to the $z = 0$ layer and the region $R_1 \leq r \leq R_2$. This means that the superconducting order parameter $\psi(\mathbf{r})$ is zero outside the disk and can be written as

$$\Psi(\mathbf{x}) = d\delta(z)\Theta(r - R_1)\Theta(R_2 - r)\psi(r, \theta). \quad (\text{F.16})$$

A variation in respect to $\mathbf{A}(\mathbf{r})$ leads to the differential equations

$$-\frac{1}{4\pi} \nabla \times \nabla \times (\mathbf{A}(\mathbf{r}) - \mathbf{A}_a(\mathbf{r})) = \begin{cases} \frac{d\delta(z)}{2m^*} \left\{ -\frac{e^*}{c} [\psi^* \frac{\hbar\nabla}{i} \psi - \psi \frac{\hbar\nabla}{i} \psi^*] + 2\frac{e^{*2}}{c^2} \mathbf{A}(\mathbf{r}) |\psi|^2 \right\} & R_1 \leq r \leq R_2 \\ 0 & \text{elsewhere} \end{cases} \quad (\text{F.17})$$

Here we see the difference of the Corbino disk geometry compared to the thin film discussed e.g. by Fetter and Hohenberg, where $R_1 = 0$ and $R_2 = \infty$. The left hand side is connected to the current density \mathbf{j} via the Maxwell equation

$$\nabla \times \nabla \times \mathbf{A} = \nabla \times \mathbf{B} = \frac{4\pi}{c} \mathbf{j}. \quad (\text{F.18})$$

Assuming a constant order parameter throughout the sample (analog to Pearl, [125], or Fetter and Hohenberg, [137]) of the form

$$\psi(r, \theta) = \psi_0 e^{in\theta} \quad (\text{F.19})$$

with n being the winding number and $|\psi_0|^2 = n_s$ where n_s is the density of superconducting electrons. Now we can introduce the London penetration length λ and the flux quantum ϕ_0 according to [123] as well as the effective penetration length Λ

$$\lambda = \sqrt{\frac{m^* c^2}{4\pi n_s e^{*2}}} \quad \phi_0 = \frac{hc}{e^*} \quad \Lambda = \frac{2\lambda^2}{d} \quad (\text{F.20})$$

Using polar coordinates, $\nabla = \hat{r}\partial_r + \frac{1}{r}\hat{\theta}\partial_\theta + \hat{z}\partial_z$, we can evaluate

$$\psi^* \frac{\nabla}{i} \psi - \psi \frac{\nabla}{i} \psi^* = 2|\psi_0|^2 \frac{1}{r} \hat{\theta} = 2n_s \frac{1}{r} \hat{\theta} \quad (\text{F.21})$$

and the differential equation for the vector potential then reads as

$$-\nabla \times \nabla \times (\mathbf{A}(\mathbf{r}) - \mathbf{A}_a(\mathbf{r})) = \begin{cases} \frac{2}{\Lambda} \delta(z) \left\{ -\frac{n\phi_0}{2\pi r} \hat{\theta} + \mathbf{A}(\mathbf{r}) \right\} & R_1 \leq r \leq R_2 \\ 0 & \text{elsewhere} \end{cases} \quad (\text{F.22})$$

As discussed earlier, the applied field is homogenous with

$$\mathbf{A}_a(\mathbf{r}) = \frac{1}{2} B_a r \hat{\theta} \quad (\text{F.23})$$

and due to the rotational symmetry, the vector potential only has a $\hat{\theta}$ component and can be written as

$$\mathbf{A}(\mathbf{r}) = f(r, z) \hat{\theta} + \frac{1}{2} B_a r \hat{\theta} \quad (\text{F.24})$$

with the reduced vector potential $f(r, z)$. This leads to a differential equation for $f(r, z)$ of the form

$$\left[\frac{\partial^2}{\partial z^2} + \frac{\partial}{\partial r} \frac{1}{r} \frac{\partial}{\partial r} r \right] f(r, z) = -\frac{4\pi}{c} j(r) \delta(z) = \begin{cases} \frac{2}{\Lambda} \delta(z) \left[f(r, z) + \frac{B_a r}{2} - \frac{n\phi_0}{2\pi r} \right], & R_1 \leq r \leq R_2, \\ 0 & \text{elsewhere.} \end{cases} \quad (\text{F.25})$$

For $R_1 \rightarrow 0$ and $R_2 \rightarrow \infty$ with $B_a = 0$ this differential equation is identical to the one used in [137] to re-derive Pearl's result.

Derivation of Integral equations

A general solution for the homogeneous part of the differential equation can be given by using the eigenfunctions of the differential operators ∂_z and $\partial_r \frac{1}{r} \partial_r r$.

$$\frac{\partial^2}{\partial z^2} e^{-\gamma|z|} = \gamma^2 e^{-\gamma|z|} - 2\delta(z)\gamma \quad (\text{F.26})$$

$$\frac{\partial}{\partial r} \frac{1}{r} \frac{\partial}{\partial r} r J_1(\gamma r) = -\gamma^2 J_1(\gamma r) \quad (\text{F.27})$$

From this it can be easily seen that for $z > 0$ the function $J_1(\gamma r)e^{-\gamma|z|}$ solves the homogeneous part of the differential equation for every γ . This is the basis for the ansatz used by Pearl, [125],

$$f(r, z) = \int_0^\infty d\gamma g(\gamma) J_1(\gamma r) e^{-\gamma|z|} \quad (\text{F.28})$$

which reduces the vector potential $f(r, z)$ to the unknown function $g(\gamma)$. After plugging the ansatz in, the differential equation reduces to

$$-\Lambda \int_0^\infty d\gamma \gamma g(\gamma) J_1(\gamma r) = \Theta(r - R_1) \Theta(R_2 - r) \left[\int_0^\infty d\gamma g(\gamma) J_1(\gamma r) + B_a \frac{r}{2} - \frac{\phi_f}{2\pi r} \right] \quad (\text{F.29})$$

Now using the orthogonal relation of the Bessel functions

$$\int_0^\infty dt J_\nu(xt) t J_\nu(yt) = \frac{1}{x} \delta(x - y) \quad (\text{F.30})$$

we can properly transform the equation into an integral equation for $g(\gamma)$ by applying

$$\int_0^\infty dr r J_1(r\eta) (\dots) \quad (\text{F.31})$$

to both sides. This transformation is also known as Hankel transform, with the interesting feature of being its own inverse, a fact we will use later. Applying the Hankel transform results in

$$-\Lambda g(\eta) = \frac{B_a}{2} \int_{R_1}^{R_2} dr r^2 J_1(r\eta) - \frac{\phi_f}{2\pi} \int_{R_1}^{R_2} dr J_1(r\eta) + \int_0^\infty d\gamma \int_{R_1}^{R_2} dr r g(\gamma) J_1(\gamma r) J_1(r\eta). \quad (\text{F.32})$$

Unlike the case discussed by Fetter and Hohenberg where $R_1 = 0$ and $R_2 = \infty$, the integrals with finite limits are not easy to handle. The kernel of the last integral can be brought into a nicer form by splitting the integral into the 2 parts

$$\int_{R_1}^{R_2} = - \int_0^{R_1} + \int_0^{R_2} \quad (\text{F.33})$$

Now the integral equation in its full form can be written as

$$\Lambda g(\eta) = h_\phi(\eta) - h_B(\eta) + \int_0^\infty d\gamma g(\gamma) \{K_1(\gamma, \eta) - K_2(\gamma, \eta)\} \quad (\text{F.34})$$

$$h_\phi(\eta) = \frac{\phi_f}{2\pi} \int_{R_1}^{R_2} dr J_1(r\eta) = \frac{\phi_f}{2\pi} \frac{1}{\eta} (J_0(R_1\eta) - J_0(R_2\eta)) \quad (\text{F.35})$$

$$h_B(\eta) = \frac{B_a}{2} \int_{R_1}^{R_2} dr r^2 J_1(r\eta) = \frac{B_a}{2} \frac{1}{\eta} (-R_1^2 J_2(R_1\eta) + R_2^2 J_2(R_2\eta)) \quad (\text{F.36})$$

$$K_{1/2}(\gamma, \eta) = \int_0^{R_{1/2}} dr J_1(\gamma r) r J_1(r\eta) \quad (\text{F.37})$$

$$= \frac{R_{1/2}}{\gamma^2 - \eta^2} \{ \eta J_0(R_{1/2}\eta) J_1(R_{1/2}\gamma) - \gamma J_0(R_{1/2}\gamma) J_1(R_{1/2}\eta) \} \quad (\text{F.38})$$

which is a **type II inhomogeneous Fredholm Integral equation**. Since the equation is linear, we can split the inhomogeneous part and treat the two functions $h_\phi(\eta)$ and $h_B(\eta)$ separately,

being equivalent to calculating the different contributions $j_\phi(r)$ and $j_B(r)$. Using the Pearl ansatz on the left hand side of equation (11.8), we can relate the current density $j(r)$ and the function $g(\gamma)$ via

$$j(r) = \frac{c}{2\pi} \int_0^\infty d\gamma \gamma g(\gamma) J_1(\gamma r) \quad (\text{F.39})$$

F.3 Limiting cases and solutions to integral equations

Using the derived integral equations for $g(\gamma)$ we can look at different scenarios and solve different limiting cases. We will split the discussion again into the response to the trapped flux ϕ_f and the response to the magnetic field B_a .

Equation for the trapped flux ϕ_f

Limit $R_2 \rightarrow \infty$ Let us start with the special case of $R_2 \rightarrow \infty$, a thin sheet with a hole of radius R_1 , in which case the integration Kernel $K_2(\eta, \gamma)$ and the inhomogeneous part $h_\phi(\eta)$ simplify to

$$\lim_{R_2 \rightarrow \infty} K_2(\eta, \gamma) = \frac{1}{\eta} \delta(\eta - \gamma) \quad (\text{F.40})$$

$$\lim_{R_2 \rightarrow \infty} h_\phi(\eta) = \frac{\phi_f}{2\pi} \frac{J_0(R_1\eta)}{\eta} \quad (\text{F.41})$$

The equation for $g(\eta)$ can then be written as

$$g(\eta) = \frac{\phi_f}{2\pi} \frac{J_0(R_1\eta)}{1 + \Lambda\eta} + \frac{\eta}{1 + \Lambda\eta} \int_0^\infty d\gamma g(\gamma) K_1(\gamma, \eta) \quad (\text{F.42})$$

for $R_1 \rightarrow 0$ we have $K_1(\gamma, \eta) \rightarrow 0$ and $J_0(0) = 1$, leading to Pearl's solution of $g(\gamma) = \frac{\phi_f}{2\pi} \frac{1}{1 + \Lambda\gamma}$. To compute the $\Lambda \rightarrow 0$ limit to compare to already obtained analytic results, it turns out to be quite useful to employ a Hankel transform once more, this time with the $J_0(x)$ basis, introducing

$$g(\eta) = \int_0^\infty dx h(x) J_0(x\eta) \quad (\text{F.43})$$

substituting $g(\eta)$ in equation (F.42)

$$\int_0^\infty dx h(x) J_0(x\eta) = \frac{\phi_f}{2\pi} \frac{J_0(R_1\eta)}{1 + \Lambda\eta} + \frac{\eta}{1 + \Lambda\eta} \int_0^\infty d\gamma \int_0^\infty dx h(x) K_1(\gamma, \eta) J_0(\gamma x) \quad (\text{F.44})$$

and using

$$\int_0^\infty d\gamma J_0(x\gamma) K_1(\gamma, \eta) = \int_0^\infty d\gamma \int_0^{R_1} dr J_0(x\gamma) r J_1(r\gamma) J_1(r\eta) \quad (\text{F.45})$$

$$\int_0^\infty d\gamma J_0(x\gamma) J_1(r\gamma) = \begin{cases} \frac{1}{r} & r > x \\ 0 & r \leq x \end{cases} \quad (\text{F.46})$$

$$\int_x^{R_1} J_1(r\eta) = \frac{1}{\eta} (J_0(x\eta) - J_0(R_1\eta)) \Theta(a - x) \quad (\text{F.47})$$

leaves us with

$$\int_0^\infty dx h(x) J_0(x\eta) = \frac{\phi_f}{2\pi} \frac{J_0(R_1\eta)}{1 + \Lambda\eta} + \frac{1}{1 + \Lambda\eta} \int_0^{R_1} dx h(x) \{J_0(x\eta) - J_0(R_1\eta)\} \quad (\text{F.48})$$

Now we will use the orthogonality of the Bessel functions. Applying $\int_0^\infty d\eta \eta J_0(\eta x)(\dots)$ to both sides we get

$$h(x) = \frac{\phi_f}{2\pi} x k(R_1, x) - x k(R_1, x) \int_0^{R_1} d\eta h(\eta) + x \int_0^{R_1} d\eta h(\eta) k(\eta, x) \quad (\text{F.49})$$

where we introduced

$$k(x, y) = \int_0^\infty d\eta \frac{J_0(x\eta)\eta J_0(y\eta)}{1 + \Lambda\eta} \quad (\text{F.50})$$

as a test, we can check the $R_1 \rightarrow 0$ limit again, in which this equation reduces to Pearls result (as it should). For $\Lambda \rightarrow 0$ we find

$$\lim_{\Lambda \rightarrow 0} k(x, y) = \frac{1}{x} \delta(x - y) \quad (\text{F.51})$$

resulting in a $h(x) = 0$ for $x > R_1$ and for $x \leq R_1$

$$\int_0^{R_1} dx h(x) = \frac{\phi_f}{2\pi} \quad (\text{F.52})$$

This integral equation for $h(x)$ has the following non-trivial solution of

$$h(x) = \frac{\phi_f}{2\pi} \frac{x}{R_1 \sqrt{R_1^2 - x^2}} \Theta(R_1 - x) \quad (\text{F.53})$$

Now we can compute $g(\gamma)$ via the inverse Hankel transform, which evaluates to

$$g(\gamma) = \int_0^\infty dx h(x) J_0(x\gamma) = \frac{\phi_f}{2\pi} \frac{\sin(R_1\gamma)}{R_1\gamma} = \frac{\phi_f}{2\pi} j_0(R_1\gamma) \quad (\text{F.54})$$

where $j_0(x)$ is the spherical Bessel function. Using the relation between $g(\gamma)$ and the current density, equation (F.39),

$$\int_0^\infty d\gamma \gamma g(\gamma) J_1(\gamma r) = \frac{2\pi}{c} j(r) \quad (\text{F.55})$$

and the integral relation

$$\int_0^\infty d\gamma \gamma j_0(\gamma) J_1(\gamma r) = \begin{cases} \frac{1}{r\sqrt{r^2 - R_1^2}} & r > R_1 \\ 0 & r < R_1 \end{cases} \quad (\text{F.56})$$

we can compute the current distribution due to the trapped flux ϕ_f as

$$j_\phi(r) = \frac{\phi_f c}{4\pi^2} \frac{1}{r\sqrt{r^2 - R_1^2}} \Theta(r - R_1) \quad (\text{F.57})$$

which is identical to the analytically obtained result in [158], obtained by mapping to an electrostatic problem. The derived integral equation contains the correct limiting cases for $\Lambda \rightarrow 0$ and $R_2 \rightarrow \infty$.

Limit $R_1 \rightarrow 0$ In the case of $R_1 \rightarrow 0$ the system is reduced to a disk and the integration kernel $K_1(\gamma, \eta)$ and the inhomogeneous part $h_\phi(\eta)$ simplify to

$$\lim_{R_1 \rightarrow 0} K_1(\gamma, \eta) = 0 \quad (\text{F.58})$$

$$\lim_{R_1 \rightarrow 0} h_\phi(\eta) = \frac{\phi_f}{2\pi} \frac{1}{\eta} (1 - J_0(R_2\eta)) \quad (\text{F.59})$$

leaving us with

$$\Lambda g(\eta) = \frac{\phi_f}{2\pi} \frac{1}{\eta} (1 - J_0(R_2\eta)) - \int_0^\infty d\gamma g(\gamma) K_2(\gamma, \eta) \quad (\text{F.60})$$

introducing (as in the previous section) $g(\eta) = \int_0^\infty dx h(x) J_0(x\eta)$ we can transform the equation to

$$\Lambda \int_0^\infty dx h(x) J_0(x\eta) = \frac{\phi_f}{2\pi} \frac{1}{\eta} (1 - J_0(R_2\eta)) - \frac{1}{\eta} \int_0^{R_2} dx h(x) \{J_0(x\eta) - J_0(R_2\eta)\} \quad (\text{F.61})$$

applying $\int_0^\infty d\eta \eta J_0(\eta t)(\dots)$ to the equation yields

$$\Lambda h(t) = \frac{\phi_f}{2\pi} (tk(0, t) - tk(R_2, t)) + tk(R_2, t) \int_0^{R_2} dx h(x) - t \int_0^{R_2} dx h(x) k(x, t) \quad (\text{F.62})$$

with

$$k(x, y) = \int_0^\infty d\gamma J_0(x\gamma) J_0(y\gamma) = \begin{cases} \frac{2K\left(\frac{y^2}{x^2}\right)}{\pi x} & x > y \\ \frac{2K\left(\frac{x^2}{y^2}\right)}{\pi y} & x < y \end{cases} \quad (\text{F.63})$$

$$yk(0, y) = 1 \quad (\text{F.64})$$

where $K(x)$ is the elliptic integral defined according to Mathematica, equation (F.77). Limiting cases like $\Lambda \rightarrow 0$ are not known nor can we calculate any analytic solutions at this point.

Equation for the applied field B_a

Setting the trapped flux $\phi_f = 0$ we will focus solely on the effect of the magnetic field in this section.

Limit $R_1 \rightarrow 0$ For the limit of vanishing inner radius $R_1 \rightarrow 0$ we find

$$\lim_{R_1 \rightarrow 0} K_1(\gamma, \eta) = 0 \quad (\text{F.65})$$

$$\lim_{R_1 \rightarrow 0} h_B(\eta) = \frac{B_a}{2} \frac{1}{\eta} R_2^2 J_2(R_2\eta) \quad (\text{F.66})$$

Resulting in the following simplified integral equations for $g(\eta)$

$$\Lambda g(\eta) = -\frac{B_a}{2} \frac{1}{\eta} R_2^2 J_2(R_2\eta) - \int_0^\infty d\gamma g(\gamma) K_2(\gamma, \eta) \quad (\text{F.67})$$

To simplify the notation we will introduce the dimensionless function $\tilde{g}(\eta)$ via $g(\eta) = \frac{B_a}{2} R_2^2 \tilde{g}(\eta)$

$$\Lambda \tilde{g}(\eta) = -\frac{1}{\eta} J_2(R_2\eta) - \int_0^\infty d\gamma \tilde{g}(\gamma) K_2(\gamma, \eta) \quad (\text{F.68})$$

This can be solved for the $\Lambda = 0$ by

$$\tilde{g}(\eta) = -\frac{4}{\pi}j_1(R_2\eta) \quad (\text{F.69})$$

with $j_1(x)$ being a spherical Bessel function. Calculating the current density

$$j_B(r) = \frac{2c}{4\pi} \int_0^\infty d\gamma \gamma g(\gamma) J_1(\gamma r) = -\frac{B_a c}{\pi^2} \frac{r}{\sqrt{R_2^2 - r^2}} \Theta(R_2 - r) \quad (\text{F.70})$$

we get the known analytic result as found in [158] and discussed earlier.

Limit $R_2 \rightarrow \infty$ In the case of the applied field B_a the limit $R_2 \rightarrow \infty$ is problematic since the inhomogeneous part $h_B(\eta)$ will diverge

$$\lim_{R_2 \rightarrow \infty} h_B(\eta) = \infty \quad (\text{F.71})$$

F.4 Numerical approach

We are able to reproduce the known limiting cases for the current density profile, but still have not solved the equations completely. The main goal in of this section is to construct an approximate expression for the full current distribution. To do so, we will first rewrite the integral equations to be dependent of $j(r)$ instead of $g(\gamma)$. Then we will construct the $j(r)$ profile based on the known limiting cases. Using the integral equations for $j(r)$ we will construct a fitting mechanism to determine any free parameter in the constructed profile.

Integral equations for the current density

The integral equation for $g(\gamma)$ can be solved in different limiting cases and once $g(\gamma)$ is known the vector potential $f(r, z)$ and the current density $j(r)$ can be calculated. Interpolating between known analytic results in the framework of $g(\gamma)$ however is tedious and considering the knowledge we have of $j(r)$ in different limits (see discussion in section 11.2) it would be convenient to work with an integral equation directly for $j(r)$. We will derive said equation in this section.

Using the Pearl ansatz on the left hand side of equation (11.8), we can relate the current density $j(r)$ and the function $g(\gamma)$ via

$$j(r) = \frac{c}{2\pi} \int_0^\infty d\gamma \gamma g(\gamma) J_1(\gamma r) \quad (\text{F.72})$$

which can be identified as the Hankel transform. The inversion of the Hankel transform is known and gives

$$g(\gamma) = \frac{2\pi}{c} \int_0^\infty dr r j(r) J_1(\gamma r) \quad (\text{F.73})$$

which can be plugged into equation (F.29) to give an integral equation for the current density $j(r)$

$$-\Lambda \frac{2\pi}{c} j(r) = \Theta(r - R_1) \Theta(R_2 - r) \left(B_a \frac{r}{2} - \frac{\phi_f}{2\pi} \frac{1}{r} + \frac{2\pi}{c} \int_0^\infty d\gamma \int_0^\infty dr' j(r') r' J_1(\gamma r') J_1(\gamma r) \right) \quad (\text{F.74})$$

with $j(r) = 0$ outside the disk we get

$$\Lambda j(r) = -\frac{B_a c}{4\pi} r + \frac{\phi_f c}{4\pi^2} - \int_{R_1}^{R_2} dr' j(r') r' k(r', r) \quad (\text{F.75})$$

$$k(r', r) = \int_0^\infty d\gamma J_1(\gamma r') J_1(\gamma r) = \begin{cases} \frac{2}{\pi b} \left(K\left(\frac{b^2}{a^2}\right) - E\left(\frac{b^2}{a^2}\right) \right) & a > b \\ \frac{2}{\pi a} \left(K\left(\frac{a^2}{b^2}\right) - E\left(\frac{a^2}{b^2}\right) \right) & a < b \end{cases} \quad (\text{F.76})$$

Where $K(x)$ and $E(x)$ are the elliptic integrals in the Mathematica definition

$$K(x) = \int_0^{\frac{\pi}{2}} d\theta \frac{1}{\sqrt{1-x\sin^2(\theta)}} \quad E(x) = \int_0^{\frac{\pi}{2}} d\theta \sqrt{1-x\sin^2(\theta)} \quad (\text{F.77})$$

With

$$\int_0^\infty d\gamma J_1(\gamma r) J_1(\gamma r') e^{-\gamma|z|} = \frac{1}{\pi\sqrt{rr'}} Q_{\frac{1}{2}} \left(\frac{z^2 + r^2 + r'^2}{2rr'} \right) \quad (\text{F.78})$$

(Prudnikov, Brychkov & Marichev Bd. II, p. 218), [160], and $Q_\nu(x)$ the Legendre function of the second kind defined as

$$Q_\nu(z) = \frac{\sqrt{\pi}\Gamma(\nu+1)}{2^{\nu+1}\Gamma(\nu+\frac{3}{2})} \frac{1}{z^{\nu+1}} {}_2F_1\left(\frac{\nu+1}{2}, \frac{\nu+2}{2}; \nu+\frac{3}{2}, \frac{1}{z^2}\right) \quad (\text{F.79})$$

using the hypergeometric function ${}_2F_1(a, b; c; x)$. For arguments $z > 1$ the Legendre function $Q_\nu(z)$ has an imaginary part, while the integral (left hand side) is always real. Taking the real part (Re) of the Legendre function, one can numerically verify, that

$$\frac{1}{\pi\sqrt{ab}} Re(Q_{\frac{1}{2}}\left(\frac{a^2+b^2}{2ab}\right)) = \begin{cases} \frac{2}{\pi b} \left(K\left(\frac{b^2}{a^2}\right) - E\left(\frac{b^2}{a^2}\right) \right) & a > b \\ \frac{2}{\pi a} \left(K\left(\frac{a^2}{b^2}\right) - E\left(\frac{a^2}{b^2}\right) \right) & a < b \end{cases} \quad (\text{F.80})$$

With this, the integral equation for $j(r)$ (inside the superconductor) can be written as

$$\Lambda j(r) = -\frac{B_a c}{4\pi} r + \frac{\phi_f c}{4\pi^2} \frac{1}{r} - \int_{R_1}^{R_2} dr' j(r') \tilde{k}\left(\frac{r}{r'}\right) \quad (\text{F.81})$$

$$\tilde{k}(x) = \frac{1}{\pi\sqrt{x}} Re \left[Q_{\frac{1}{2}} \left(\frac{1}{2} \left(x + \frac{1}{x} \right) \right) \right] \quad (\text{F.82})$$

This is the integral equation for $j(r)$ we were looking for. Due to the nature of the kernel, an analytic solution is not known.

Integral equations for $f(r, z)$ dependent on $j(r)$ and $B(r, z)$ dependent on $j(r)$

With the relation between $g(\gamma)$ and $j(r)$ from equation (F.73) we can also calculate the magnetic field as a function of $j(r)$ using the ansatz for the vector potential $f(r, z)$

$$\begin{aligned} f(r, z) &= \int_0^\infty d\gamma g(\gamma) J_1(\gamma r) e^{-\gamma|z|} \\ &= \frac{2}{c} \int_{R_1}^{R_2} dr' j(r') \sqrt{\frac{r'}{r}} Re \left[Q_{\frac{1}{2}} \left(\frac{z^2 + r^2 + r'^2}{2rr'} \right) \right] \end{aligned} \quad (\text{F.83})$$

with the equation for the magnetic field

$$B_r(r, z) = -\frac{\partial}{\partial z} f(r, z) \quad (\text{F.84})$$

$$B_z(r, z) = \frac{1}{r} \frac{\partial}{\partial r} r f(r, z) + B_a \quad (\text{F.85})$$

Using the relation $\frac{1}{r} \partial_r r J_1(\gamma r) = \gamma J_0(\gamma r)$ and the integrals

$$\int_0^\infty d\gamma J_1(\gamma r) \gamma J_1(\gamma r') e^{-\gamma|z|} = \frac{|z|k}{4\pi(1-k^2)(rr')^{\frac{3}{2}}} [(2-k^2)E(k^2) - 2(1-k^2)K(k^2)]$$

$$\equiv b_r(r, r', z) \quad (\text{F.86})$$

$$k = \frac{2\sqrt{rr'}}{\sqrt{z^2 + (r+r')^2}} \quad (\text{F.87})$$

(Prudnikov, Brychkov & Marichev Bd. II, p. 220), [160],

$$\int_0^\infty d\gamma J_0(\gamma r) \gamma J_1(\gamma r') e^{-\gamma|z|} = \frac{k}{8\pi r'^{\frac{5}{2}} r^{\frac{3}{2}} (1-k^2)} [k^2(r'^2 - r^2 - z^2)E(k^2) + 4rr'(1-k^2)K(k^2)]$$

$$\equiv b_z(r, r', z) \quad (\text{F.88})$$

(Prudnikov, Brychkov & Marichev Bd. II, p. 220), [160]¹. The magnetic field can be determined to be

$$B_r(r, z) = \frac{2\pi}{c} \int_{R_1}^{R_2} dr' r' j(r') b_r(r, r', z) \quad (z \neq 0) \quad (\text{F.89})$$

$$B_z(r, z) = \frac{2\pi}{c} \int_{R_1}^{R_2} dr' r' j(r') b_z(r, r', z) + B_a \quad (\text{F.90})$$

The integral equation for $j(r)$ can be used to find an approximate solution to the current profile by using the known cases and limits to construct an approximation whose parameters are fitted to produce the best solution to equation (F.81). Since we are dealing with a linear equation, we can split the current density into two parts, one due to the trapped flux $j_\phi(r)$ and one due to the applied field $j_B(r)$.

Trapped flux ($\phi_f \neq 0$, $B_a = 0$)

To simplify the equations, let us introduce the rescaled current density $\tilde{j}_\phi(r)$ according to

$$j_\phi(r) = \frac{\phi_f c}{4\pi^2} \tilde{j}_\phi(r) \quad (\text{F.91})$$

leading to the integral equation

$$\Lambda \tilde{j}_\phi(r) = \frac{1}{r} - \int_{R_1}^{R_2} dr' \tilde{j}_\phi(r') \tilde{k}\left(\frac{r}{r'}\right) \quad (\text{F.92})$$

¹Note that [160] uses the Elliptic integrals as defined by Gradshteyn-Ryzhik which relates to the definition used here via $E_{GR}(x) = E(x^2)$ and $K_{GR}(x) = K(x^2)$.

The approximate form for the current-density used is

$$\tilde{j}_\phi(r) = \frac{c_0 + c_1 \frac{r}{R_2} + c_2 \frac{r^2}{R_2^2}}{r \sqrt{(r + R_1 + \Lambda)(r - R_1 + \Lambda)} \sqrt{\left(1 - \frac{r}{R_2} + \frac{\Lambda}{R_2}\right) \left(1 + \frac{r}{R_2} + \frac{\Lambda}{R_2}\right)}} \quad (\text{F.93})$$

with the free parameters $\{c_0, c_1, c_2\}$.

$$\lim_{R_1 \rightarrow 0} \lim_{R_2 \rightarrow \infty} \tilde{j}_\phi(r) = \frac{c_0}{r(r + \Lambda)} \quad \text{with } c_0 = 1 \text{ this becomes the approximate Pearl solution} \quad (\text{F.94})$$

$$\lim_{\Lambda \rightarrow 0} \lim_{R_2 \rightarrow \infty} \tilde{j}_\phi(r) = \frac{c_0}{r \sqrt{r^2 - R_1^2}} \quad \text{with } c_0 = 1 \text{ this becomes the exact solution} \quad (\text{F.95})$$

and for $\Lambda = 0$ we have a square-root divergence at both the inner and outer radius, as seen in thin strips and numerics e.g. (Brandt and Clem [180]), making this a reasonable approximation. The coefficients $\{c_0, c_1, c_2\}$ are determined by minimizing the quadratic deviation of $\Lambda \tilde{j}_\phi(r) + \int_{R_1}^{R_2} dr' \tilde{j}_\phi(r') \tilde{k}(r/r')$ to the inhomogeneity $1/r$ over several equidistant points N

$$\min_{\{c_0, c_1, c_2\} \in \mathbb{R}} \left[\sum_i^N \left(\Lambda \tilde{j}_\phi(r_i) + \int_{R_1}^{R_2} dr' \tilde{j}_\phi(r') \tilde{k}\left(\frac{r_i}{r'}\right) - \frac{1}{r_i} \right)^2 \right] \quad (\text{F.96})$$

In figure F.2 an example for the current density profile is shown. The fitted coefficients $\{c_0, c_1, c_2\}$

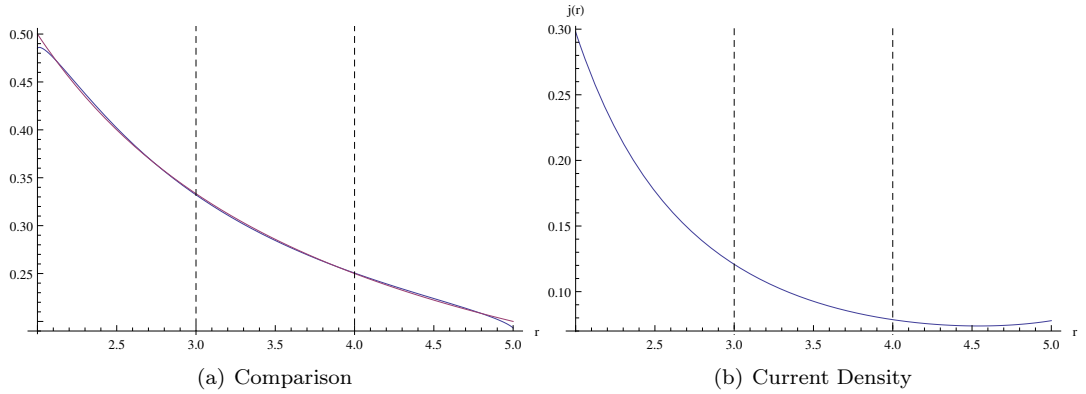
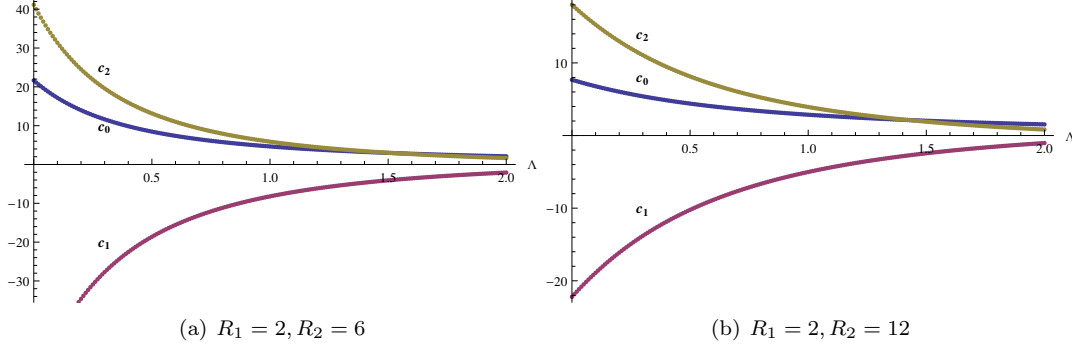


Figure F.2: On the left the comparison of the inhomogeneity $\frac{1}{r}$ (purple curve) with the integral part $\Lambda j(r) + \int_{R_1}^{R_2} dr' j(r') k(r/r')$ (blue curve) is shown. The exact solution would lead to an exact match of these two figures. This example is calculated for $\Lambda = 1$, $R_1 = 2$ and $R_2 = 5$, the dashed lines mark the distance Λ from the borders. On the right hand side the best approximation for the current density is shown.

for different Λ and two sets of radii are shown in figure F.3

Figure F.3: Fitted coefficients $\{c_0, c_1, c_2\}$ for different Λ and fixed Radii.

Applied magnetic field ($\phi_f = 0, B_a \neq 0$)

For the case of the applied field, we introduced the rescaled current density $\tilde{j}_B(r)$ according to

$$j_B(r) = -\frac{B_a c}{4\pi} \tilde{j}_B(r) \quad (\text{F.97})$$

leading to the integral equation

$$\Lambda \tilde{j}_B(r) = r - \int_{R_1}^{R_2} dr' \tilde{j}_B(r') \tilde{k}\left(\frac{r}{r'}\right) \quad (\text{F.98})$$

Here the approximate current density

$$\tilde{j}_B(r) = \frac{R_2 \left(d_0 + d_1 \frac{r}{R_2} + d_2 \frac{r^2}{R_2^2} + d_4 \frac{r^4}{R_2^4} \right)}{\sqrt{(r + R_1 + \Lambda)(r - R_1 + \Lambda)} \sqrt{\left(1 - \frac{r}{R_2} + \frac{\Lambda}{R_2}\right) \left(1 + \frac{r}{R_2} + \frac{\Lambda}{R_2}\right)}} \quad (\text{F.99})$$

with the limiting case

$$\lim_{\Lambda \rightarrow 0} \lim_{R_1 \rightarrow 0} \tilde{j}_B(r) = \frac{R_2^2 \left(d_0 + d_1 \frac{r}{R_2} + d_2 \frac{r^2}{R_2^2} + d_4 \frac{r^4}{R_2^4} \right)}{r \sqrt{R_2^2 - r^2}} \quad \text{exact for } d_0 = d_1 = d_4 = 0, d_2 = 1 \quad (\text{F.100})$$

Analog to the trapped flux calculation we determine the coefficients $\{d_0, d_1, d_2, d_4\}$ by minimizing

$$\min_{\{d_0, d_1, d_2, d_4\} \in \mathbb{R}} \left[\sum_i^N \left(\Lambda \tilde{j}_B(r_i) + \int_{R_1}^{R_2} dr' \tilde{j}_B(r') \tilde{k}\left(\frac{r_i}{r'}\right) - r_i \right)^2 \right] \quad (\text{F.101})$$

by splitting the interval $[R_1, R_2]$ into N equidistant points $\{r_i\}$. The fitted coefficients $\{d_0, d_1, d_2, d_4\}$ for different Λ and two sets of radii are shown in figure F.5

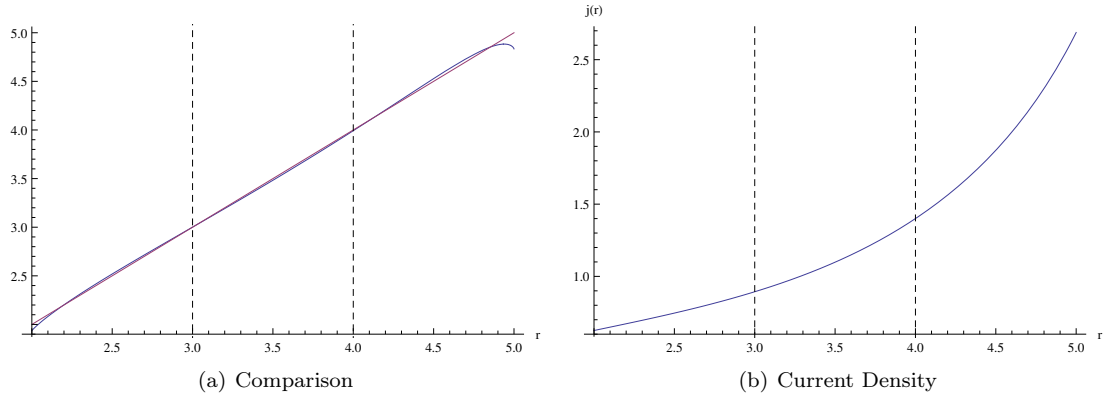


Figure F.4: On the left the comparison of the inhomogeneity r (purple curve) with the integral part $\Lambda j(r) + \int_{R_1}^{R_2} dr' j(r') k(r/r')$ (blue curve) is shown. The exact solution would lead to an exact match of these two figures. This example is calculated for $\Lambda = 1$, $R_1 = 2$ and $R_2 = 5$, the dashed lines mark the distance Λ from the borders. On the right hand side the best approximation for the current density is shown.

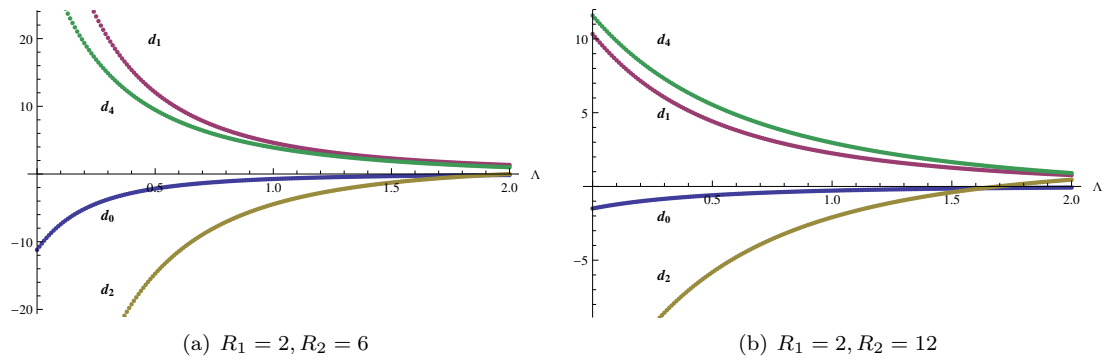


Figure F.5: Fitted coefficients $\{d_0, d_1, d_2, d_4\}$ for different Λ and fixed Radii.

Bibliography

- [1] D. P. Landau and E. M. Lifshitz. *Statistical Physics*. 1970.
- [2] J. M. Yeomans. *Statistical Mechanics of Phase Transitions*. 1992.
- [3] J. Cardy. *Scaling and Renormalization in Statistical Physics*. Cambridge Lecture Notes in Physics 5. Cambridge University Press, 1996.
- [4] S.-K. Ma. *Modern Theory of Critical Phenomena*. Frontiers in Physics. W. A. Benjamin, Inc., 1976.
- [5] P. Chaikin and T. Lubensky. *Principles of condensed matter physics*. Cambridge, 1995.
- [6] L. D. Landau and E. M. Lifshitz. *Quantum Mechanics*. Course of Theoretical Physics. Butterworth-Heinemann, 3rd edition, 1977.
- [7] D. C. Mattis. *The Theory of Magnetism*. Springer Series in Solid-State Sciences. Springer Berlin Heidelberg, 1981.
- [8] A. Auerbach. *Interacting Electrons and Quantum Magnetism*. Graduate Texts in Contemporary Physics. Springer Verlag, 1994.
- [9] E. Ising. Beitrag zur Theorie des Ferromagnetismus. *Zeitschrift für Physik*, **31**(1), 253–258, 1925. ISSN 0044-3328.
- [10] A. Altland and B. Simons. *Condensed Matter Field Theory*. Cambridge University Press, second edition, 2010.
- [11] R. Peierls. On Ising’s model of ferromagnetism. *Mathematical Proceedings of the Cambridge Philosophical Society*, **32**, 477–481, 10 1936. ISSN 1469-8064.
- [12] L. Onsager. Crystal Statistics. I. A Two-Dimensional Model with an Order-Disorder Transition. *Phys. Rev.*, **65**, 117–149, Feb 1944.
- [13] N. Mermin and H. Wagner. Absence of Ferromagnetism or Antiferromagnetism in One- or Two-Dimensional Isotropic Heisenberg Models. *Phys. Rev. Lett.*, **17**, 1133–1136, Nov 1966.
- [14] V. L. Berezinskii. Violation of long range order in one-dimensional and two-dimensional systems with a continuous symmetry group. I. Classical systems. *JETP*, **32**, 493–500, 1971.
- [15] J. M. Kosterlitz and D. J. Thouless. Ordering, metastability and phase transitions in two-dimensional systems. *Journal of Physics C: Solid State Physics*, **6**(7), 1181, 1973.
- [16] J. Villain. La structure des substances magnetiques. *Journal of Physics and Chemistry of Solids*, **11**(3-4), 303–309, 1959. ISSN 0022-3697.
- [17] A. Yoshimori. A New Type of Antiferromagnetic Structure in the Rutile Type Crystal. *Journal of the Physical Society of Japan*, **14**(6), 807–821, 1959.

- [18] F. Li, T. Nattermann, and V. L. Pokrovsky. Vortex Domain Walls in Helical Magnets. *Phys. Rev. Lett.*, **108**, 107203, Mar 2012.
- [19] M. Mostovoy. Ferroelectricity in Spiral Magnets. *Phys. Rev. Lett.*, **96**, 067601, Feb 2006.
- [20] X. G. Wen, F. Wilczek, and A. Zee. Chiral spin states and superconductivity. *Phys. Rev. B*, **39**, 11413–11423, Jun 1989.
- [21] D. I. Khomskii. Spin chirality and nontrivial charge dynamics in frustrated Mott insulators: spontaneous currents and charge redistribution. *Journal of Physics: Condensed Matter*, **22**(16), 164209, 2010.
- [22] A. Kolezhuk and T. Vekua. Field-induced chiral phase in isotropic frustrated spin chains. *Phys. Rev. B*, **72**, 094424, Sep 2005.
- [23] J.-C. Domenge, P. Sindzingre, C. Lhuillier, and L. Pierre. Twelve sublattice ordered phase in the J_1 - J_2 model on the kagomé lattice. *Phys. Rev. B*, **72**, 024433, Jul 2005.
- [24] E. A. Turov. The Magnetism of the Rare-Earth Metals. In S. Krupcka and J. Sternberg, editors, *Elements of Theoretical Magnetism*. ILIFFE Books LTD, 1968.
- [25] J. Jensen and A. R. Mackintosh. *Rare Earth Magnetism Structures and Excitations*. CLARENDON PRESS, 1991.
- [26] P. G. DeGennes. Interactions indirectes entre couches 4f dans les métaux de terres rares. *J. Phys. Radium*, **23**(8-9), 510–521, 1962.
- [27] Y. Ishikawa, K. Tajima, D. Bloch, and M. Roth. Helical spin structure in manganese silicide MnSi. *Solid State Communications*, **19**(6), 525–528, jul 1976. ISSN 0038-1098.
- [28] M. Uchida, Y. Onose, Y. Matsui, and Y. Tokura. Real-Space Observation of Helical Spin Order. *Science*, **311**(5759), 359–361, 2006.
- [29] S. S. P. Parkin, M. Hayashi, and L. Thomas. Magnetic Domain-Wall Racetrack Memory. *Science*, **320**(5873), 190–194, 2008.
- [30] D. Khomskii. Classifying multiferroics: Mechanisms and effects. *Physics*, **2**, 20, Mar 2009.
- [31] S.-W. Cheong and M. Mostovoy. Multiferroics: a magnetic twist for ferroelectricity. *Nat Mater*, **6**(1), 13–20, Jan 2007. ISSN 1476-1122. 10.1038/nmat1804.
- [32] T.-H. Arima. Spin-Driven Ferroelectricity and Magneto-Electric Effects in Frustrated Magnetic Systems. *Journal of the Physical Society of Japan*, **80**(5), 052001, 2011.
- [33] H. Katsura, N. Nagaosa, and A. V. Balatsky. Spin Current and Magnetoelectric Effect in Noncollinear Magnets. *Phys. Rev. Lett.*, **95**, 057205, Jul 2005.
- [34] T. Kimura and Y. Tokura. Magnetoelectric phase control in a magnetic system showing cycloidal/conical spin order. *Journal of Physics: Condensed Matter*, **20**(43), 434204, 2008.
- [35] L. C. Chapon, G. R. Blake, M. J. Gutmann, S. Park, N. Hur, P. G. Radaelli, and S.-W. Cheong. Structural Anomalies and Multiferroic Behavior in Magnetically Frustrated TbMn_2O_5 . *Phys. Rev. Lett.*, **93**, 177402, Oct 2004.

- [36] A. A. Bush, V. N. Glazkov, M. Hagiwara, T. Kashiwagi, S. Kimura, K. Omura, L. A. Prozorova, L. E. Svistov, A. M. Vasiliev, and A. Zheludev. Magnetic phase diagram of the frustrated $S = \frac{1}{2}$ chain magnet LiCu_2O_2 . *Phys. Rev. B*, **85**, 054421, Feb 2012.
- [37] O. Heyer, N. Hollmann, I. Klassen, S. Jodlauk, L. Bohatý, P. Becker, J. A. Mydosh, T. Lorenz, and D. Khomskii. A new multiferroic material: MnWO_4 . *Journal of Physics: Condensed Matter*, **18**(39), L471, 2006.
- [38] V. Gnezdilov, P. Lemmens, A. A. Zvyagin, V. O. Chervanovskii, K. Lamonova, Y. G. Pashkevich, R. K. Kremer, and H. Berger. Magnetic crossover and complex excitation spectrum of the ferromagnetic/antiferromagnetic spin- $\frac{1}{2}$ chain system $\alpha\text{-TeVO}_4$. *Phys. Rev. B*, **78**, 184407, Nov 2008.
- [39] F. Cinti, A. Rettori, M. G. Pini, M. Mariani, E. Micotti, A. Lascialfari, N. Papinutto, A. Amato, A. Caneschi, D. Gatteschi, and M. Affronte. Two-Step Magnetic Ordering in Quasi-One-Dimensional Helimagnets: Possible Experimental Validation of Villain's Conjecture about a Chiral Spin Liquid Phase. *Phys. Rev. Lett.*, **100**, 057203, Feb 2008.
- [40] H. Schenck, V. L. Pokrovsky, and T. Nattermann. Vector Chiral Phases in the Frustrated 2D XY Model and Quantum Spin Chains. *Phys. Rev. Lett.*, **112**, 157201, Apr 2014.
- [41] D. Niermann, C. P. Grams, P. Becker, L. Bohatý, H. Schenck, and J. Hemberger. Critical Slowing Down near the Multiferroic Phase Transition in MnWO_4 . *Phys. Rev. Lett.*, **114**, 037204, Jan 2015.
- [42] S. Sachdev. *Quantum Phase Transitions*. Cambridge University Press, 1999.
- [43] A. K. Kolezhuk. Large- S Approach to Chiral Phases in Frustrated Spin Chains. *Progress of Theoretical Physics Supplement*, **145**, 29–36, 2002.
- [44] P. Bak and D. Mukamel. Physical realizations of $n \geq 4$ -component vector models. III. Phase transitions in Cr, Eu, MnS_2 , Ho, Dy, and Tb. *Phys. Rev. B*, **13**, 5086–5094, Jun 1976.
- [45] H. Kawamura. Erratum: Renormalization-group analysis of chiral transitions. *Phys. Rev. B*, **42**, 2610–2610, Aug 1990.
- [46] A. Hubert. *Theorie der Domänenwände in geordneten Medien*, volume 26 of *Lecture Notes in Physics*. Springer-Verlag Berlin, 1974.
- [47] A. A. Nersisyan, A. O. Gogolin, and F. H. L. Eßler. Incommensurate Spin Correlations in Spin-1/2 Frustrated Two-Leg Heisenberg Ladders. *Phys. Rev. Lett.*, **81**, 910–913, Jul 1998.
- [48] H. J. Mikeska and A. K. Kolezhuk. *One-dimensional magnetism*. Lecture Notes in Physics vol. 645. Springer Verlag, 2004.
- [49] H. Kawamura. Renormalization-group analysis of chiral transitions. *Phys. Rev. B*, **38**, 4916–4928, Sep 1988.
- [50] H. Kawamura. Universality of phase transitions of frustrated antiferromagnets. *Journal of Physics: Condensed Matter*, **10**(22), 4707, 1998.
- [51] H. Schulz. *Statistische Physik*. Verlag Harri Deutsch, 2005.

- [52] A. L. Fetter and J. D. Walecka. *Quantum Theory of Many-Particle Systems*. McGraw-Hill Book Company, 1971.
- [53] A. Patashinskii and V. L. Pokrovskii. *Fluctuation Theory of Phase Transitions*. Pergamon Press, 1979.
- [54] E. Pytte. Spurious First-Order Phase Transitions in the Self-Consistent Phonon Approximation. *Phys. Rev. Lett.*, **28**, 895–897, Apr 1972.
- [55] R. M. Hornreich, M. Luban, and S. Shtrikman. Critical Behavior at the Onset of \mathbf{k} -Space Instability on the λ -Line. *Phys. Rev. Lett.*, **35**, 1678–1681, Dec 1975.
- [56] A. O. Sorokin and A. V. Syromyatnikov. Chiral spin liquid in two-dimensional XY helimagnets. *Phys. Rev. B*, **85**, 174404, May 2012.
- [57] A. Sorokin and A. Syromyatnikov. Erratum: Chiral spin liquid in two-dimensional XY helimagnets [Phys. Rev. B 85, 174404 (2012)]. *Phys. Rev. B*, **86**, 059904, Aug 2012.
- [58] E. Weschke, H. Ott, E. Schierle, C. Schüßler-Langeheine, D. V. Vyalikh, G. Kaindl, V. Leiner, M. Ay, T. Schmitte, H. Zabel, and P. J. Jensen. Finite-Size Effect on Magnetic Ordering Temperatures in Long-Period Antiferromagnets: Holmium Thin Films. *Phys. Rev. Lett.*, **93**, 157204, Oct 2004.
- [59] M. Hase, H. Kuroe, K. Ozawa, O. Suzuki, H. Kitazawa, G. Kido, and T. Sekine. Magnetic properties of $\text{Rb}_2\text{Cu}_2\text{Mo}_3\text{O}_{12}$ including a one-dimensional spin-1/2 Heisenberg system with ferromagnetic first-nearest-neighbor and antiferromagnetic second-nearest-neighbor exchange interactions. *Phys. Rev. B*, **70**, 104426, Sep 2004.
- [60] G. Castilla, S. Chakravarty, and V. J. Emery. Quantum Magnetism of CuGeO_3 . *Phys. Rev. Lett.*, **75**, 1823–1826, Aug 1995.
- [61] J. Riera and A. Dobry. Magnetic susceptibility in the spin-Peierls system CuGeO_3 . *Phys. Rev. B*, **51**, 16098–16102, Jun 1995.
- [62] K. Hikomitsu, N. Hiroshi, A. Yoshitami, A. Takayuki, and G. Tsuneaki. Susceptibility and high-field magnetization of one-dimensional $S=12$ Heisenberg antiferromagnet with next-nearest exchange interaction. *Physica B: Condensed Matter*, **284-288**, Part 2(0), 1631–1632, jul 2000. ISSN 0921-4526.
- [63] N. Maeshima, M. Hagiwara, Y. Narumi, K. Kindo, T. C. Kobayashi, and K. Okunishi. Magnetic properties of a $S = 1/2$ zigzag spin chain compound $(\text{N} 2 \text{ H} 5)\text{CuCl} 3$. *Journal of Physics: Condensed Matter*, **15**(21), 3607, 2003.
- [64] M. Hase, K. Ozawa, and N. Shinya. Magnetic properties of $\text{Cu}_6\text{Ge}_6\text{O}_{18-x}\text{H}_2\text{O}$ ($x=0-6$): A compound of $S = 1/2$ Heisenberg competing antiferromagnetic chains coupled by interchain interaction. *Phys. Rev. B*, **68**, 214421, Dec 2003.
- [65] M. Hase, K. Ozawa, and N. Shinya. Magnetic properties of a three-dimensional antiferromagnet formed by three bonds, $\text{Cu}_6\text{Ge}_6\text{O}_{18-x}\text{H}_2\text{O}$ ($x=0-6$). *Journal of Magnetism and Magnetic Materials*, **272-276**, Part 2(0), 869–871, 2004. ISSN 0304-8853.
- [66] T. Masuda, A. Zheludev, A. Bush, M. Markina, and A. Vasiliev. Competition between Helimagnetism and Commensurate Quantum Spin Correlations in LiCu_2O_2 . *Phys. Rev. Lett.*, **92**, 177201, Apr 2004.

- [67] G. Kamieniarz, M. Bielinski, G. Szukowski, R. Szymczak, S. Dyeyev, and J.-P. Renard. Finite temperature quantum transfer-matrix simulations of the frustrated spin-1/2 chains. *Computer Physics Communications*, **147**(1-2), 716–719, 2002. ISSN 0010-4655.
- [68] Y. Mizuno, T. Tohyama, S. Maekawa, T. Osafune, N. Motoyama, H. Eisaki, and S. Uchida. Electronic states and magnetic properties of edge-sharing Cu-O chains. *Phys. Rev. B*, **57**, 5326–5335, Mar 1998.
- [69] M. Matsuda and K. Katsumata. Magnetic properties of a quasi-one-dimensional magnet with competing interactions: SrCuO₂. *Journal of Magnetism and Magnetic Materials*, **140-144**, Part 3(0), 1671–1672, Feb 1995. ISSN 0304-8853.
- [70] M. Matsuda, K. Katsumata, K. M. Kojima, M. Larkin, G. M. Luke, J. Merrin, B. Nachumi, Y. J. Uemura, H. Eisaki, N. Motoyama, S. Uchida, and G. Shirane. Magnetic phase transition in the S= zigzag-chain compound SrCuO₂. *Phys. Rev. B*, **55**, R11953–R11956, May 1997.
- [71] T. Masuda, A. Zheludev, B. Roessli, A. Bush, M. Markina, and A. Vasiliev. Spin waves and magnetic interactions in LiCu₂O₂. *Phys. Rev. B*, **72**, 014405, Jul 2005.
- [72] T. Masuda, A. Zheludev, A. Bush, M. Markina, and A. Vasiliev. Masuda *et al.* Reply. *Phys. Rev. Lett.*, **94**, 039706, Jan 2005.
- [73] H. Kikuchi, M. Chiba, and T. Kubo. Possible gapless chiral phase in a frustrated S = 1 1D anti-ferromagnet, CaV₂O₄. *Canadian Journal of Physics*, **79**(11-12), 1551–1555, 2001.
- [74] A. Lascialfari, R. Ullu, M. Affronte, F. Cinti, A. Caneschi, D. Gatteschi, D. Rovai, M. G. Pini, and A. Rettori. Specific heat and μ^+ SR measurements in Gd(hfac)₃NiTiPr molecular magnetic chains: Indications for a chiral phase without long-range helical order. *Phys. Rev. B*, **67**, 224408, Jun 2003.
- [75] M. Affronte, A. Caneschi, C. Cucci, D. Gatteschi, J. C. Lasjaunias, C. Paulsen, M. G. Pini, A. Rettori, and R. Sessoli. Low-temperature thermodynamic properties of molecular magnetic chains. *Phys. Rev. B*, **59**, 6282–6293, Mar 1999.
- [76] T. Nattermann. Private Communication, 2013.
- [77] S. Kim. Vortex interaction in Josephson-junction ladders. *Physics Letters A*, **229**(3), 190–194, 1997. ISSN 0375-9601.
- [78] F. Kusmartsev, D. Faruque, and D. Khomskii. Quasiclassical method for Josephson network in magnetic field. *Physics Letters A*, **249**(5-6), 541–554, 1998. ISSN 0375-9601.
- [79] A. A. Golubov, M. Y. Kupriyanov, and E. Il'ichev. The current-phase relation in Josephson junctions. *Rev. Mod. Phys.*, **76**, 411–469, Apr 2004.
- [80] A. K. Feofanov, V. A. Oboznov, V. V. Bol'ginov, J. Lisenfeld, S. Poletto, V. V. Ryazanov, A. N. Rossolenko, M. Khabipov, D. Balashov, A. B. Zorin, P. N. Dmitriev, V. P. Koshelets, and A. V. Ustivnov. Implementation of superconductor/ferromagnet/ superconductor π -shifters in superconducting digital and quantum circuits. *Nature*, **6**, 593–597, Jun 2010.
- [81] O. Bourgeois, P. Gandit, A. Sulpice, J. Chaussy, J. Lesueur, and X. Grison. Transport in superconductor/ferromagnet/superconductor junctions dominated by interface resistance. *Phys. Rev. B*, **63**, 064517, Jan 2001.

- [82] E. Goldobin, D. Koelle, R. Kleiner, and R. G. Mints. Josephson Junction with a Magnetic-Field Tunable Ground State. *Phys. Rev. Lett.*, **107**, 227001, Nov 2011.
- [83] P. Martinoli and C. Leemann. Two Dimensional Josephson Junction Arrays. *Journal of Low Temperature Physics*, **118**(5-6), 699–731, 2000. ISSN 0022-2291.
- [84] S. Herbert, L. Gómez, D. Mast, R. Newrock, C. Wilks, and C. Falco. Fabrication of 3D proximity coupled Josephson junction arrays. *Superlattices and Microstructures*, **18**(1), 53–, 1995. ISSN 0749-6036.
- [85] J. Villain. Chiral order in helimagnets. *Annals of the Israel Physical Society*, **2**, 565, 1978.
- [86] T. Garel and S. Doniach. On the critical behaviour of two-dimensional XY helimagnets. *Journal of Physics C: Solid State Physics*, **13**(31), L887, 1980.
- [87] Y. Okwamoto. Phase Transitions of Two-Dimensional Helical XY Models. *Journal of the Physical Society of Japan*, **53**(8), 2613–2621, 1984.
- [88] P. Lecheminant, T. Jolicoeur, and P. Azaria. Phase transitions in the one-dimensional spin- SJ_1-J_2XY model. *Phys. Rev. B*, **63**, 174426, Apr 2001.
- [89] T. Hikihara, M. Kaburagi, and H. Kawamura. Ground-state phase diagrams of frustrated spin- S XXZ chains: Chiral ordered phases. *Phys. Rev. B*, **63**, 174430, Apr 2001.
- [90] O. Dimitrova. Chiral spin liquid in a two-dimensional two-component helical magnet. *Phys. Rev. B*, **90**, 014409, Jul 2014.
- [91] H. Kleinert and V. Schulte-Frohlinde. *Critical Properties of ϕ^4 -Theories*. World Scientific, 2001.
- [92] T.-H. Arima. Ferroelectricity Induced by Proper-Screw Type Magnetic Order. *Journal of the Physical Society of Japan*, **76**(7), 073702, 2007.
- [93] I. Dzyaloshinskii. Theory of Helicoidal Structures in Antiferromagnets. I. Nonmetals . *JETP*, **19**(4), 960, 1964.
- [94] T. Moriya. New Mechanism of Anisotropic Superexchange Interaction. *Phys. Rev. Lett.*, **4**, 228–230, Mar 1960.
- [95] E. Soergel. Piezoresponse force microscopy (PFM). *Journal of Physics D: Applied Physics*, **44**(46), 464003, 2011.
- [96] F. Chernous'ko. A local variation method for the numerical solution of variational problems. *{USSR} Computational Mathematics and Mathematical Physics*, **5**(4), 234–242, 1965. ISSN 0041-5553.
- [97] A. Erdélyi, W. Magnus, F. Oberhettinger, and F. G. Tricomi. *Higher Transcendental Functions*, volume Vol I. McGraw-Hill Book Company, 1953.
- [98] G. Lautenschläger, H. Weitzel, T. Vogt, R. Hock, A. Böhm, M. Bonnet, and H. Fuess. Magnetic phase transitions of $MnWO_4$ studied by the use of neutron diffraction. *Phys. Rev. B*, **48**, 6087–6098, Sep 1993.
- [99] K. Taniguchi, N. Abe, T. Takenobu, Y. Iwasa, and T. Arima. Ferroelectric Polarization Flop in a Frustrated Magnet $MnWO_4$ Induced by a Magnetic Field. *Phys. Rev. Lett.*, **97**, 097203, Aug 2006.

- [100] P. Tolédano, B. Mettout, W. Schranz, and G. Krexner. Directional magnetoelectric effects in MnWO_4 : magnetic sources of the electric polarization. *Journal of Physics: Condensed Matter*, **22**(6), 065901, 2010.
- [101] M. Hamermesh. *Group Theory And Its Application To Physical Problems*. Addison-Wesley Series In Physics. Addison-Wesley, 1962.
- [102] O. Kovalev. *Representations of the Crystallographic Space Groups*. Gordon and Breach Science Publishers, 2nd edition, 1993.
- [103] K. Olbrychski. Abstract Definition and Representations of a Space Group. *physica status solidi (b)*, **3**(10), 1868–1875, 1963. ISSN 1521-3951.
- [104] E. F. Bertaut. Representation analysis of magnetic structures. *Acta Crystallographica Section A*, **24**(1), 217–231, 1968. ISSN 1600-5724.
- [105] E. F. Bertaut. MAGNETIC STRUCTURE ANALYSIS AND GROUP THEORY. *J. Phys. Colloques*, **32**, C1–462–C1–470, 1971.
- [106] S. Matityahu, A. Aharony, and O. Entin-Wohlman. Landau theory for the phase diagram of multiferroic $\text{Mn}_{1-x}(\text{Fe,Zn,Mg})_x\text{WO}_4$. *Phys. Rev. B*, **85**, 174408, May 2012.
- [107] K. B. Varnashev. The stability of a cubic fixed point in three dimensions from the renormalization group. *Journal of Physics A: Mathematical and General*, **33**(16), 3121, 2000.
- [108] A. Aharony. Critical Behavior of Magnets with Dipolar Interactions. III. Antiferromagnets. *Phys. Rev. B*, **8**, 3349–3357, Oct 1973.
- [109] A. Aharony. *Dependence of Universal Critical Behaviour on Symmetry and Range of Interaction*. Phase Transitions and Critical Phenomena Vol. 6. Academic Press Inc. London, 1976.
- [110] E. Brézin, J. C. L. Guillou, and J. Zinn-Justin. Discussion of critical phenomena for general n -vector models. *Phys. Rev. B*, **10**, 892–900, Aug 1974.
- [111] A. B. Harris, A. Aharony, and O. Entin-Wohlman. Order parameters and phase diagrams of multiferroics. *Journal of Physics: Condensed Matter*, **20**(43), 434202, 2008.
- [112] P. C. Hohenberg and B. I. Halperin. Theory of dynamic critical phenomena. *Rev. Mod. Phys.*, **49**, 435–479, Jul 1977.
- [113] R. Folk and G. Moser. Critical dynamics: a field-theoretical approach. *Journal of Physics A: Mathematical and General*, **39**(24), R207, 2006.
- [114] V. Prudnikov, A. Ivanov, and A. Fedorenko. Critical dynamics of spin systems in the four-loop approximation. *Journal of Experimental and Theoretical Physics Letters*, **66**(12), 835–840, 1997. ISSN 0021-3640.
- [115] S. Wansleben and D. P. Landau. Monte Carlo investigation of critical dynamics in the three-dimensional Ising model. *Phys. Rev. B*, **43**, 6006–6014, Mar 1991.
- [116] H.-O. Heuer. Critical dynamics of the three-dimensional Ising model: A Monte Carlo study. *Journal of Statistical Physics*, **72**(3-4), 789–827, 1993. ISSN 0022-4715.

- [117] K. Lauritsen and N. Ito. Spectral method determination of dynamic exponents for Ising models. *Physica A: Statistical Mechanics and its Applications*, **202**(1-2), 224–236, 1994. ISSN 0378-4371.
- [118] R. Guida and J. Zinn-Justin. Critical exponents of the N -vector model. *Journal of Physics A: Mathematical and General*, **31**(40), 8103, 1998.
- [119] H. K. Onnes. Further experiments with liquid helium. C. On the change of electric resistance of pure metals at very low temperatures, etc. IV. The resistance of pure mercury at helium temperatures. *Leiden Comm.*, (120b), 1911.
- [120] H. K. Onnes. Further experiments with liquid helium. D. On the change of electric resistance of pure metals at very low temperatures, etc. V. The disappearance of the resistance of mercury. *Leiden Comm.*, (112b), 1911.
- [121] H. K. Onnes. Further experiments with liquid helium. G. On the electrical resistance of pure metals, etc. VI. On the sudden change in the rate at which the resistance of mercury disappears. *Leiden Comm.*, (124c), 1911.
- [122] W. Meissner and R. Ochsenfeld. Ein neuer Effekt bei Eintritt der Supraleitflüssigkeit. *Naturwissenschaften*, **21**(44), 787–788, 1933. ISSN 0028-1042.
- [123] M. Tinkham. *Introduction to Superconductivity*. McGraw-Hill, 1996.
- [124] A. A. Abrikosov. On the Magnetic Properties of Superconductors of the Second Group. *Soviet Phys JETP*, **5**, 1174, 1957.
- [125] J. Pearl. Current distribution in superconduction films carrying quantized fluxoids. *Applied Physics Letters*, **5**(4), 65–66, 1964.
- [126] J. Pearl. *Distinctive properties of quantized vortices in superconducting films*. Jan 1964.
- [127] U. Essmann and H. Träuble. The direct observation of individual flux lines in type II superconductors. *Physics Letters A*, **24**(10), 526–527, may 1967. ISSN 0375-9601.
- [128] A. Finkler, Y. Segev, Y. Myasoedov, M. L. Rappaport, L. Ne’eman, D. Vasyukov, E. Zeldov, M. E. Huber, J. Martin, and A. Yacoby. Self-Aligned Nanoscale SQUID on a Tip. *Nano Letters*, **10**(3), 1046–1049, 2010. PMID: 20131810.
- [129] T. Giamarchi and P. L. Doussal. Moving Glass Phase of Driven Lattices. *Phys. Rev. Lett.*, **76**, 3408–3411, Apr 1996.
- [130] T. Giamarchi and P. L. Doussal. Bragg- and Moving-glasses: a theory of disordered vortex lattices. *Physica C: Superconductivity*, **282-287**, Part 1(0), 363–366, 1997. ISSN 0921-4534.
- [131] F. Pardo, F. de la Cruz, P. L. Gammel, E. Bucher, and D. Bishop. Observation of smectic and moving-Bragg-glass phases in flowing vortex lattices. *Nature*, **396**, 348–350, Nov 1998.
- [132] E. Zeldov and L. Embon. Private Communication. 2013.
- [133] J. Bardeen, L. Cooper, and J. Schrieffer. Theory of Superconductivity. *Phys. Rev.*, **108**, 1175–1204, Dec 1957.
- [134] F. London and H. London. The Electromagnetic Equations of the Supraconductor. *Royal Society of London Proceedings Series A*, **149**, 71–88, March 1935.

- [135] V. L. Ginzburg and L. D. Landau. To the Theory of Superconductivity. *Eksp. Teor. Fiz.*, **20**, 1064, 1950. [The English translation of this paper can be found in L.D. Landau, Collected Papers, Pergamon Press, Oxford, 1965].
- [136] L. Gor'kov. Microscopic derivation of the Ginzburg-Landau equations in the theory of superconductivity. *JETP*, **36**(9), 1364, 1959.
- [137] A. L. Fetter and P. C. Hohenberg. The Mixed State of Thin Superconducting Films in Perpendicular Fields. *Phys. Rev.*, **159**, 330–343, Jul 1967.
- [138] H. P. Myers. *Introductory Solid State Physics*. Taylor & Francis, 1997.
- [139] J. Bass and K. H. Fischer. *Group III Crystal and Solid State Physics*, volume 15 of *Landolt-Börnstein: Numerical Data and Functional Relationships in Science and Technology*. 1982.
- [140] G. D. Cody and R. E. Miller. Magnetic Transitions of Superconducting Thin Films and Foils. III. Pb, Sn, and In. *Phys. Rev. B*, **5**, 1834–1843, Mar 1972.
- [141] J. Bardeen and M. J. Stephen. Theory of the Motion of Vortices in Superconductors. *Phys. Rev.*, **140**, A1197–A1207, Nov 1965.
- [142] V. Kopylov, A. Koshelev, I. Schegolev, and T. Togonidze. The role of surface effects in magnetization of high-Tc superconductors. *Physica C: Superconductivity*, **170**(3-4), 291–297, 1990. ISSN 0921-4534.
- [143] L. Burlachkov. Magnetic relaxation over the Bean-Livingston surface barrier. *Phys. Rev. B*, **47**, 8056–8064, Apr 1993.
- [144] E. H. Brandt. Vortex-vortex interaction in thin superconducting films. *Phys. Rev. B*, **79**, 134526, Apr 2009.
- [145] L. Burlachkov, V. B. Geshkenbein, A. E. Koshelev, A. I. Larkin, and V. M. Vinokur. Giant flux creep through surface barriers and the irreversibility line in high-temperature superconductors. *Phys. Rev. B*, **50**, 16770–16773, Dec 1994.
- [146] P. W. Anderson and Y. B. Kim. Hard Superconductivity: Theory of the Motion of Abrikosov Flux Lines. *Rev. Mod. Phys.*, **36**, 39–43, Jan 1964.
- [147] M. R. Beasley, R. Labusch, and W. W. Webb. Flux Creep in Type-II Superconductors. *Phys. Rev.*, **181**, 682–700, May 1969.
- [148] E. Zeldov, J. R. Clem, M. McElfresh, and M. Darwin. Magnetization and transport currents in thin superconducting films. *Phys. Rev. B*, **49**, 9802–9822, Apr 1994.
- [149] E. H. Brandt and G. P. Mikitik. Meissner-London Currents in Superconductors with Rectangular Cross Section. *Phys. Rev. Lett.*, **85**, 4164–4167, Nov 2000.
- [150] I. L. Maksimov and A. A. Elistratov. Edge barrier and structure of the critical state in superconducting thin films. *JETP Letters*, **61**(3), 208, 1995.
- [151] T. Schuster, H. Kuhn, and E. H. Brandt. Flux penetration into flat superconductors of arbitrary shape: Patterns of magnetic and electric fields and current. *Phys. Rev. B*, **54**, 3514–3524, Aug 1996.
- [152] A. A. B. Brojeny and J. R. Clem. Magnetic-field and current-density distributions in thin-film superconducting rings and disks. *Phys. Rev. B*, **68**, 174514, Nov 2003.

- [153] E. H. Brandt and M. Indenbom. Type-II-superconductor strip with current in a perpendicular magnetic field. *Phys. Rev. B*, **48**, 12893–12906, Nov 1993.
- [154] L. Prigozhin. Solution of Thin Film Magnetization Problems in Type-II Superconductivity. *Journal of Computational Physics*, **144**(1), 180–193, 1998. ISSN 0021-9991.
- [155] E. H. Brandt. Supercurrents and vortices in {SQUIDS} and films of various shapes. *Physica C: Superconductivity*, **460-462**, Part 1(0), 327–330, 2007. ISSN 0921-4534.
- [156] E. H. Brandt. Thin superconductors and SQUIDS in perpendicular magnetic field. *Phys. Rev. B*, **72**, 024529, Jul 2005.
- [157] E. Bronson, M. P. Gelfand, and S. B. Field. Equilibrium configurations of Pearl vortices in narrow strips. *Phys. Rev. B*, **73**, 144501, Apr 2006.
- [158] M. B. Ketchen, W. J. Gallagher, A. W. Kleinsasser, S. Murphy, and J. R. Clem. DC SQUID Flux Focuser. SQUID '85 - Superconducting Quantum Interference Devices and their Applications, pages 865–871. de Gruyter, 1985.
- [159] L. Radzihovsky. Thermal depinning and transverse-field tilting transitions in a planar vortex array pinned by a columnar defect. *Phys. Rev. B*, **73**, 104504, Mar 2006.
- [160] A. Prudnikov, Y. Brychkov, and O. Marichev. Volume 2: Special Functions. **2**, 1998.
- [161] O. Narayan and D. Fisher. Nonlinear fluid flow in random media: Critical phenomena near threshold. *Phys. Rev. B*, **49**, 9469–9502, Apr 1994.
- [162] D. W. Braun, G. W. Crabtree, H. G. Kaper, A. E. Koshelev, G. K. Leaf, D. M. Levine, and V. M. Vinokur. Structure of a Moving Vortex Lattice. *Phys. Rev. Lett.*, **76**, 831–834, Jan 1996.
- [163] L. Elliott, S. Theodore, and M. Daniel. Two soluble models of an antiferromagnetic chain. *Annals of Physics*, **16**(3), 407–466, dec 1961. ISSN 0003-4916.
- [164] F. D. M. Haldane. 'Luttinger liquid theory' of one-dimensional quantum fluids. I. Properties of the Luttinger model and their extension to the general 1D interacting spinless Fermi gas. *Journal of Physics C: Solid State Physics*, **14**(19), 2585, 1981.
- [165] A. Dutta, U. Divakaran, D. Sen, B. K. Chakrabarti, T. F. Rosenbaum, and G. Aeppli. Quantum phase transitions in transverse field spin models: From Statistical Physics to Quantum Information. *ArXiv e-prints*, December 2010.
- [166] T. Holstein and H. Primakoff. Field Dependence of the Intrinsic Domain Magnetization of a Ferromagnet. *Phys. Rev.*, **58**, 1098–1113, Dec 1940.
- [167] P. W. Anderson. An Approximate Quantum Theory of the Antiferromagnetic Ground State. *Phys. Rev.*, **86**, 694–701, Jun 1952.
- [168] R. Kubo. The Spin-Wave Theory of Antiferromagnetics. *Phys. Rev.*, **87**, 568–580, Aug 1952.
- [169] E. Fradkin. *Field Theories of Condensed Matter Systems*. Frontiers in Physics. Addison-Wesley Publishing Company, 1991.
- [170] E. Manousakis. The spin- $\frac{1}{2}$ Heisenberg antiferromagnet on a square lattice and its application to the cuprous oxides. *Rev. Mod. Phys.*, **63**, 1–62, Jan 1991.

-
- [171] A. K. Kolezhuk. Quantum chiral phases in frustrated easy-plane spin chains. *Phys. Rev. B*, **62**, R6057–R6060, Sep 2000.
- [172] C. Kittel. *Einführung in die Festkörperphysik*. Oldenbourg, 8 edition, 1989.
- [173] A. W. Manjunath, T. Sankarappa, R. Ramanna, J. S. Ashwajeet, T. Sujatha, and P. Sarvanan. Low Temperature Electrical Resistivity Studies in Lead Thin Films. *Journal of Nano- and Electronic Physics*, **5**(3), 03026, 2013.
- [174] A. Eiling and J. S. Schilling. Pressure and temperature dependence of electrical resistivity of Pb and Sn from 1-300K and 0-10 GPa-use as continuous resistive pressure monitor accurate over wide temperature range; superconductivity under pressure in Pb, Sn and In. *Journal of Physics F: Metal Physics*, **11**(3), 623, 1981.
- [175] R. E. Glover. Currents and Fields in a Superconducting Film Carrying a Steady Current: Discussion. In G. M. Graham and A. C. H. Hallett, editors, *Proceedings of the VIIth International Conference on Low Temperature Physics*, page 416. Univeristy of Toronto Press: Toronto, 1961. see discussion of paper by Marcus.
- [176] L. N. Cooper. Current Flow in Thin Superconducting Films. In G. M. Graham and A. C. H. Hallett, editors, *Proceedings of the VIIth International Conference on Low Temperature Physics*, page 416. Univeristy of Toronto Press: Toronto, 1961.
- [177] P. M. Marcus. Currents and Fields in a Superconducting Film Carrying a Steady Current. In G. M. Graham and A. C. H. Hallett, editors, *Proceedings of the VIIth International Conference on Low Temperature Physics*, page 418. Univeristy of Toronto Press: Toronto, 1961.
- [178] E. H. Rhoderick and E. M. Wilson. Current Distribution in Thin Superconducting Films. *Nature*, **194**(4834), 1167–1168, jun 1962. 10.1038/1941167b0.
- [179] R. E. Glover and H. T. Coffey. Critical Currents in Thin Planar Films. *Rev. Mod. Phys.*, **36**, 299–302, Jan 1964.
- [180] E. H. Brandt and J. R. Clem. Superconducting thin rings with finite penetration depth. *Phys. Rev. B*, **69**, 184509, May 2004.

Ich versichere, dass ich die von mir vorgelegte Dissertation selbständig angefertigt, die benutzten Quellen und Hilfsmittel vollständig angegeben und die Stellen der Arbeit - einschließlich Tabellen, Karten und Abbildungen -, die anderen Werken im Wortlaut oder dem Sinn nach entnommen sind, in jedem Einzelfall als Entlehnung kenntlich gemacht habe; dass diese Dissertation noch keiner anderen Fakultät oder Universität zur Prüfung vorgelegen hat; dass sie - abgesehen von unten angegebenen Teilpublikationen - noch nicht veröffentlicht worden ist sowie, dass ich eine solche Veröffentlichung vor Abschluss des Promotionsverfahrens nicht vornehmen werde. Die Bestimmungen der Promotionsordnung sind mir bekannt. Die von mir vorgelegte Dissertation ist von Prof. Dr. Thomas Nattermann betreut worden

Ort, Datum

Hannes Schenck

Teilpublikationen:

- H. Schenck, V. L. Pokrovsky and T. Nattermann
Vector chiral phases in frustrated 2D XY model and quantum spin chains
Physical Review Letters **112** 157201 (2014)
- D. Niermann, C. P. Grams, P. Becker, L. Bohatý, H. Schenck and J. Hemberger
Critical slowing down near the multiferroic phase transition in MnWO₄
Physical Review Letters **114** 037204 (2015)